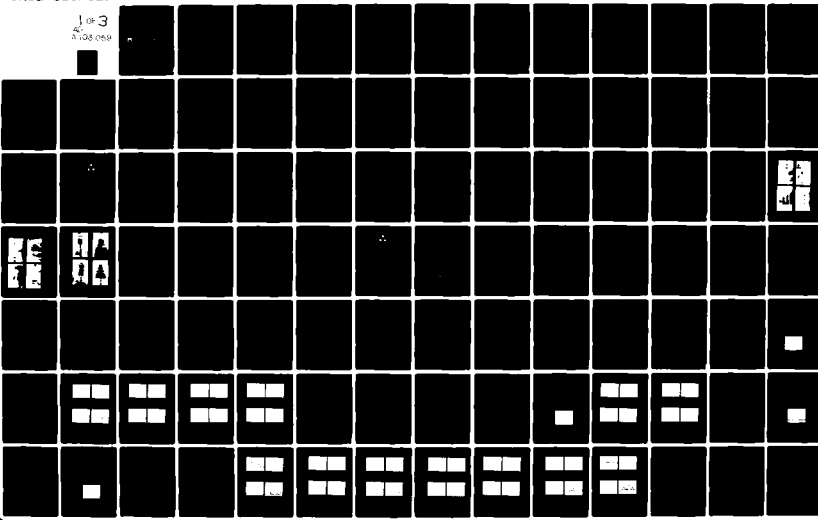


AD-A103 059

MISSION RESEARCH CORP ALBUQUERQUE NM
EXPERIMENTAL AND ANALYTICAL METHODS FOR THE CHARACTERIZATION OF--ETC(U)
SEP 80 A K AGRAWAL, J R BARNUM, L D SCOTT F29601-78-C-0082
AFWL-TR-80-35 NL

UNCLASSIFIED

1 of 3
AD-A103 059



AFWL-TR-80-35

(1) LEVEL II

AFWL-TR-
80-35

AD A 103 059



EXPERIMENTAL AND ANALYTICAL METHODS FOR THE CHARACTERIZATION OF B-52 AIRCRAFT MULTICONDUCTOR CABLE NETWORK

Ashok K. Agrawal, et al

Mission Research Corporation
1400 San Mateo Blvd, SE
Albuquerque, NM 87108

September 1980

Final Report

DTIC
ELECTE
S D
AUG 19 1981
B

Approved for public release; distribution unlimited.

REF FILE COPY

AIR FORCE WEAPONS LABORATORY
Air Force Systems Command
Kirtland Air Force Base, NM 87117

81 8 18 079

This final report was prepared by Mission Research Corporation, Albuquerque, New Mexico, under Contract F29601-78-C-0082, Job Order 37630132 with the Air Force Weapons Laboratory, Kirtland Air Force Base, New Mexico. Captain Howard G. Hudson (NTYEII) was the Laboratory Project Officer-in-Charge.

When US Government drawings, specifications, or other data are used for any purpose other than a definitely related Government procurement operation, the Government thereby incurs no responsibility nor any obligation whatsoever, and the fact that the Government may have formulated, furnished, or in any way supplied the said drawings, specifications, or other data, is not to be regarded by implication or otherwise, as in any manner licensing the holder or any other person or corporation, or conveying any rights or permission to manufacture, use, or sell any patented invention that may in any way be related thereto.

This report has been authored by a contractor of the United States Government. Accordingly, the United States Government retains a nonexclusive, royalty-free license to publish or reproduce the material contained herein, or allow others to do so, for the United States Government purposes.

This report has been reviewed by the Public Affairs Office and is releasable to the National Technical Information Service (NTIS). At NTIS, it will be available to the general public, including foreign nations.

This technical report has been reviewed and is approved for publication.

Howard G. Hudson
HOWARD G. HUDSON
Captain, USAF
Project Officer

J. Philip Castillo
J. PHILIP CASTILLO
Chief, Electromagnetics Branch

FOR THE DIRECTOR:

Norman K. Blocker
NORMAN K. BLOCKER
Chief, Applied Physics Division

DO NOT RETURN THIS COPY. RETAIN OR DESTROY.

~~UNCLASSIFIED~~

SECURITY CLASSIFICATION OF THIS PAGE (When Data Entered)

DD FORM 1 JAN 73 1473 EDITION OF 1 NOV 65 IS OBSOLETE

UNCLASSIFIED

SECURITY CLASSIFICATION OF THIS PAGE (When Data Entered)

UNCLASSIFIED

SECURITY CLASSIFICATION OF THIS PAGE(When Data Entered)

Block No. 20 (Continued)

bulkhead penetrations are characterized and included in the model. A comparison of measured bulk current transfer ratios in the aircraft and in the laboratory along with calculated results is presented. ←

UNCLASSIFIED

SECURITY CLASSIFICATION OF THIS PAGE(When Data Entered)

CONTENTS

<u>Section</u>		<u>Page</u>
I	INTRODUCTION	15
II	CABLE DESCRIPTION	19
	1. B-52 AIRCRAFT CABLE	19
	2. CABLE MOCKUP IN THE LABORATORY	24
	3. SIMPLIFIED CABLE MODEL	27
III	MEASUREMENTS OF THE PARAMETERS OF THE CABLE	42
	1. MEASUREMENT OF THE COMMON-MODE CHARACTERISTIC IMPEDANCE OF THE FOUR-CONDUCTOR LINE	43
	2. CALCULATION OF THE COMMON-MODE CHARACTERISTIC IMPEDANCE OF THE FOUR-CONDUCTOR LINE	52
	3. MEASUREMENT OF THE COMMON-MODE CHARACTERISTICS OF THE FOUR-CONDUCTOR LINE WITH PERIODIC DISCONTINU- ITIES	54
	A. Four-Wire Line Supported By Periodic Metallic Ribs	57
	B. Four-Wire Line Supported by Periodic Metallic Ribs and Clamps	59
	C. Four-Wire Line Passing Through Periodic Bulk- head Penetrations	61
IV	MEASURED RESULTS	64
	1. UNIFORM FOUR-WIRE LINE	64
	A. Uniform Four-Wire Line Excited in the Common Mode	74
	2. B-52 AIRCRAFT MULTICONDUCTOR CABLE	78
	A. Time-Domain Measurements	79
	B. Frequency-Domain Measurements	80

CONTENTS (Continued)

<u>Section</u>		<u>Page</u>
3.	SIMULATED CABLE IN THE LABORATORY	80
A.	Time-Domain Measurements	81
B.	Frequency-Domain Measurements	81
4.	EQUIVALENT FOUR-WIRE CABLE	82
5.	SIMPLIFIED CABLE MODEL	83
6.	COMPARISON BETWEEN AIRCRAFT AND LABORATORY MEASURED RESULTS	83
A.	Time-Domain Results	83
B.	Frequency-Domain Results	120
V	ANALYTICAL MODELING BY A SINGLE TRANSMISSION LINE	122
1.	MODEL	122
2.	MODEL PARAMETERS	122
3.	ANALYSIS	123
4.	RESULTS	125
5.	RECOMMENDATIONS	127
VI	VALIDITY OF CALCULATIONAL METHODS FOR AIRCRAFT CABLE ASSESSMENT	132
1.	TRANSMISSION LINE GEOMETRY	132
2.	REVIEW OF THE TRANSMISSION LINE SOLUTIONS	134
3.	CALCULATED MULTICONDUCTOR RESPONSE	139
4.	THE SINGLE LINE APPROXIMATION TO A MULTICONDUCTOR CABLE RESPONSE	162
5.	CONCLUDING REMARKS	171

CONTENTS (Concluded)

<u>Section</u>		<u>Page</u>
VII CONCLUSIONS AND OBSERVATIONS		174
REFERENCES		179
APPENDIX A - DETAILED DESCRIPTION OF THE CLAMPLING LOCATIONS ON THE AIRCRAFT CABLE AND THE LABORATORY CABLE MODEL		183
APPENDIX B - MEASURED INPUT IMPEDANCE AND ADMITTANCE DATA (FOUR-WIRE LINE OVER STYROFOAM BLOCKS)		199
APPENDIX C - MEASURED INPUT IMPEDANCE AND ADMITTANCE DATA (FOUR-WIRE LINE OVER RIBS)		209
APPENDIX D - MEASURED INPUT IMPEDANCE AND ADMITTANCE DATA (FOUR-WIRE LINE OVER RIBS WITH CLAMPS)		219
APPENDIX E - MEASURED INPUT IMPEDANCE AND ADMITTANCE DATA (FOUR-WIRE LINE THROUGH 2" BULKHEADS)		229

Accession For	
NTIS GRA&I	<input checked="" type="checkbox"/>
DTIC TAB	<input type="checkbox"/>
Unannounced	<input type="checkbox"/>
Justification	
By	
Distribution/	
Availability Codes	
Avail and/or	
Dist	Special
A	

ILLUSTRATIONS

<u>Figure</u>		<u>Page</u>
1	Cable position relative to the skin and girders running parallel to the skin, and extending below the bottom of the fuel tank.	20
2	Cable position relative to the bottom of the fuel tank and bulkheads.	21
3	Cable position around the girder in the aft section.	22
4	Cross-section of four-wire cable.	25
5	Comparison of ribs in the aircraft and in the laboratory (side view).	26
6	Laboratory simulated cable mock-up (Section 1, Station 648-694, total length 87 inches).	28
7	Laboratory simulated cable mock-up (Section 2, Station 694-805, total length 111.5 inches).	29
8	Laboratory simulated cable mock-up (Section 3, Station 805-917, total length 112.3 inches).	30
9	Laboratory simulated cable mock-up (Section 4, Station 917-1028, total length 127.8 inches).	31
10	Laboratory simulated cable mock-up (Section 5, Station 1028-1237, total length 216.7 inches).	32
11	Laboratory simulated cable mock-up (Section 6, Station 1237-1327, total length 102 inches).	33
12	Laboratory simulated cable mock-up (Section 7, Station 1327-1484, total length 163.5 inches).	34
13	Laboratory simulated cable mock-up (Section 8, Station 1484, total length 180 inches).	35
14	Laboratory simulated cable mock-up (Section 9, Station 148-1528.5, total length 53.5 inches).	36
15	Photographs showing the layout of the cable in the laboratory.	37

ILLUSTRATIONS (Continued)

<u>Figure</u>		<u>Page</u>
16	Photographs showing the layout of the cable in the laboratory.	38
17	Photographs showing the layout of the cable in the laboratory.	39
18	Simplified cable model containing eight uniform sections.	41
19	Cross-section of four-wire line over a ground plane.	44
20	Multiconductor experimental setup.	45
21	Swept impedance block diagram.	46
22	Schematic diagram of the measurement method.	47
23	(a) Equivalent circuit for unit cell of a loaded transmission line; (b) cascade connection of basic unit-cell networks.	55
24	Periodic structure terminated in a load Z_L .	56
25	Four-wire cable over a rib.	57
26	Four-wire line supported by a rib and a clamp.	60
27	Four-wire line through a bulkhead penetration.	62
28	Uniform four-wire line over a ground plane.	65
29	Pulse generator output signal: Vert. sens. 5 V/div, horiz. sens. 2 ns/div, 50Ω termination on the scope.	65
30	Voltage waveform at the load end, with wire 1 driven at the input end. Horizontal scale: 10 ns/div.	67
31	Current waveforms at the load end, with wire 1 driven at the input end. Horizontal scale: 10 ns/div.	68
32	Voltage waveforms at the load end, with wire 4 driven at the input end. Horizontal scale: 10 ns/div.	69

ILLUSTRATIONS (Continued)

<u>Figure</u>		<u>Page</u>
33	Current waveforms at the load end, with wire 4 driven at the input end. Horizontal scale: 10 ns/div.	70
34	Setup for the measurement of currents.	71
35	Uniform four-wire line over a ground plane, excited in the common mode.	75
36	Pulse generator output signal. Vert. sens. 5 V/div, horiz. sens. 5 ns/div, 50- Ω termination on the scope.	75
37	Voltage waveforms at the load end, when the line is excited in common mode. Horizontal scale: 5 ns/div.	76
38	Current waveforms at the load, when the line is excited in common mode. Horizontal scale: 5 ns/div.	77
39	Input waveform used to drive the aircraft cable. Vertical scale: 5V/div; Horizontal scale: 2 ns/div, 50- Ω termination on the scope.	79
40	Input waveform used to drive the laboratory cable model. Vertical scale: 5 V/div; Horizontal scale: 2 ns/div; 50- Ω termination on the scope.	81
41	Current waveforms at Station 1489, with the cable driven at the input end, Station 1528.5, in the common mode. Horizontal scale: 10 ns/div.	84
42	Current waveforms at Station 1471, with the cable driven at the input end, Station 1528.5, in the common mode. Horizontal scale: 10 ns/div; Vertical scale: 40 mA/div.	85
43	Current waveforms at Station 1422, with the cable driven at the input end, Station 1528.5, in the common mode. Horizontal scale: 10 ns/div; Vertical scale: 40 mA/div.	86
44	Current waveforms at Station 1382, with the cable driven at the input end, Station 1528.5, in the common mode. Horizontal scale: 10 ns/div; Vertical scale: 40 mA/div.	87
45	Current waveforms at Station 1342, with the cable driven at the input end, Station 1528.5, in the common mode. Horizontal scale: 10 ns/div; Vertical scale: 40 mA/div.	88

ILLUSTRATIONS (Continued)

<u>Figure</u>		<u>Page</u>
46	Current waveforms at Station 990, with the cable driven at the input end, Station 1528.5, in the common mode. Horizontal scale: 20 ns/div; Vertical scale: 20 mA/div.	89
47	Current waveforms at Station 940, with the cable driven at the input end, Station 1528.5, in the common mode. Horizontal scale: 20 ns/div; Vertical scale: 20 mA/div.	90
48	Current transfer ratio at Station 1471, with reference at Station 1489.	91
49	Current transfer ratio at Station 1471, with reference at Station 1489.	92
50	Current transfer ratio at Station 1471, with reference at Station 1489.	93
51	Current transfer ratio at Station 1442, with reference at Station 1489.	94
52	Current transfer ratio at Station 1442, with reference at Station 1489.	95
53	Current transfer ratio at Station 1442, with reference at Station 1489.	96
54	Current transfer ratio at Station 1412, with reference at Station 1489.	97
55	Current transfer ratio at Station 1412, with reference at Station 1489.	98
56	Current transfer ratio at Station 1412, with reference at Station 1489.	99
57	Current transfer ratio at Station 1382, with reference at Station 1489.	100
58	Current transfer ratio at Station 1382, with reference at Station 1489.	101
59	Current transfer ratio at Station 1382, with reference at Station 1489.	102

ILLUSTRATIONS (Continued)

<u>Figure</u>		<u>Page</u>
60	Current transfer ratio at Station 940, with reference at Station 1489.	103
61	Current transfer ratio at Station 940, with reference at Station 1489.	104
62	Current transfer ratio at Station 940, with reference at Station 1489.	105
63	Current transfer ratio at Station 940, with reference at Station 1489.	106
64	Short-circuit input-impedance data - aircraft cable.	107
65	Open-circuit input-admittance data - aircraft cable.	108
66	Short-circuit input-impedance data - simulated cable (lab).	109
67	Open-circuit input-admittance data - simulated cable (lab).	110
68	Short-circuit input-impedance data - four-wire cable (lab).	111
69	Open-circuit input-admittance data - four-wire cable (lab).	112
70	Short-circuit input-impedance data - simplified cable (lab).	113
71	Open-circuit input-admittance data - simplified cable (lab).	114
72	Current waveforms along the length of the aircraft cable.	115
73	Current waveforms on the simulated cable at Station 1382 in presence of other cables running parallel to it. Horizontal scale: 10 ns/div; Vertical scale: 40 mA/div.	117

ILLUSTRATIONS (Continued)

<u>Figure</u>		<u>Page</u>
74	Current waveforms on the simulated cable at Station 990 and 940 in presence of other cables passing through the bulkheads. Horizontal scale: 20 ns/div; Vertical scale: 20 mA/div.	119
75	Model of a transmission line with shunt capacitances.	124
76	A section of the transmission line with a shunt capacitance.	124
77	Magnitude of transfer current ratio $ I_{1471}/I_{1489} $ at Station 1471.	128
78	Magnitude of transfer current ratio at Station 1471.	129
79	Magnitude of transfer current ratio $ I_{940}/I_{1489} $ at Station 940.	130
80	Magnitude of transfer current ratio at Station 940.	131
81	Geometry of four-wire multiconductor line excited by an incident, step planewave.	133
82	Histogram of current eigenmode velocities for the four-wire transmission line of Figure 19.	140
83	Histograms showing the four normalized current eigenmodes for the four-wire line of Figure 19.	141
84	Field coupling vector for wire i of multiconductor line over a ground plane.	143
85	Transient wire currents at load end ($z=0$) for each wire of multiconductor line for various load conditions.	144
86	Transient wire voltages at load end ($z=0$) for each wire for the multiconductor line for various load impedances.	147
87	Total transient current at $z=0$.	148
88	Average transient voltage at $z=0$.	150

ILLUSTRATIONS (Continued)

<u>Figure</u>		<u>Page</u>
89	Plot of the transient wire current (any wire) at z=0 for averaged (L'_{nm}) and (C'_{nm}) matrices.	152
90	Plot of total transient current at z=0 for averaged (L'_{nm}) and (C'_{nm}) matrices.	153
91	Plot of transient wire currents at z=0 for all modes having the same velocity.	155
92	Plot of total transient load current at z=0 for all modes having the same velocity.	157
93	Plot of transient wire currents for unbalanced load.	159
94	Plot of total transient load current at z=0 for case of unbalanced load impedance.	161
95	Plot of the time dependent single wire current at z=0, using SNGLIN (Ref. 25) modeling assumptions.	164
96	Plot of the time dependent, single wire current at z=0, using reflection coefficient modeling assumptions (Ref. 10).	169
B1	Short-circuit input impedance data - four-wire line over styrofoam blocks.	200
B2	Short-circuit input-impedance data - four-wire line over styrofoam blocks.	201
B3	Short-circuit input-impedance data - four-wire line over styrofoam blocks.	202
B4	Short-circuit input-impedance data - four-wire line over styrofoam blocks.	203
B5	Open-circuit input-admittance data - four-wire line over styrofoam blocks.	204
B6	Open-circuit input-admittance data - four-wire line over styrofoam blocks.	205

ILLUSTRATIONS (Continued)

<u>Figure</u>		<u>Page</u>
B7	Open-circuit input-admittance data - four-wire line over styrofoam blocks.	206
B8	Open-circuit input-admittance data - four-wire line over styrofoam blocks.	207
B9	Open-circuit input-admittance data - four-wire line over styrofoam blocks.	208
C1	Short-circuit input-impedance data - four-wire line over ribs.	210
C2	Short-circuit input-impedance data - four-wire line over ribs.	211
C3	Short-circuit input-impedance data - four-wire line over ribs.	212
C4	Short-circuit input-impedance data - four-wire line over ribs.	213
C5	Open-circuit input-admittance data - four-wire line over ribs.	214
C6	Open-circuit input-admittance data - four-wire line over ribs.	215
C7	Open-circuit input-admittance data - four-wire line over ribs.	216
C8	Open-circuit input-admittance data - four-wire line over ribs.	217
C9	Open-circuit input-admittance data - four-wire line over ribs.	218
D1	Short-circuit input-impedance data - four-wire line over ribs with clamps.	220
D2	Short-circuit input-impedance data - four-wire line over ribs with clamps.	221

ILLUSTRATIONS (Continued)

<u>Figure</u>		<u>Page</u>
D3	Short-circuit input-impedance data - four-wire line over ribs with clamps.	222
D4	Short-circuit input-impedance data - four-wire line over ribs with clamps.	223
D5	Open-circuit input-admittance data - four-wire line over ribs with clamps.	224
D6	Open-circuit input-admittance data - four-wire line over ribs with clamps.	225
D7	Open-circuit input-admittance data - four-wire line over ribs with clamps.	226
D8	Open-circuit input-admittance data - four-wire line over ribs with clamps.	227
D9	Open-circuit input-admittance data - four-wire line over ribs with clamps.	228
E1	Short-circuit input-impedance data - four-wire line through 2" bulkheads.	230
E2	Short-circuit input-impedance data - four-wire line through 2" bulkheads.	231
E3	Short-circuit input-impedance data - four-wire line through 2" bulkheads.	232
E4	Short-circuit input-impedance data - four-wire line through 2" bulkheads.	233
E5	Open-circuit input-admittance data - four-wire line through 2" bulkheads.	234
E6	Open-circuit input-admittance data - four-wire line through 2" bulkheads.	235
E7	Open-circuit input-admittance data - four-wire line through 2" bulkheads.	236

ILLUSTRATIONS (Concluded)

<u>Figure</u>		<u>Page</u>
E8	Open-circuit input-admittance data - four-wire line through 2" bulkheads.	237
E9	Open-circuit input-admittance data - four-wire line through 2" bulkheads.	238

TABLES

<u>Table</u>		<u>Page</u>
1	Bulk quantities for four wire line at $z=0$ load (diagonal)	149
2	Summary of single wire current response using SNGLIN (Ref. 25) Modeling Assumptions	165
3	Summary of single wire current response using reflection coefficient modeling assumptions (Ref. 10)	170
4	Summary of single wire response using common mode impedance assumptions of Section III	172

SECTION I

INTRODUCTION

The distribution of EMP energy within an aircraft after penetration of the aircraft's skin has long been a problem of considerable interest. The energy from the point of penetration is propagated to the circuit elements via closely coupled multiconductor cables. The multiconductor cables are generally made of conductors with different insulating materials, resulting in a cross-sectionally inhomogeneous medium. Such cables often have branches where some of the conductors of the cable branch and/or some other conductors may join the cable. These cables have large number of discontinuities such as clamps, ribs, bulkheads, etc., and the distance between the cable and skin of the aircraft changes randomly along the length, resulting in a nonuniform cable.

The analysis of such multiconductor cables is very complex. In theory, it is possible to solve this problem exactly, but for a typical aircraft, due to the complexity of the system, it may not be practical to attempt to solve this problem exactly. In the past, Tesche and Liu developed a computer code for the analysis of multiconductor line networks (Ref. 1). Recently, the problem of transient analysis of multiconductor lines excited by nonuniform electromagnetic fields has been discussed in detail (Refs. 2, 3). Under contracts F29601-76-C-0091 and F29601-77-C-0040, Mission Research Corporation (MRC) developed improved techniques for making transient and CW measurements on multiconductor line segments (Refs. 4, 5). Measurement techniques to measure the per-unit-length parameters of uniform multiconductor lines were developed (Refs. 6, 7). The transient measurements on a multiconductor line with a branch were made and the transient analysis of such a cable was presented (Ref. 8). The computer code in Reference 1 was successful in duplicating the transient responses measured by MRC under a laboratory environment (Ref. 9). The code was only marginally successful in computing results to compare with measurements made on a power cable

tested in the TACAMO Add-on Testing program (Ref. 9). It is concluded in this report that the poor comparisons between analytical data and data taken on board an aircraft result primarily from the complex cable environment on the aircraft which is difficult to model in the computer model.

To predict more accurately the response of a multiconductor cable in an aircraft, the computer code (Ref. 1) will have to be modified drastically to account for a large number of discontinuities on the cable. Analytical models for clamps, metallic ribs, and bulkheads need to be developed for multiconductor cables in order to include their effect on the multiconductor line response. The equivalent circuits for ribs and clamps for single-wire line have been developed (Refs. 11, 12).

An often used technique for analyzing internal interaction problems is to model multiconductor transmission lines by single-wire transmission lines. The formulation and analysis in this case is simple, and the computer programs needed to obtain numerical results are relatively simple and can be implemented on a small computer. The single-line model of the multiconductor transmission line represents the bulk or common-mode propagation on the multiconductor line. Since the individual wires in multiconductor cables in a typical aircraft are closely coupled, the coupling to the cable from an external electromagnetic field can be described, in many cases, by common-mode coupling. If the incident field varies along the length of the cable, other modes are also excited. Since the multiconductor cables are not terminated in diagonal loads, the reflections at the loads also give rise to other modes.

In performing a simplified analysis with a single-line model, it is desirable to determine the equivalent single-line parameters in terms of the parameters defining the multiconductor line. This is done by assuming that the single line has the same characteristics as the common-mode characteristics of the multiconductor line. To assure this

requirement, it is necessary to choose an optimum load impedance and characteristic impedance for the single-line model, using knowledge of the multiconductor line. The procedure to determine the common-mode characteristic impedance of the multiconductor line will be discussed in this report. The method to determine an optimum load will not be discussed in this report, however, this problem has been addressed in Ref. 10.

This report presents the results of CW and transient measurements made on a multiconductor cable in a B-52 (G-model) aircraft and in the laboratory. The cable in the laboratory is the replica of the B-52 aircraft cable with all the discontinuities which are practically feasible to introduce in the laboratory environment. Comparisons of measurement results obtained on the aircraft and in the laboratory will allow determination of the effects of the aircraft environment on multiconductor cable response.

Three different models are considered in the laboratory. The first model is an attempt to model the aircraft in the laboratory as close as possible by modeling the discontinuities such as metallic ribs, cable clamps, bulkheads etc. This model is driven in the same manner as the aircraft cable. The second model is the same as the first model, except that the cable is simplified at the driving end. The third model is a simplified version of the second model consisting of eight uniform sections, each containing only periodic discontinuities.

In Section II, the cable geometry is described, both in the aircraft and laboratory. In Section III, the parameters of the cable are determined using the measurement techniques developed earlier. The per-unit-length parameters of the uniform sections of the cable are measured. The perturbations on the segments of the aircraft cables often occur at periodic intervals. The propagation characteristics of such periodic structures are also measured in Section III. In Section IV, measured results for the aircraft cable and the laboratory cable are presented. Measurements are also made on a simplified multiconductor model. This model consists of a number of uniform sections, each containing uni-

formly spaced discontinuities. This configuration is easier to model analytically and provides an estimate of errors due to simplifications in the model. A comparison of these results on the aircraft and in the laboratory is presented. This comparison shows the effects of the aircraft environment on multiconductor cable response.

Section V presents the comparison of the calculated and measured results. The calculated results are obtained for the single-line model of the multiconductor cable. In Section VI, the response of a multiconductor cable excited by an external electromagnetic field is studied when the loads are varied. This parameteric study provides an estimate of the effect of variation in loads on the induced currents in the loads, for a given external electromagnetic field. Also presented in Section VI is the validity of the single-line model for the prediction of multiconductor cable response. Several methods for the calculation of the equivalent single-line parameters are compared.

The detailed geometrical configurations of these models are described in Section II.

SECTION II

CABLE DESCRIPTION

1. B-52 AIRCRAFT CABLE

A four-wire AC power cable (31-3115-54) was selected for measurements. This cable delivers power from engine #1 power box (A181) in the forward wheel well to the EMP hydraulic pump #1 in the aft section. The cable consists of three 8-gauge wires (1X388A8A, 1X389A8B, 1X390A8C) and one 20-gauge (M889A20) wire. The 8-gauge wire is stranded tinned copper with polyvinylchloride insulation and a white glass braid jacket. The MIL number for this wire is MIL-W-5086A, Type II, AN-8. The 20-gauge wire is also stranded tinned copper with polyvinylchloride insulation and a clear nylon jacket. The MIL number for this wire is MIL-W-5086A, Type I, AN-20.

The cable is routed through the aircraft from the front wheel well to the aft section. For almost the entire length of the cable run, the cable runs on the port side of the aircraft close to either the bottom of the fuel tank or the skin. The geometrical configuration of the cable is shown in Figures 1 and 2. In the aft section the cable runs around a large structural girder from the port to the starboard side of the aircraft, and then runs a short distance to the EMP hydraulic pump #1. The cable configuration around the girder is shown in Figure 3. The geometrical configuration shown in Figures 1, 2 and 3 was partly obtained by actual physical measurements on the aircraft. The dimensions provided in the Boeing Company T.O.s differ from the actual cable dimensions in the aircraft, particularly in the bomb bay section. The T.O.'s contain inaccurate information about the relative position of the cable with respect to ground (skin), and lack information on the other objects which might affect the cable response.

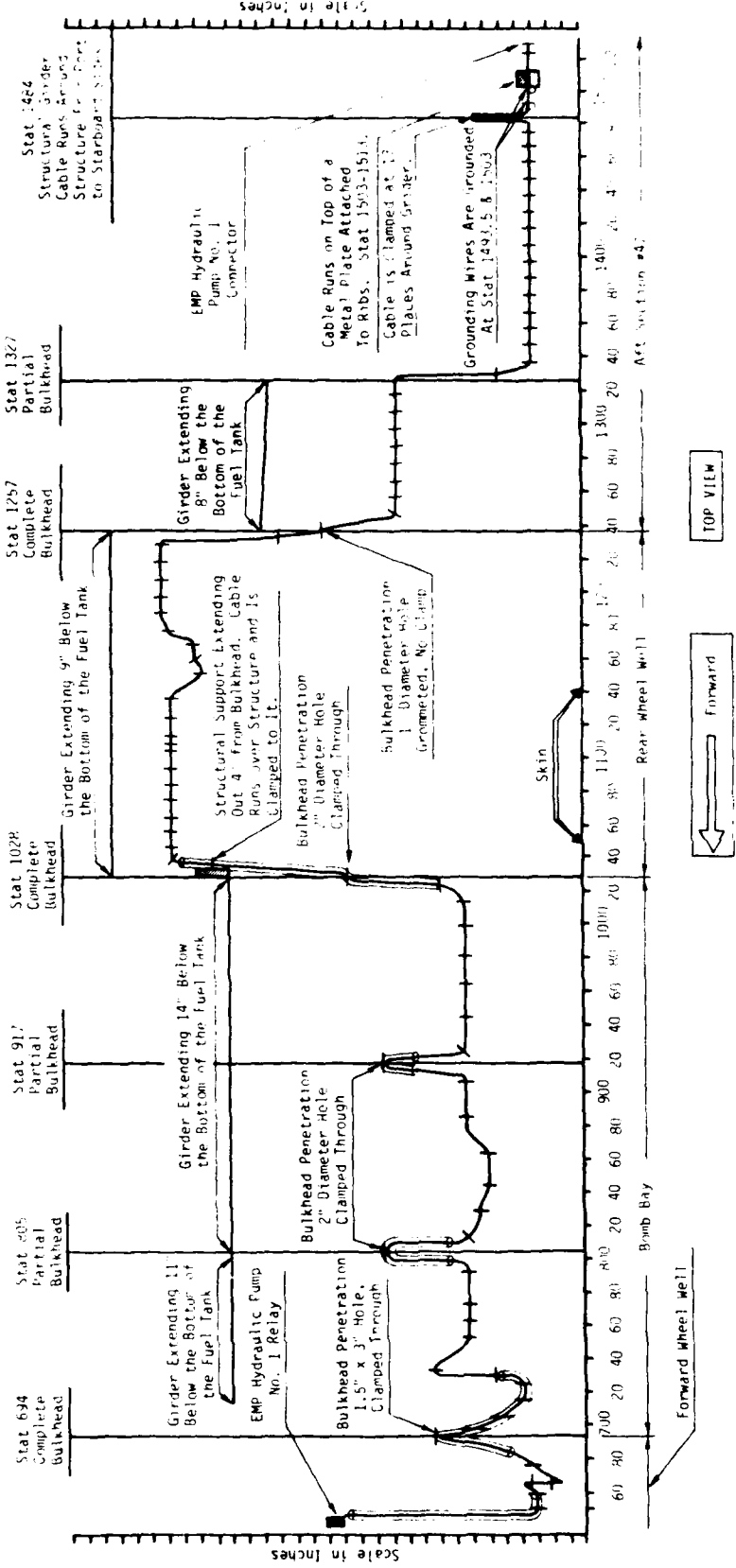


Figure 1. Cable position relative to the skin, and extending below the bottom of the fuel tank. Slashes through the cable represent clamp positions. Cylinders around some sections of the cable represent large cable bundles. The horizontal scale represents the station numbers on the aircraft.

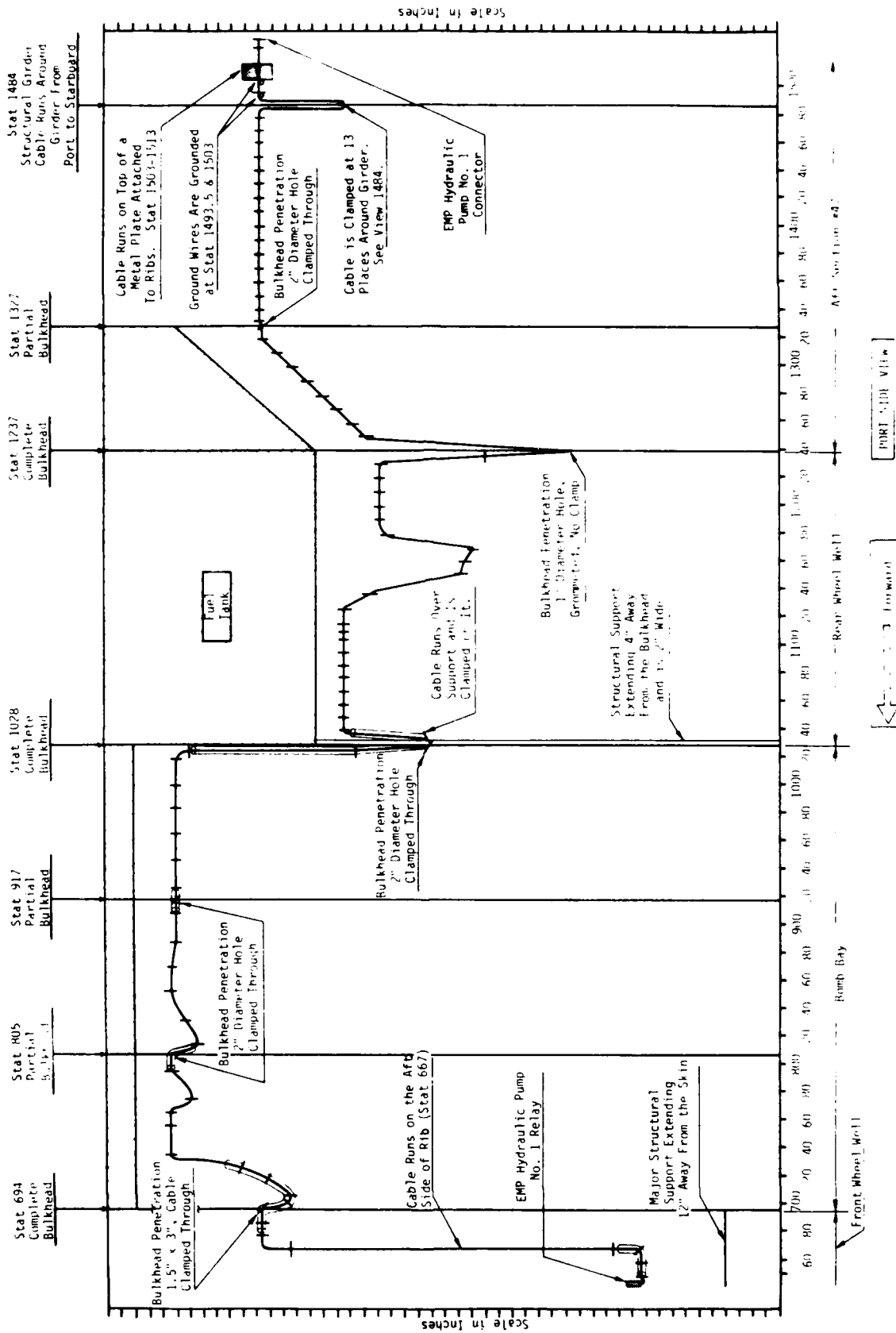


Figure 2. Cable position relative to the bottom of the fuel tank and bulkheads. Slashes through cable represent position of clamps. Cylinders around some sections of the cable represent large bundle. The horizontal scale represents the station numbers on the aircraft

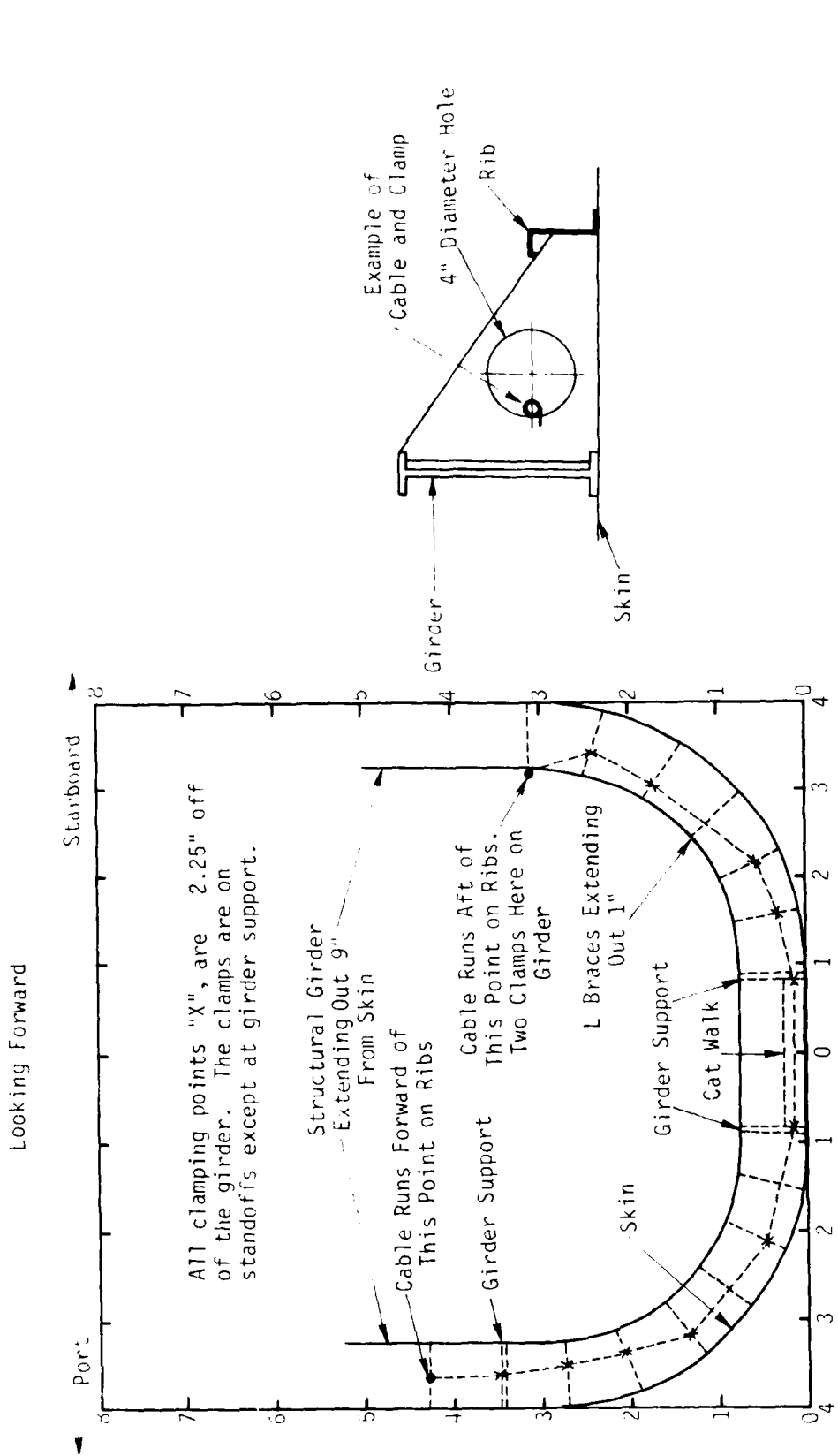


Figure 3. Cable position around the girder in the aft section.

The cable is routed through the aircraft in such a way that it encounters a large number of discontinuities. Some of these discontinuities, such as ribs, clamps on ribs, and clamps on standoffs, are periodic over short distances. Other types of discontinuities that the cable encounters are major structures, electrical equipment, electrical cables, and the fuel tanks.

The skin, fuel tanks, and structural girders are used as ground plane references, as can be seen in Figures 1 and 2. The control cables run parallel more than six inches away from the cable, and do not affect the cable response appreciably. Electrical cables run parallel to the cable for the entire length. In the front wheel well and bomb bay, other cables are running parallel to the cable, the closest being three inches. In the rear wheel well, other cables run within one inch of the cable. In the aft section under the fuel tank, there are no other cables within six inches. Once past the fuel tank, the closest cable running parallel is three inches away from the cable. In the aft section along the girder, there are no other cables close to the cable. Past the girder, the cable encounters other cables, hydraulic lines, structures, and equipment.

When the cable passes through a bulkhead, it is usually clamped on to the bulkhead. This is the case for all the bulkheads except for one which is grommeted. Several other cables also pass through the same bulkheads, and these cables are bundled together with the test cable. These bundles usually extend for a couple of feet on either side of the bulkheads before they branch again.

Throughout its length, the cable is anchored every ten or eighteen inches by clamps, and the clamps are in turn anchored to ribs or standoffs. When the cable is clamped to ribs, other cables run parallel and are usually about 3 inches away. But when the cable is clamped on standoffs, other cables run parallel one to three inches away.

For clarity, this cable is referred to as aircraft cable in the rest of this report.

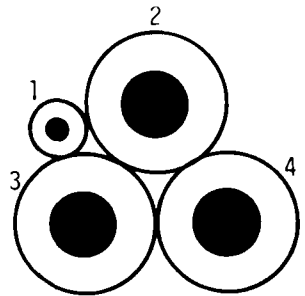
At Station 1528.5, the cable is terminated at a connector P2279 (part number MS3108E24-10S) which is connected to the EMP hydraulic pump #1. Two other wires join this connector and are grounded a few feet away from the connector. In addition, these two wires are bundled together with the test cable. A detailed description of the cable in the aircraft is given in Appendix A.

2. CABLE MOCKUP IN THE LABORATORY

A four-conductor cable was mocked up in the laboratory to simulate the multiconductor cable on the B-52 aircraft. The physical characteristics of the aircraft cable are simulated as close as possible. The purpose of this effort is to estimate the effects of the aircraft environment on the response of the multiconductor cable as compared to the laboratory environment.

The laboratory cable is basically a two dimensional simulation of the aircraft cable. The cable is made up of four-wires whose cross-section is shown in Figure 4. The wires used in the simulated cable are the same as those in the aircraft cable, described in Section I. The aircraft skin is simulated by a 91.44 m wide flat aluminum ground plane. At places where the aircraft cable is in a corner, between two parallel plates, or in a trough, the cable over the ground plane has the appropriate height to equate the common-mode characteristic impedance of the two configurations.

The cable is tied with lacing cord approximately every eight inches, so that a uniform cross-section is maintained throughout its length. The mock-up contains the discontinuities such as clamps, ribs, and bulkheads. Some major structural discontinuities are not simulated in the laboratory. The ribs are simulated by wrapping aluminum foil on a rectangular piece of wood of length 0.76 m. The ribs are grounded to the ground plane with a conducting aluminum tape. The clamps used in the laboratory are



Wire #1 OD = 0.19812 cm

ID = 0.1016 cm

Wire #2, 3, 4 OD = 0.6096 cm

ID = 0.42926 cm

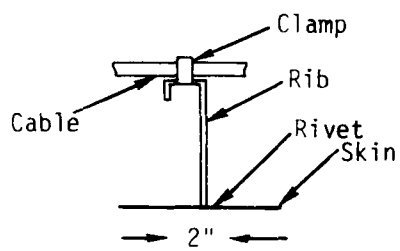
Figure 4. Cross-section of four-wire cable.

the same as those used in the aircraft (part number MS21919-DG8). A comparison between the actual ribs (two types) used in the aircraft and the ribs in the laboratory is shown in Figure 5.

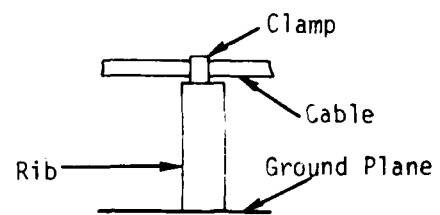
Along some portions of the length of the aircraft cable, the cable clamps are tied to metallic standoffs. In the laboratory, the cable is supported on the styrofoam blocks and the clamps are grounded to the ground plane with a strip of copper tape having an inductance equivalent to the standoffs.

The bulkheads are modeled by an aluminum plate 0.158 cm thick. The bottom of the plate is taped down to the ground plane with a conducting tape, and holes are cut in the plates to match the size and shape of the actual bulkhead penetrations in the aircraft. The distance to the center of the hole and ground plane was matched to that of the closest ground plane in the aircraft.

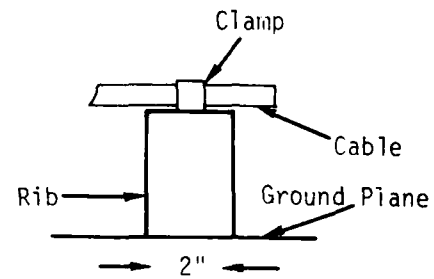
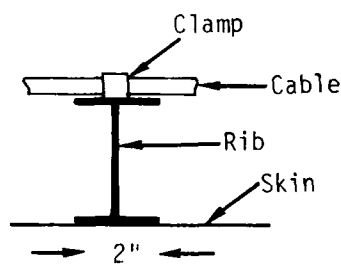
Actual Rib



Model Rib



(a)



(b)

Figure 5. Comparison of ribs in the aircraft and in the laboratory (side view).

In the aircraft, most bulkhead penetrations are shared with other cables that are bundled together with the test cable. These other cables extend a few feet on both sides of the bulkhead before they branch out. Due to the presence of these other cables in the bulkhead penetrations, the positioning of the test cable in the bulkhead penetrations is slightly different than that in the aircraft.

The geometrical configuration of the simulated cable is shown in Figures 6 through 14. Figures 15 through 17 show the photographs of different sections of the simulated cable in the laboratory. This cable is referred to as Simulated Cable in the rest of this report.

3. SIMPLIFIED CABLE MODEL

The simulated cable (replica of the aircraft cable) has large numbers of discontinuities spaced nonuniformly along the cable, and it is very difficult to model all these discontinuities in an analytical model. To overcome this difficulty, a simplified model of the aircraft model was constructed in the laboratory. This simplified model provided a comparison between the measured results on a simplified model and the actual cable model.

The simplified cable model consists of eight uniform sections, each containing only periodic discontinuities. The simplified model does not contain any bulkhead penetrations. In sections where the cable was supported on standoffs, the average height of the cable was determined, and all the clamps were placed at a periodic spacing. The clamps were grounded to the ground plane by strips of copper tape.

In some sections, the ribs occur at periodic spacing, and no modification was made to these sections. In sections where the ribs occur at nonperiodic spacings, the average spacing was determined and the ribs were placed at periodic spacings. Also, the average height of the cable and the average width of the ribs were used in these periodic sections.

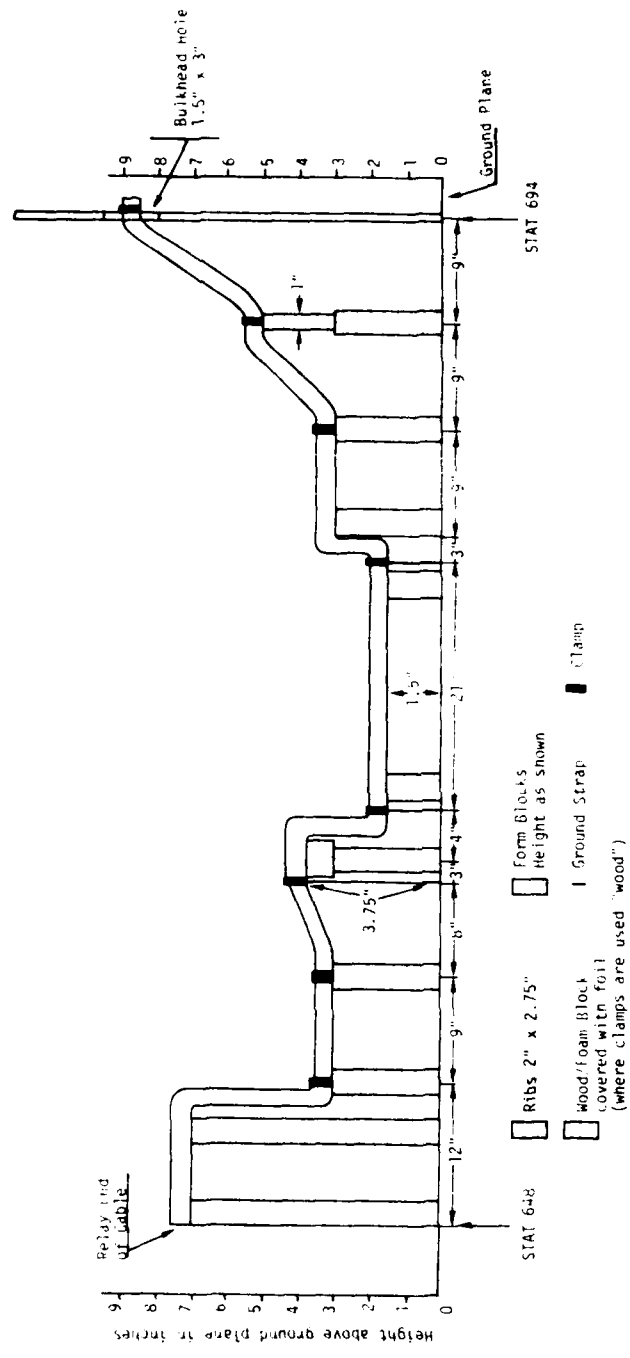


Figure 6. Laboratory simulated cable mock-up (Section 1, Station 648-694, total length 87 inches).

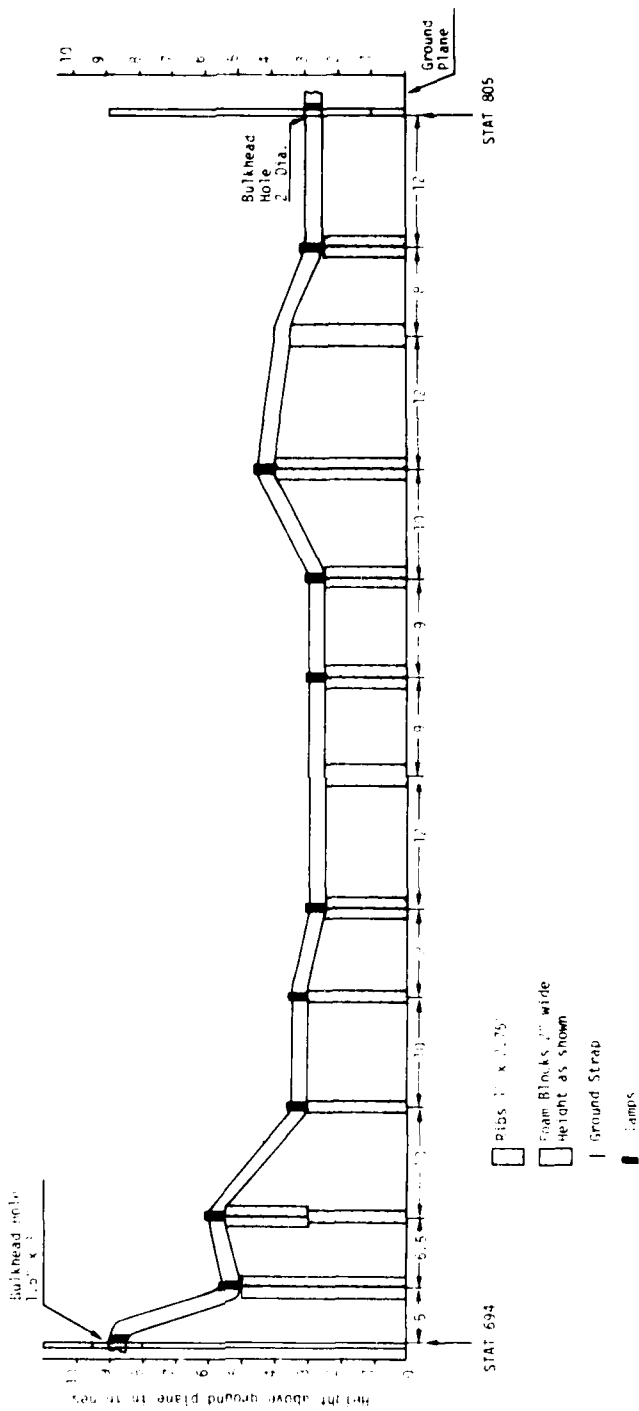


Figure 7. Laboratory simulated cable mock-up (Section 2, Station 694-805, total length 111.5 inches).

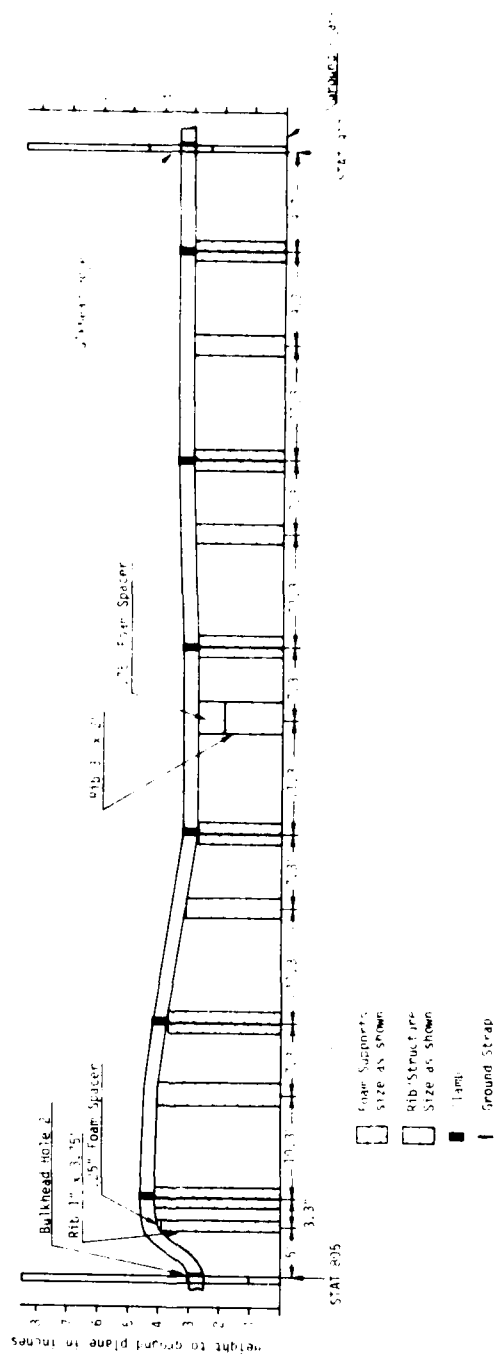


Figure 8. Laboratory simulated cable mock-up (Section 3, Station 694-805, total length 111.5 inches).

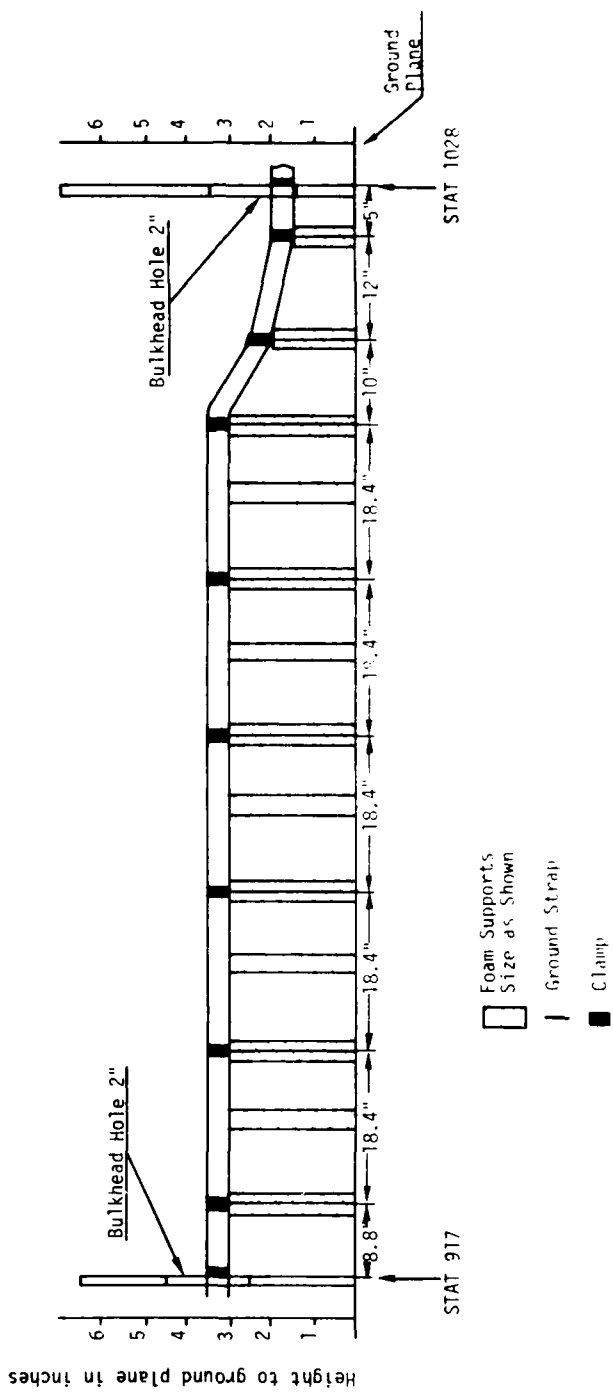


Figure 9. Laboratory simulated cable mock-up (Section 4, Station 917-1028, total length 127.8 inches).

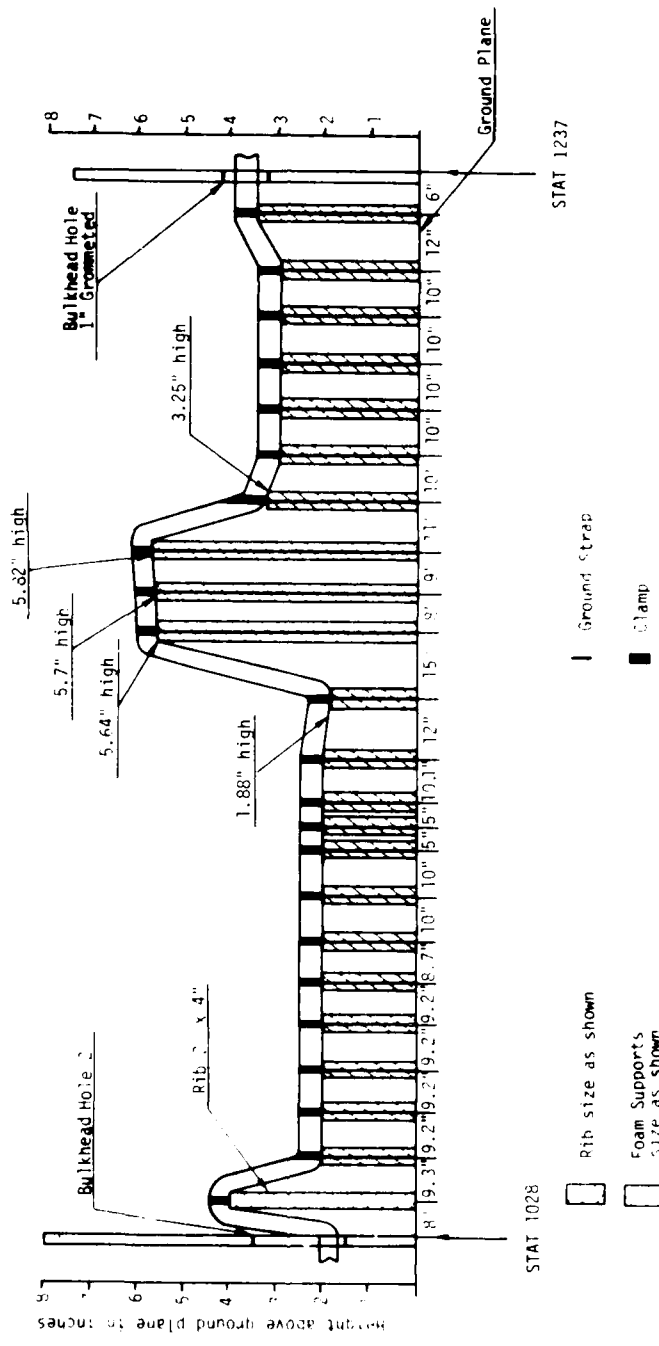


Figure 10. Laboratory simulated cable mock-up (Section 5, Station 1028-1237, total length 216.7 inches).

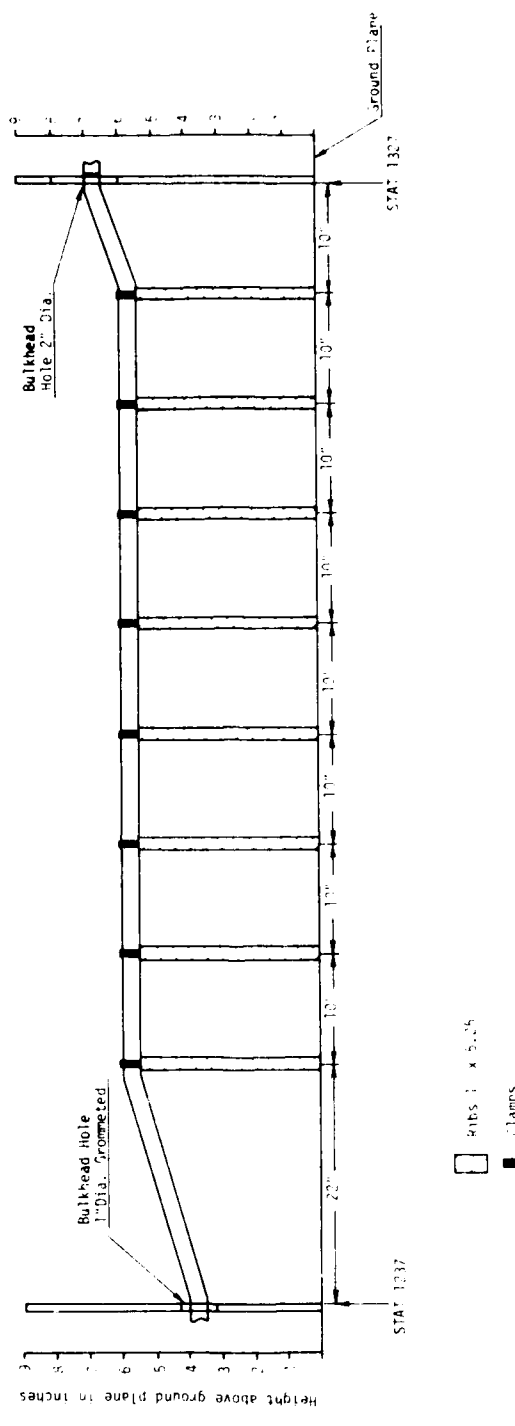


Figure 11. Laboratory simulated cable mock-up (Section 6, Station 1237-1327, total length 102 inches).

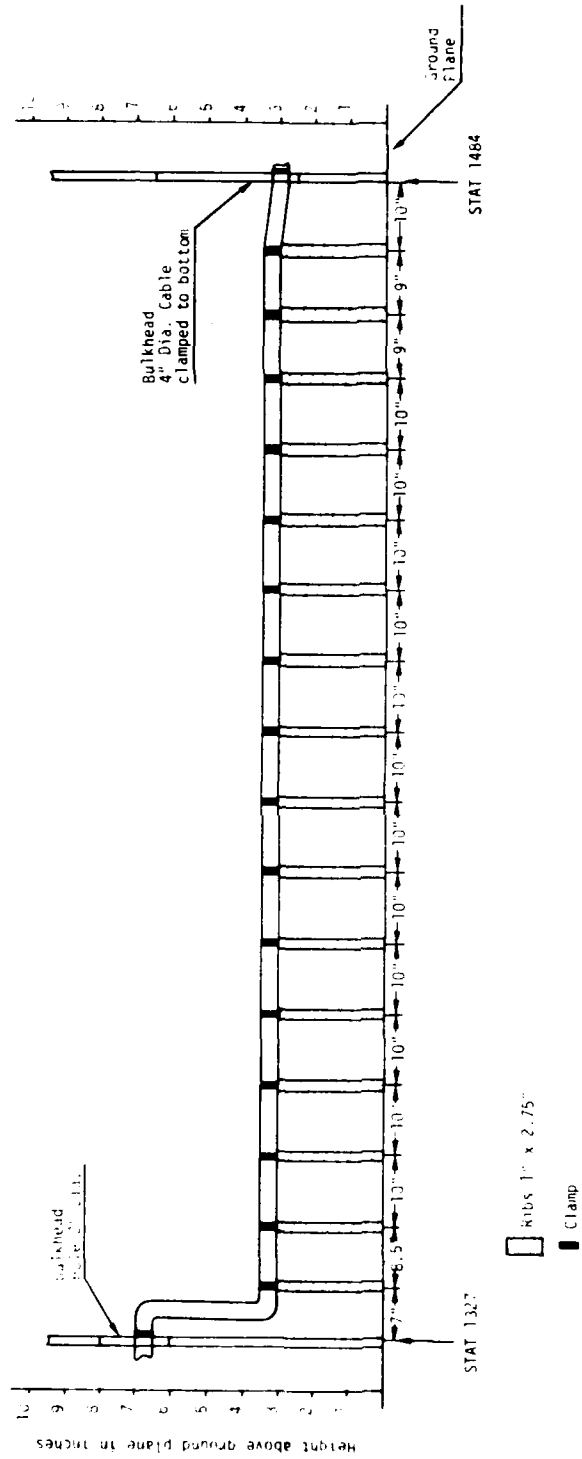


Figure 12. Laboratory simulated cable mock-up (Section 7, Station 1327-1484, total length 163.5 inches).

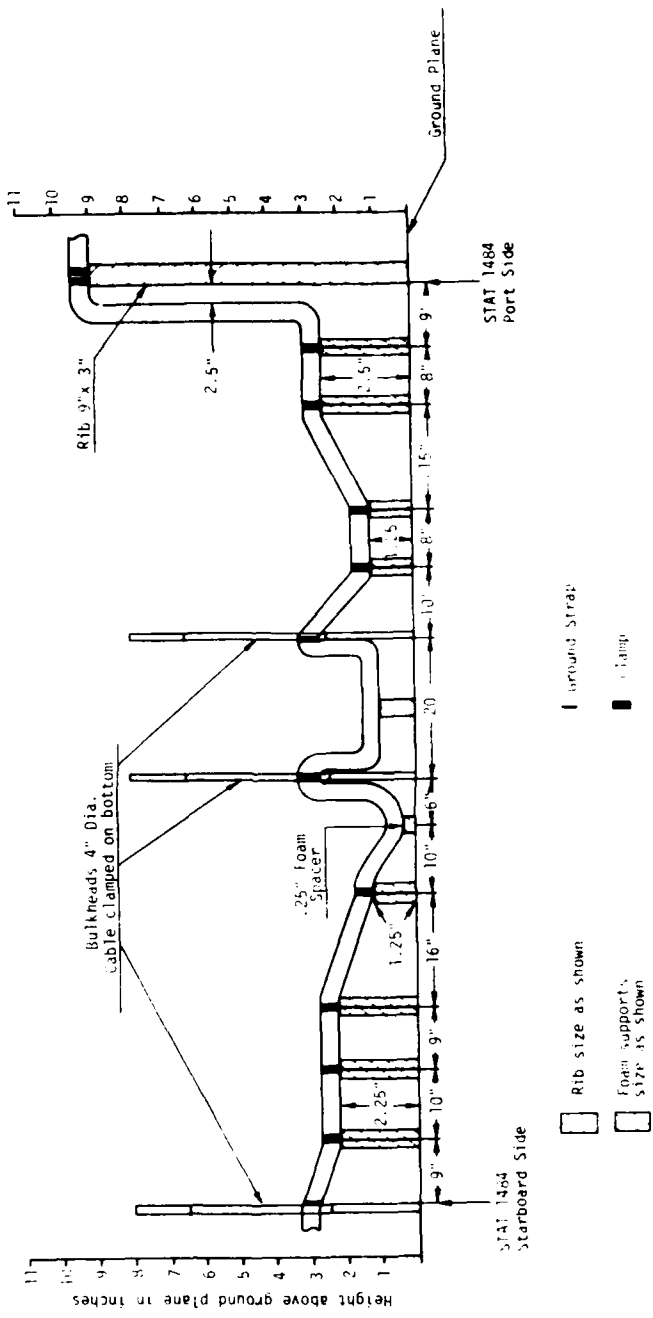


Figure 13. Laboratory simulated cable mock-up (Section 8, Station 1484, total length 180 inches).

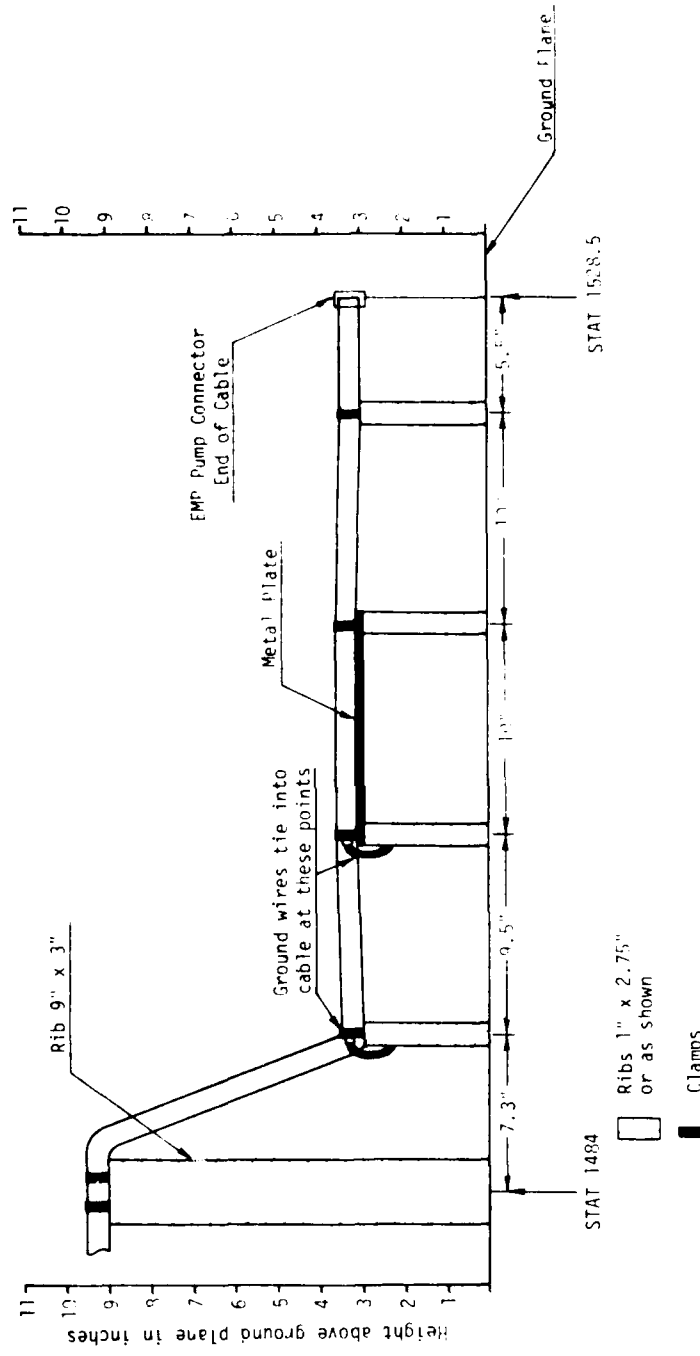
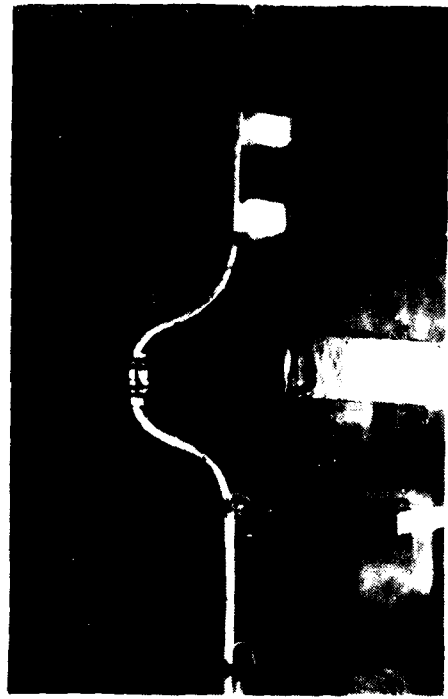


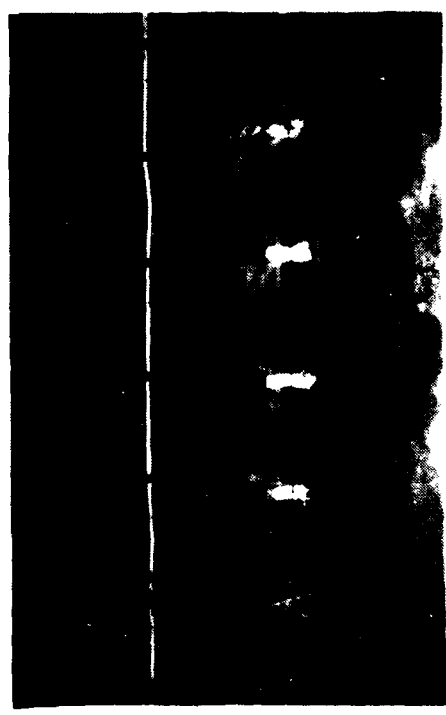
Figure 14. Laboratory simulated cable mock-up (Section 9, Station 148-1528.5, total length 53.5 inches).



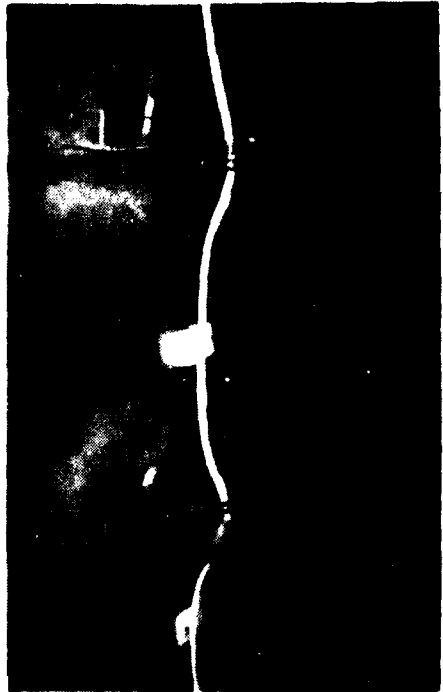
(a) Cable between stations 1484 and 1528.5.



(b) Large rib at the station 1484.

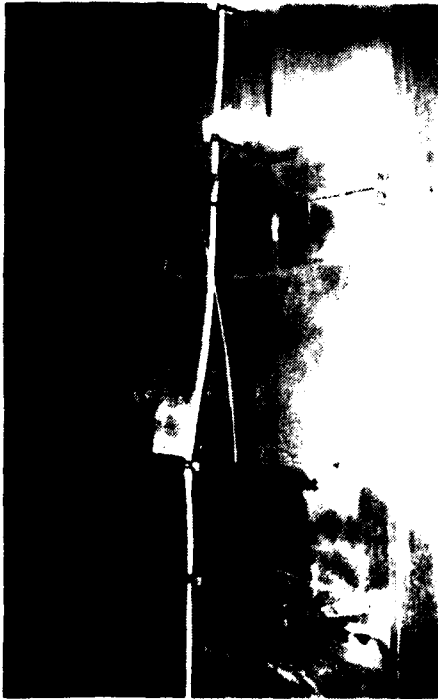


(c) Cable between stations 1475 and 1427.

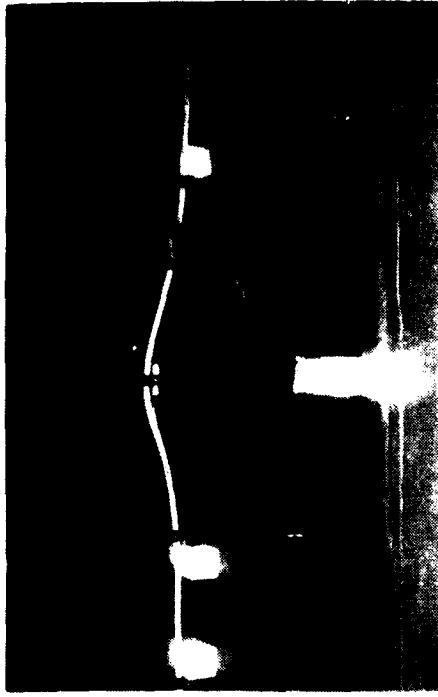


(d) Cable between two bulkheads at the station 1484.

Figure 15. Photographs showing the layout of the cable in the laboratory.



(a) Cable between Stations 1266 and 1218.



(b) Cable between stations 1046 and 1026.



(c) Cable between stations 715 and 667.



(d) Cable between stations 675 and 648.

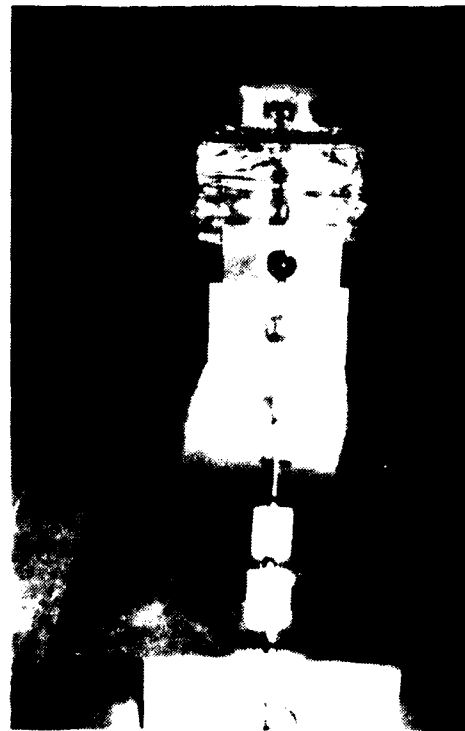
Figure 16. Photographs showing the layout of the cable in the laboratory.



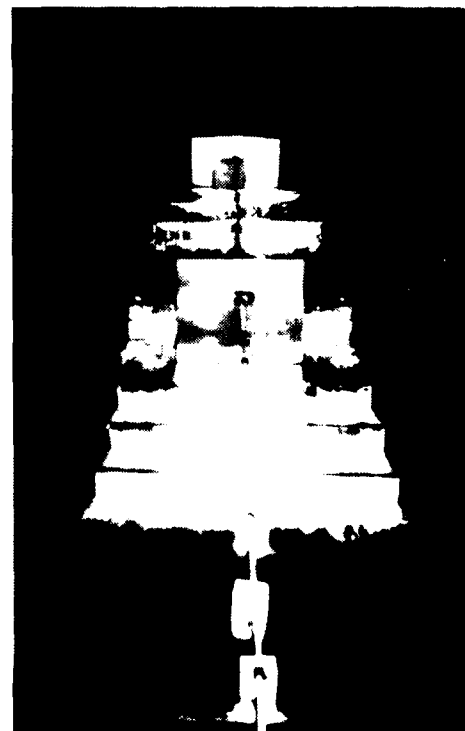
(a) Cable between stations 981 and 810.



(b) Cable between 1357 and 1028.



(c) Cable between stations 1484 and 1528.5.



(d) Cable between stations 754 and 648.

Figure 17. Photographs showing the layout of the cable in the laboratory.

Due to the smoothing of the cable, the cable run was about 15 inches longer than the simulated cable run in longitudinal dimension. However, the actual length of the wires were the same as that of the simulated cable.

The geometrical configuration of the simplified cable model is shown in Figure 18.

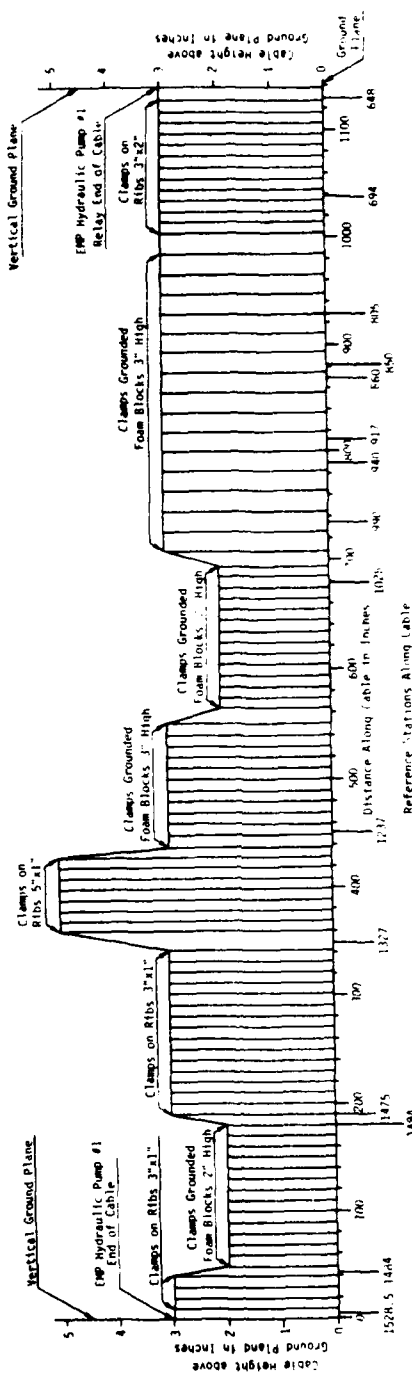


Figure 18. Simplified cable model containing eight uniform sections. The vertical lines represent the position of clamps on ribs, grounded, or on foam blocks.

SECTION III

MEASUREMENTS OF THE PARAMETERS OF THE CABLE

The multiconductor cable is modeled by a single-wire transmission line in this report. Such a model represents the common-mode propagation on the multiconductor line. When all the conductors of a multiconductor transmission line are excited with the same voltage sources, the propagation on the line is described as common-mode. To perform an analysis with a single-line model of the multiconductor line, it is desirable to determine the equivalent single-line parameters (common-mode parameters) of the multiconductor line.

Propagation on lossless multiconductor transmission lines is completely specified by the per-unit-length inductance and capacitance matrices and the characteristic-impedance matrices of the multiconductor line. The velocities of the propagation modes can be determined from the inductance and capacitance matrices. The calculation of the per-unit-length inductance and capacitance matrices for a multiconductor line in an inhomogeneous medium is quite involved. In general, the numerical methods are employed for the calculation of the inductance and capacitance parameters for a line in an inhomogeneous medium. These numerical procedures require computer codes which are very involved. However, these parameters can be measured using the procedures described in Reference 6. The method of determining the common-mode characteristic impedance and the common-mode propagation velocity from the multiconductor line parameters will be described in this section.

The multiconductor cable in the B-52 aircraft is a nonuniform cable with a large number of discontinuities. The per-unit-length parameters of the uniform sections can be measured in the laboratory and these uniform sections can be put in a cascade for the analysis of the multiconductor line. The analysis procedure used is described in Section V. Some of the discontinuities such as clamps and ribs occur periodically over a uniform section

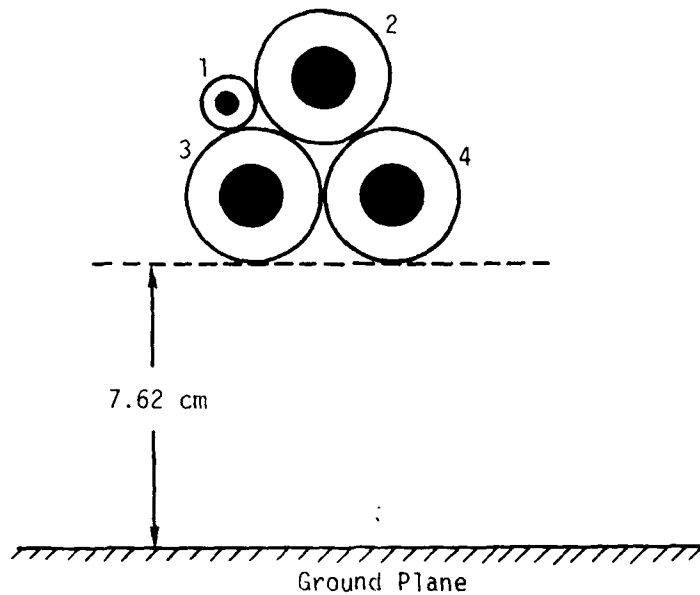
of the cable, so the capacitive loading due to these discontinuities on the otherwise uniform line can be determined by treating the line as a periodic structure (Ref. 13). From the common-mode characteristic impedance of the multiconductor line, an equivalent radius of the single-conductor line can be calculated by equating the characteristic impedance of the single-conductor line to the common-mode characteristic impedance of the multiconductor line. From this equivalent radius for the common-mode, the characteristic impedance of the multiconductor line can be calculated at various heights above the ground plane. Thus, we need only to measure the common-mode characteristic impedance of the multiconductor line at one height above the ground plane.

1. MEASUREMENT OF THE COMMON-MODE CHARACTERISTIC IMPEDANCE OF THE FOUR-CONDUCTOR LINE

The cross-section of the uniform four-conductor line is shown in Figure 19 and is the same as that of the simulated cable, shown in Figure 4. The experimental setup used to find the uniform multiconductor-line parameters is shown in Figure 20. For this case the line was 5.33-m long and supported 7.62 cm above a 0.92 m by 6-m aluminum ground plane. The wires were terminated in pin jacks so that each could be driven or terminated as required and a shorting ground plate was provided at each end to provide a low-impedance current path when a short circuit was required. A block diagram of the measurement setup is shown in Figure 21.

The voltage and current probes were selected to minimize probe loading effects. An active voltage probe with an input impedance of $1 M\Omega$ shunted by a capacitance of 1 pF was utilized for these measurements. The current probe was a clamp-on type with an insertion impedance of less than 0.1 Ω .

The short- and open-circuit input impedance matrix of the multiconductor line was measured in order to determine the parameters of the



Wire #1 OD = 0.19812 cm

ID = 0.1016 cm

Wire #2, 3, 4 OD = 0.6096 cm

ID = 0.42926 cm

Figure 19. Cross-section of four-wire line over a ground plane.

line. The short-circuit input-impedance measurements were performed with the far end shorted (grounded) and the near end of all but the driven wire open (Figure 22a). The current in the driven wire and the voltage on each of the four wires were measured with probes and the ratio of voltage to current was recorded as a function of frequency. This procedure was repeated for each wire in order to isolate the self- and mutual-impedance terms in the circuit equations

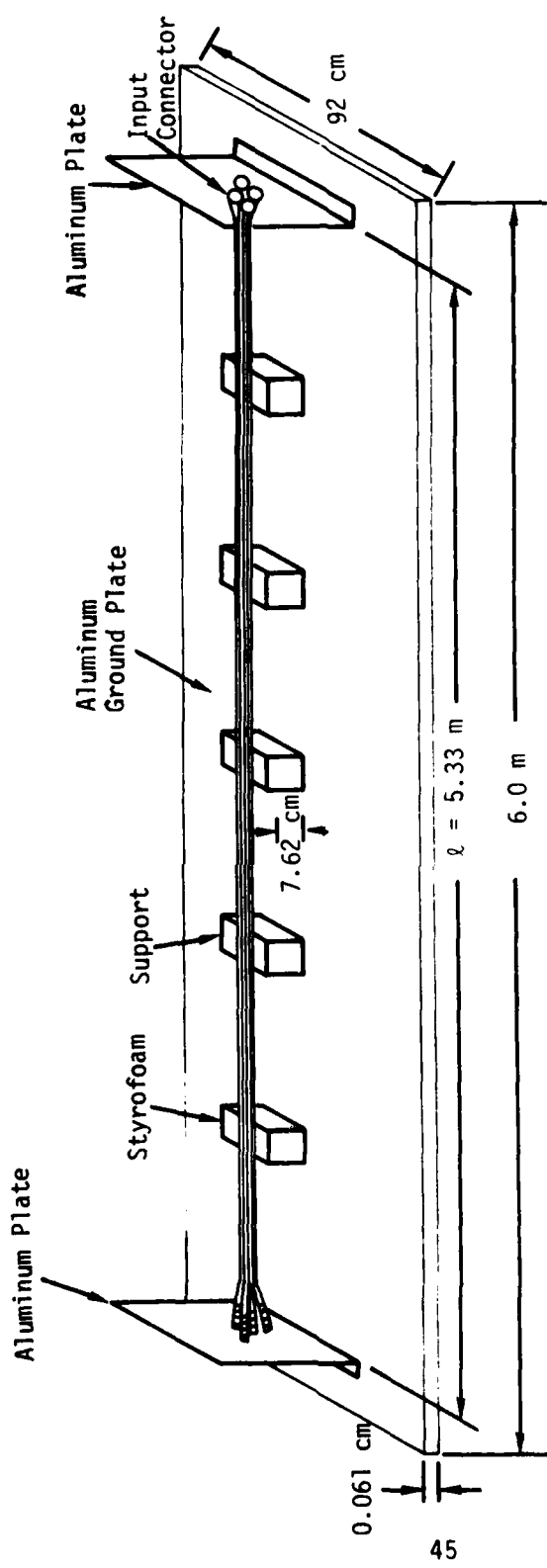


Figure 20. Multiconductor experimental setup.

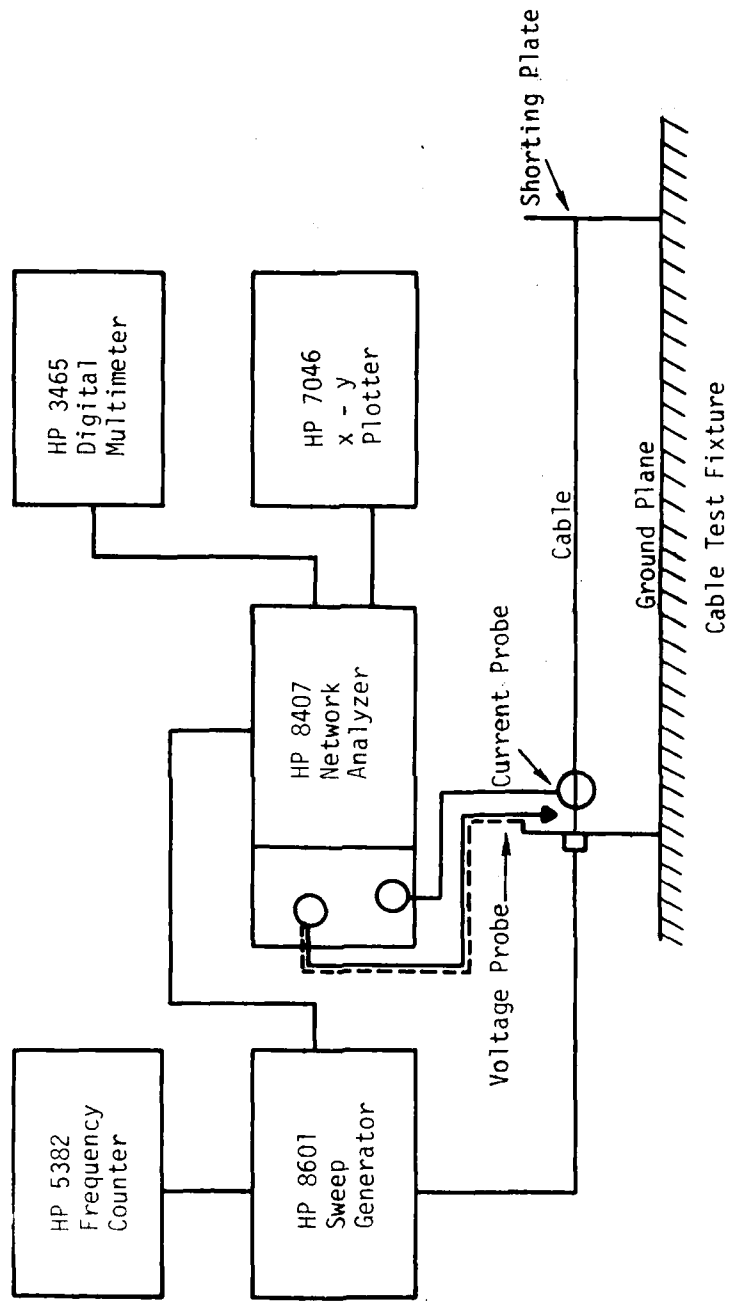
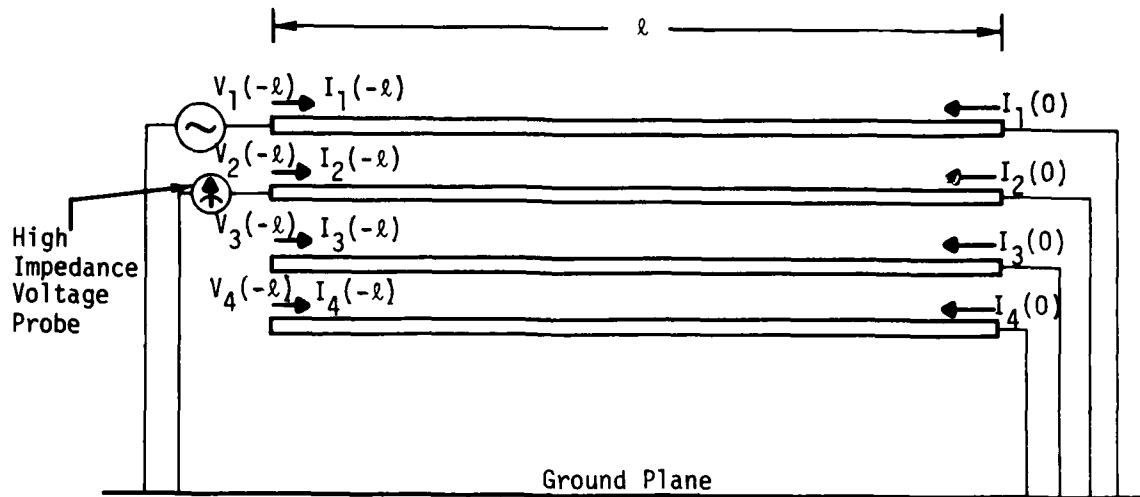
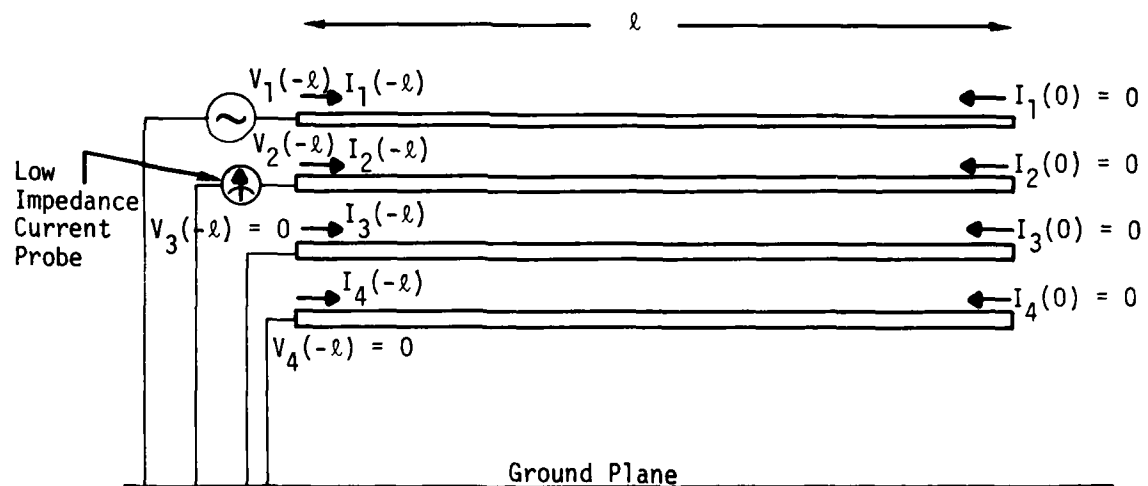


Figure 21. Swept impedance block diagram.



(a) Short-circuit input impedance measurements



(b) Open-circuit input admittance measurements

Figure 22. Schematic diagram of the measurement method.

$$V_1 = Z_{11}I_1 + Z_{12}I_2 + Z_{13}I_3 + Z_{14}I_4$$

$$V_2 = Z_{21}I_1 + Z_{22}I_2 + Z_{23}I_3 + Z_{24}I_4 \quad (1)$$

$$V_3 = Z_{31}I_1 + Z_{32}I_2 + Z_{33}I_3 + Z_{34}I_4$$

$$V_4 = Z_{41}I_1 + Z_{42}I_2 + Z_{43}I_3 + Z_{44}I_4$$

The impedances are given by

$$Z_{nm}^{sc} = \frac{V_n}{I_m} \quad , \quad \text{for } n = 1, 2, 3, 4 \\ \quad \quad \quad m = 1, 2, 3, 4 \quad (2)$$

The open-circuit input-admittance measurements were performed with the far end open and the near end of all but the driven wire shorted (Figure 22b). The voltage on the driven wire and the current in each of the three wires were measured with probes and the ratio of current to voltage was measured as a function of frequency. This procedure was repeated for each wire in order to isolate the self- and mutual-admittance terms in the equations

$$I_1 = Y_{11}V_1 + Y_{12}V_2 + Y_{13}V_3 + Y_{14}V_4$$

$$I_2 = Y_{21}V_1 + Y_{22}V_2 + Y_{23}V_3 + Y_{24}V_4$$

$$I_3 = Y_{31}V_1 + Y_{32}V_2 + Y_{33}V_3 + Y_{34}V_4$$

$$I_4 = Y_{41}V_1 + Y_{42}V_2 + Y_{43}V_3 + Y_{44}V_4 \quad (3)$$

The admittances are given by

$$Y_{nm}^{oc} = \frac{I_n}{V_m} \quad , \quad \text{for } n = 1, 2, 3, 4 \\ m = 1, 2, 3, 4 \quad (4)$$

The open-circuit input-impedance matrix is obtained by inverting the open-circuit input-admittance matrix, i.e.,

$$[Z_{nm}^{oc}] = [Y_{nm}^{oc}]^{-1} \quad (5)$$

The per-unit-length inductance and capacitance matrices and the characteristic-impedance matrix of the multiconductor line are determined by the procedure described in Reference 6. The measured data is shown in Appendix B.

The characteristic-impedance matrix and the per-unit-length inductance and capacitance matrices calculated from the measured data are:

$$[Z_{Cnm}] = \begin{bmatrix} 283.225 & 199.109 & 199.064 & 179.267 \\ 199.109 & 236.378 & 191.213 & 191.181 \\ 199.064 & 191.213 & 232.498 & 189.060 \\ 179.267 & 191.181 & 189.060 & 235.166 \end{bmatrix} \text{ ohms}$$

$$[L_{nm}] = \begin{bmatrix} 1.1279 & 0.7115 & 0.7108 & 0.6117 \\ 0.7115 & 0.8909 & 0.6649 & 0.6607 \\ 0.7108 & 0.6649 & 0.8798 & 0.6548 \\ 0.6117 & 0.6607 & 0.6548 & 0.8726 \end{bmatrix} \mu\text{H/m}$$

$$[C_{nm}] = \begin{bmatrix} 50.623 & -22.055 & -25.244 & -0.788 \\ -22.055 & 88.593 & -27.823 & -34.455 \\ -25.244 & -27.823 & 91.908 & -33.441 \\ -0.788 & -34.455 & -33.441 & 77.067 \end{bmatrix} \text{ pF/m}$$

The propagation velocities of the modes (inverse square root of the eigenvalues of the matrix product $[L_{nm}][C_{nm}]$) are:

$$v_1 = 2.8 \times 10^8 \text{ m/s}$$

$$v_2 = 2.021 \times 10^8 \text{ m/s}$$

$$v_3 = 2.059 \times 10^8 \text{ m/s}$$

$$v_4 = 1.955 \times 10^8 \text{ m/s}$$

The fastest-traveling mode is the common mode, traveling with a velocity of $2.8 \times 10^8 \text{ m/s}$.

The common-mode characteristic impedance of the multiconductor line can be determined from the characteristic-impedance matrix $[Z_{C_{nm}}]$. Consider the following relationship between voltages and currents at any point along the line, for a line terminated in matched loads at both ends,

$$I_1 = Y_{c_{11}} V_1 + Y_{c_{12}} V_2 + Y_{c_{13}} V_3 + Y_{c_{14}} V_4$$

$$I_2 = Y_{c_{21}} V_1 + Y_{c_{22}} V_2 + Y_{c_{23}} V_3 + Y_{c_{24}} V_4$$

$$I_3 = Y_{c_{31}} V_1 + Y_{c_{32}} V_2 + Y_{c_{33}} V_3 + Y_{c_{34}} V_4$$

$$I_4 = Y_{c_{41}} V_1 + Y_{c_{42}} V_2 + Y_{c_{43}} V_3 + Y_{c_{44}} V_4 \quad (6)$$

where $[Y_{C_{nm}}]$ is the characteristic-admittance matrix of the multiconductor line and is defined as the inverse of the characteristic-impedance matrix $[Z_{C_{nm}}]$.

When the voltages on all the conductors of a multiconductor transmission line are equal, the only mode which travels on the line is the common mode. Thus from Equation 6, when $V_1 = V_2 = V_3 = V_4 = V$,

$$\begin{aligned} I_1 &= \left(Y_{c_{11}} + Y_{c_{12}} + Y_{c_{13}} + Y_{c_{14}} \right) V \\ I_2 &= \left(Y_{c_{21}} + Y_{c_{22}} + Y_{c_{23}} + Y_{c_{24}} \right) V \\ I_3 &= \left(Y_{c_{31}} + Y_{c_{32}} + Y_{c_{33}} + Y_{c_{34}} \right) V \\ I_4 &= \left(Y_{c_{41}} + Y_{c_{42}} + Y_{c_{43}} + Y_{c_{44}} \right) V \end{aligned} \quad (7)$$

The common-mode characteristic admittance is defined as

$$Y_{c_{\text{comm}}} = \frac{I_1 + I_2 + I_3 + I_4}{V} \quad (8)$$

or

$$Y_{c_{\text{comm}}} = \sum_{n=1}^{4,4} Y_{c_{nm}} \quad (9)$$

The characteristic-admittance matrix, obtained by inverting the characteristic-impedance matrix, is

$$[Y_{c_{nm}}] = \begin{bmatrix} 1.032 \times 10^{-2} & -4.514 \times 10^{-3} & -4.938 \times 10^{-3} & -2.256 \times 10^{-4} \\ -4.514 \times 10^{-3} & 1.773 \times 10^{-2} & -5.181 \times 10^{-3} & -6.807 \times 10^{-3} \\ -4.938 \times 10^{-3} & -5.181 \times 10^{-3} & 1.821 \times 10^{-2} & -6.660 \times 10^{-3} \\ -2.256 \times 10^{-4} & -6.807 \times 10^{-3} & -6.660 \times 10^{-3} & 1.531 \times 10^{-2} \end{bmatrix} \text{ mhos}$$

From the above matrix, the common-mode characteristic admittance is

$$Y_{c_{\text{comm}}} = 4.919 \times 10^{-3} \text{ mho}$$

and the common-mode characteristic impedance is

$$Z_{c_{\text{comm}}} = 203.29 \text{ ohms}$$

From this impedance, the equivalent radius of the cable is calculated to be 0.5471 cm.

The common-mode characteristic impedance can also be calculated from the common-mode capacitance per-unit-length of the line and the common-mode propagation velocity, using the relation

$$Z_{c_{\text{comm}}} = \frac{1}{v_{\text{comm}} c_{\text{comm}}} \quad (10)$$

The common-mode capacitance per unit length is defined the same way as the common-mode characteristic impedance. The common-mode capacitance per unit length calculated from the per-unit-length matrix is 17.5675 pF.

2. CALCULATION OF THE COMMON-MODE CHARACTERISTIC IMPEDANCE OF THE FOUR-CONDUCTOR LINE

The common-mode characteristic impedance of the multiconductor line can also be calculated from the cross-sectional geometry of the line. The calculation of the inductance and capacitance parameters for a system of conductors in an inhomogeneous medium is a complex problem in general. Recently, the method of moments (Ref. 14) has been applied to solve the capacitance matrix for dielectric insulated ribbon cables, and the method of multiseries expansion has been applied to solve the capacitance matrix of a multiconductor line enclosed in a shielded tube (Ref. 15). These methods will have to be extended in order to calculate the per-unit-length capacitance matrix of a multiconductor line in an inhomogeneous medium

(that is, line made with dielectric insulated conductors) over a ground plane.

A good approximation to the common-mode characteristic impedance of the multiconductor line in an inhomogeneous medium, over a ground plane, can be calculated by using the parameters of the line in a homogeneous medium of air. If the height of the transmission line is large compared to the equivalent radius of the line, this approximation works very well, because the change in the capacitance due to dielectric around conductors is small. The per-unit-length capacitance matrix of the multiconductor line in a homogeneous medium can be calculated by solving the integral equations involving charges and voltages. A computer code CAPCODE (Ref. 16) is used for this purpose. The per-unit-length capacitance matrix of the four-conductor line, as shown in Figure 29, obtained from the CAPCODE is

$$[C_{nm}] = \begin{bmatrix} 31.31 & -14.78 & -14.75 & -0.47 \\ -14.78 & 53.76 & -14.26 & -20.34 \\ -14.75 & -14.26 & 53.98 & -20.21 \\ -0.47 & -20.34 & -20.21 & 46.37 \end{bmatrix} \text{ pF/m}$$

The common-mode capacitance per-unit-length is defined as

$$C_{c_{\text{comm}}} = \sum_{n=1}^{4,4} C_{nm} \quad (11)$$

Thus the common-mode capacitance per-unit-length of the four-conductor line is 15.79 pF/m. The common-mode characteristic impedance of the four-conductor line can be calculated from the following relation,

$$Z_{c_{\text{comm}}} = \frac{1}{v_0 C_{\text{comm}}} \quad (12)$$

where v_0 is the speed of light.

The common-mode characteristic impedance of the line from the above relation is 211.1 ohms. Note that the difference between the calculated and the measured result is only 3.8 percent. The per-unit-length inductance matrix of the multiconductor line can be calculated by using the following relation, since the presence of dielectrics does not change the inductance values.

$$[L_{nm}] = \frac{1}{V_0^2} [C_{nm}]^{-1} \quad (13)$$

3. MEASUREMENT OF THE COMMON-MODE CHARACTERISTICS OF THE FOUR-CONDUCTOR LINE WITH PERIODIC DISCONTINUITIES

Some of the discontinuities on the aircraft cable such as metallic ribs, ribs and clamps, etc., occur at periodic intervals in some sections of the cable. The transmission line loaded at periodic intervals with identical obstacles are referred to as periodic structures. These periodic structures have two basic properties, namely (1) passband stop-band characteristics, and (2) support of waves with phase velocities much less than the velocity of light (Ref. 13). The metallic ribs and clamps essentially add a shunt capacitance at periodic intervals to the smooth line, without affecting the per-unit-length inductance of the line. If the spacing between the added lumped capacitors is small compared with the wavelength, then in the low-frequency limit, the single line (or common-mode propagation) will appear to be electrically smooth, with a phase velocity

$$v_p = \left[\left(C + \frac{C_0}{d} \right) L \right]^{-1/2} \quad (14)$$

where C_0/d is the amount of lumped capacitance added per unit length (a capacitor added at intervals d). C and L are the per-unit-length capacitance and inductance of the line (common-mode).

For a transmission line loaded with a capacitance at periodic intervals d , an equivalent network of a basic section is a shunt normalized susceptance \bar{B} with a length $d/2$ of transmission line on either side, as in Figure 23a. Figure 23b illustrates the voltage-current relationships at the input and output of the n th section in the infinitely long cascade connection.

For a terminated transmission line, if the load is terminated at the n th terminal plane, as shown in Figure 24, the line behaves like a smooth

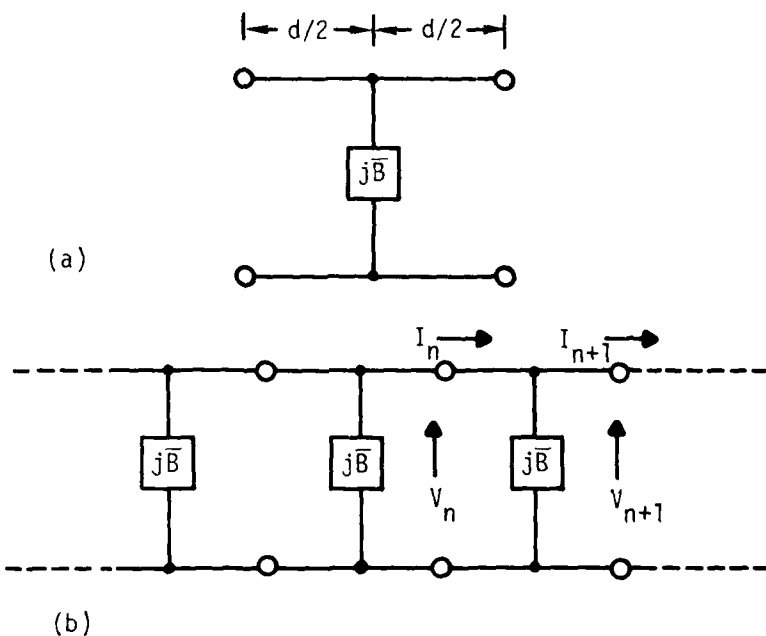


Figure 23. (a) Equivalent circuit for unit cell of a loaded transmission line; (b) cascade connection of basic unit-cell networks.

transmission line with characteristic impedance and propagation velocity of the periodically loaded line. The input impedance of the line in Figure 24 is given by (Ref. 13)

$$Z_{IN} = Z_C' \frac{Z_L + jZ_C' \tan N\beta d}{Z_C' + Z_L \tan N\beta d} \quad (15)$$

where Z_C' is the characteristic impedance of the periodic structure.

Thus the characteristic impedance and the per-unit-length inductance and capacitance of the periodically loaded line can be determined using the same procedure used for the uniform line. From these parameters, the capacitive loading due to a single discontinuity on the common-mode propagation can be determined. The per-unit-length inductance and capacitance matrices and the characteristic-impedance matrix of the four-

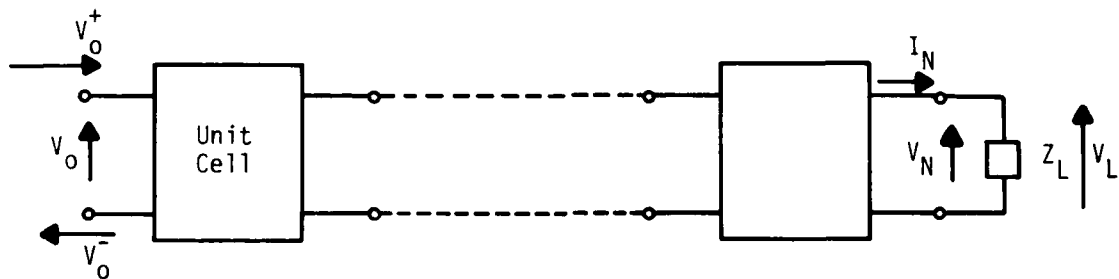


Figure 24. Periodic structure terminated in a load Z_L .

conductor line with periodic discontinuities are determined using the same procedure as described earlier. From these matrices the characteristics of the common-mode propagation on the periodically loaded line can be determined. The capacitance of the individual discontinuities can be calculated by comparing the common-mode characteristic impedances and the propagation velocities of the uniform line and the periodically loaded line.

A. Four-Wire Line Supported By Periodic Metallic Ribs

The four-wire cable (Figure 4) was supported on 2.54 x 7.62 cm metallic ribs spaced 25.4 cm apart. The cross-sectional geometry of one rib supporting the cable is shown in Figure 25. The test set up was the same as that of Figure 20. Twenty ribs were used in the test set up. The short- and open-circuit input impedance and admittance data is shown in Appendix C.

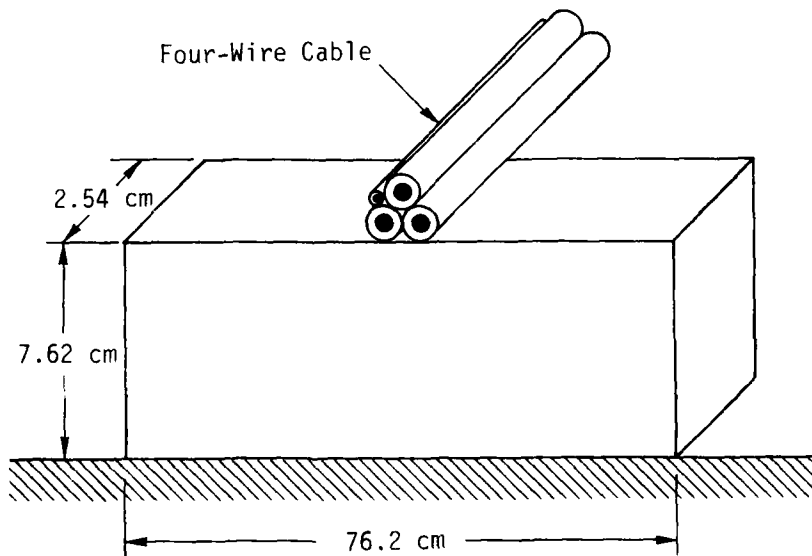


Figure 25. Four-wire cable over a rib.

From the measured data, the calculated characteristic impedance and per-unit-length inductance and capacitance matrices are:

$$[Z_{C_{nm}}] = \begin{bmatrix} 228.04 & 141.976 & 138.087 & 117.555 \\ 141.976 & 176.443 & 127.43 & 126.124 \\ 138.087 & 127.43 & 163.395 & 120.948 \\ 117.555 & 126.124 & 120.948 & 163.208 \end{bmatrix} \text{ ohms}$$

$$[L_{nm}] = \begin{bmatrix} 1.0968 & 0.6744 & 0.6759 & 0.5745 \\ 0.6744 & 0.8378 & 0.6216 & 0.6161 \\ 0.6759 & 0.6216 & 0.8253 & 0.6102 \\ 0.5745 & 0.6161 & 0.6102 & 0.8186 \end{bmatrix} \mu\text{H/m}$$

$$[C_{nm}] = \begin{bmatrix} 51.275 & -23.615 & -25.220 & -0.589 \\ -23.615 & 92.563 & -27.388 & -34.983 \\ -25.220 & -27.388 & 99.312 & -32.850 \\ -0.589 & -34.983 & -32.850 & 83.105 \end{bmatrix} \text{ pF/m}$$

The characteristic-admittance matrix, obtained by inverting the characteristic-impedance matrix, is

$$[Y_{C_{nm}}] = \begin{bmatrix} 1.045 \times 10^{-2} & -4.714 \times 10^{-3} & -5.052 \times 10^{-3} & -1.419 \times 10^{-4} \\ -4.714 \times 10^{-3} & 1.843 \times 10^{-2} & -5.228 \times 10^{-3} & -6.927 \times 10^{-3} \\ -5.052 \times 10^{-3} & -5.228 \times 10^{-3} & 1.945 \times 10^{-3} & -6.738 \times 10^{-3} \\ -1.419 \times 10^{-4} & -6.972 \times 10^{-3} & -6.738 \times 10^{-3} & 1.661 \times 10^{-2} \end{bmatrix} \text{ mho}$$

From the above matrix, the common-mode characteristic admittance, $Y_{C_{comm}}$, is 7.248×10^{-3} mho, and the common-mode characteristic impedance, $Z_{C_{comm}}$, is 137.96 ohms.

The common-mode propagation velocity, obtained from the inverse of the square root of the eigenvalues of the matrix product $[L_{nm}][C_{nm}]$, is 2.1142×10^8 m/sec. The common-mode per-unit-length capacitance of the line can be obtained by using Equation 10. Thus, from Equation 10

$$C' = 34.28 \text{ pF}$$

The per-unit-length capacitance of the line is given by the relation

$$C' = C_{\text{comm}} + \frac{C_0}{d} \quad (16)$$

where C_{comm} is the per-unit-length common-mode capacitance of the four-conductor line without ribs, C_0 is the capacitance of an individual rib, and d is the spacing between the ribs. From Equation 16,

$$C_0 = 4.245 \text{ pF}$$

B. Four-Wire Line Supported By Periodic Metallic Ribs and Clamps

The four-wire line (Figure 4) was supported on 2.54×6.985 cm ribs and clamps spaced 25.4 cm apart. The cross-sectional geometry of one such rib and clamp supporting the cable is shown in Figure 26. The cable clamps were tied to the ribs with a screw. The resultant height of the cable center was 7.62 cm above the ground plane. Twenty ribs and clamps were used in the set up. The short- and open-circuit input impedance and admittance data is shown in Appendix D.

From the measured data, the calculated characteristic-impedance and per-unit-length inductance and capacitance matrices are:

$$[Z_{C_{nm}}] = \begin{bmatrix} 196.953 & 114.403 & 115.207 & 96.699 \\ 114.403 & 146.127 & 104.445 & 104.965 \\ 115.207 & 104.445 & 143.567 & 102.574 \\ 96.699 & 104.965 & 102.574 & 147.068 \end{bmatrix} \text{ ohms}$$

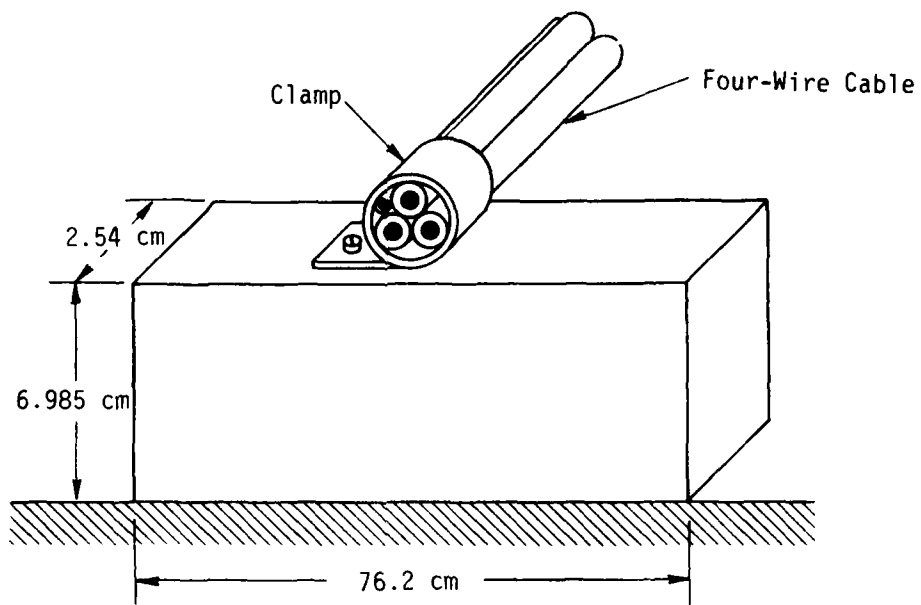


Figure 26. Four-wire line supported by a rib and a clamp.

$$[L_{nm}] = \begin{bmatrix} 1.0727 & 0.6654 & 0.6688 & 0.5761 \\ 0.6654 & 0.8330 & 0.6162 & 0.6194 \\ 0.6688 & 0.6162 & 0.8138 & 0.6070 \\ 0.5761 & 0.6194 & 0.6070 & 0.8292 \end{bmatrix} \mu\text{H/m}$$

$$[C_{nm}] = \begin{bmatrix} 54.636 & -23.662 & -25.773 & -0.658 \\ -23.662 & 100.056 & -27.178 & -35.187 \\ -25.773 & -27.178 & 99.734 & -31.378 \\ -0.658 & -35.187 & -33.378 & 82.924 \end{bmatrix} \text{pF/m}$$

The characteristic-admittance matrix, obtained by inverting the characteristic-impedance matrix, is

$$[Y_{C_{nm}}] = \begin{bmatrix} 1.097 \times 10^{-2} & -4.695 \times 10^{-3} & -5.240 \times 10^{-3} & -2.090 \times 10^{-4} \\ -4.695 \times 10^{-3} & 1.935 \times 10^{-2} & -5.279 \times 10^{-3} & -7.042 \times 10^{-3} \\ -5.240 \times 10^{-3} & -5.279 \times 10^{-3} & 1.965 \times 10^{-3} & -6.491 \times 10^{-3} \\ -2.090 \times 10^{-4} & -7.042 \times 10^{-3} & -6.491 \times 10^{-3} & 1.649 \times 10^{-2} \end{bmatrix} \text{ pF/m}$$

From the above matrix, the common-mode characteristic admittance, $Y_{C_{comm}}$, is 8.549×10^{-3} mho, and the common-mode characteristic impedance, $Z_{C_{comm}}$, is 116.972 ohms.

The common-mode propagation velocity, obtained from the inverse of the square root of the eigenvalues of the matrix product $[L_{nm}][C_{nm}]$, is 2.014×10^8 m/sec. From Equation 10, the common-mode per-unit-length capacitance, C' , is 42.447 pF.

From Equation 16, the capacitance of the cable clamp and the rib is found to be 6.3916 pF.

C. Four-Wire Line Passing Through Periodic Bulkhead Penetrations

The four-wire line (Figure 4) was supported on 5.08 cm diameter penetrations in a 40.64 x 35.56 cm aluminum plates spaced 48.514 cm apart. The cross-section configuration is shown in Figure 26. Ten bulkhead penetrations were used in the set up. The short- and open-circuit input impedance and admittance data is shown in Appendix E.

From the measured data, the calculated characteristic-impedance and per-unit-length inductance and capacitance matrices are:

$$[Z_{C_{nm}}] = \begin{bmatrix} 269.116 & 180.481 & 181.096 & 160.071 \\ 180.481 & 212.692 & 168.972 & 168.168 \\ 181.096 & 168.972 & 209.580 & 166.001 \\ 160.071 & 168.168 & 166.001 & 211.268 \end{bmatrix} \text{ ohms}$$

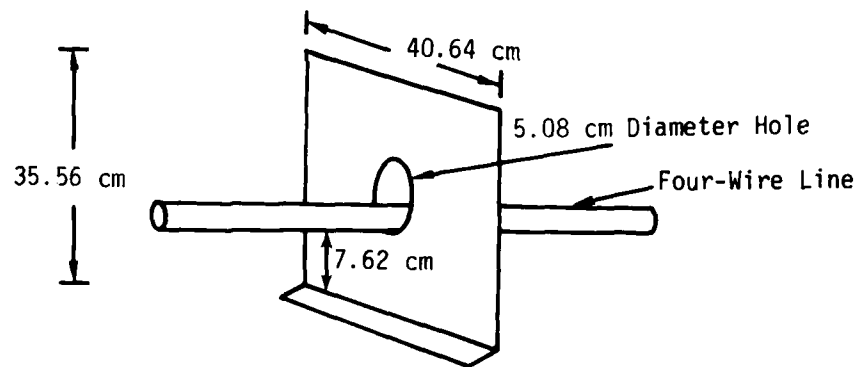


Figure 27. Four-wire line through a bulkhead penetration.

$$[L_{nm}] = \begin{bmatrix} 1.1220 & 0.7025 & 0.7032 & 0.6061 \\ 0.7025 & 0.8721 & 0.6516 & 0.6520 \\ 0.7032 & 0.6516 & 0.8563 & 0.6409 \\ 0.6061 & 0.6520 & 0.6409 & 0.8662 \end{bmatrix} \mu\text{H/m}$$

$$[C_{nm}] = \begin{bmatrix} 49.923 & -22.398 & -25.494 & -64.607 \\ -22.398 & 90.731 & -27.703 & -34.634 \\ -25.494 & -27.703 & 93.247 & -33.252 \\ -0.646 & -34.634 & -33.252 & 76.094 \end{bmatrix} \text{pF/m}$$

The characteristic-admittance matrix, obtained by inverting the characteristic-impedance matrix, is

$$[Y_{C_{nm}}] = \begin{bmatrix} 1.030 \times 10^{-2} & -4.562 \times 10^{-3} & -5.078 \times 10^{-3} & -1.844 \times 10^{-4} \\ -4.562 \times 10^{-3} & 1.823 \times 10^{-2} & -5.296 \times 10^{-3} & -6.894 \times 10^{-3} \\ -5.078 \times 10^{-3} & -5.296 \times 10^{-3} & 1.865 \times 10^{-2} & -6.590 \times 10^{-3} \\ -1.844 \times 10^{-4} & -6.894 \times 10^{-3} & -6.590 \times 10^{-3} & 1.554 \times 10^{-2} \end{bmatrix} \text{mho}$$

From the above matrix, the common-mode characteristic admittance, $Y_{C_{comm}}$, is 5.511×10^{-3} mho, and the common-mode characteristic impedance, $Z_{C_{comm}}$, is 181.448 ohms.

The common-mode propagation velocity, obtained from the inverse of the square root of the eigenvalues of the matrix product $[L_{nm}][C_{nm}]$, is 2.539×10^8 m/sec. From Equation 10, the per-unit-length common-mode capacitance of the line, C' , is 21.7 pF/m. From Equation 16, the capacitance of the bulkhead penetration is found to be 1.049 pF.

SECTION IV

MEASURED RESULTS

In this section, the measured response of a uniform multiconductor cable, a B-52 aircraft multiconductor cable, and three levels of simulated multiconductor cable in the laboratory environment are presented. Transient response of the uniform four-conductor cable was measured. The four-conductor cable is the same as the B-52 aircraft multiconductor cable. The common-mode current transfer functions at several locations along the cable were measured for the aircraft and the laboratory cables, both in the frequency and time domains. Three different models were considered in the laboratory. The first model was a replica of the B-52 aircraft cable, where the driving conditions were similar to those in the aircraft. In the second model, the cable at the input was approximated with a four-wire cable with an aluminum plate at the input. The analysis of this model is easier than the first model, since the first model involves six conductors at the input, the extra two conductors run only a short distance. The third model is a simplified version of the second model. This model consists of eight different uniform sections, each containing periodic discontinuities. A comparison between the results of these three models and the results of aircraft cable are presented in this section. A comparison between the calculated and measured results is presented in the next section.

1. UNIFORM FOUR-WIRE LINE

Figure 28 shows the four-wire line over a ground plane. The cross-sectional configuration of the line is shown in Figure 19. The conductors are terminated in 50-ohm loads at both the ends. A step-function source, with a 50-ohm source impedance, is used to drive one of the conductors of the line. Figure 29 shows the step function as viewed on the 200-MHz oscilloscope.

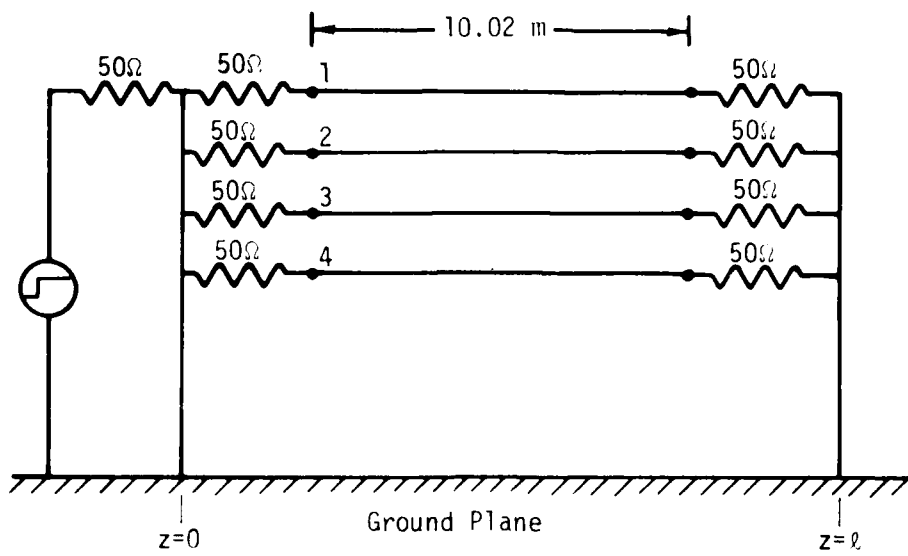


Figure 28. Uniform four-wire line over a ground plane.

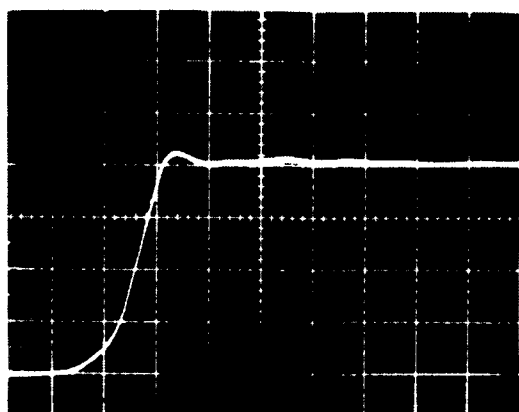


Figure 29. Pulse generator output signal: Vert sens. 5 V/div, horiz. sens. 2 ns/div, 50- Ω termination on the scope.

Figures 30 and 31 show the voltage and current waveforms recorded at the load end, when wire 1 is driven at the input. Figures 32 and 33 show the voltage and current waveforms recorded at the load end, when wire 4 is driven at the input. These waveforms show only two modes propagating on the line. In general, there are N modes of propagation on a $N+1$ conductor line in an inhomogeneous dielectric medium. Degeneracy may occur due to symmetry. The propagation velocities of the modes, measured in Section III, are 2.8×10^8 , 2.021×10^8 , 2.059×10^8 , and 1.955×10^8 meters/sec. Since the last three velocities are nearly equal, these propagation modes cannot be resolved in time. The first velocity corresponds to the common mode. The total voltage or current on a conductor is the sum of the voltages or currents, respectively, of all the modes on that conductor.

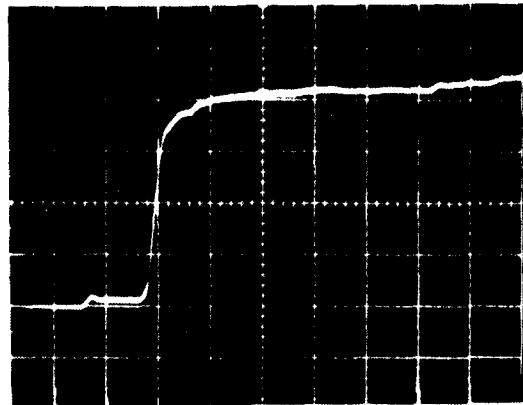
In measuring individual currents in a multiconductor cable, there is a danger of extraneous pick-up on the probe from other conductors, giving an erroneous result. To avoid this extraneous pick-up on the probe, the setup shown in Figure 34 was used for the measurement of the load currents. The wires are diverted at 90 degrees at the load end and grounded to the aluminum plate. The current probe is inserted at the ground end of the wire. This setup reduces the undesirable pick-up on the probe from other conductors.

The voltages on the conductors at the load end can be calculated using the procedure described in Reference 8. The formulas to calculate the amplitude of the modes are given below.

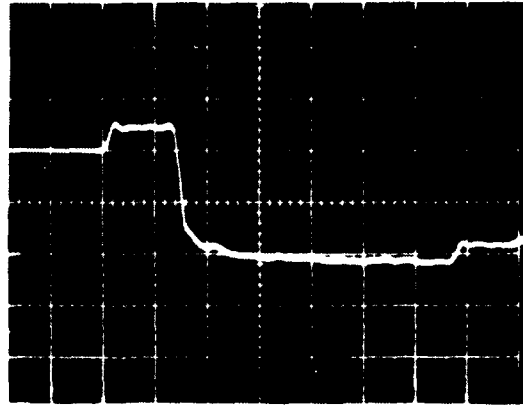
The voltage wave, traveling in the forward direction at $Z=0$ can be obtained from the relation,

$$[V_{f_n}(0,t)] = [Z_{c_{nm}}][Z_{c_{nm}} + Z_{s_{nm}}]^{-1}[V_{s_n}(0,t)] \quad (17)$$

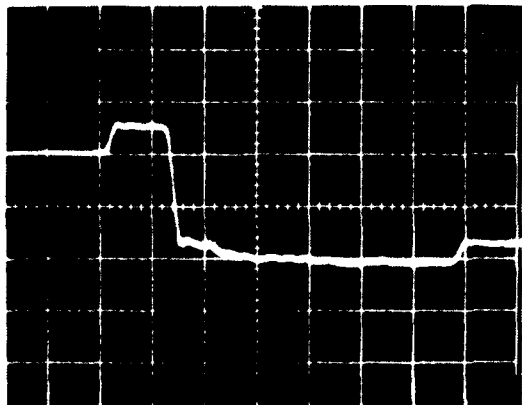
where $[Z_{c_{nm}}]$ is the characteristic-impedance matrix of the line, $[Z_{s_{nm}}]$ the termination-impedance matrix at the driven end, and $[V_{s_n}(0,t)]$ the



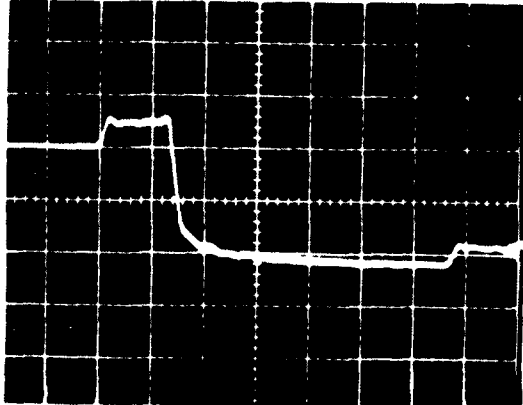
(a) Voltage waveform on wire 1.
Vertical scale: 2 V/div.



(b) Voltage waveform on wire 2.
Vertical scale: 1 V/div.

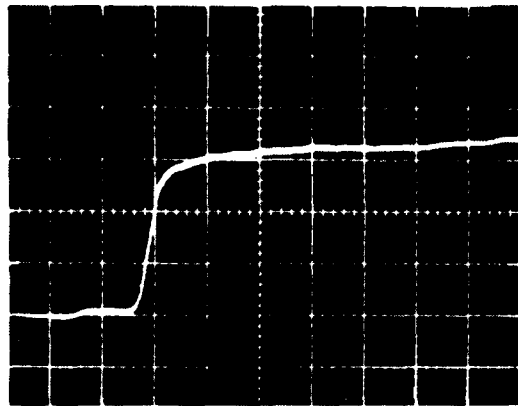


(c) Voltage waveform on wire 3.
Vertical scale: 1 V/div.

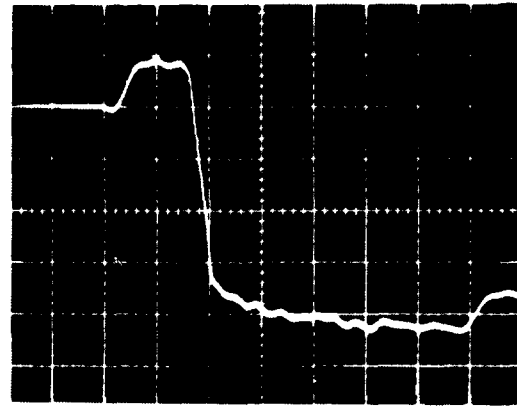


(d) Voltage waveform on wire 4.
Vertical scale: 1 V/div.

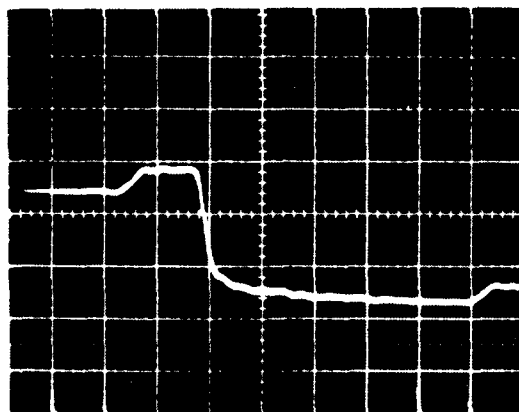
Figure 30. Voltage waveform at the load end, with wire 1 driven at the input end. Horizontal scale: 10 ns/div.



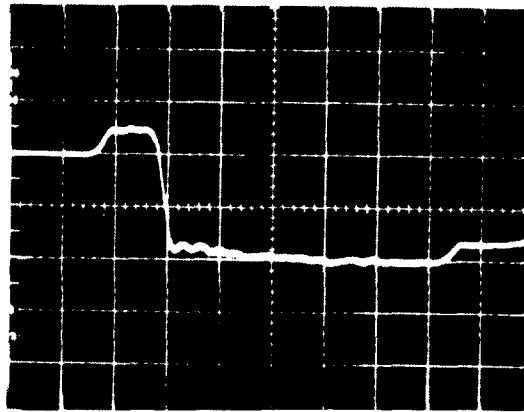
(a) Current waveform on wire 1.
Vertical scale: 50 mA/div.



(b) Current waveform on wire 2.
Vertical scale: 10 mA/div.

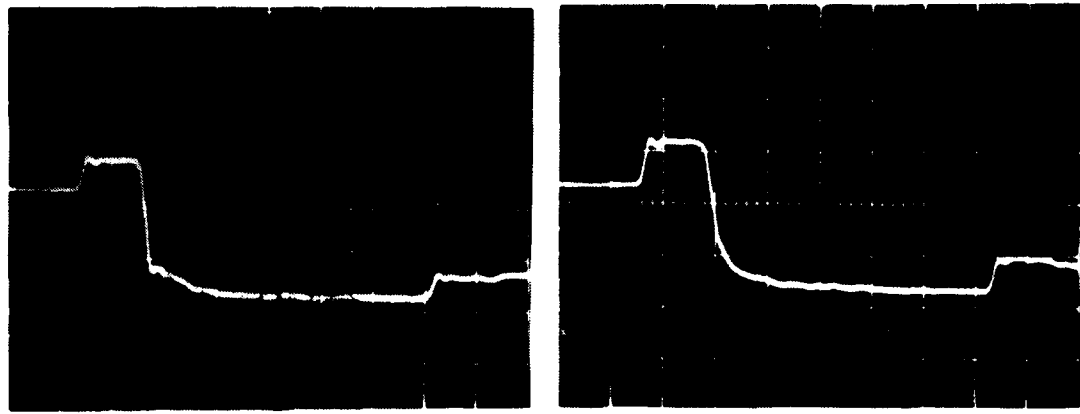


(c) Current waveform on wire 3.
Vertical scale: 20 mA/div.



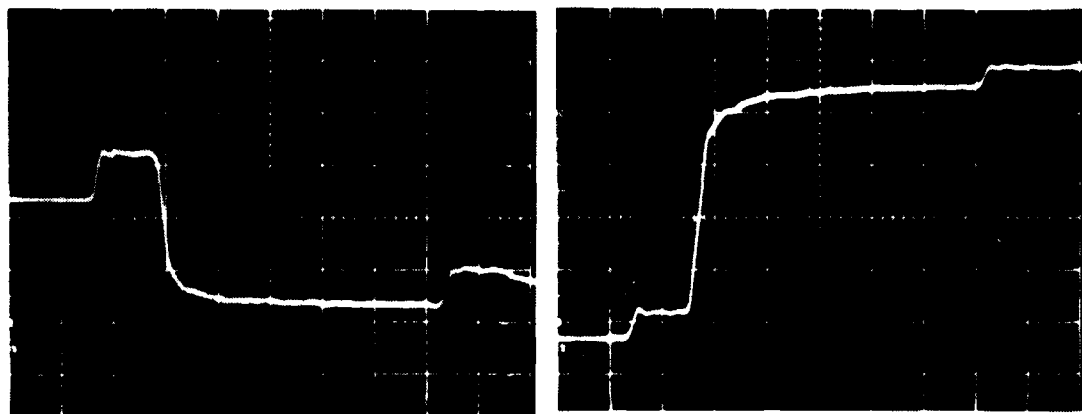
(d) Current waveform on wire 4.
Vertical scale: 20 mA/div.

Figure 31. Current waveforms at the load end, with wire 1 driven at the input end. Horizontal scale: 10 ns/div.



(a) Voltage waveform on wire 1.
Vertical scale: 1 V/div.

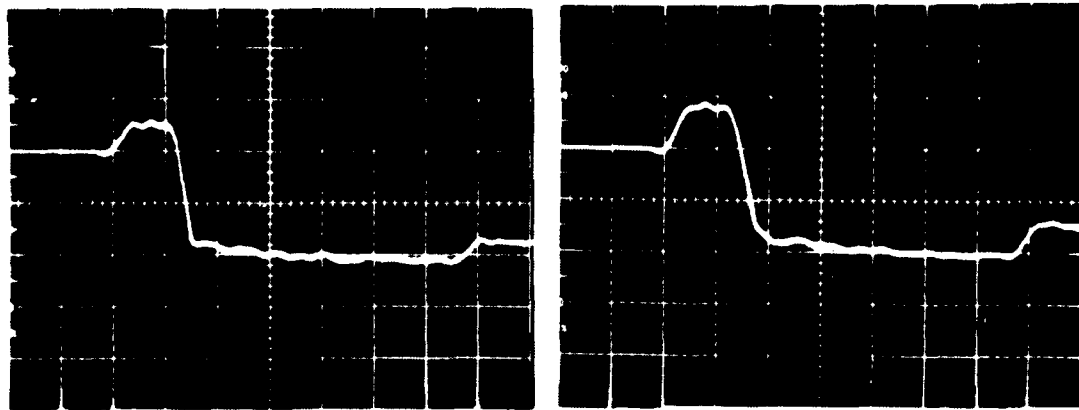
(b) Voltage waveform on wire 2.
Vertical scale: 1 V/div.



(c) Voltage waveform on wire 3.
Vertical scale: 1 V/div.

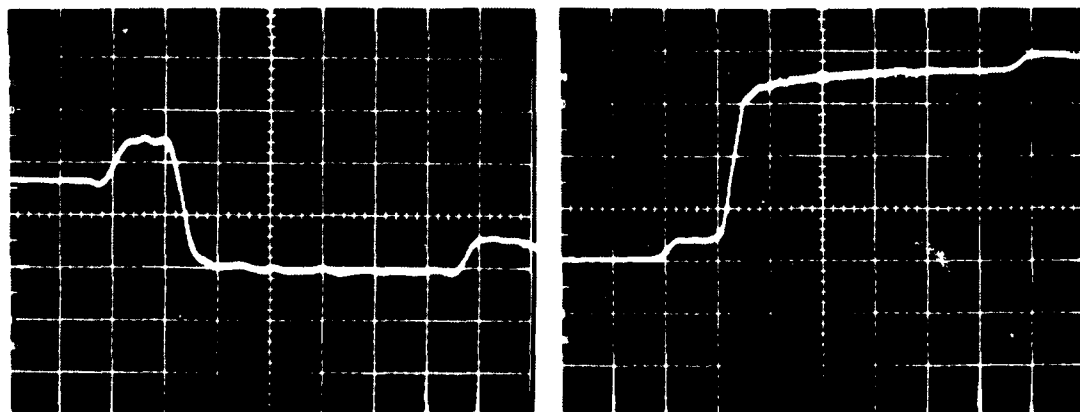
(d) Voltage waveform on wire 3.
Vertical scale: 2 V/div.

Figure 32. Voltage waveforms at the load end, with wire 4 driven at the input end. Horizontal scale: 10 ns/div.



(a) Current waveform on wire 1.
Vertical scale: 20 mA/div.

(b) Current waveform on wire 2.
Vertical scale: 20 mA/div.



(c) Current waveform on wire 3.
Vertical scale: 20 mA/div.

(d) Current waveform on wire 4.
Vertical scale: 50 mA/div.

Figure 33. Current waveforms at the load end, with wire 4 driven at the input end. Horizontal scale: 10 ns/div.

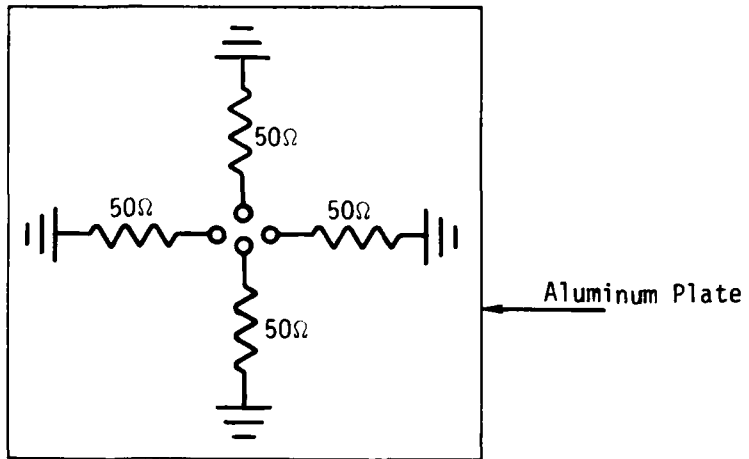


Figure 34. Setup for the measurement of currents.

source-voltage vector at $z=0$. The forward-traveling voltage vector at any point z can be obtained from the relation

$$[V_{f_n}(z,t)] = [V_{nm}][A_m(t - \tau_m)] \quad (18)$$

where $[V_{nm}]$ is the (voltage) eigenvector matrix of the matrix product $[L_{nm}] \cdot [C_{nm}]$, $\tau_m = z/v_m$ is the transit time of the m th mode, and $[A_m]$ is an unknown vector. The vector $[A_m]$ can be calculated from the following relation

$$[V_{f_n}(0,t)] = [V_{nm}][A_m(t)] \quad (19)$$

The line is assumed to be lossless and the waves travel unattenuated. The voltage transmission coefficient at the load is given by the relation

$$[\tau_{nm}] = 2[Z_{Lnm}][Z_{Lnm} + Z_{Cnm}]^{-1} \quad (20)$$

where $[Z_{Lnm}]$ is the impedance matrix of the termination network at the load. The load-voltage vector for a mode can be obtained from the incident-voltage vector at the load for that mode by premultiplying it by the transmission coefficient as

$$[V_{Ln}(\ell, t)]_m = 2[Z_{Lnm}][Z_{Lnm} + Z_{Cnm}]^{-1}[V_{fn}(\ell, t)]_m \quad (21)$$

where $[V_{Ln}(\ell, t)]_m$ is the load-voltage vector for the mth mode, and $[V_{fn}(\ell, t)]_m$ is the incident-voltage vector for the mth mode.

The total voltage on a conductor is obtained by adding the contributions of all the modes. The currents in the conductors can be calculated using the similar procedure, the current eigenvector matrix $[I_{nm}]$ are employed instead of voltage eigenvector matrix in Equation 18. The current eigenvector matrix $[I_{nm}]$ is the eigenvector of the matrix product $[C_{nm}][L_{nm}]$, and the current transmission coefficient at the load is given by the relation

$$[\tau_{nm}] = 2[Z_{Cnm}][Z_{Lnm} + Z_{Cnm}]^{-1} \quad (22)$$

The load-current vector for a mode can be obtained from the incident-current vector at the load for that mode by premultiplying it by the current transmission coefficient as

$$[I_{Ln}(\ell, t)]_m = 2[Z_{Lnm} + Z_{Cnm}][I_{fn}(\ell, t)]_m \quad (23)$$

where $[I_{Ln}(\ell, t)]_m$ is the load-current vector for the mth mode and $[I_{fn}(\ell, t)]_m$ is the incident-current vector for the mth mode.

The following are the calculated and measured results:

a) Wire 1 Driven

Load Voltages	Measured	Calculated
V_{L_1}	8.5 volts	8.919 volts
V_{L_2}	-2.2 volts	-2.345 volts
V_{L_3}	-2.2 volts	-2.346 volts
V_{L_4}	-2.05 volts	-2.0917 volts

Load Currents	Measured	Calculated
I_{L_1}	165 mA	178.38 mA
I_{L_2}	-41 mA	-46.9 mA
I_{L_3}	-42 mA	-46.92 mA
I_{L_4}	-40 mA	-41.83 mA

b) Wire 4 Driven

Load Voltages	Measured	Calculated
V_{L_1}	-2.03 volts	-2.19 volts
V_{L_2}	-2.1 volts	-2.38 volts
V_{L_3}	-2.1 volts	-2.33 volts
V_{L_4}	9.6 volts	9.95 volts

Load Currents	Measured	Calculated
I_{L_1}	-40 mA	-43.8 mA
I_{L_2}	-40 mA	-47.6 mA
I_{L_3}	-35 mA	-46.7 mA
I_{L_4}	180 mA	199 mA

A. Uniform Four-Wire Line Excited in the Common Mode

Figure 35 shows the four-wire line excited in common mode. When the excitation voltages on all the conductors are identical, only common mode propagates on the line. All the conductors are connected together at the input end and are driven by a rectangular pulse source. Figure 36 shows the square pulse as viewed on the 200-MHz oscilloscope. At the other end, the conductors are terminated in 50-ohm loads.

Figures 37 and 38 show the voltage and current waveforms recorded at the load end, as viewed on the 200-MHz oscilloscope. Setup of Figure 34 was used for the measurements at the load.

The load voltages and currents can be calculated by using Equations 21 and 23. The source-voltage vector at the driven end for the common-mode excitation is given by the following relation

$$[V_{S_n}(0,t)] = \begin{bmatrix} V_o(t) \\ V_o(t) \\ V_o(t) \\ V_o(t) \end{bmatrix} \quad (24)$$

where $V_o(t)$ is the voltage at the input terminals of the line.

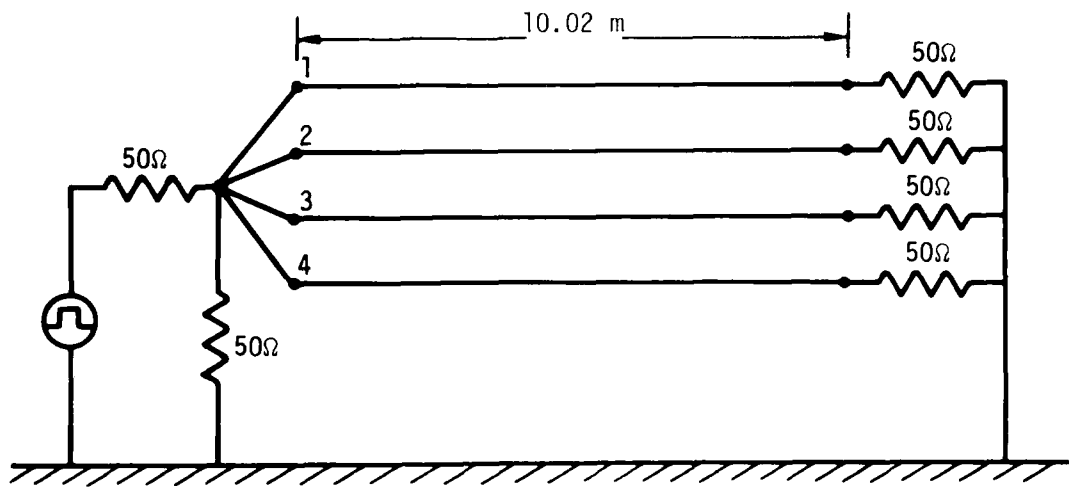


Figure 35. Uniform four-wire line over a ground plane, excited in the common mode.

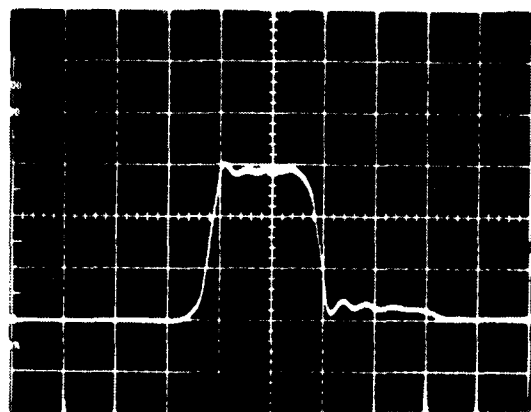
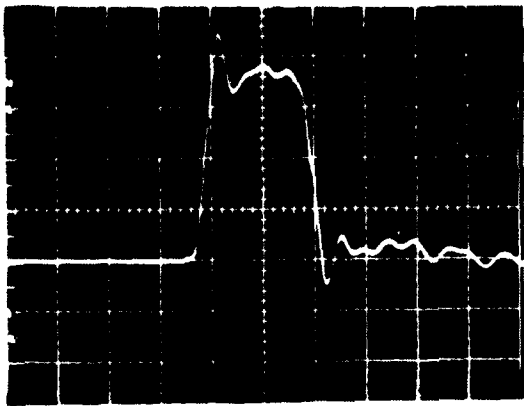
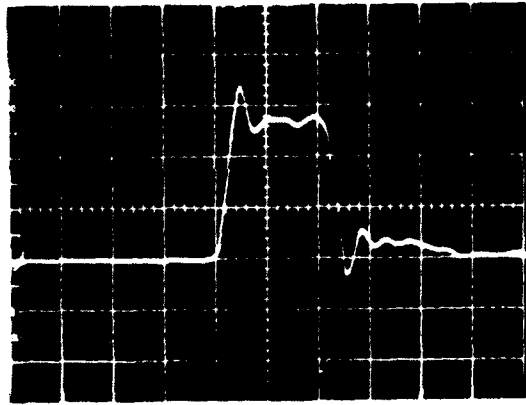


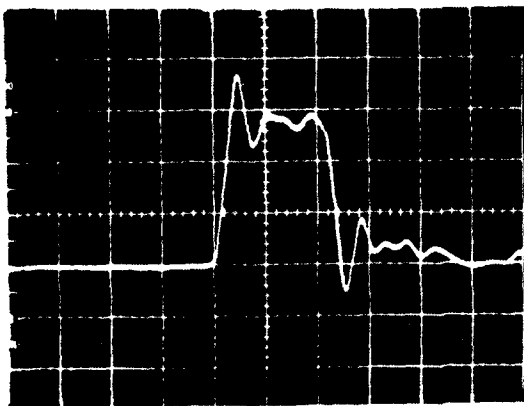
Figure 36. Pulse generator output signal. Vert. sens. 5 V/div, horiz. sens. 5 ns/div, 50- Ω termination on the scope.



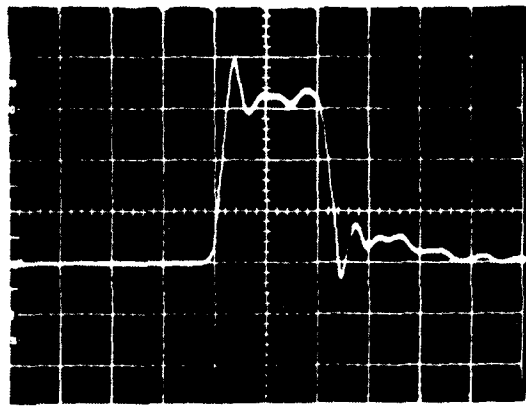
(a) Voltage waveform on wire 1.
Vertical scale: 0.5 V/div.



(b) Voltage waveform on wire 2.
Vertical scale: 1 V/div.

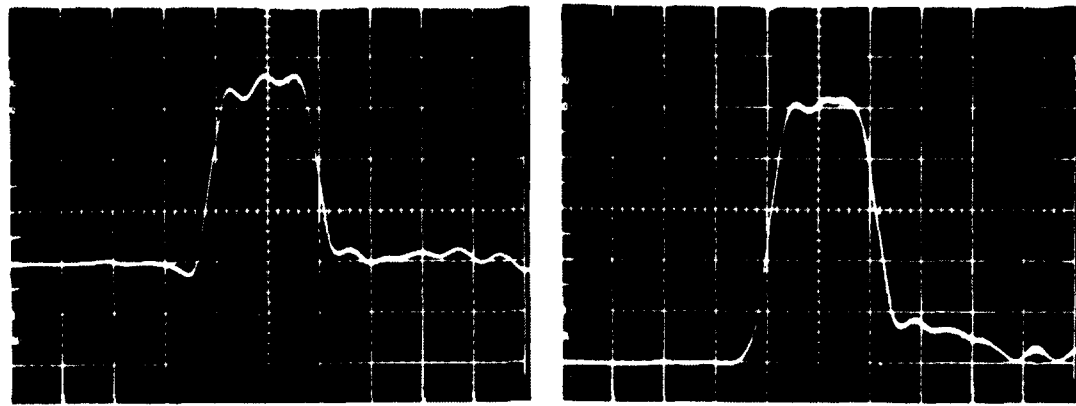


(c) Voltage waveform on wire 3.
Vertical scale: 1 V/div.



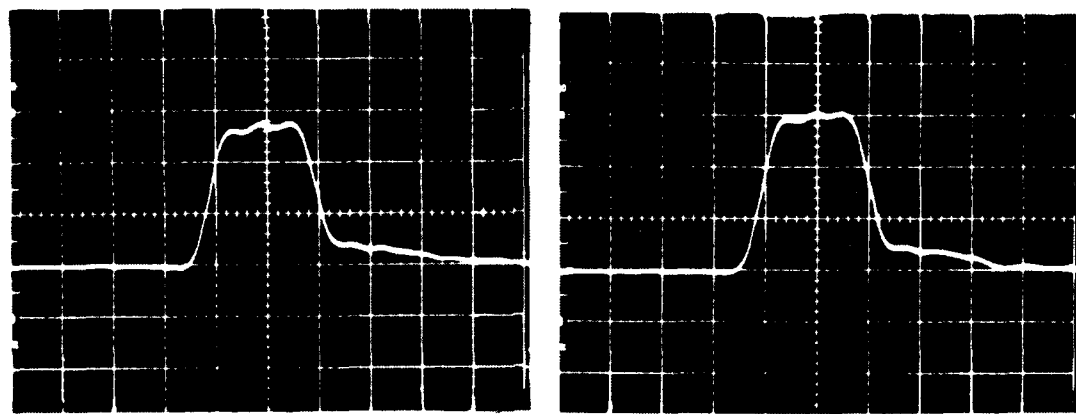
(d) Voltage waveform on wire 4.
Vertical scale: 1 V/div.

Figure 37. Voltage waveforms at the load end, when the line is excited in common mode. Horizontal scale: 5 ns/div.



(a) Current waveform on wire 1.
Vertical scale: 10 mA/div.

(b) Current waveform on wire 2.
Vertical scale: 10 mA/div.



(c) Current waveform on wire 3.
Vertical scale: 20 mA/div.

(d) Current waveform on wire 4.
Vertical scale: 20 mA/div.

Figure 38. Current waveforms at the load, when the line is excited in common mode. Horizontal scale: 5 ns/div.

The following are the calculated measured results:

Load Voltages	Measured	Calculated
V_{L_1}	1.87 volts	1.885 volts
V_{L_2}	2.7 volts	2.723 volts
V_{L_3}	2.9 volts	2.909 volts
V_{L_4}	3.2 volts	3.22 volts
Load Currents	Measured	Calculated
I_{L_1}	36 mA	37.7 mA
I_{L_2}	52 mA	54.46 mA
I_{L_3}	55 mA	58.18 mA
I_{L_4}	61 mA	64.42 mA

2. B-52 AIRCRAFT MULTICONDUCTOR CABLE

Measurements on the aircraft multiconductor cable, described in Section II, were made during the early part of this work in July 1979. The response of the cable was measured both in the frequency and the time domain. The cable was excited in the common mode at the EMP hydraulic pump #1, Station 1528.5. The conductors were driven by the single source (common mode) and one ground wire was used as the reference conductor. The reference wire is grounded to the skin of the aircraft about two feet away from the input end. The other ground wire was left open at the input

connector. Thus for a short distance the cable is a six-conductor line with four conductors driven in the common mode. A desirable way of exciting the cable, for the purpose of analysis, would be to use the aircraft skin as the ground plane at the input end, with two grounding wires removed. This could not be done due to the restrictions on any alterations on the aircraft and the limited access to the aircraft. Past the grounding wires, the cable is a four-wire line over a ground plane, the ground plane being the aircraft skin or the major structures, such as fuel tanks, girders, etc.

A. Time-Domain Measurements

The cable was excited in the common mode by connecting all the conductors together, with a pulse shown in Figure 39, as viewed on the 200-MHz oscilloscope. At the other end of the cable, Station 648, all

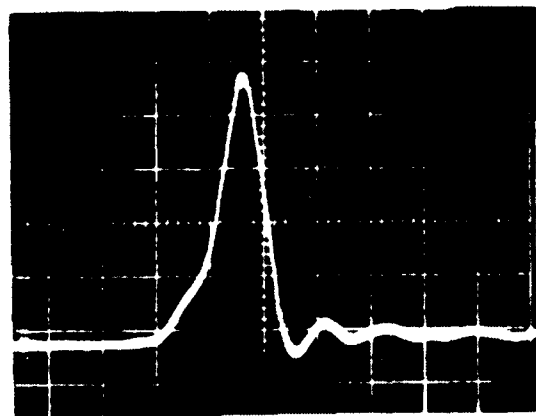


Figure 39. Input waveform used to drive the aircraft cable. Vertical scale: 5 V/div; Horizontal scale: 2 ns/div, 50-ohm termination on the scope.

the wires were connected together and terminated in a 50-ohm load. The current waveforms were measured at several locations along the cable with a 5-ohm current probe (AILTEC 91555-1). Figures 41a, 42a, 43a, 44a, 45a, 46a, and 47a show the current waveforms at Stations 1489, 1471, 1422, 1382, 1342, 990, and 940, respectively. A discussion of these results will be presented later in this section.

B. Frequency-Domain Measurements

The cable was excited in the common mode by connecting all the conductors together, with a sweep generator (1-100 MHz). At the other end of the cable, Station 648, all the conductors were connected together and terminated in a 50-ohm load. The current transfer ratios were measured at several locations along the cable. The current at Station 1489 was used as the reference current. Two 75-feet long matched coaxial cables were used to measure the current transfer ratios. Figures 48a, 51a, 54a, 57a, and 60a show the magnitudes of the current transfer ratio at Stations 1471, 1442, 1412, 1382, and 940, respectively, as a function of frequency. Figures 49a, 52a, 55a, 58a, and 62a show the phases of the current transfer ratio at Stations 1471, 1442, 1412, 1382, and 940, respectively, as a function of frequency. Figure 64 shows the short-circuit common-mode input impedance of the cable as a function of frequency, when the other end of the cable is terminated in a short circuit. Figure 65 shows the open-circuit common-mode input admittance of the cable as a function of frequency, when the other end of the cable is terminated in an open circuit. A discussion of these results will be presented later in this section.

? SIMULATED CABLE IN THE LABORATORY

Measurements were made on the laboratory model of the aircraft cable, shown in Figures 6 through 14, both in the frequency and the time domain. The cable was excited in the same manner as the aircraft cable. One of the grounding wires (Figure 14) was used as a reference conductor and the other grounding wire was left open at the input end. The cable was excited at Station 1528.5.

A. Time-Domain Measurements

The cable was excited in the common mode by connecting all the conductors together, with a pulse shown in Figure 40, as viewed on the 200-MHz oscilloscope. At the other end of the cable, Station 648, all the wires were connected together and terminated in a 50-ohm load. The current waveforms were measured at several locations, same as the aircraft cable, along the cable with a 5-ohm current probe. Figures 41b, 42b, 43b, 44b, 45b, 46b, and 47b show the current waveforms at Stations 1489, 1471, 1422, 1382, 990, and 940, respectively.

B. Frequency-Domain Measurements

The cable was excited in the common mode at the input end, and terminated in a 50-ohm load at the other end. The current at Station 1489 was used as the reference current. Figures 48b, 51b, 54b, 57b, and 60b show the magnitudes of the current transfer ratio at Stations 1471, 1442, 1412, 1382, and 940, respectively, as a function of frequency (1-100 MHz)

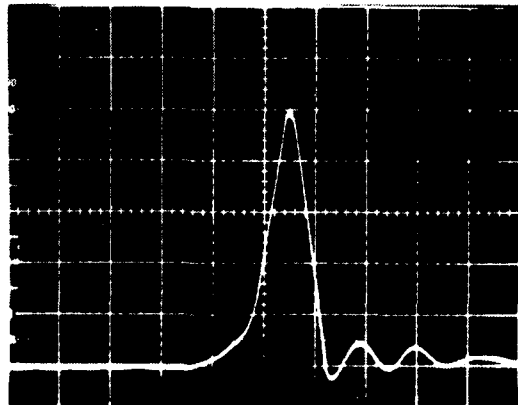


Figure 40. Input waveform used to drive the laboratory cable model.
Vertical scale: 5 V/div; Horizontal scale: 2 ns/div;
50-ohm termination on the scope.

Figures 49b, 52b, 55b, 58b, and 62b show the phases of the current transfer ratio at Stations 1472, 1442, 1412, 1382, and 940, respectively, as a function of frequency. Figure 66 shows the short-circuit common-mode input impedance of the cable as a function of frequency, when the other end of the cable is terminated in a short-circuit. Figure 67 shows the open-circuit common-mode input admittance of the cable as a function of frequency, when the other end of the cable is terminated in an open circuit.

4. EQUIVALENT FOUR-WIRE CABLE

For the purpose of comparison between the measured and calculated results, the ground wires at the input end of the simulated cable were removed, and an aluminum plate was used as the ground reference. The setup at the input end is the same as in Figure 20. The resultant cable is a four-wire cable above a ground plane.

Measurements made on the simulated cable were repeated for the four-wire cable, both in the frequency and the time domain. The cable was excited in the common mode at the input end, the ground plane was used as the reference. Figures 41c, 42c, 43c, 44c, 45c, 46c, and 47c show the transient current waveforms at Stations 1489, 1471, 1422, 1382, 990, and 940, respectively. The driving pulse used is the same as shown in Figure 40. Figures 48c, 51c, 54c, 57c, and 61a, show the magnitudes of the current transfer ratio at Stations 1471, 1442, 1412, 1382, and 940, respectively, as a function of frequency (1-100 MHz). Figures 50a, 53a, 56a, 59a and 63a show the phases of the current transfer ratio at Stations 1471, 1442, 1412, 1382, and 940, respectively, as a function of frequency (1-100 MHz). Figure 68 shows the short-circuit common-mode input impedance of the cable as a function of frequency. Figure 69 shows the open-circuit common-mode input admittance of the cable as a function of frequency.

5. SIMPLIFIED CABLE MODEL

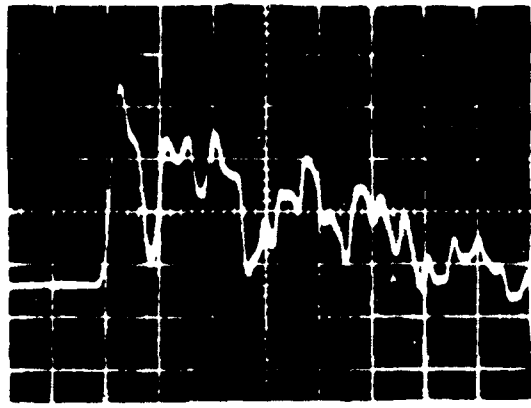
The measurements described in 2 and 3 were repeated for the simplified cable model, described in Section II. Figures 41d, 42d, 43d, 44d, 45d, 46d, and 47d show the transient current waveforms at Stations 1489, 1471, 1422, 1382, 1342, 990, and 940, respectively. The driving pulse was the same as shown in Figure 40. Figures 48d, 51d, 54d, 57d, and 61a show the magnitudes of the current transfer ratio at Stations 1471, 1442, 1412, 1382, and 940, respectively, as a function of frequency (1-100 MHz). Figures 50b, 53b, 56b, 59b, and 63b show the phases of the current transfer ratio at Stations 1471, 1442, 1412, 1382, and 940, respectively, as a function of frequency (1-100 MHz). Figure 70 shows the short-circuit common-mode input impedance of the cable as a function of frequency. Figure 71 shows the open-circuit common-mode input admittance of the cable as a function of frequency.

6. COMPARISON BETWEEN AIRCRAFT AND LABORATORY MEASURED RESULTS

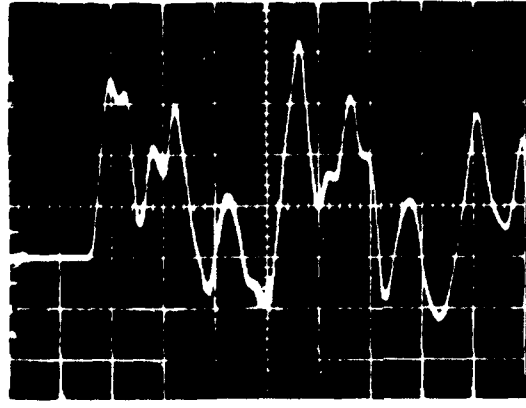
A. Time-Domain Results

The current waveforms at Stations 1489, 1471, 1422, 1382, 1342, 990, and 940, are shown in Figures 41 through 47, respectively, for the aircraft cable, simulated cable, four-wire cable and simplified cable. These figures show a comparison between the current waveforms for the four different configurations of the cable. The simulated cable is the closest representation of the aircraft cable. The four-wire cable is similar to the simulated cable except at the input end, where the ground wires are removed and the ground plane is used as the reference conductor. The simplified cable model is used to determine the errors due to simplification in the model.

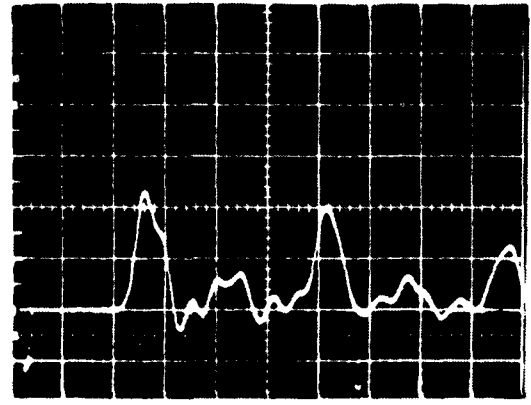
Figure 72 shows the current waveform on the aircraft cable along its length. The vertical sensitivity for waveforms at Station 940 and 990 is 20 mA/div, and for the rest of the stations it is 20 mA/div. It can be seen from Figure 72 that the pulse becomes more dispersive as it travels down the line, indicating that losses and mode conversion are present in the line. The decrease in amplitude of the pulses occurs as a result of multiple



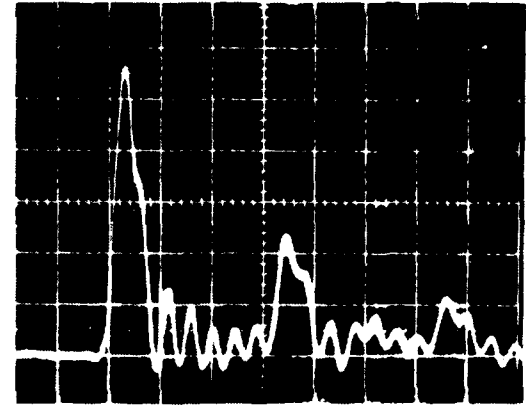
(a) Air-raft cable data. Vertical scale: 40 mA/div.



(b) Simulated cable (lab) data. Vertical scale: 40 mA/div.

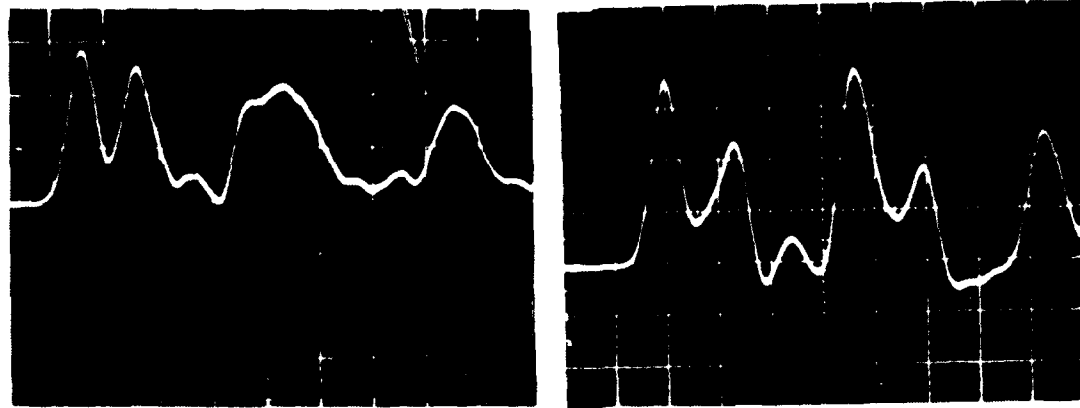


(c) Four-wire cable (lab) data. Vertical scale: 100 mA/div.



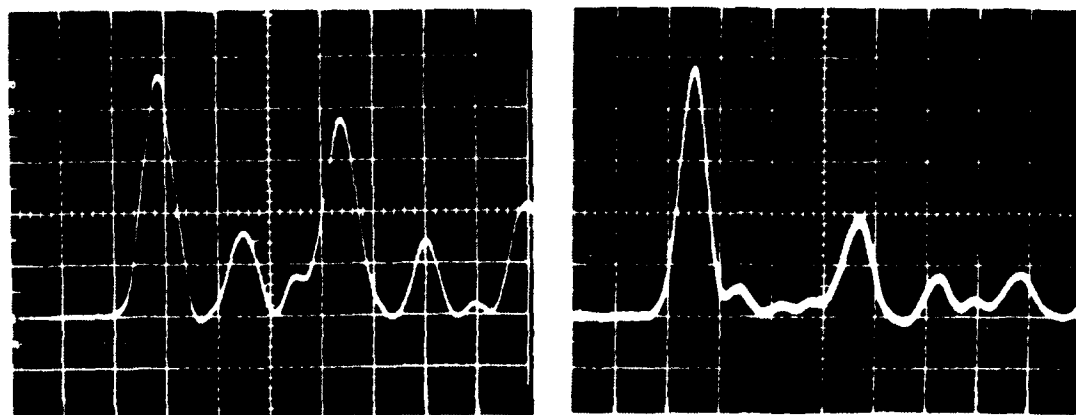
(d) Amplified (c) (d) data. Vertical scale: 4 mA/div.

Figure 41. Current waveforms at station 1489, with the cable driven at the input end, Station 1528.5, in the "chain" mode.
Horizontal scale: 10 ms/div.



(a) Aircraft cable data.

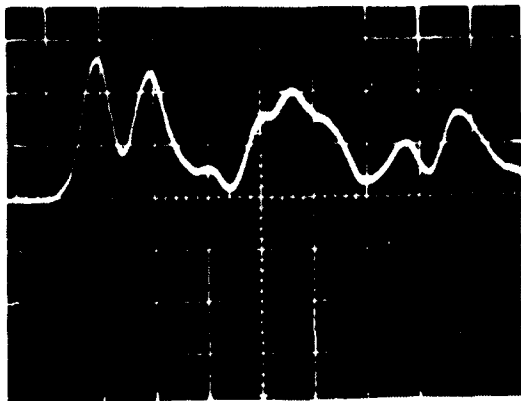
(b) Simulated cable (lab) data.



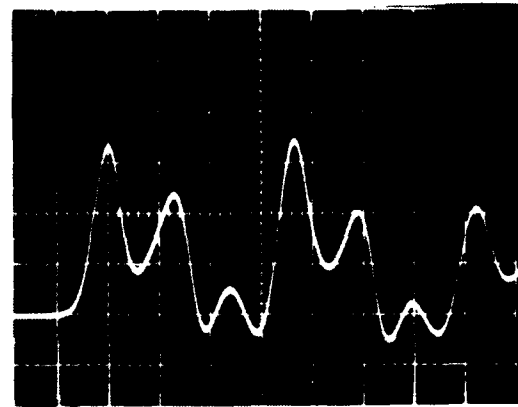
(c) Four-wire cable (lab) data.

(d) Simplified cable (lab) data.

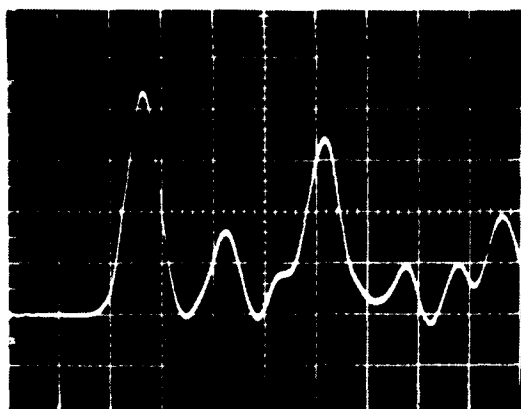
Figure 42. Current waveforms at Station 1471, with the cable driven at the input end, Station 1528.5, in the common mode.
Horizontal scale: 10 ns/div; Vertical scale: 40 mA/div.



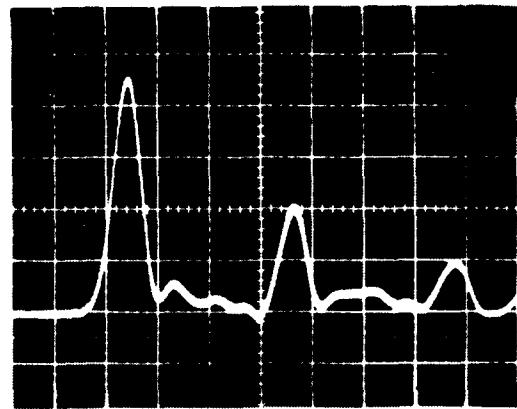
(a) Aircraft cable data.



(b) Simulated cable (lab) data.

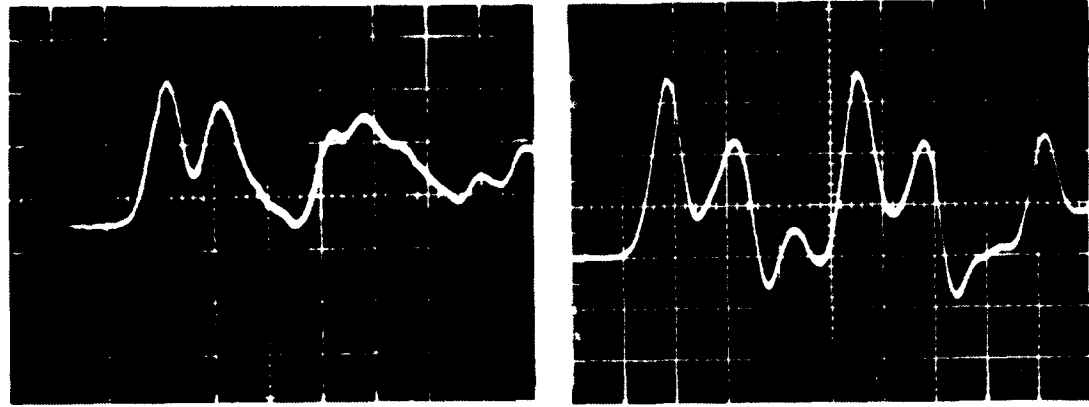


(c) Four-wire cable (lab) data.



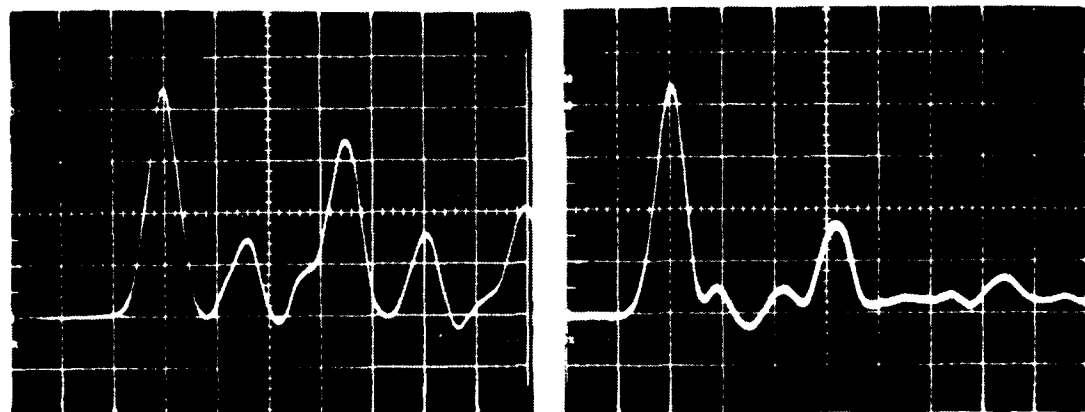
(d) Simplified cable (lab) data.

Figure 43. Current waveforms at Station 1422, with the cable driven at the input end, Station 1528.5, in the common mode.
Horizontal scale: 10 ns/div; Vertical scale: 40 mA/div.



(a) Aircraft cable data.

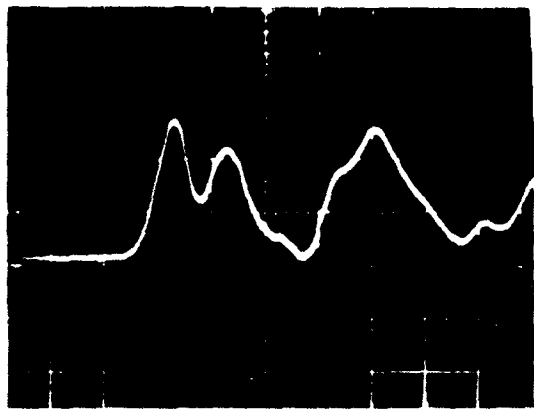
(b) Simulated cable (lab) data.



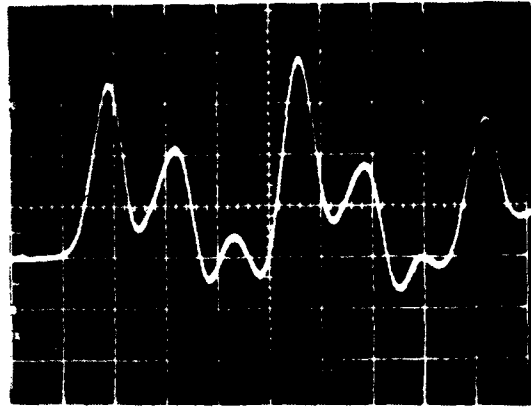
(c) Four-wire cable (lab) data.

(d) Simplified cable (lab) data.

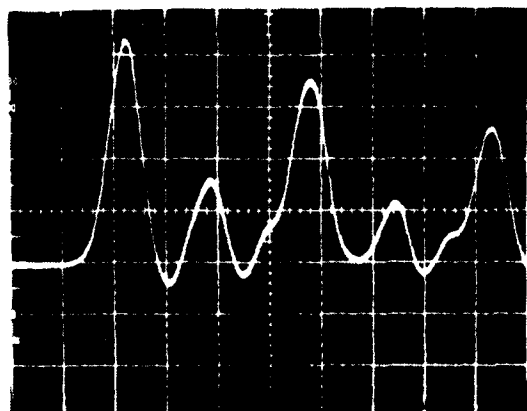
Figure 44. Current waveforms at Station 1382, with the cable driven at the input end, Station 1528.5, in the common mode.
Horizontal scale: 10 ns/div; Vertical scale: 40 mA/div.



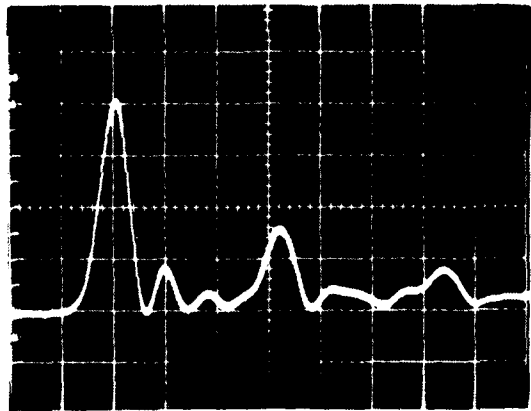
(a) Aircraft cable data.



(b) Simulated cable (lab) data.

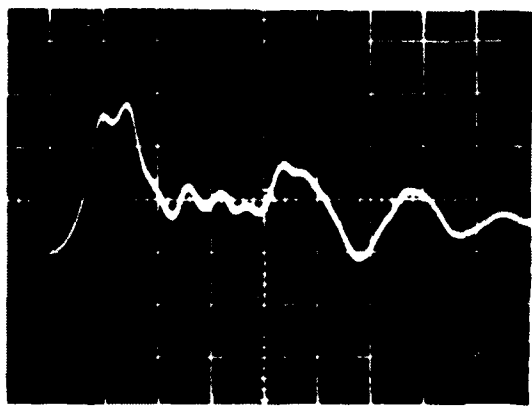


(c) Four-wire cable (lab) data.

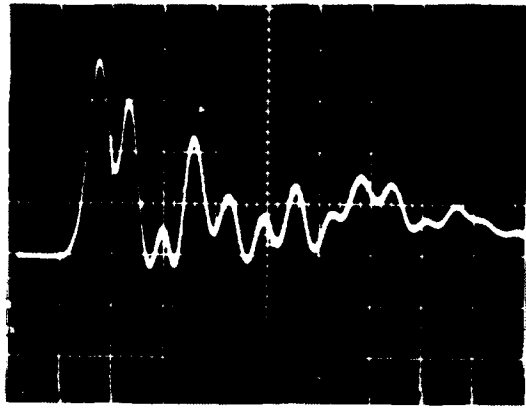


(d) Simplified cable (lab) data.

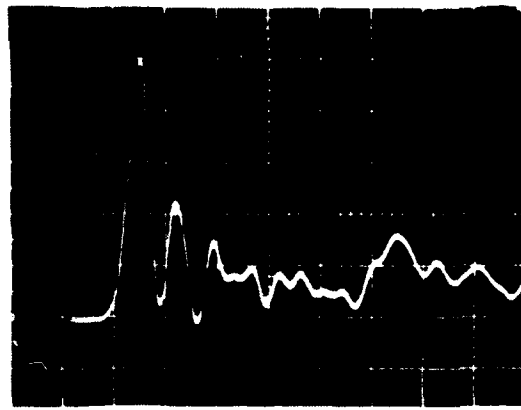
Figure 45. Current waveforms at Station 1342, with the cable driven at the input end, Station 1528.5, in the common mode.
Horizontal scale: 10 ns/div; Vertical scale: 40 mA/div.



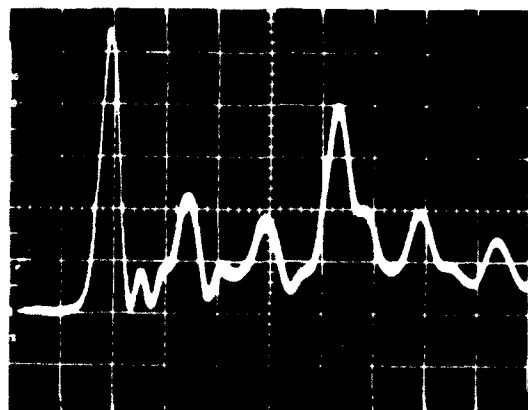
(a) Aircraft cable data.



(b) Simulated cable (lab) data.

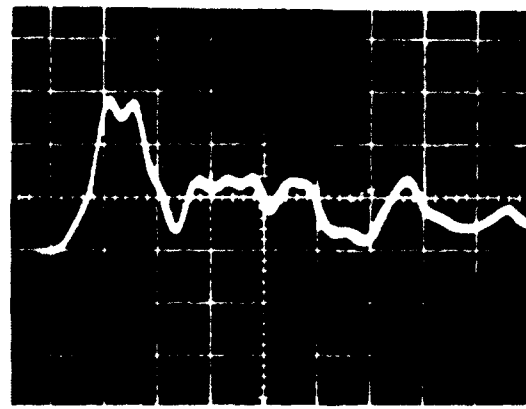


(c) Four-wire cable (lab) data.

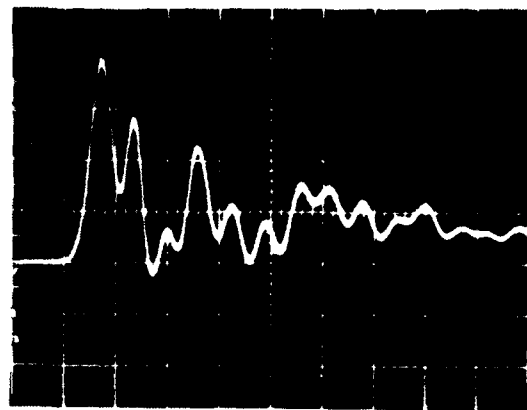


(d) Simplified cable (lab) data.

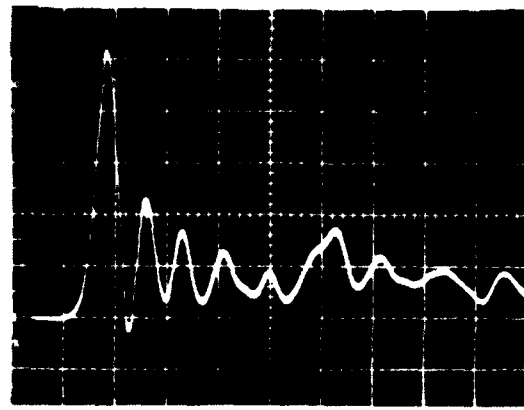
Figure 46. Current waveforms at Station 990, with the cable driven at the input end, Station 1528.5, in the common mode.
Horizontal scale: 20 ns/div; Vertical scale: 20 mA/div.



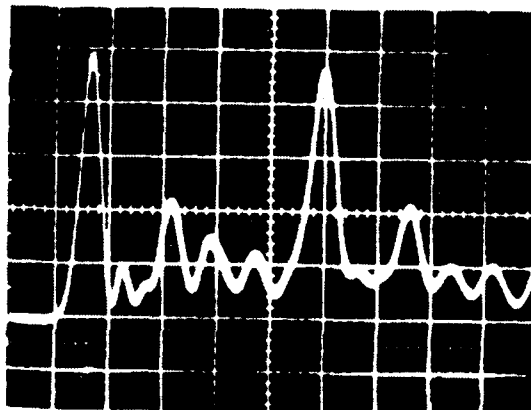
(a) Aircraft cable data.



(b) Simulated cable (lab) data.



(c) Four-wire cable (lab) data.



(d) Simplified cable (lab) data.

Figure 47. Current waveforms at Station 940, with the cable driven at the input end, Station 1528.5, in the common mode.
Horizontal scale: 20 ns/div; Vertical scale: 20 mA/div.

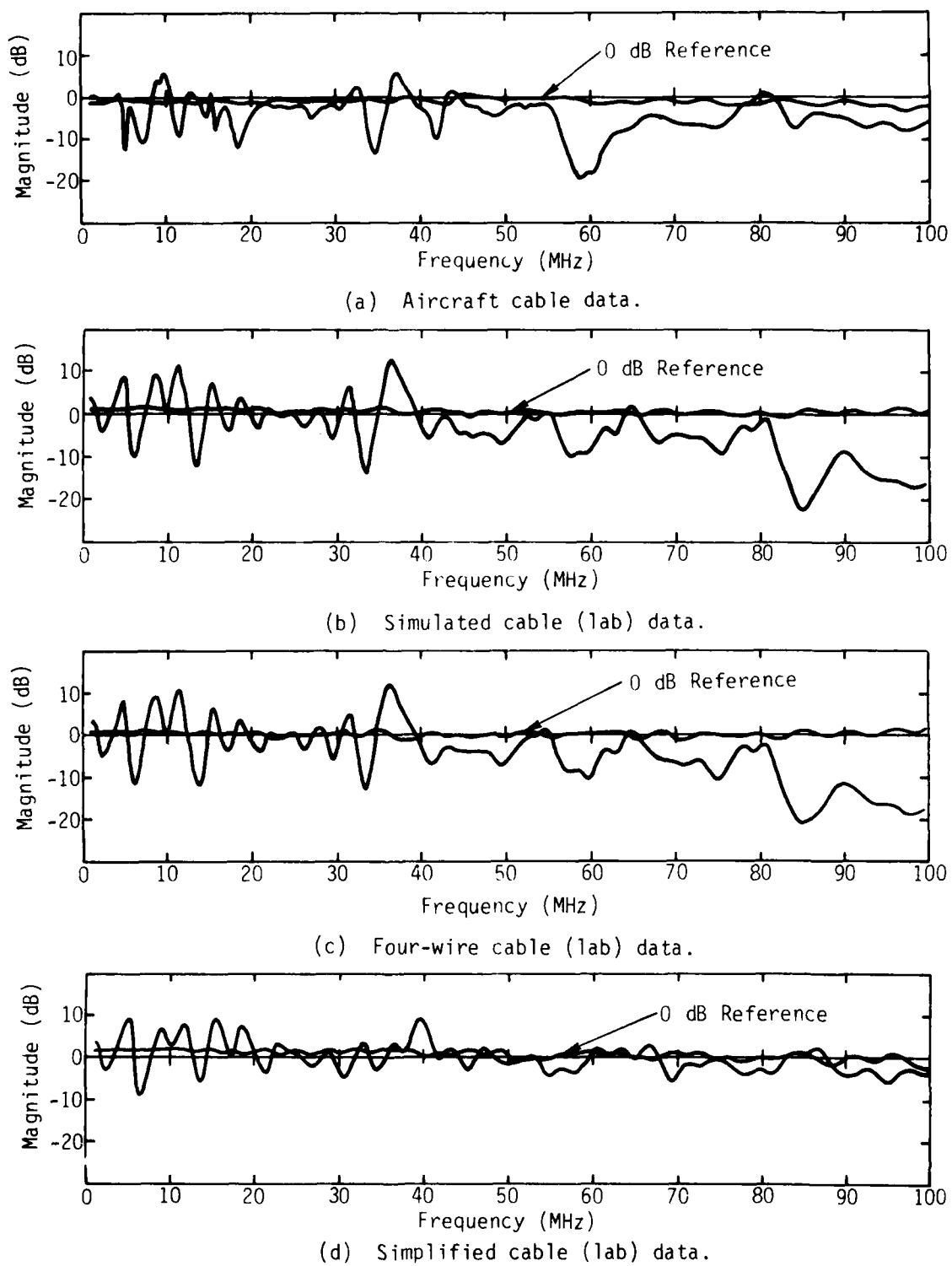
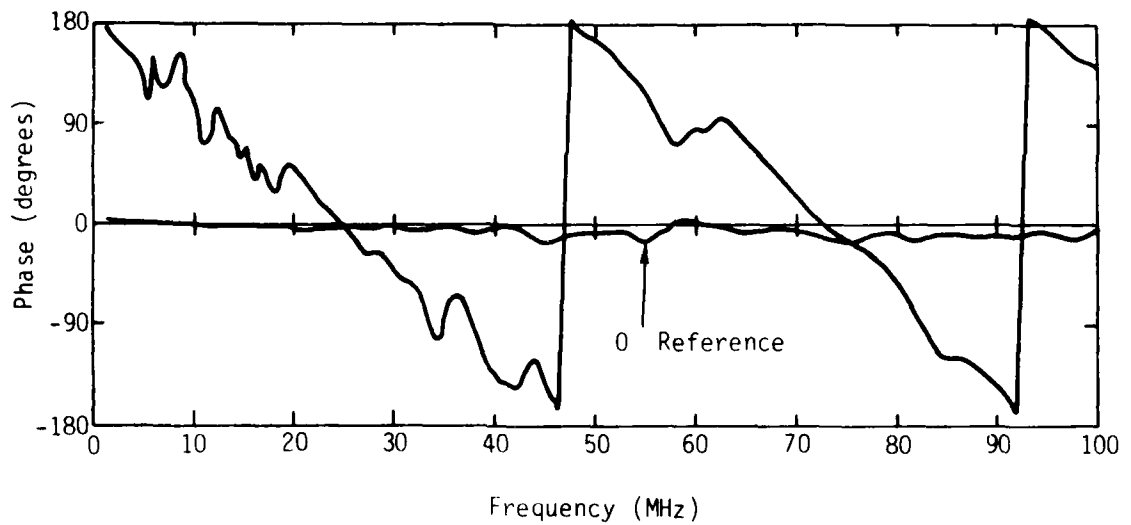
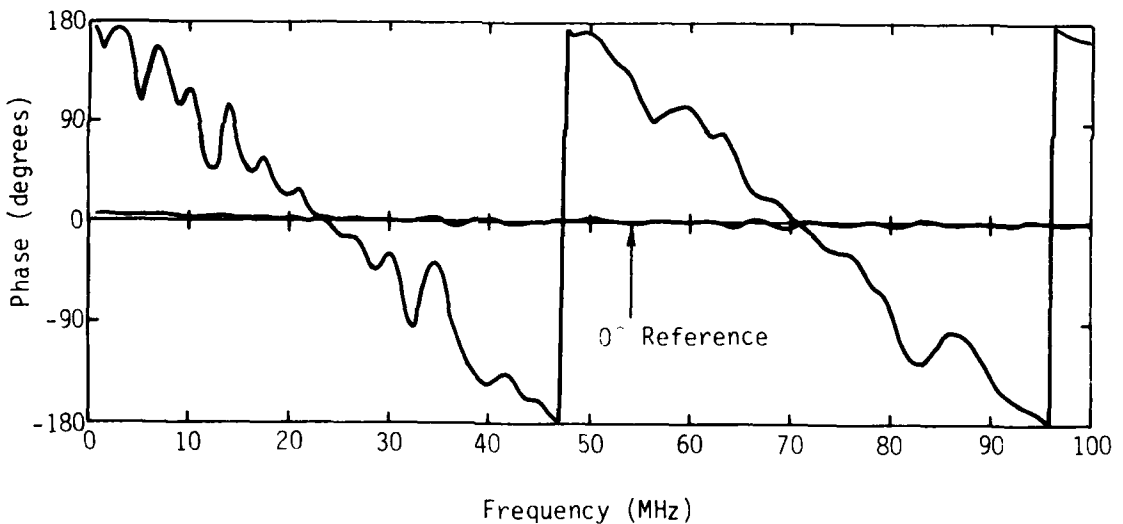


Figure 48. Current transfer ratio at Station 1471, with reference at Station 1489.

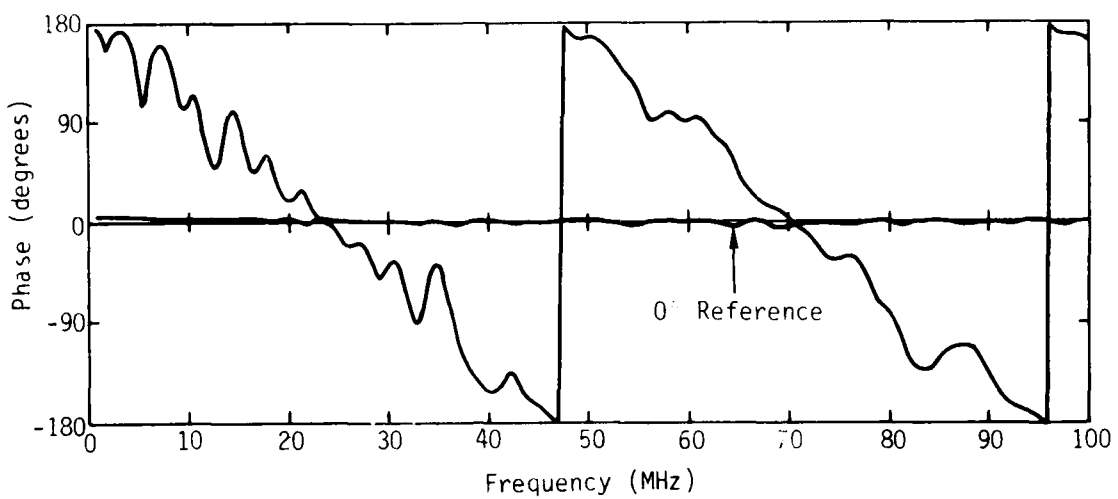


(a) Aircraft cable data.

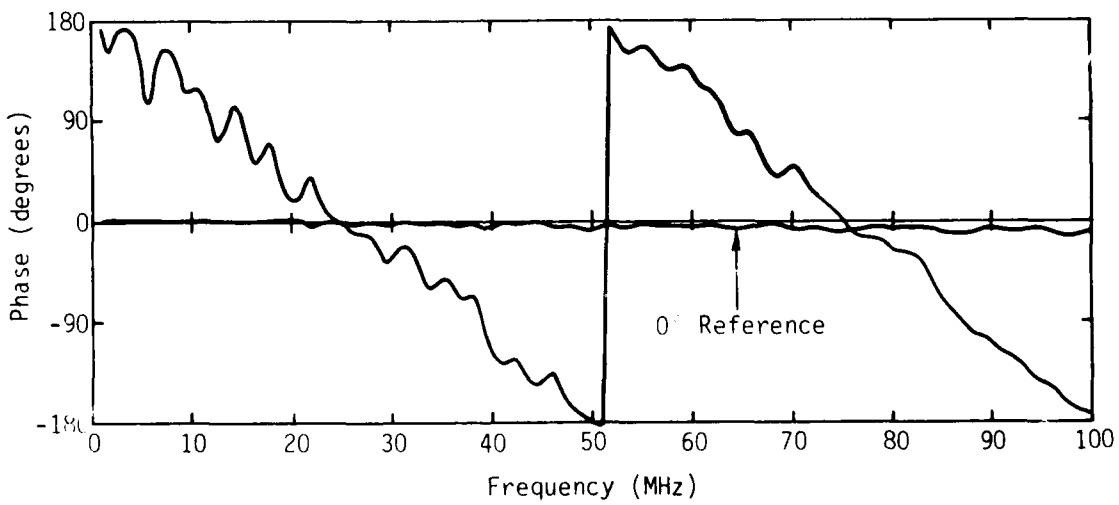


(b) Simulated cable (lab) data.

Figure 49. Current transfer ratio at Station 1471, with reference at Station 1489.



(a) Four-wire cable (lab) data.



(b) Simplified cable (lab) data.

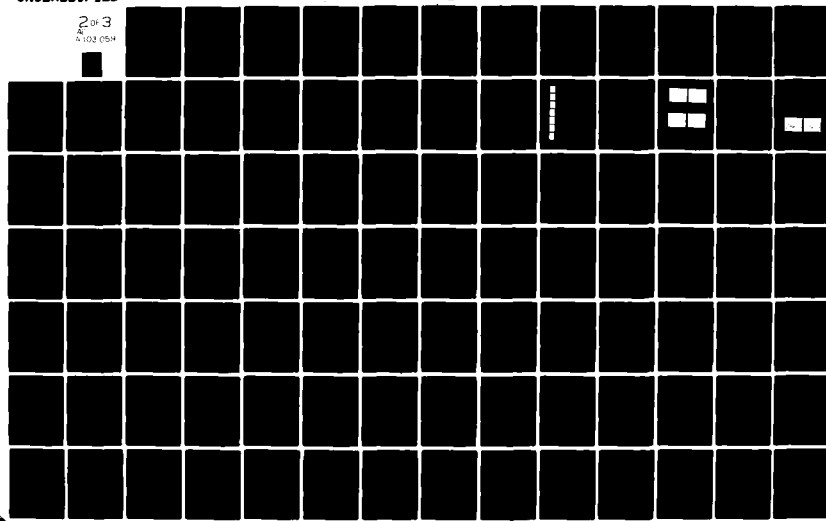
Figure 50. Current transfer ratio at Station 1471, with reference at Station 1489.

AD-A103 059

MISSION RESEARCH CORP ALBUQUERQUE NM
EXPERIMENTAL AND ANALYTICAL METHODS FOR THE CHARACTERIZATION OF--ETC(U)
SEP 80 A K AGRAWAL, J R BARNUM, L D SCOTT F29601-78-C-0082
AFWL-TR-80-35 NL

UNCLASSIFIED

2 of 3
A-103 059



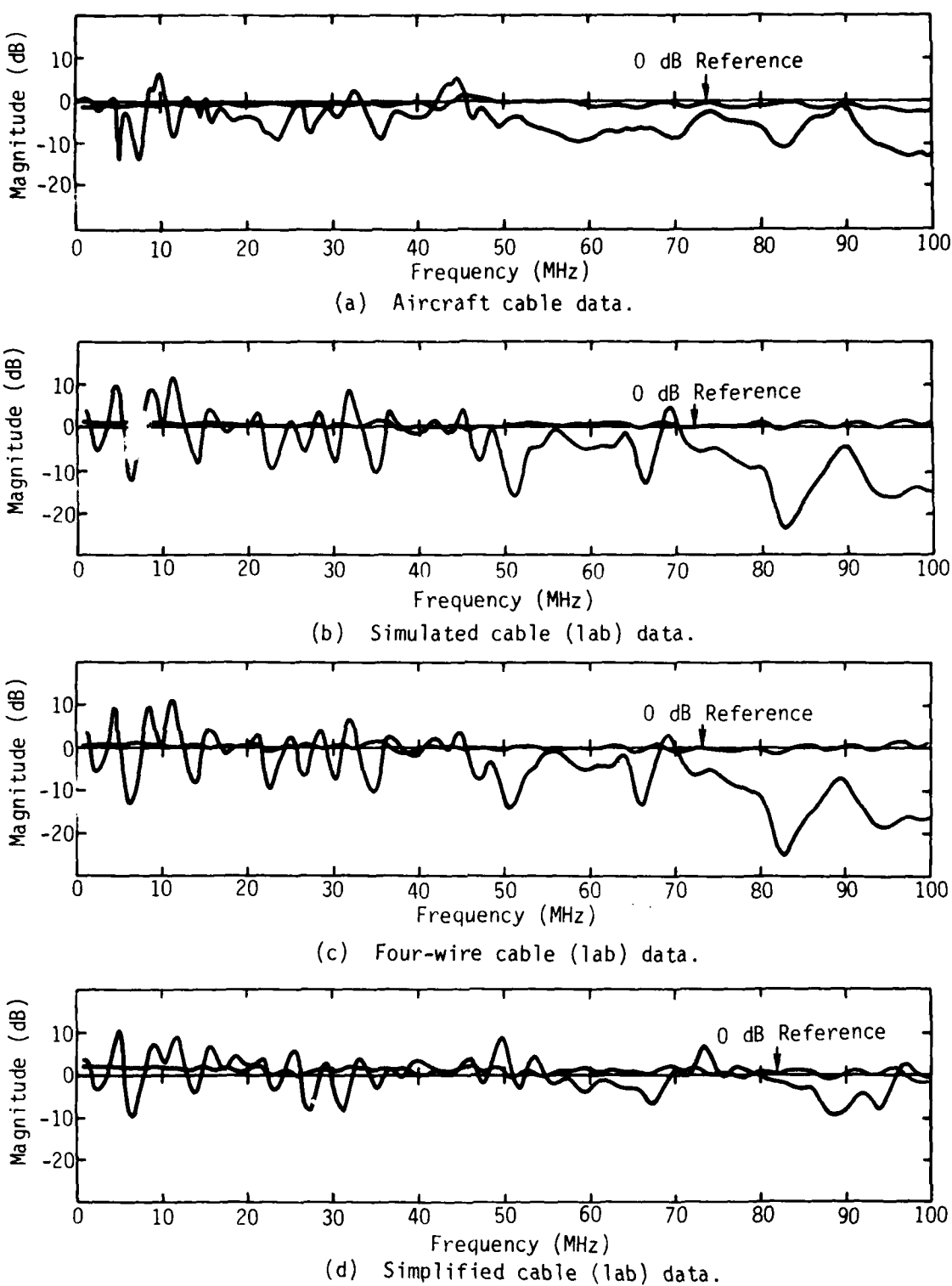
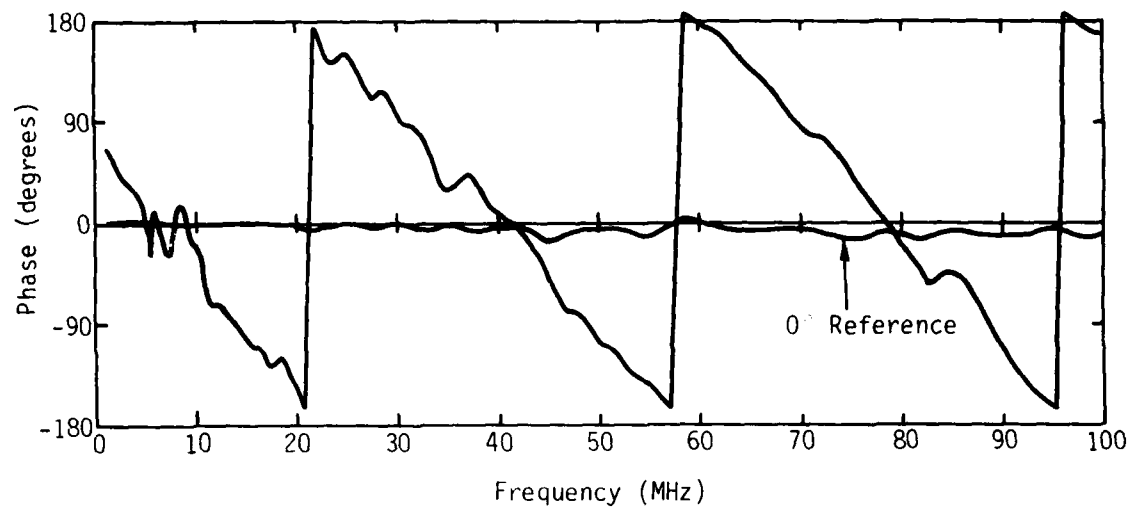
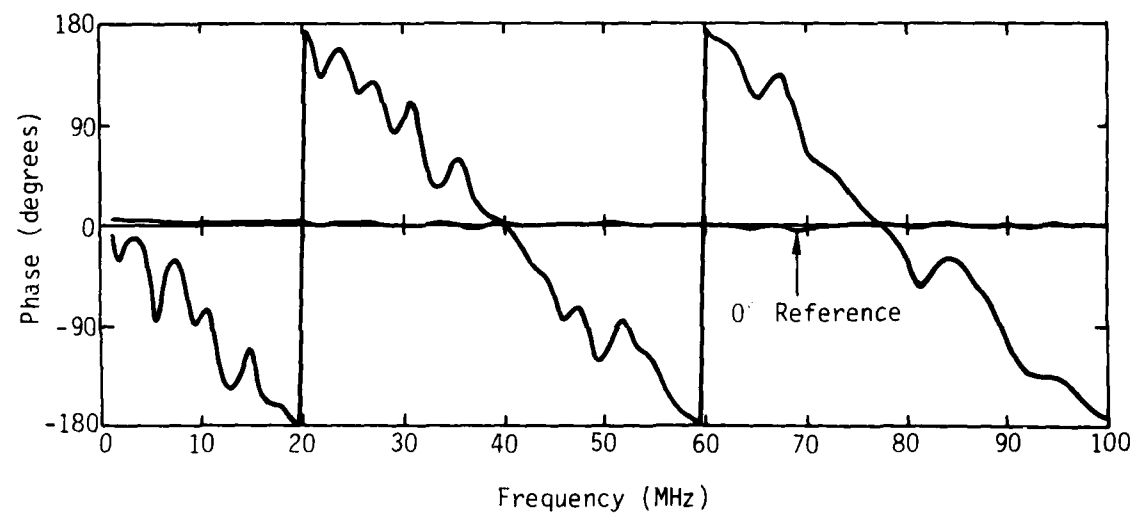


Figure 51. Current transfer ratio at Station 1442, with reference at Station 1489.

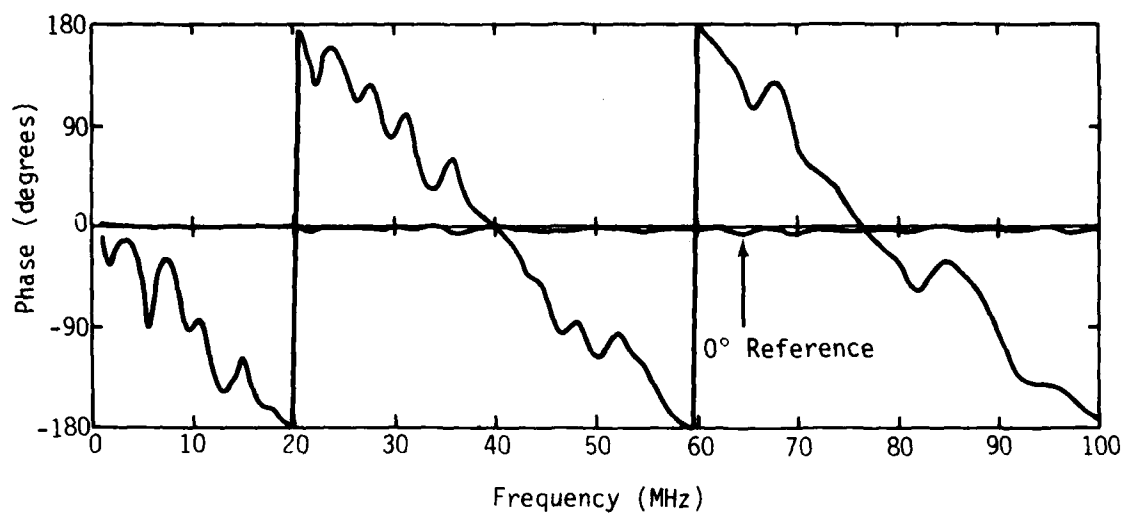


(a) Aircraft cable data.

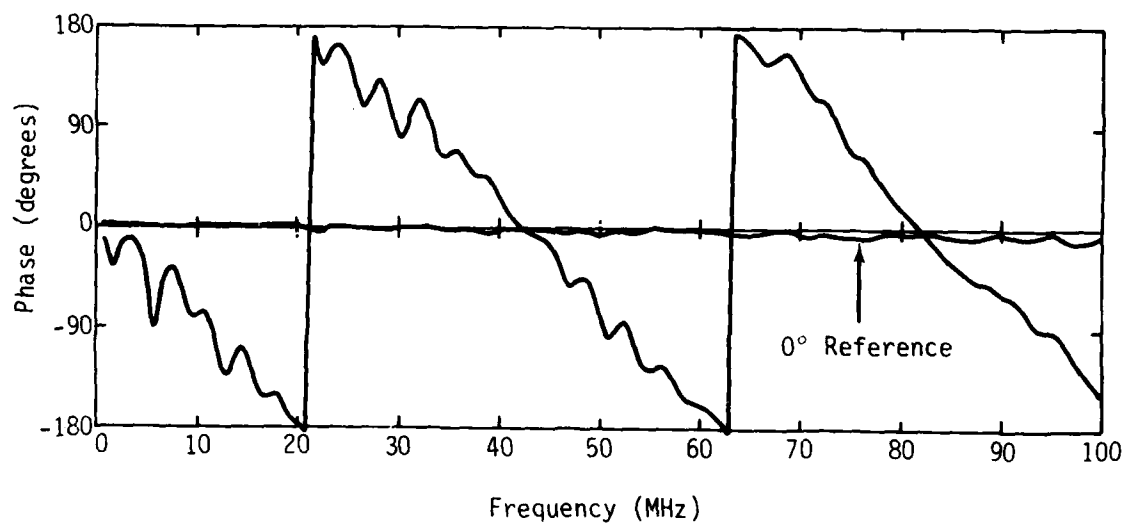


(b) Simulated cable (lab) data.

Figure 52. Current transfer ratio at Station 1442, with reference at Station 1489.

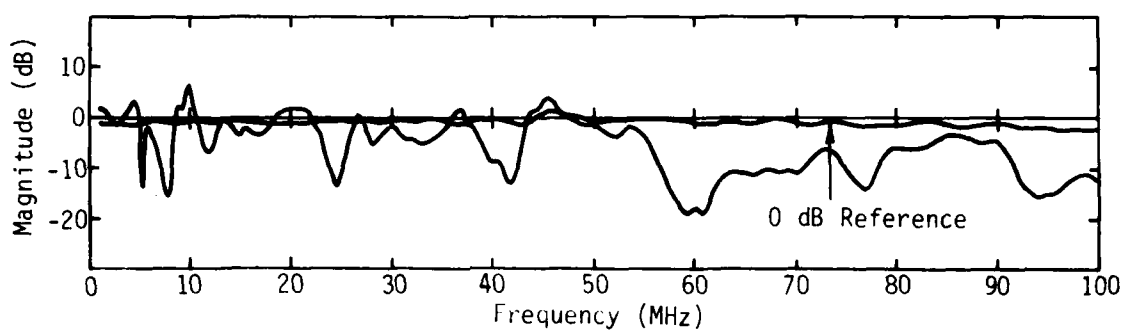


(a) Four-wire cable (lab) data.

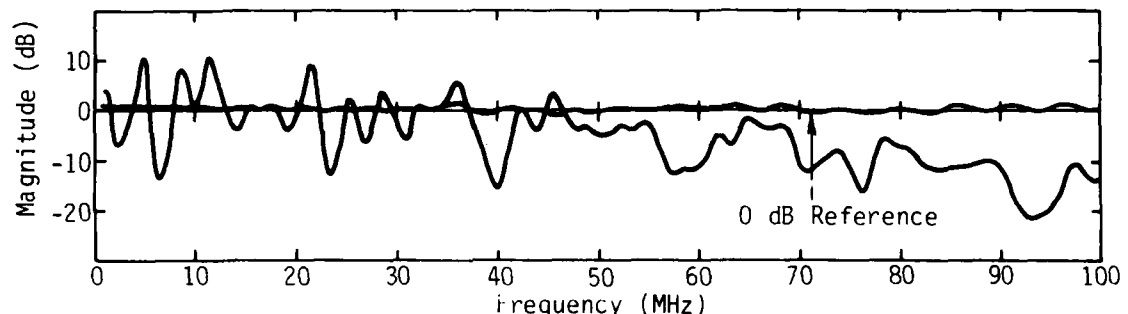


(b) Simplified cable (lab) data.

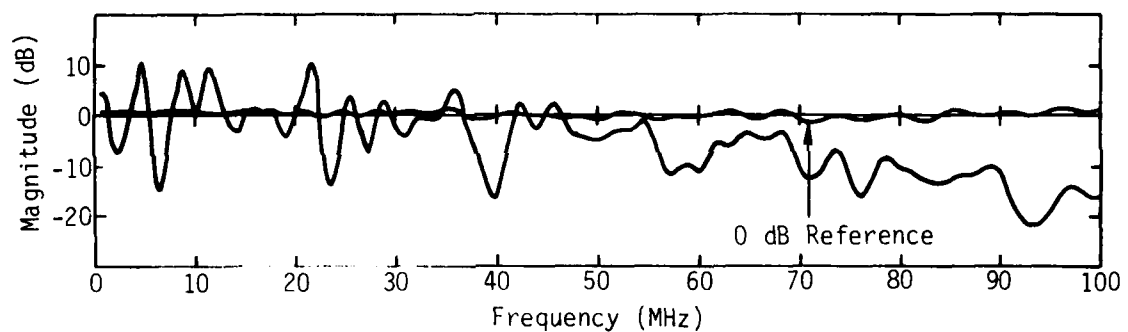
Figure 53. Current transfer ratio at Station 1442, with reference at Station 1489.



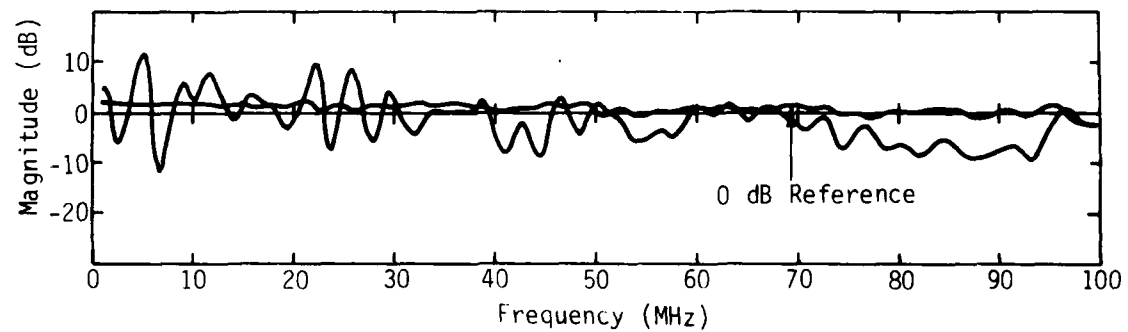
(a) Aircraft cable data.



(b) Simulated cable (lab) data.

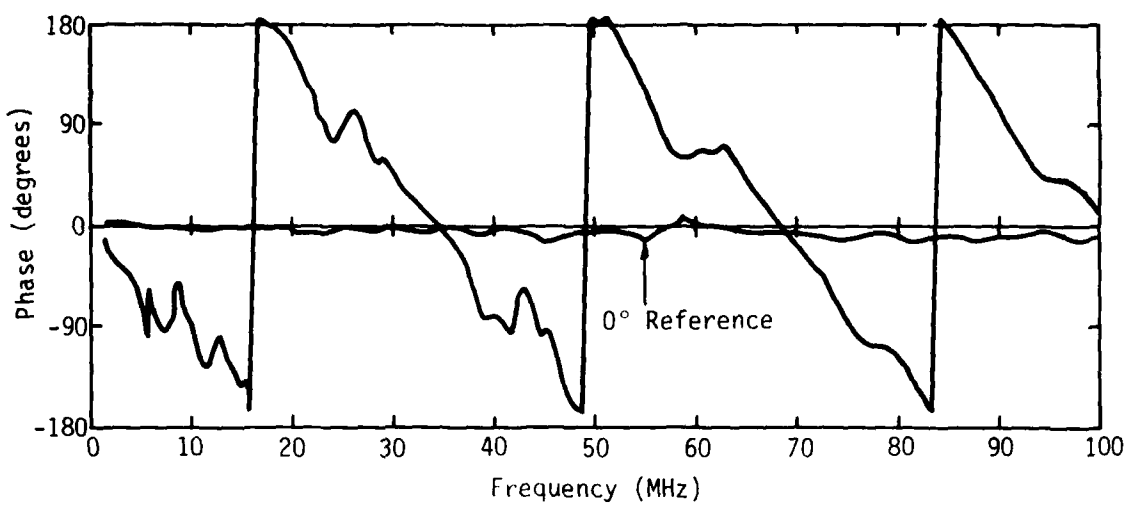


(c) Four-wire cable (lab) data.

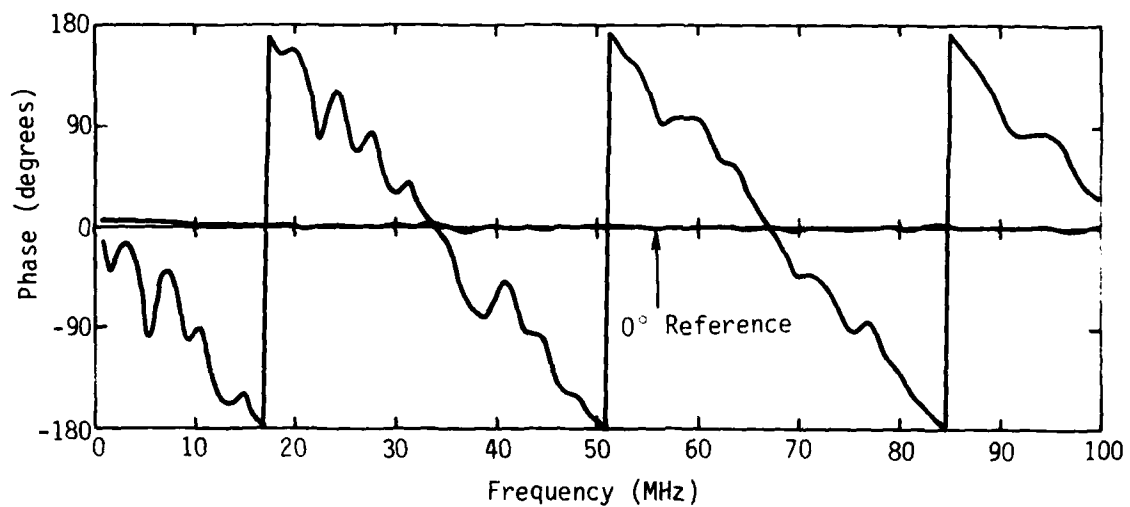


(d) Simplified cable (lab) data.

Figure 54. Current transfer ratio at Station 1412, with reference at Station 1489.

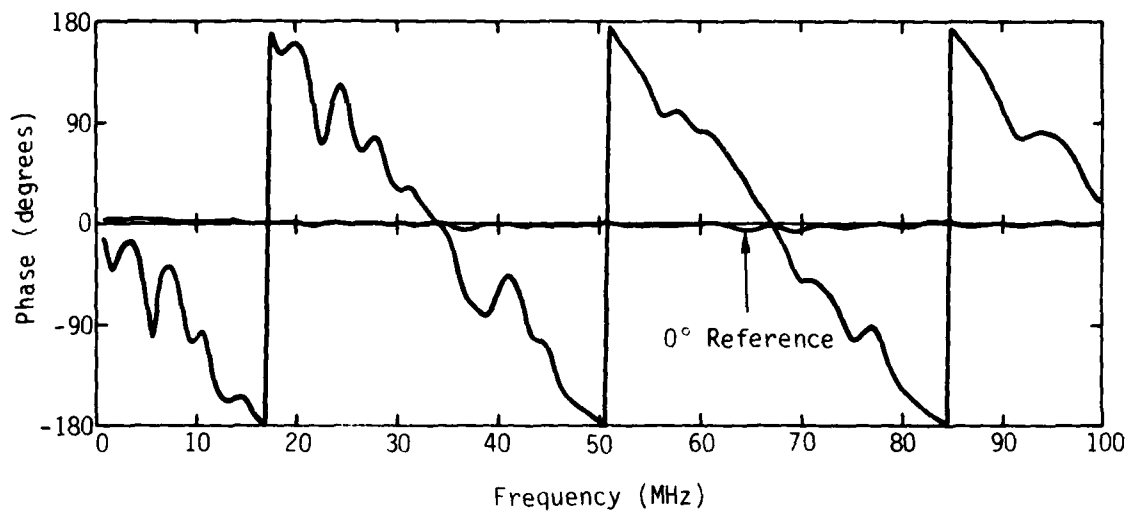


(a) Aircraft cable data.

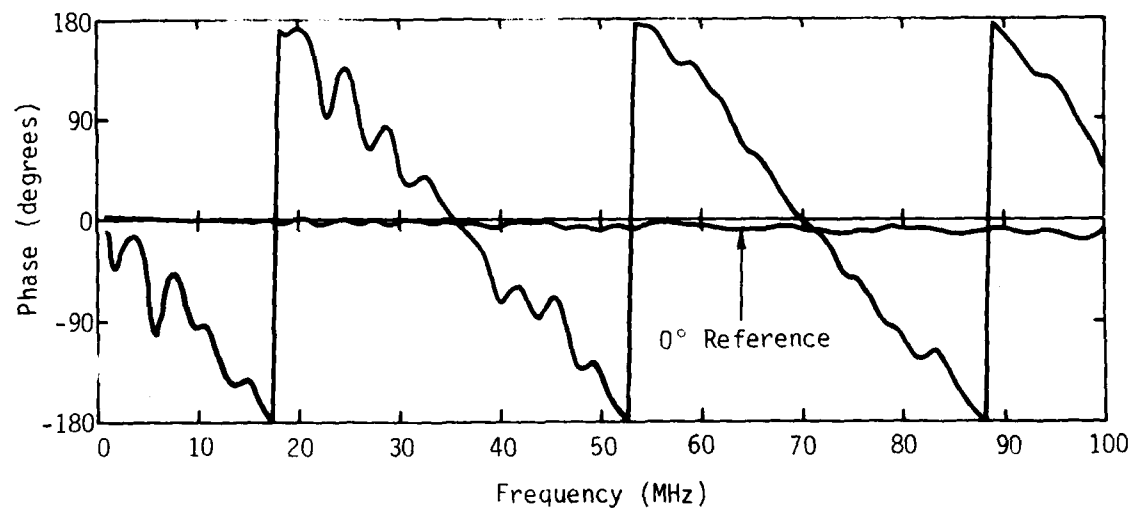


(b) Simulated cable (lab) data.

Figure 55. Current transfer ratio at Station 1412, with reference at Station 1489.



(a) Four-wire cable (lab) data.



(b) Simplified cable (lab) data.

Figure 56. Current transfer ratio at Station 1412, with reference at Station 1489.

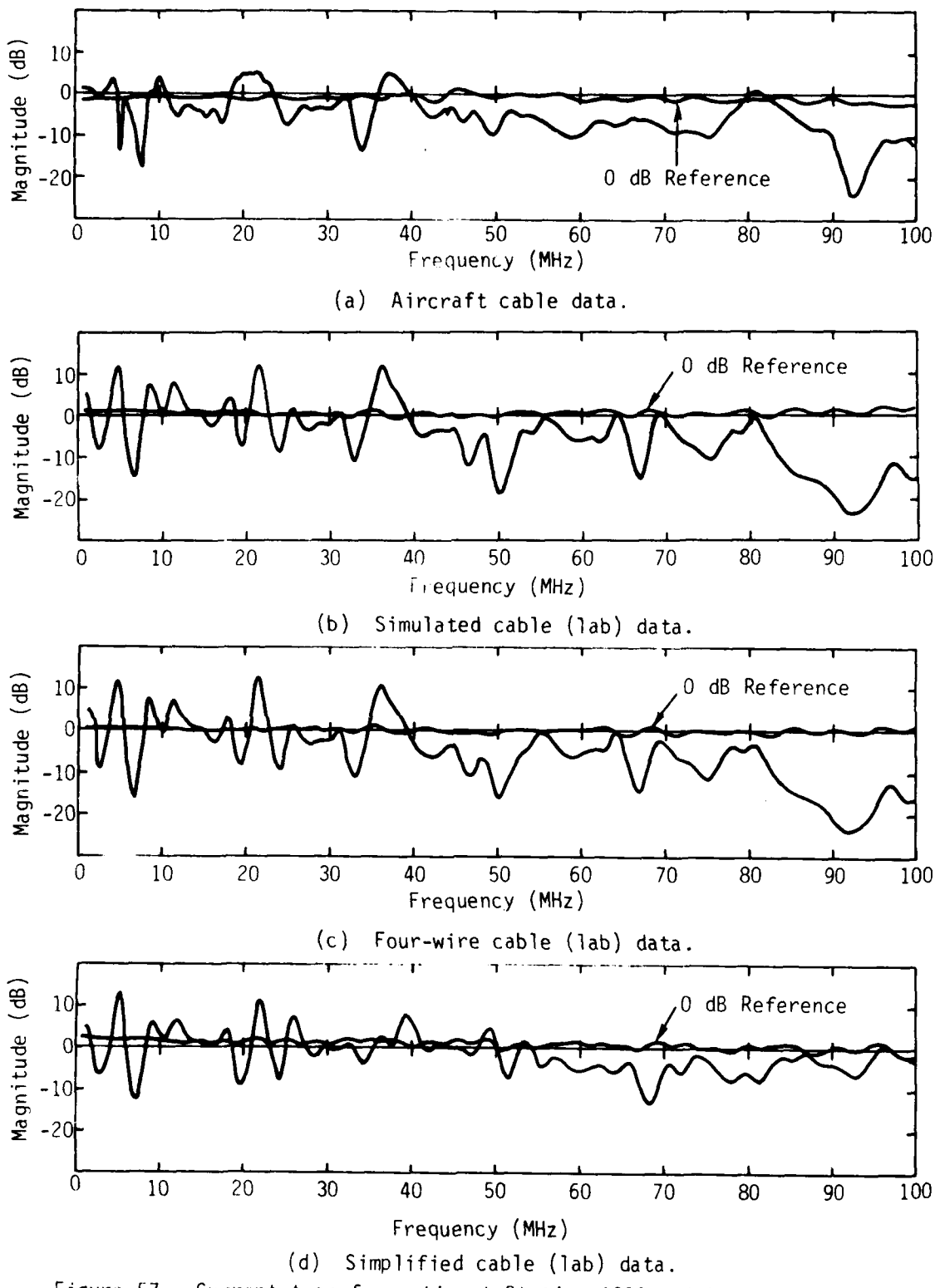
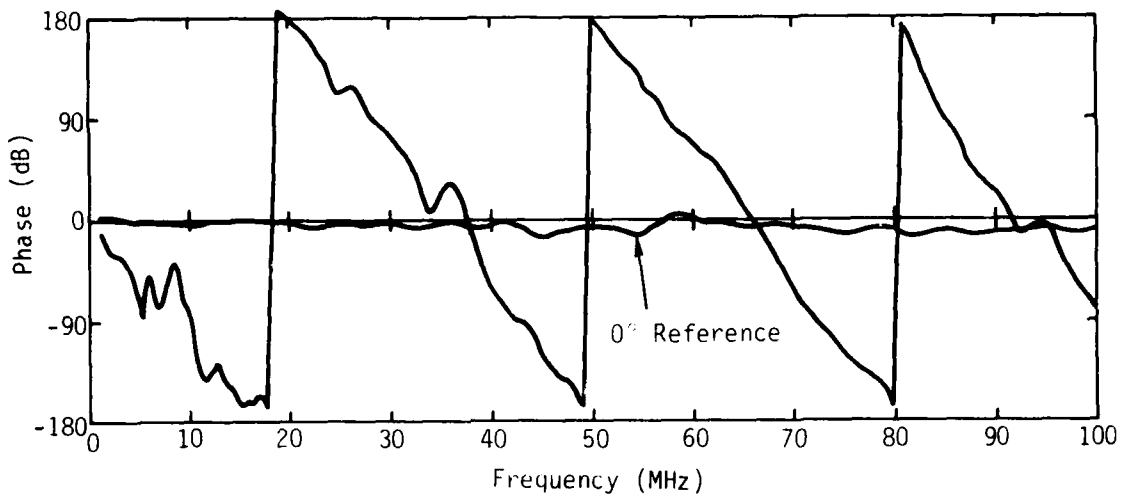
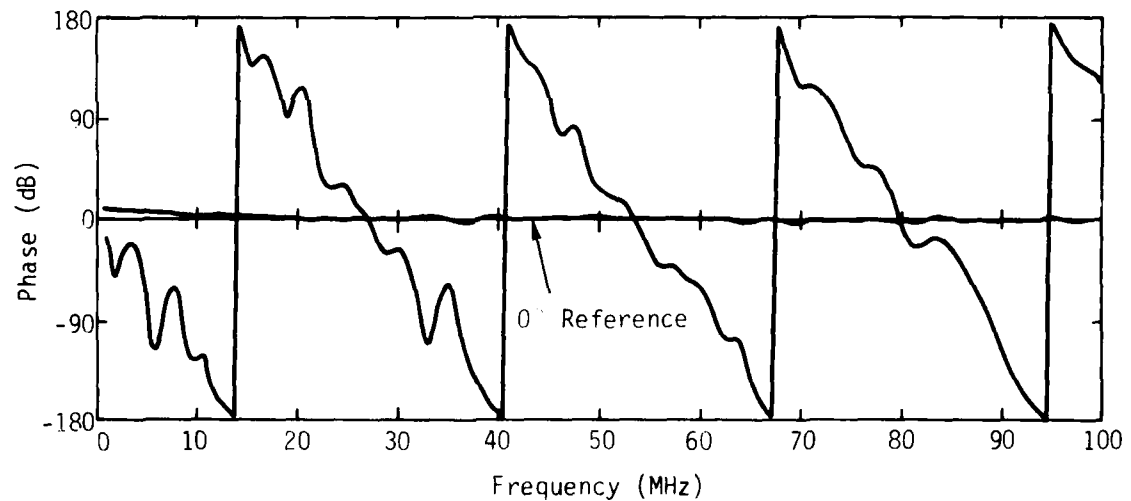


Figure 57. Current transfer ratio at Station 1382, with reference at Station 1489.

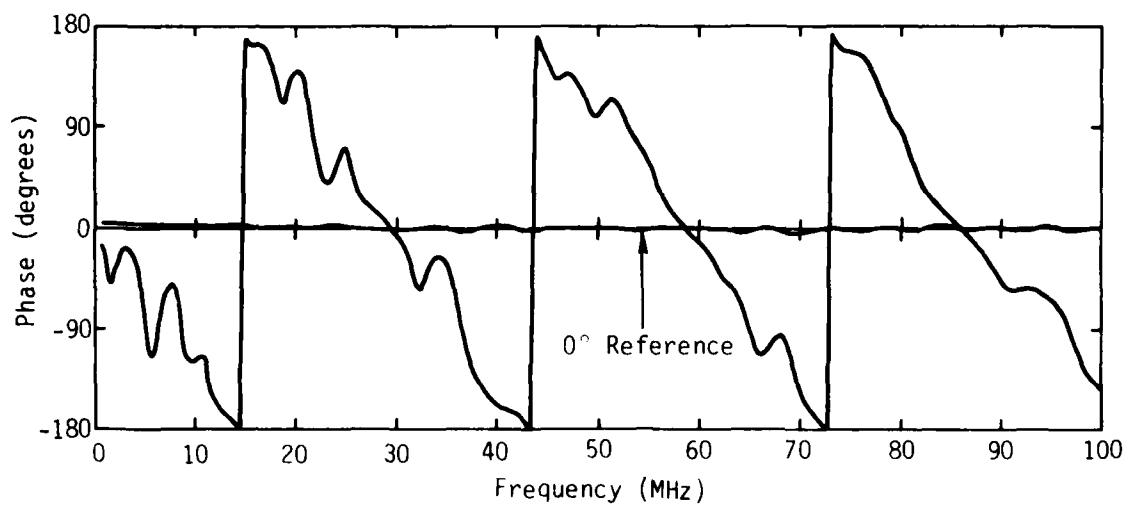


(a) Aircraft cable data.

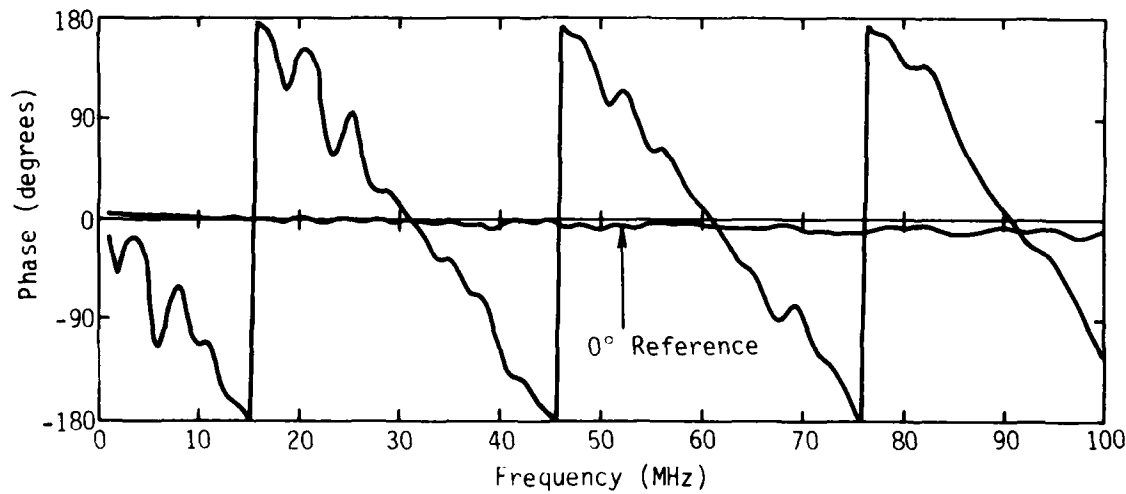


(b) Simulated cable (lab) data.

Figure 58. Current transfer ratio at Station 1382, with reference at Station 1489.

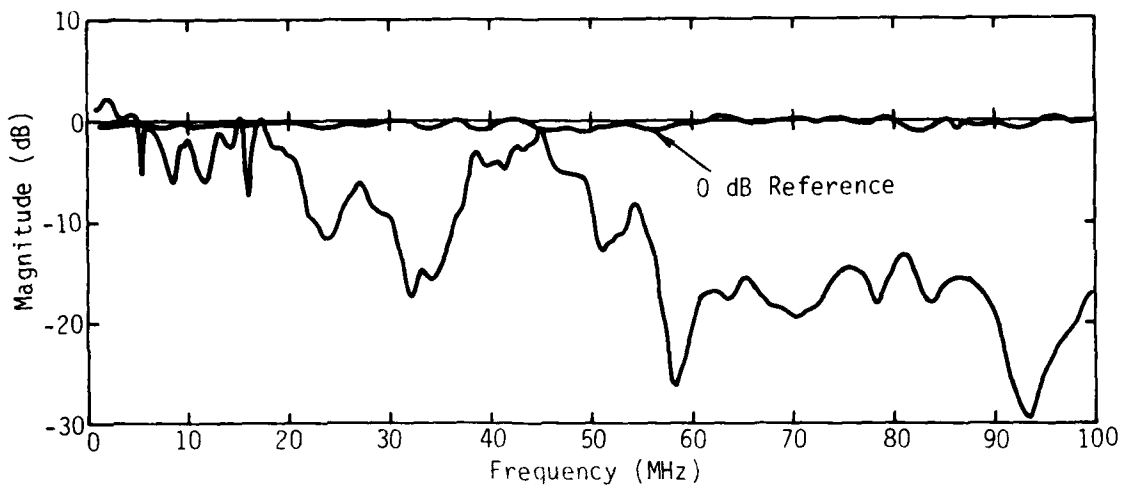


(a) Four-wire cable (lab) data.

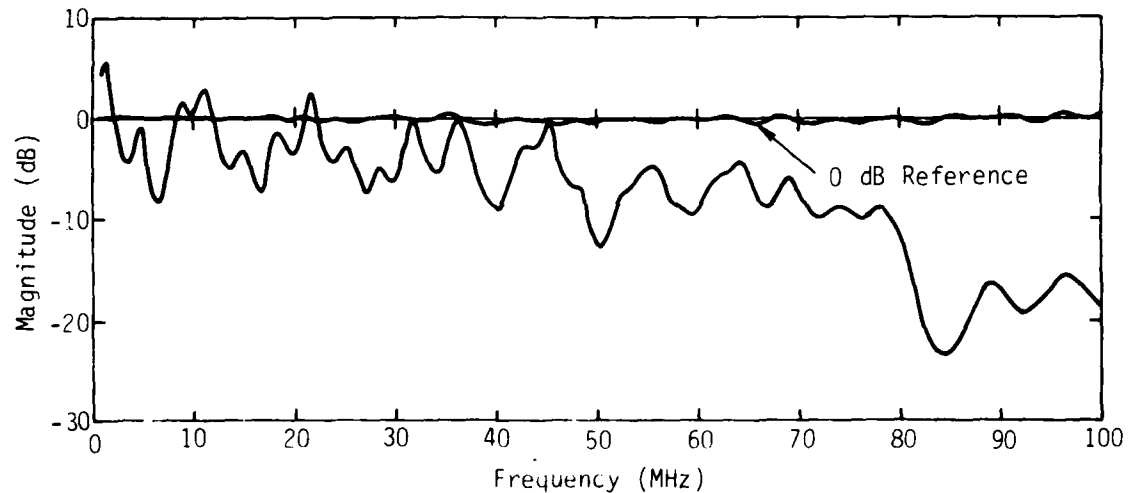


(b) Simplified cable (lab) data.

Figure 59. Current transfer ratio at Station 1382, with reference at Station 1489.

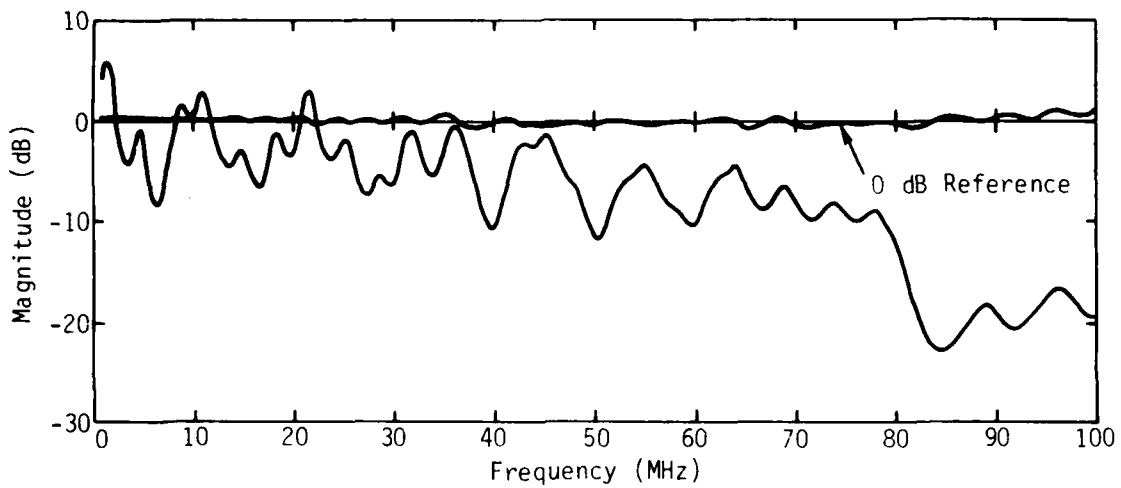


(a) Aircraft cable data.

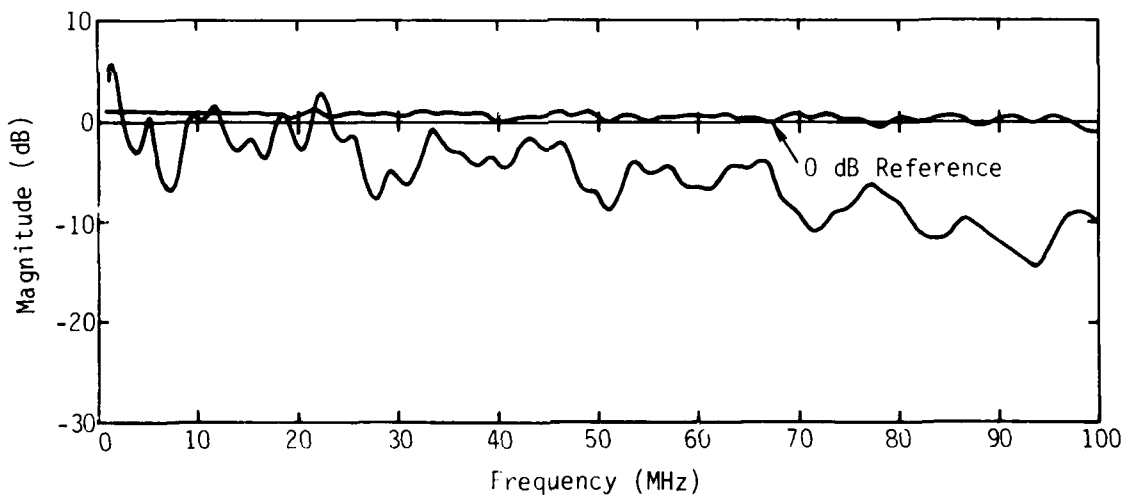


(b) Simulated cable (lab) data.

Figure 60. Current transfer ratio at Station 940, with reference at Station 1489.

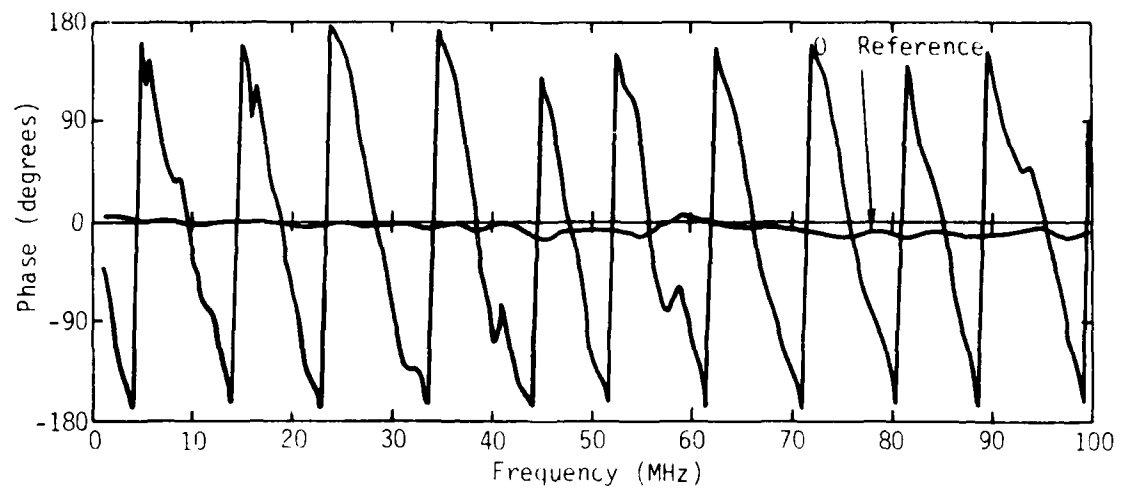


(a) Four-wire cable (lab) data.

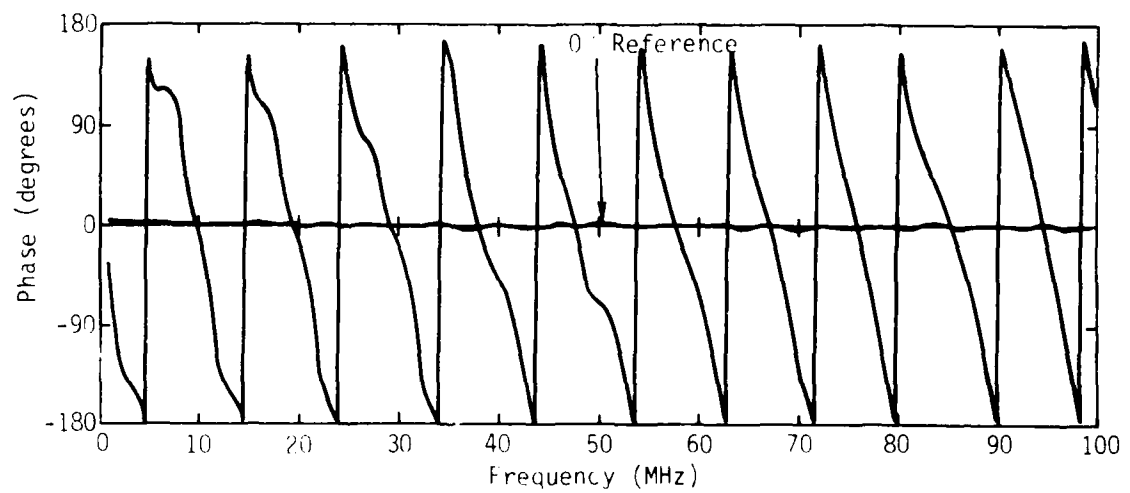


(b) Simplified cable (lab) data.

Figure 61. Current transfer ratio at Station 940, with reference at Station 1489.

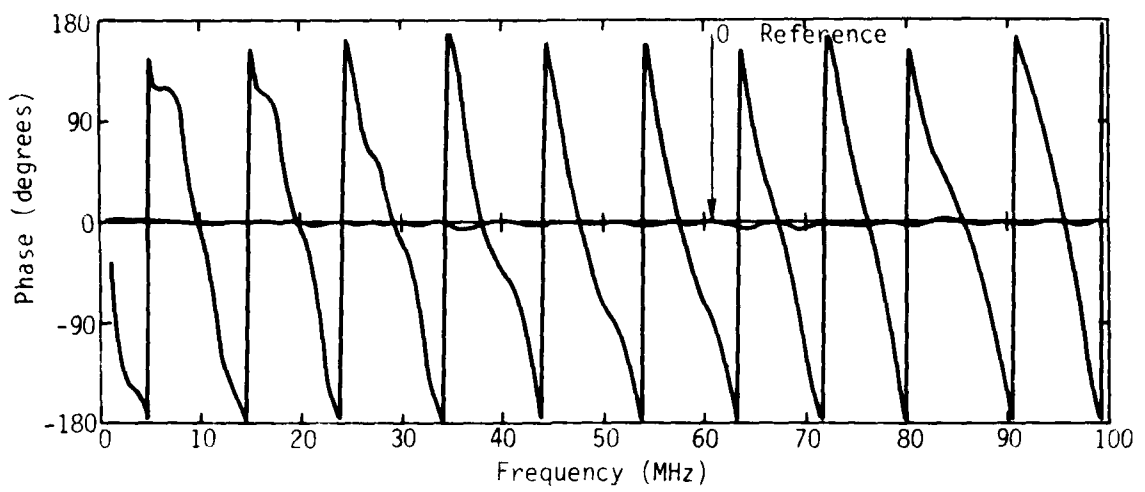


(a) Aircraft cable data.

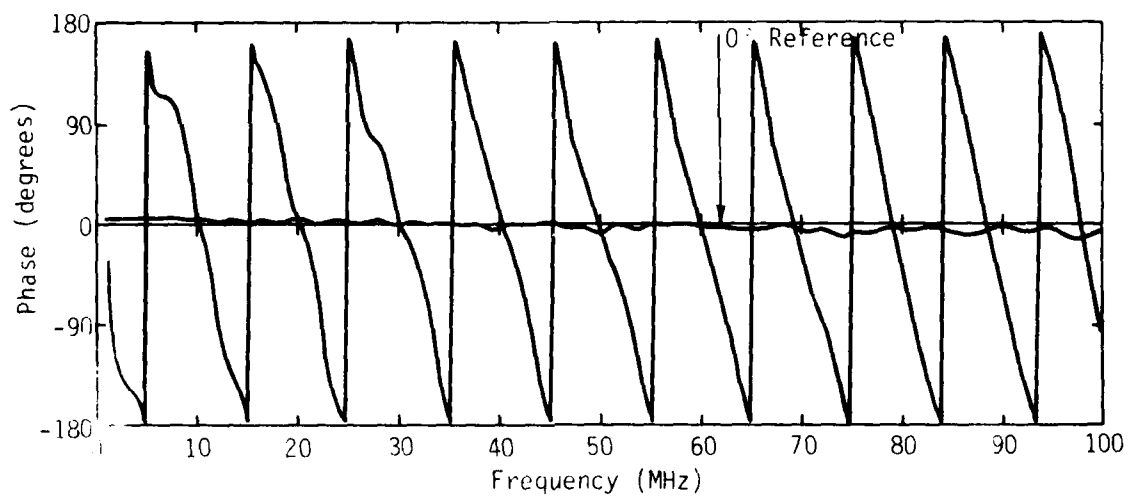


(b) Simulated cable (lab) data.

Figure 62. Current transfer ratio at Station 940, with reference at Station 1489.

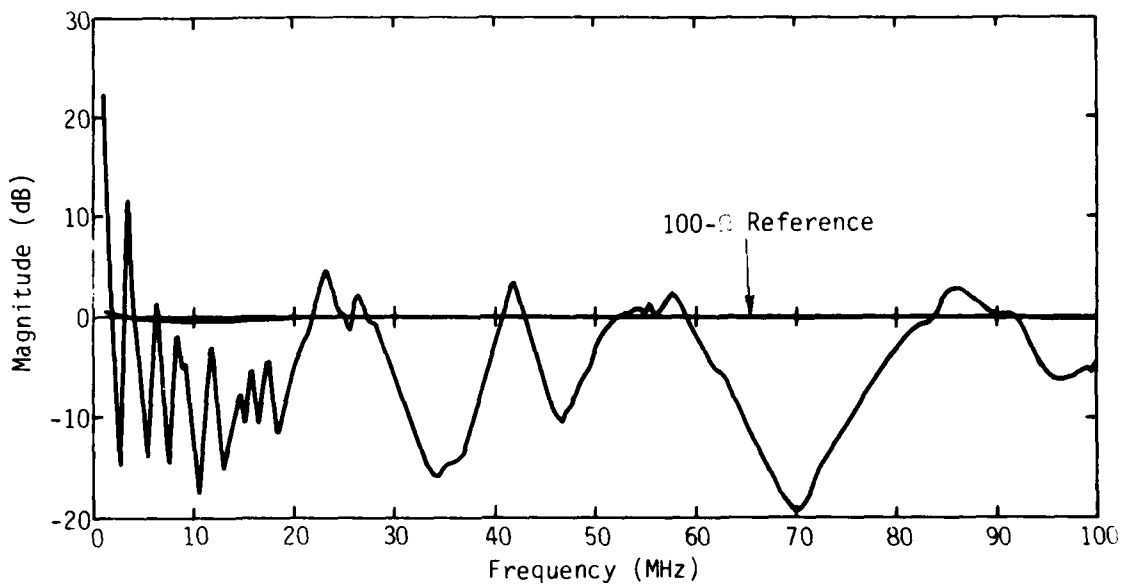


(a) Four-wire cable (lab) data.

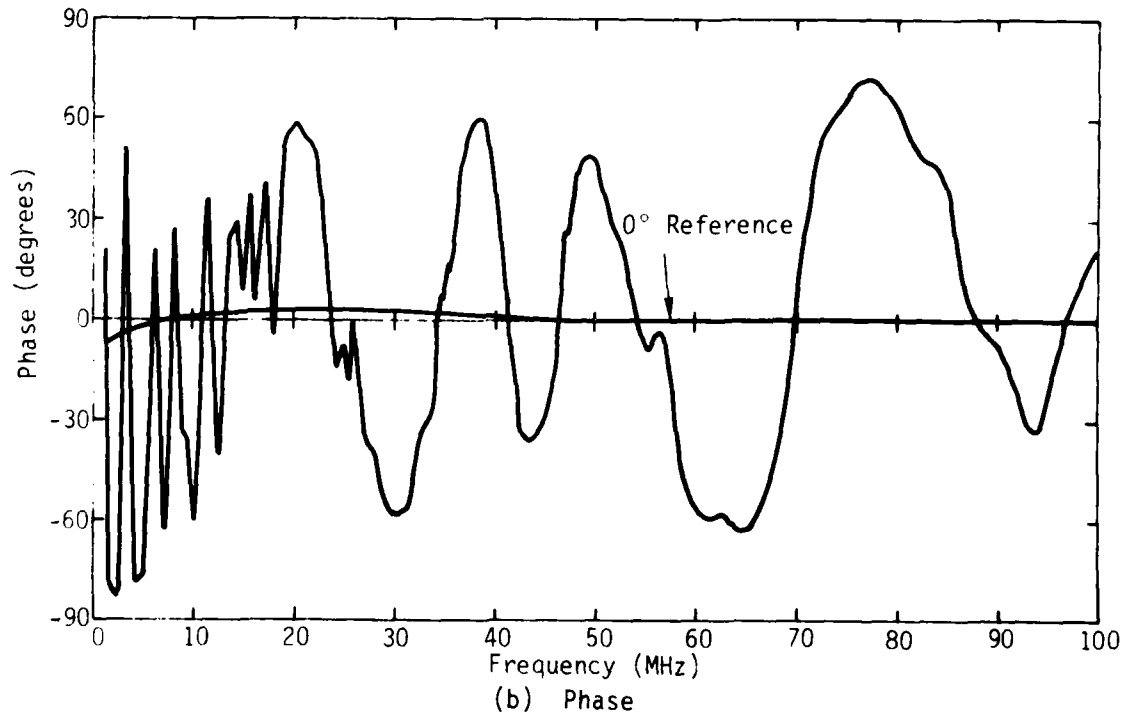


(b) Simplified cable (lab) data.

Figure 63. Current transfer ratio at Station 940, with reference at Station 1489.

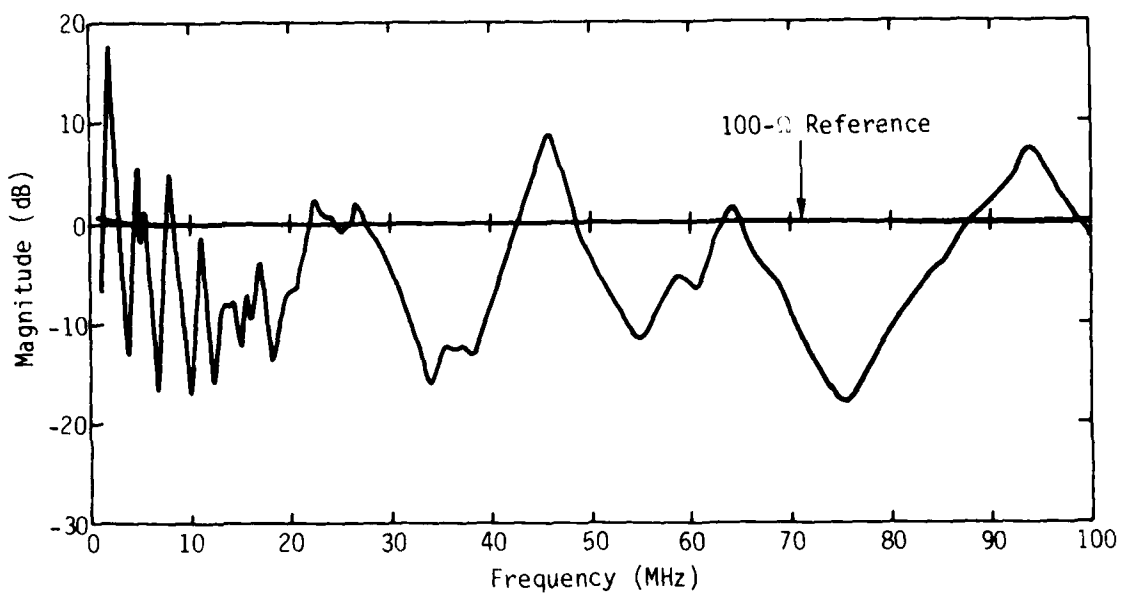


(a) Magnitude.

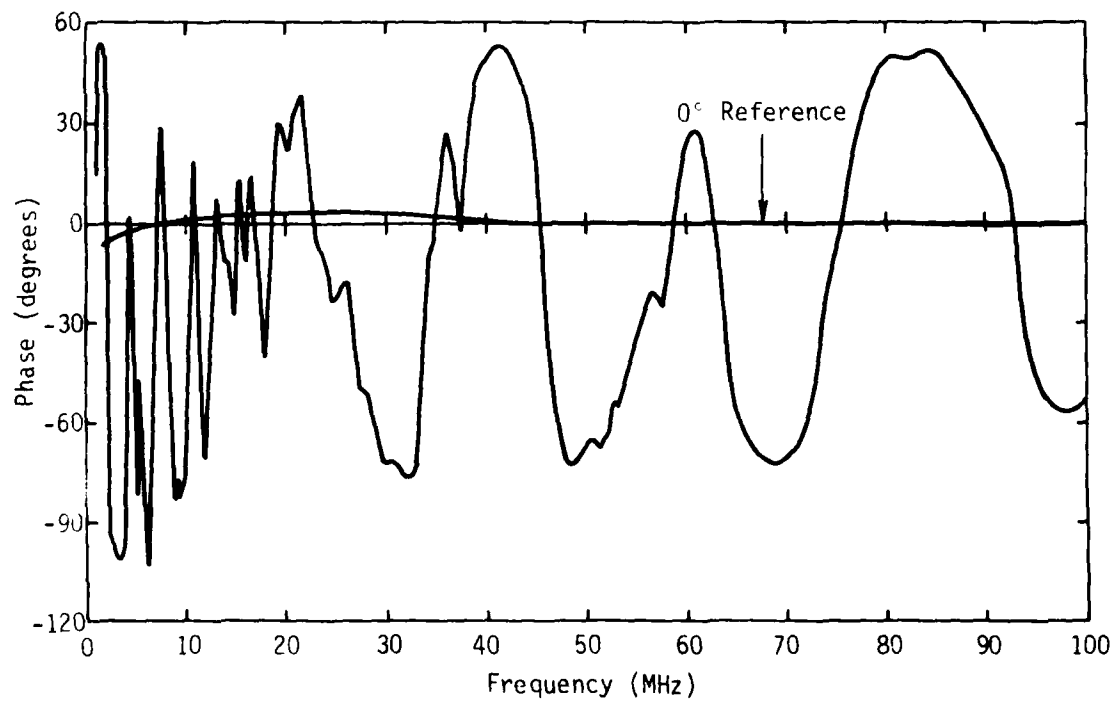


(b) Phase

Figure 64. Short-circuit input-impedance data - aircraft cable.



(a) Magnitude.



(b) Phase.

Figure 65. Open-circuit input-admittance data - aircraft cable.

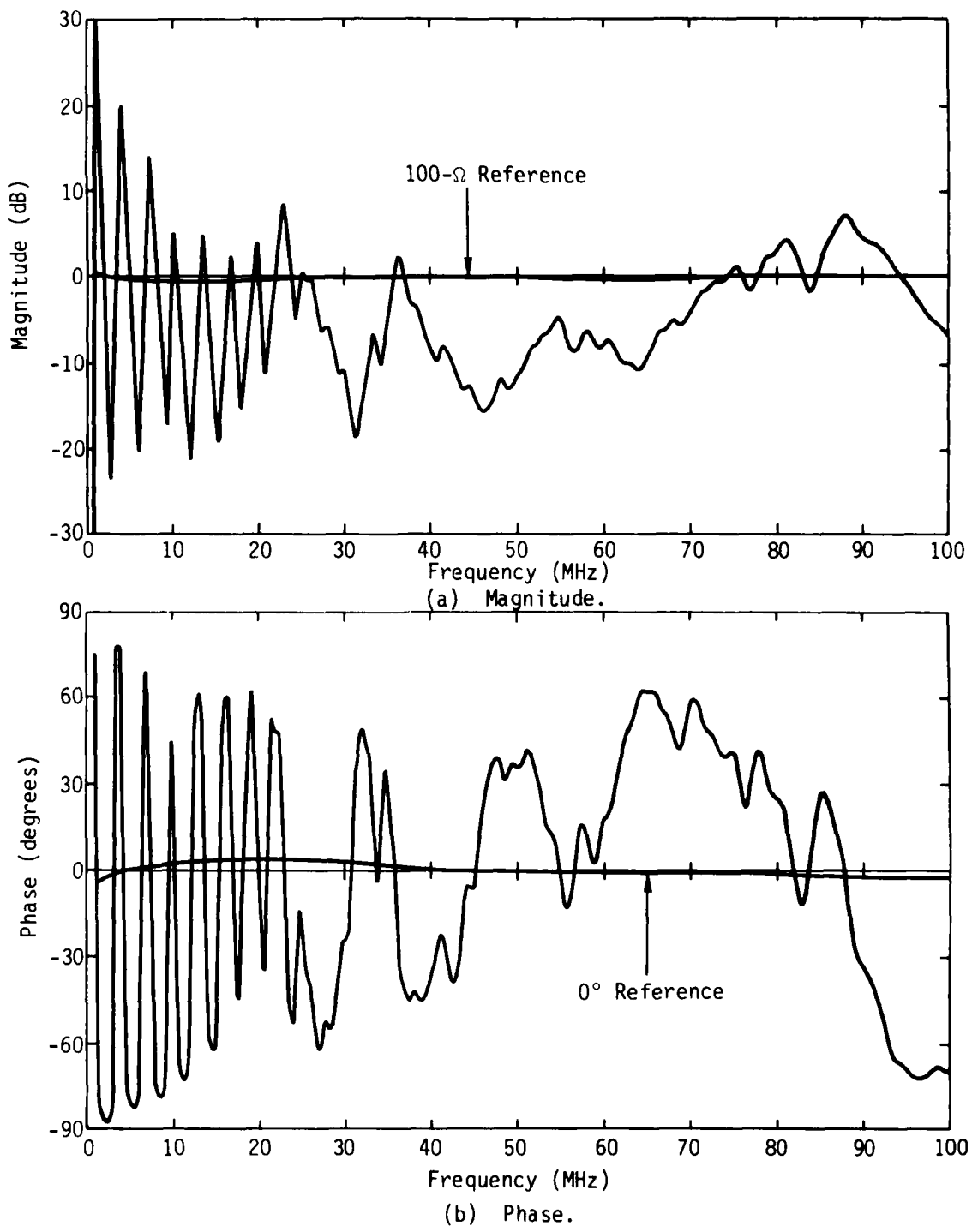


Figure 66. Short-circuit input-impedance data - simulated cable (lab).

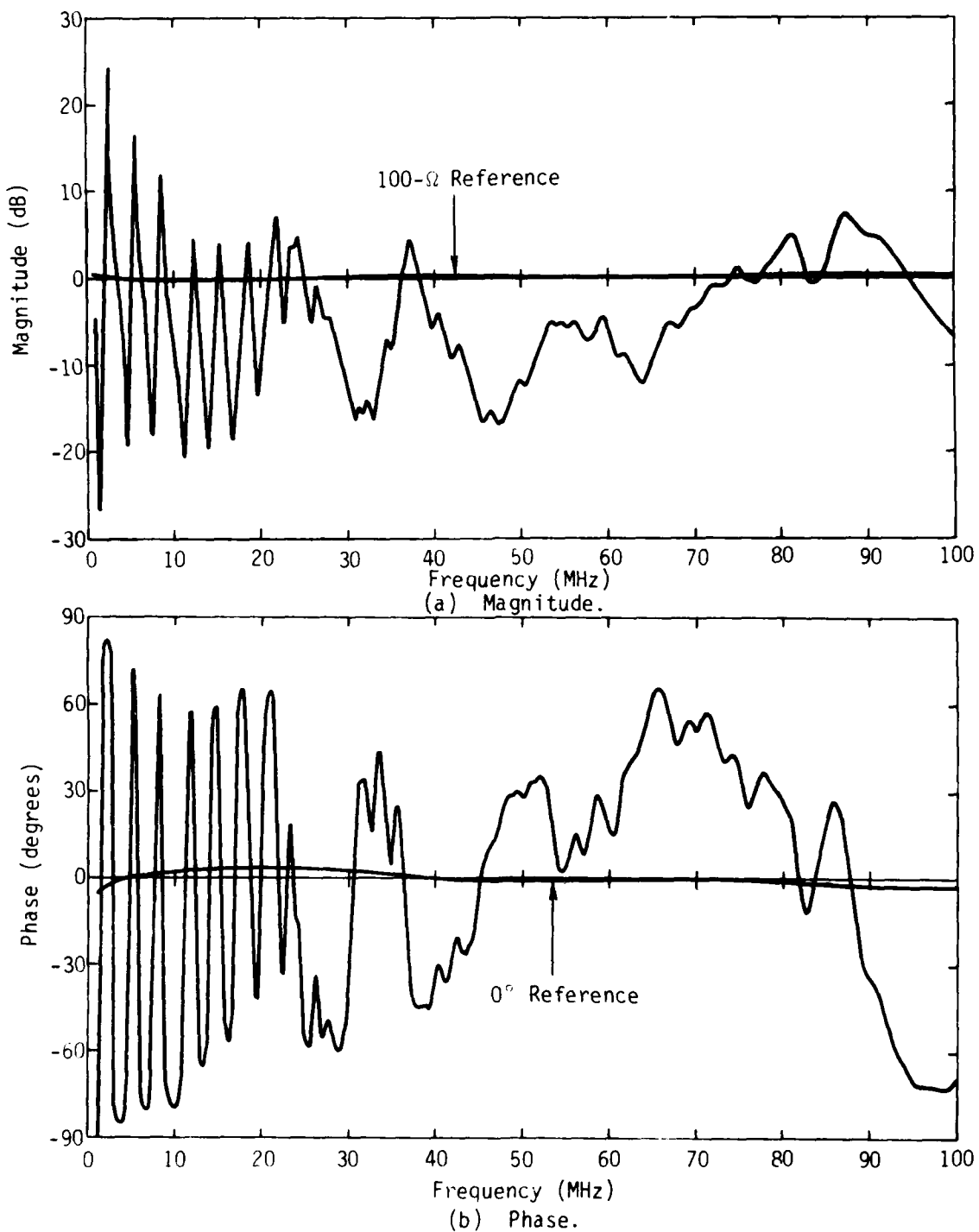


Figure 67. Open-circuit input-admittance data - simulated cable (lab).

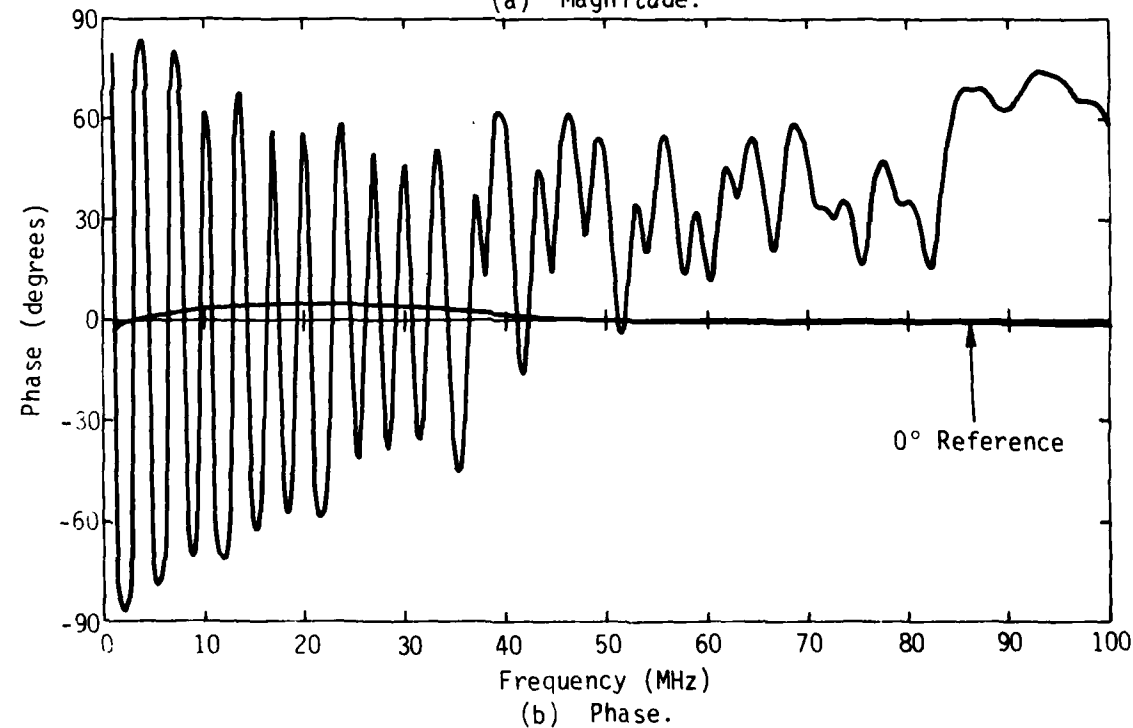
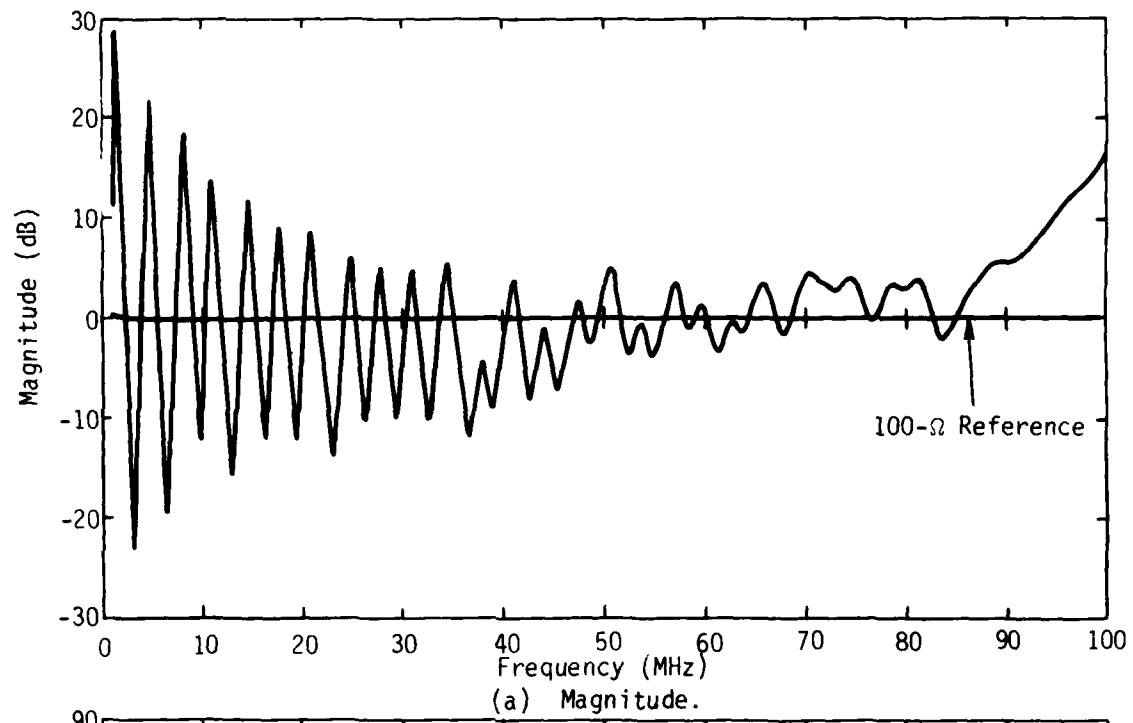


Figure 68. Short-circuit input-impedance data - four-wire cable (lab).

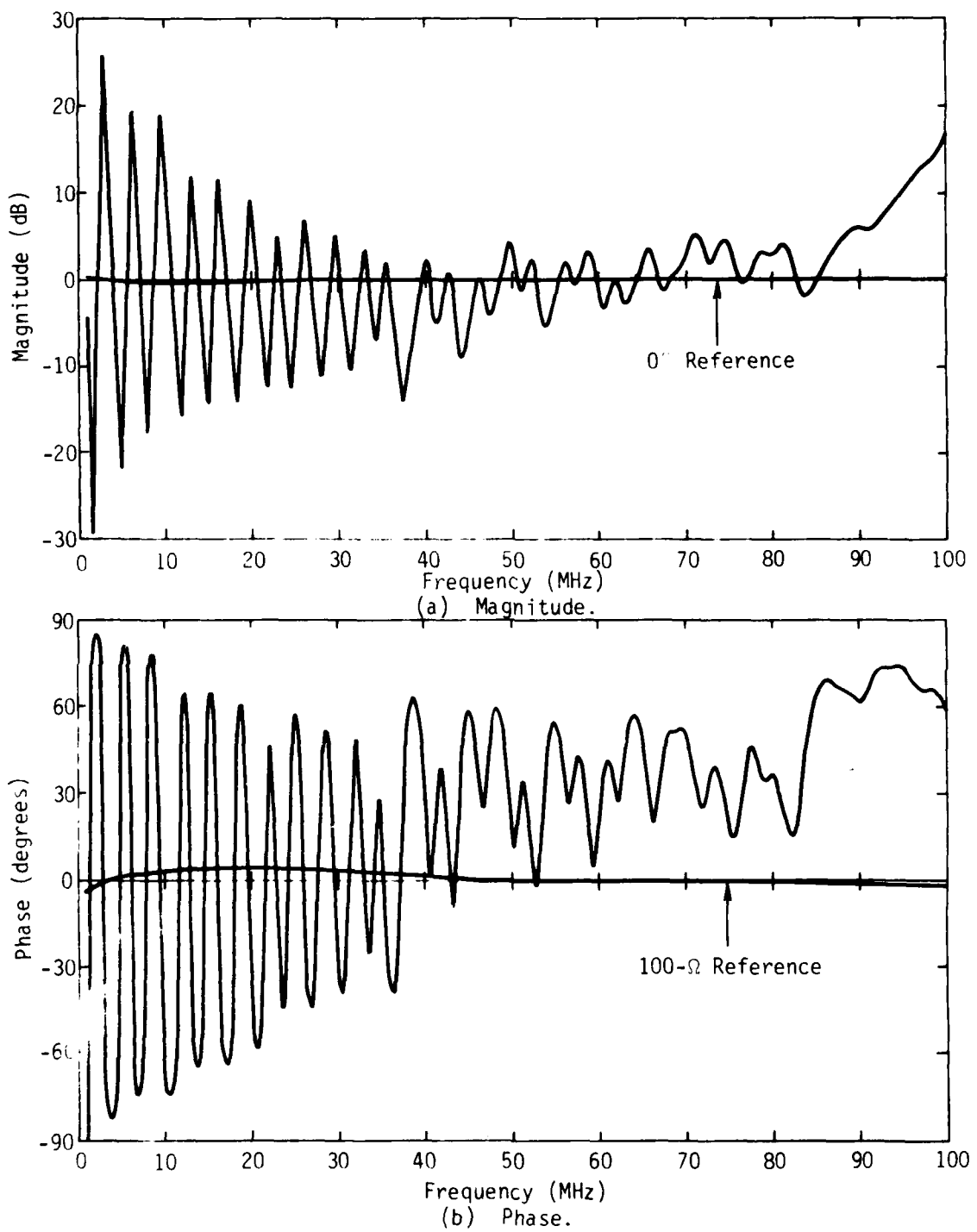


Figure 69. Open-circuit input-admittance data - four-wire cable (lab).

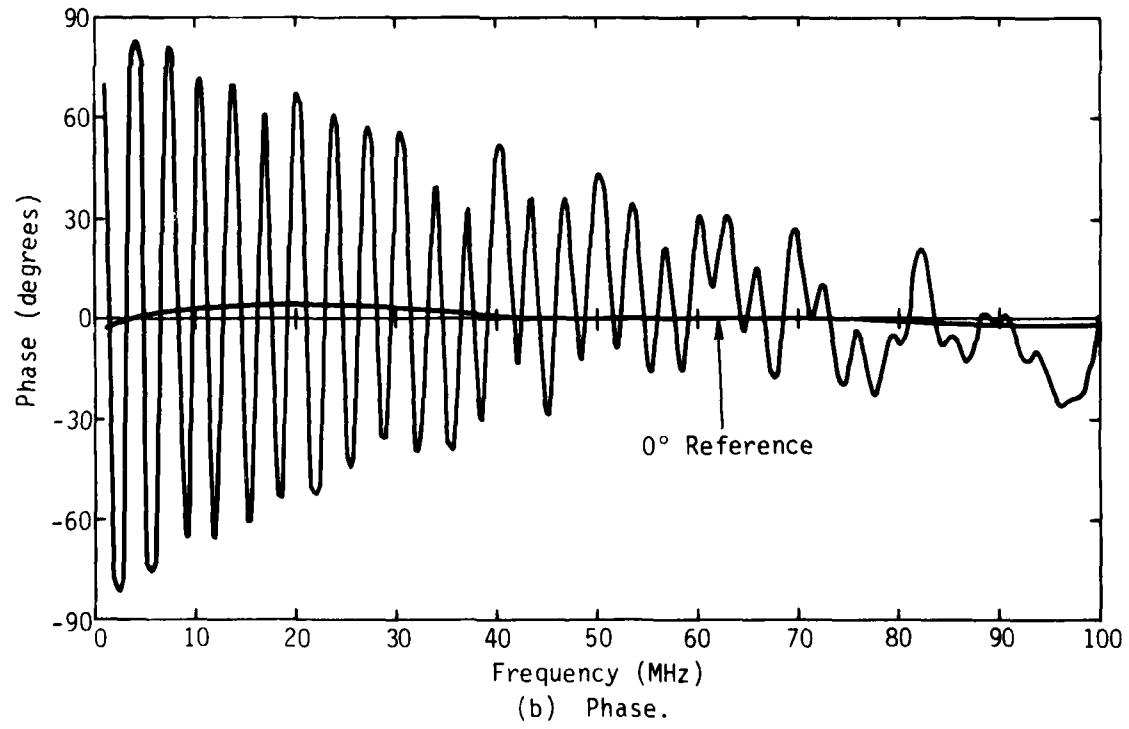
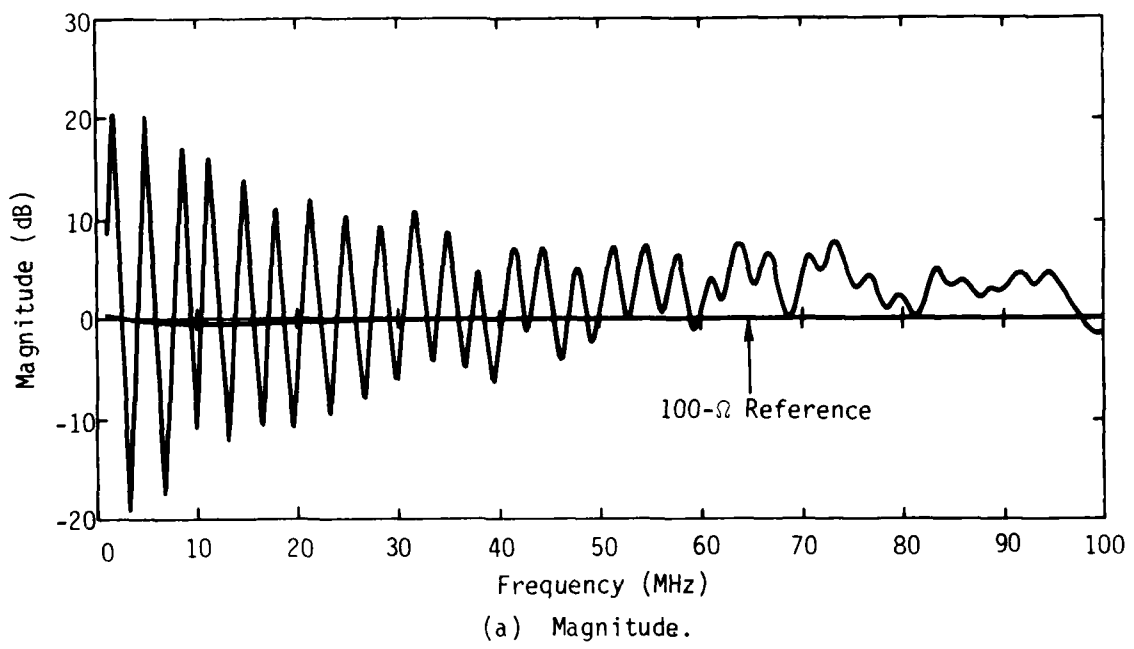


Figure 70. Short-circuit input-impedance data - simplified cable (lab).

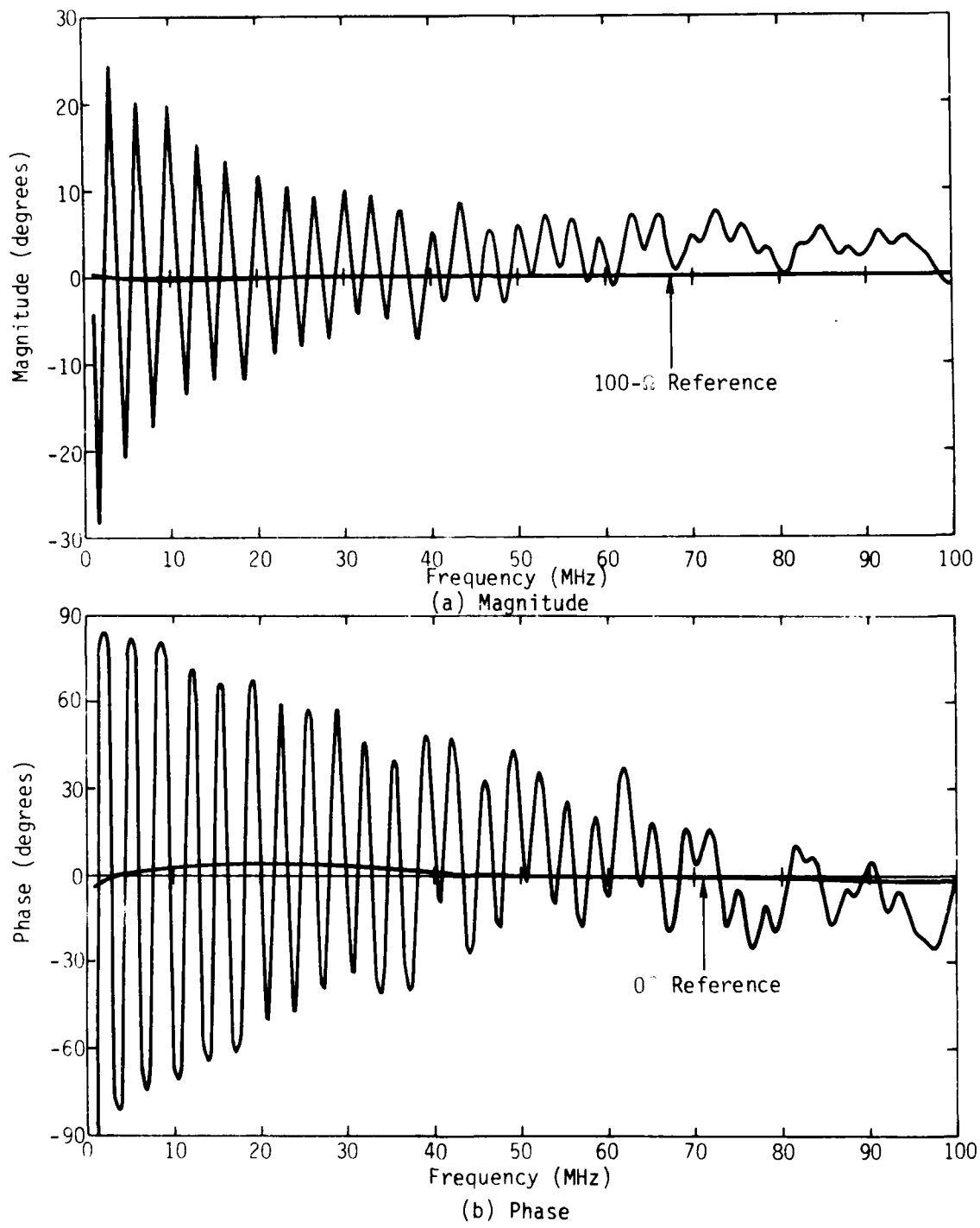


Figure 71. Open-circuit input-admittance data - simplified cable (lab).

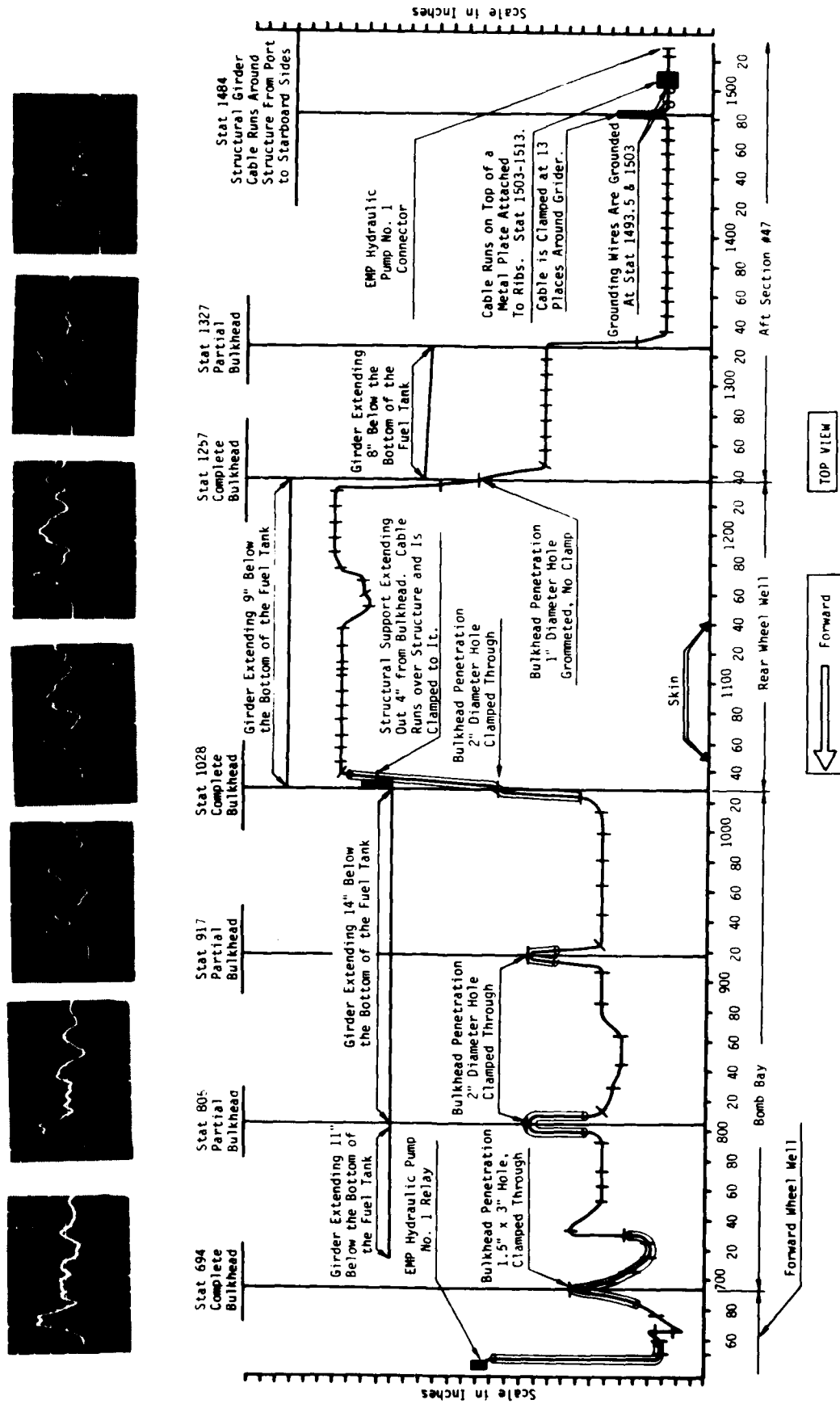
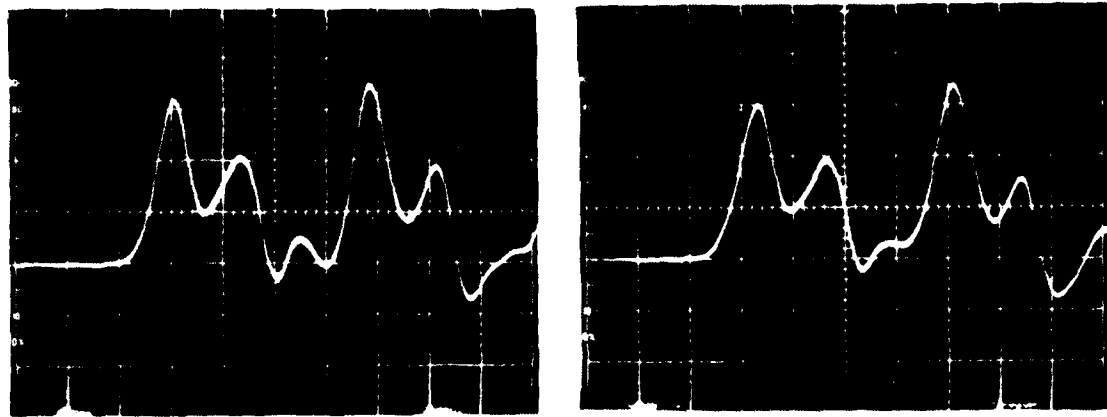


Figure 72. Current waveforms along the length of the aircraft cable.

reflections along the line due to discontinuities, and the losses in the line. An attempt was made to pinpoint the locations of the discontinuities which give rise to successive pulses. It was concluded that these discontinuities giving rise to successive pulses cannot be located, because there are a large number of closely spaced discontinuities on the cable. Moreover, the reflections from both sides of the measurement point compound the problem even further.

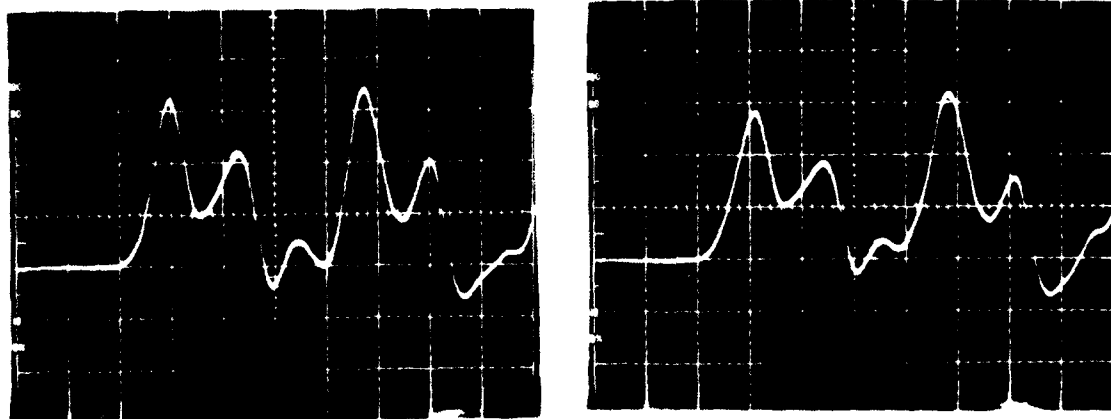
Comparison between the aircraft data and the laboratory models shows that the simulated cable data is the closest to the aircraft data, as was expected. Let us compare the data at Station 1472 for example. The amplitudes of the first pulse on the aircraft cable, simulated cable, four-wire cable, and the simplified cable are approximately 112 mA, 136 mA, 180 mA, and 188 mA, respectively. The amplitudes of the first pulse on the simulated cable, four-wire cable, and the simplified cable are higher, as compared to the pulse on the aircraft cable, by 21.4, 60, and 67.8 percent, respectively. The second pulse arrives about 10 ns later on the aircraft cable, about 13 ns later on the simulated cable, and about 15 ns later on the four-wire cable. The second pulse cannot be resolved on the simplified cable. The amplitudes of the second pulse on the simulated cable and four-wire cable are 90 percent and 64 percent, respectively, of the pulse in the aircraft cable. The third pulse arrives about 30 ns later on the simulated and four-wire cable, and 32 ns later on the simplified cable. The amplitudes of this pulse on the aircraft cable, simulated cable, four-wire cable, and the simplified cable are, respectively, 100 mA, 92 mA, 60 m, and 72 mA. These comparisons show that the cable could be represented by the four-wire cable or the simplified cable, when the peak currents are of major interest, for example, for the determination of the damage to the circuit elements due to EMP. The simpler cable models were found to overestimate the first peak current. Similar comparisons can be made for the waveforms at other stations.

Figure 73 shows the effects of other cables running parallel to the cable on the current waveform at Station 1382 for the simulated cable.



(a) A four-wire cable between Stations 1327 and 1484, 7.6 cm away from the cable.

(b) Two four-wire cables, one on each side, between Stations 1327 and 1484, 7.6 cm away from the cable.



(c) Two four-wire cables, one on each side, between Stations 1327 and 1484, 12.7 cm away from the cable.

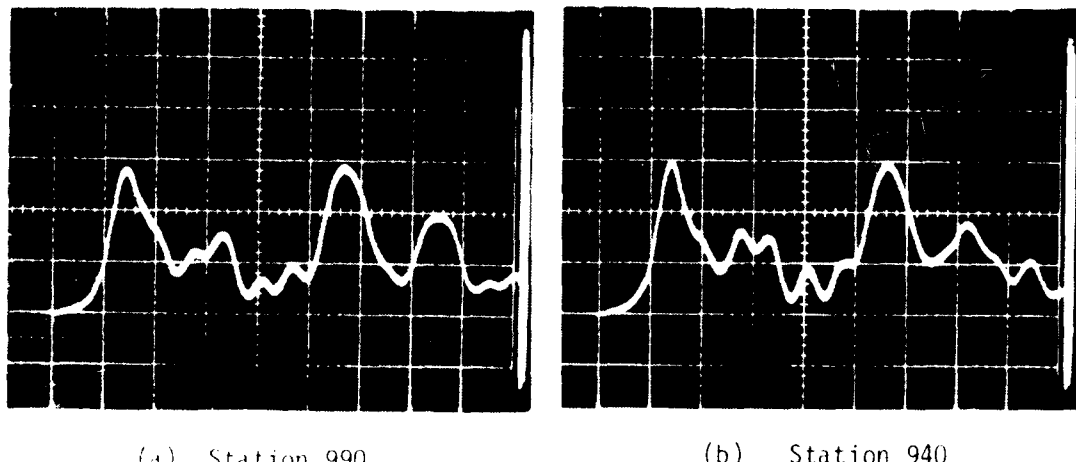
(d) Setup same as that of b; in addition, a cable and a steel rod were placed parallel to the cable between Stations 1528.5 and 1491.

Figure 73. Current waveforms on the simulated cable at Station 1382 in presence of other cables running parallel to it. Horizontal scale: 10 ns/div; Vertical scale: 40 mA/div.

In Figure 73a, a four-wire cable (similar to the aircraft cable) was placed parallel to the simulated cable, 7.6 cm away from it, between Stations 1327 and 1484. Comparison between Figures 44b and 73a shows that the amplitude of the first pulse in Figure 73a is about 7 percent less than that in Figure 44b. The amplitudes of the successive pulses in Figure 73a are slightly smaller than those in Figure 44b. The shape of the pulse remains unaltered. In Figure 73b, another four-wire cable (similar to the aircraft cable) was placed parallel to the simulated cable on the other side, 7.6 cm away from it, between Stations 1327 and 1484. The amplitude of the first pulse in Figure 73b is about 12 percent less than that in Figure 44b. The shape of the pulse remains roughly the same. These comparisons show that the amplitudes of the pulses reduce when the other cables are present, indicating the coupling of the energy to the adjacent cables. The waveform of Figure 73b is in better agreement, as compared to the waveform of Figure 44b, with the waveform of Figure 44a (aircraft cable). These comparisons show that the agreement between the laboratory data and the aircraft data improves when some other cables are brought near the cable in the laboratory, simulating the aircraft environment more closely.

The configuration of the cable for the current waveform of Figure 73c was the same as that for Figure 73b, except that the cables are 12.7 cm away from the main cable. The current waveform in Figure 73c shows that the effects of the adjacent cables on the reduction of the amplitudes of the pulses are less compared to those in Figure 73b. The comparison between Figures 73b and 44b indicates that we need to consider the adjacent cables only within about 15 cm. The configuration of the cable for the current waveform of Figure 73d was the same as that for Figure 73b, except that another cable and a steel rod (1.25 cm diameter) were placed, 5 cm away from the cable, one on each side of the cable, between Stations 1528.5 and 1491. The comparison between the waveforms in Figures 73b and 73 d shows that there is very little change in the new amplitudes due to the additional cable and the steel rod.

Figure 74 shows the current waveforms at Stations 990 and 940. The configuration for the waveforms in Figure 74 was the same as for Figure 73d; in addition, some other cables were routed through bulkheads at Stations 694, 805, 917 and 1028, extending about two feet on either side of the bulkhead. A bundle of three eight-gauge wires was used at Station 1028 and 917, and was laced together with the main cable. At Stations 805 and 694, a bundle of four twenty-gauge wires was used, and was laced together with the main cable. These perturbations were introduced to see the effect of closely coupled bundles which pass through the same bulkheads. The comparison of current waveforms in Figure 74a and 74b with Figures 46a and 47a, respectively, shows that the waveforms in Figure 74 are in a better agreement with the aircraft data, as compared to the laboratory models without any perturbations. The waveform in Figure 74 is more dispersed and somewhat resembles the aircraft cable data (Figures 46a and 46b). The amplitudes of the first pulse are also in close agreement.



(a) Station 990.

(b) Station 940

Figure 74: Current waveforms on the simulated cable at Station 990 and 940 in presence of other cables passing through the bulkheads. Horizontal scale: 20 ns/div; Vertical scale: 20 mA/div.

The above comparisons show that the discrepancies between the simulated cable data and the aircraft data are due to the unaccounted discontinuities in the aircraft, which were not simulated in the laboratory. In the above configurations, some of these discontinuities were introduced, and it was found that the laboratory data tend to agree better with the aircraft data as more and more discontinuities are introduced.

B. Frequency-Domain Results

The transfer current ratio at Stations 1471, 1442, 1412, 1382, and 940 are shown in Figures 48 through 63, as a function of frequency (1-100 MHz). The reference current is at Station 1489. The comparisons between the magnitudes of the current transfer ratios at Stations 1471, 1441, 1412, 1382, and 940 for the aircraft cable show that the attenuation increases as we move towards the load end. Also, these current transfer ratios show that the attenuation is higher at higher frequencies, indicating higher losses in the line.

Let us compare the current transfer ratios for different laboratory models with the aircraft cable at Station 1441. Figure 51 shows the magnitude of the current transfer ratios at Station 1442 for the aircraft cable, simulated cable, four-wire cable, and the simplified cable. The discrepancies between the aircraft cable data and the simulated cable data are higher at higher frequencies (> 40 MHz). Figures 52 and 53 show the phases of the current transfer ratios at Station 1442 for the aircraft cable, simulated cable. The phase of the current transfer ratio of the simulated cable compares fairly well with that of the aircraft cable. From Figures 51b and 51c, it can be seen that there is a only slight difference between the current transfer ratios for the simulated and four-wire cables, indicating that the cable could be approximately modeled by the four-wire cable. Comparison between the simplified cable and the simulated cable response is not so good.

The experimental data will be compared with analytically predicted data in the next section.

Figures 64 through 71 show the short-circuit input impedance and the open-circuit input admittance for different cable models, including the aircraft cable, as a function of frequency. It is difficult to draw any conclusions from the input impedance and the admittance data, since due to the presence of a large number of discontinuities and the nonuniform character of the cable, the input impedance or the admittance is a complex function of frequency.

SECTION V
ANALYTICAL MODELING BY A SINGLE TRANSMISSION LINE

1. MODEL

The main objective of the analytical comparison is to find a simple method that can reasonably model the complicated multiconductor cable inside the B-52 aircraft. Modeling by the multiconductor transmission line code, QV7TA (Ref. 17), is the logical approach for the four-wire cable. The code calculates individual wire currents, the algebraic sum of them is the bulk current. However, simpler methods may be possible that give reasonable accuracies. In the experiments, only bulk currents were measured. Thus, the modeling by a single transmission line is considered to be appropriate.

In this modeling, the cable bundle is represented by a one-wire transmission line above a ground plane. The height of this single line is the same as the mean height of the multi-wire cable. An equivalent radius can be established that would give rise to a characteristic impedance of the line very close to the bulk current impedance of the actual cable bundle. In this study, we model the single wire by a varying degree of complexity to observe the trade-off between modeling details and accuracies.

2. MODEL PARAMETERS

For the multiconductor cable situated approximately 7.62 cm above a ground plane, the characteristic impedance is approximately 211 Ω. Using the relation

$$Z_0 = (\epsilon_0/2\pi) \cosh^{-1} (2h/d) \quad (25)$$

where ϵ_0 is the intrinsic impedance of free space, h is the height of the wire above ground and d is the diameter of the wire. Using the values for Z_0 and h , the equivalent diameter of the modeled single wire is found to be

$$d = 0.90 \text{ cm.}$$

Note that the above equivalent representation is based on the assumption that the cable bundle is sufficiently far away from the ground plane.

The effects of the rib and the cable clamp can be represented by shunt capacitances (Refs. 11, 12). However, analyses performed in References 11 and 12 are for single transmission lines only. In the actual case, the multiconductor cable is very close to the rib, and in the case of the cable clamp, is encompassed tightly by the clamp. Due to the closeness of the cable to the surface, the concept of equivalent diameter is no longer accurate as it tends to underestimate the capacitance values. We thus make use of the laboratory measured capacitance values for the analysis.

The measured values are:

$$7.62 \text{ cm} \times 2.54 \text{ cm rib} \quad C = 4.2 \text{ pF}$$

$$6.985 \text{ cm} \times 2.54 \text{ cm rib + clamp} \quad C = 6.3 \text{ pF}$$

3. ANALYSIS

The method of analysis uses the transmission matrix method, which was used in the analysis of a transmission line with periodic loads (Ref. 10). This method is particularly suited for this case as it provides flexible ways of incorporating line sections with different lengths, with different shunt capacitance values.

A typical line model looks like the one in Figure 75. There are M sections of the line, and a typical section is shown in Figure 76. The section has a length l_i , characteristic impedances $Z_{0,i}$ and shunt capacitance C_i . The transmission matrix \bar{T}_i is defined by

$$\begin{bmatrix} V_i \\ I_i \end{bmatrix} = \bar{T}_i \begin{bmatrix} V_{i+1} \\ I_{i+1} \end{bmatrix} \quad (26)$$

and for a lossless transmission line, \bar{T}_i is given by (Ref. 13),

$$\bar{T}_i = \begin{bmatrix} \cos k l_i + j(Z_{0,i}/Z_i) \sin k l_i & j Z_{0,i} \sin k l_i \\ \cos k l_i / Z_i + j(1/Z_{0,i}) \sin k l_i & \cos k l_i \end{bmatrix} \quad (27)$$

here, k is the propagation constant of the line, and $Z_i = 1/(j\omega C_i)$ is the impedance of the capacitance.

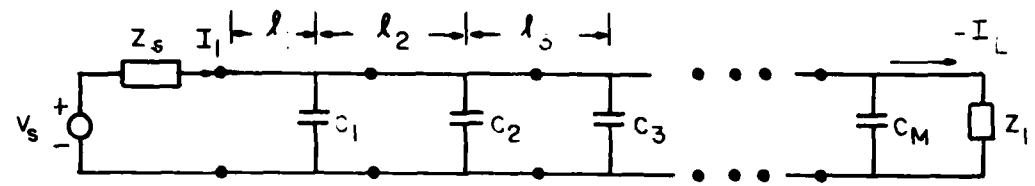


Figure 75. Model of a transmission line with shunt capacitances.

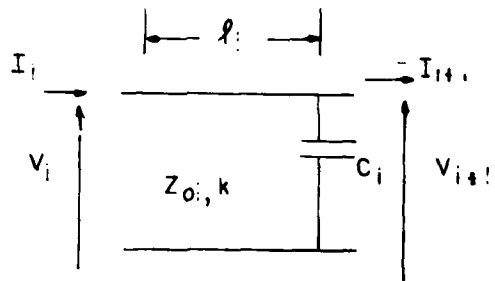


Figure 76. A section of the transmission line with a shunt capacitance.

The network transmission matrix $\overset{=}{T}_N$ can be obtained by

$$\begin{bmatrix} V_1 \\ I_1 \end{bmatrix} = \underset{i=1}{\overset{M}{\prod}} \overset{=}{T}_i \cdot \begin{bmatrix} V_L \\ -I_L \end{bmatrix} = \overset{=}{T}_N \begin{bmatrix} V_L \\ -I_L \end{bmatrix} \quad (28)$$

$$= \begin{bmatrix} A_N & B_N \\ C_N & D_N \end{bmatrix} \begin{bmatrix} V_L \\ -I_L \end{bmatrix}$$

The terminal relations are

$$V_s = V_1 - I_1 Z_s \quad (29)$$

$$V_L = I_L Z_L \quad (30)$$

Solving Equations 28, 29 and 30, we obtain

$$I_L = -(V_s/Z_s) \{1/[Z_L(C_N + A_N/Z_s) + (D_N + B_N/Z_s)]\} \quad (31)$$

and V_L , V_1 and I_1 are given by Equations 30 and 28.

To obtain the current I_{j+1} say, we first obtain the transmission matrix from $i = 1$ to $i = j$ viz

$$\begin{bmatrix} V_1 \\ I_1 \end{bmatrix} = \underset{i=1}{\overset{j}{\prod}} \overset{=}{T}_i \cdot \begin{bmatrix} V_{j+1} \\ -I_{j+1} \end{bmatrix} \quad (32)$$

$$= \begin{bmatrix} A_j & B_j \\ C_j & D_j \end{bmatrix} \begin{bmatrix} V_{j+1} \\ -I_{j+1} \end{bmatrix}$$

$$I_{j+1} = \frac{C_j V_1 - A_j I_1}{A_j D_j - B_j C_j} \quad (33)$$

4. RESULTS

We present the results for two transfer current ratios along the line. The reference position is at station 1489, and the two positions where the transfer current ratios are calculated are at station 1471 and station 940. At each station, six cases are computed so that one could observe the change in computed results as the modeling complexity increases.

These six cases are:

- (i) A uniform line terminated by 50- Ω resistances
- (ii) A line with one characteristic impedance and 98 capacitances, each capacitance has the same value ($C = 6.3 \text{ pF}$). The number 98 corresponds to number of cable clamps and/or ribs.
- (iii) A line with one characteristic impedance and 6 divisions. Within each division, the capacitance values are the same. There are altogether 98 capacitances.
- (iv) A line with 6 divisions, within each division, the capacitance values are the same. Capacitance values and characteristic impedances of different divisions may be different.
- (v) Same as (iv), except there are 7 capacitances being added in to model the bulkheads, the capacitance value is 10 pF.
- (vi) Same as (v), except the extra capacitance values are 15 pF.

It is to be noted that in (v) and (vi), the capacitance values are introduced to demonstrate effects of large discontinuities that may appear along the line. The exact places where these capacitances are modeled may not correlate directly to practical situations.

The order of these six cases shows an increase in the complexity of geometrical modeling, and can be considered as modeling more closely to the real cable (in the laboratory or on the aircraft). However, the physical model is greatly simplified from the real situation as it does not take couplings to neighboring objects into account, nor is it of sufficient detail in modeling for the many bends, twists, etc. of the real cable.

The first four cases for station 1471 are presented in Figure 77. As can be observed, the increase in the modeling complexity,

- a. increases the oscillation of the response,
- b. reduces somewhat the peak values,
- c. slightly shifts the frequency where peaks occur,
- d. causes virtually no difference in these curves at relatively low frequency (below 5 MHz).

The next two cases are presented in Figure 78. We observe that the effect of adding capacitances due to bulkheads tends to:

- a. have virtually no effect at low frequencies (below 20 MHz)
- b. significantly alter the response curve at higher frequency
- c. have higher storage capacity at higher frequencies.

Comparing these calculated results with the measured results (Figure 48), it can be concluded that the low frequency portions agree fairly well. In general, the two sets of data have very comparable magnitudes and peaks and valleys which are readily identified, with the exception that the frequencies at which they occur may not exactly coincide. At higher frequencies, the measured curves show considerably lower magnitudes. This is attributed to the losses along the line, which are more prominent at higher frequencies. The difference in the peak frequencies suggests that the capacitance values used may need changing.

In Figures 79 and 80, similar results are presented for station 940. Similar observations can be made. It is evident that the measured results exhibit more loss at high frequencies in this case. This is not surprising because the observation point is so much farther down the line.

5. RECOMMENDATIONS

From the results shown, it can be concluded that:

- a. it is necessary to include losses in the model,
- b. the actual propagation velocity needs to be accurately determined for the use in the model,
- c. to obtain very accurate results, it is necessary to model in great geometrical detail, and have very accurate capacitance values,
- d. for moderate accuracy (within a few dB), the results of case (ii) is quite adequate.

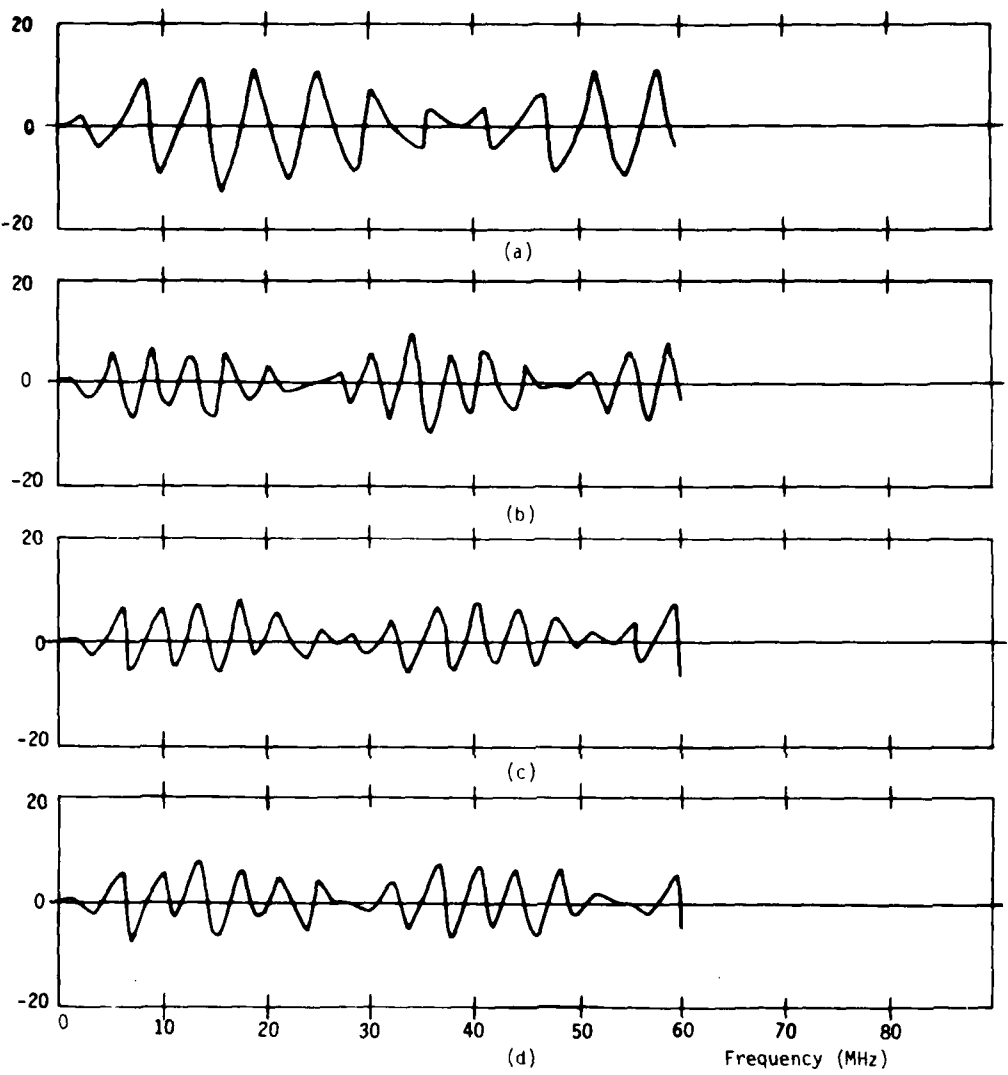


Figure 77. Magnitude of transfer current ratio $|I_{1471}/I_{1489}|$ at station 1471.

- (a) Smooth line
- (b) With 98 capacitance $C = 6.3 \text{ pF}$
- (c) With 6 divisions, same Z_C throughout
- (d) With 6 divisions, different Z_C values

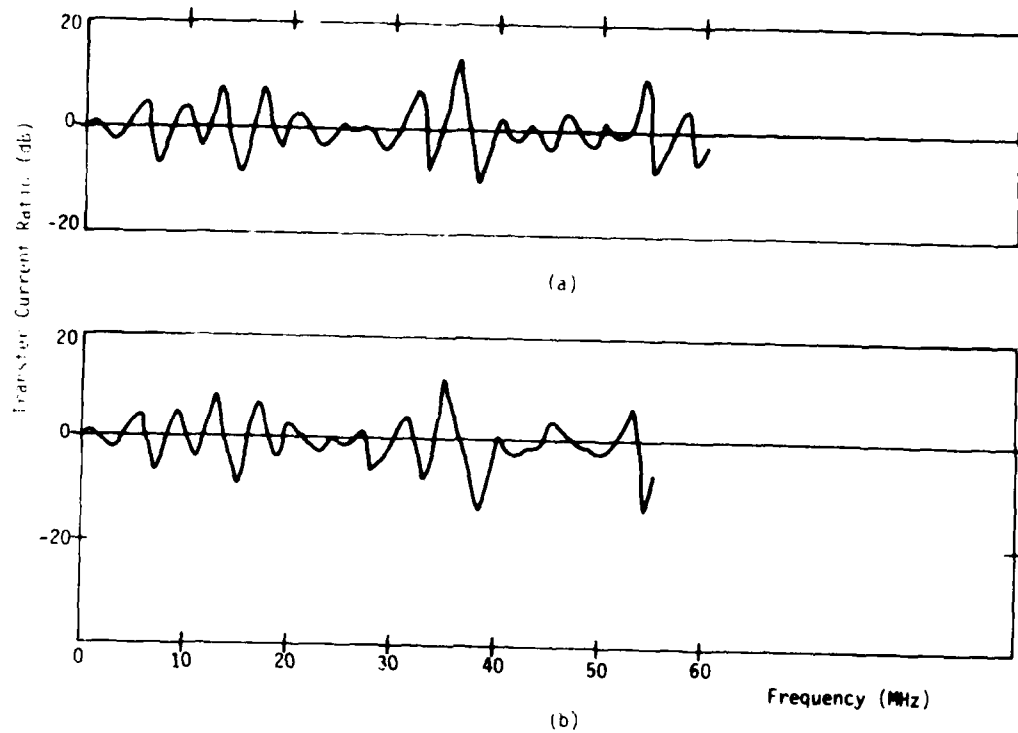


Figure 78. Magnitude of transfer current ratio at station 1471.

- (a) With 10 added capacitance of 10 pF
- (b) With 10 added capacitance of 15 pF

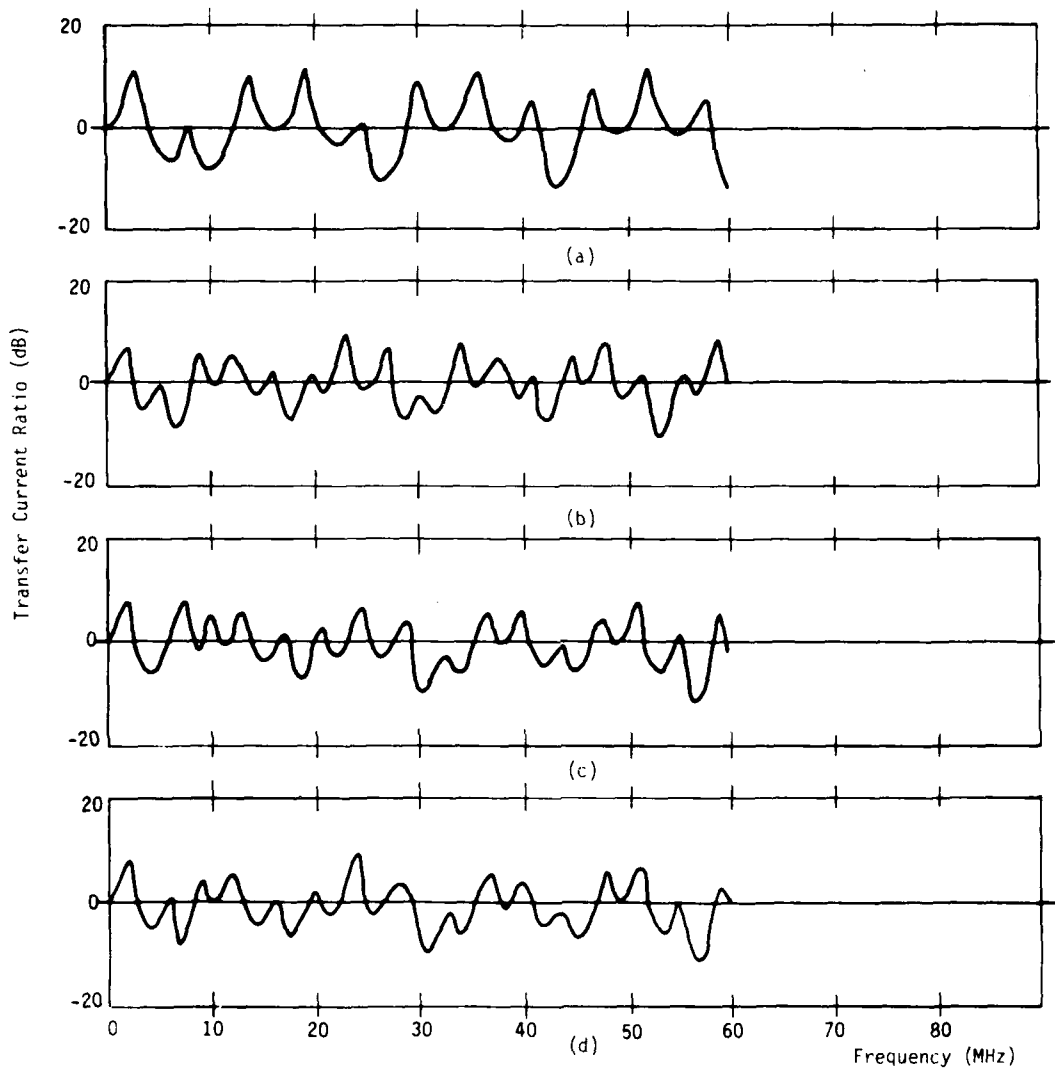


Figure 79. Magnitude of transfer current ratio $|I_{940}/I_{1489}|$ at station 940.

- (a) Smooth line
- (b) With 98 capacitance $C = 6.3 \text{ pF}$
- (c) With 6 divisions, same Z_C throughout
- (d) With 6 divisions, different Z_C values

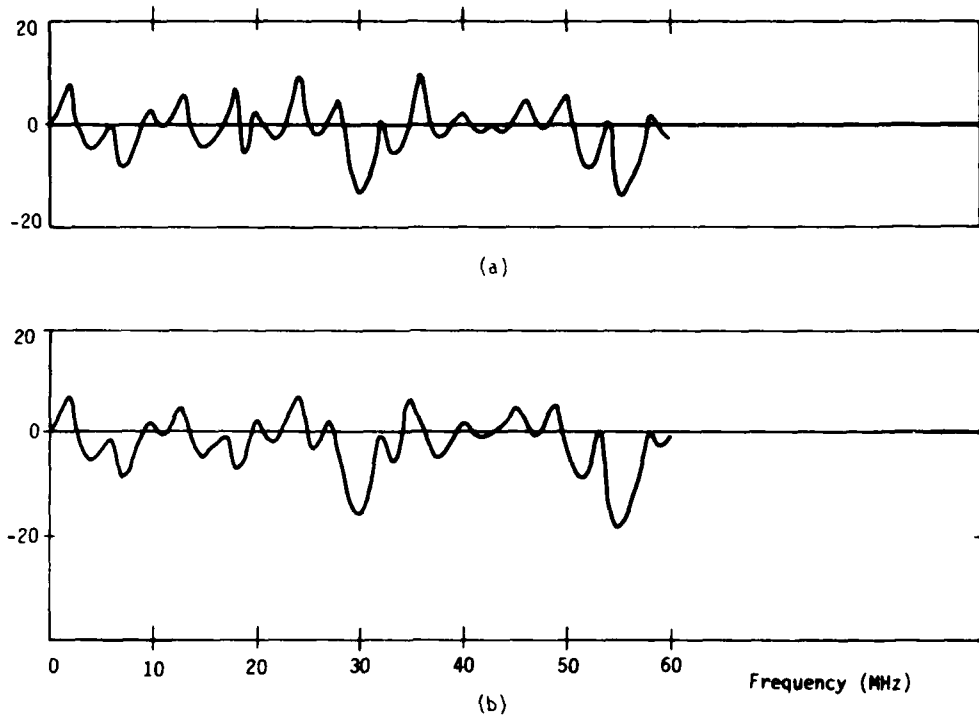


Figure 80. Magnitude of transfer current ratio at station 940.

- (a) With 10 added capacitance of 10 pF
- (b) With 10 added capacitance of 15 pF

SECTION VI

VALIDITY OF CALCULATIONAL METHODS FOR AIRCRAFT CABLE ASSESSMENT

Over the past few years, a number of different calculational models for predicting cable response to EMP have been developed. Reference 18 presents a summary of a few computer codes used for this purpose. In addition to these, a single line approximation for a multiconductor transmission line has been developed (Ref. 19), as well as a general multiconductor network analysis code (Ref. 20). This section discusses some of the details of the various types of analyses and illustrates some typical results for a field-excited transmission line under various loading configurations. In addition, the correspondence between a single line calculation and a multiconductor calculation is presented.

1. TRANSMISSION LINE GEOMETRY

Figure 81 shows a four-wire multiconductor transmission line which is located above a perfectly conducting ground plane. At each end of the line, there is a generalized matrix impedance termination and the excitation of the line is due to an incident plane electromagnetic wave with \vec{E} in the \hat{x} direction (broadside incidence). For purposes of this discussion, the temporal behavior of this incident field is assumed to be a step function of 1 volt/meter, since the arrival times of various current waves on the line are clearly observable, thereby permitting a better understanding of the physical behavior of the line and the validation of accuracy of the modeling.

The transmission line used in this study is the same four-wire line previously discussed in Section 3. Figure 19 shows the cross section of this line, along with the various dimensions. The measured inductance and capacitive coefficient matrices, (L'_{nm}) and (C'_{nm}) , and the corresponding characteristic impedance matrix (Z'_{Cnm}) have all been presented in Sec. 3 of this report. This line is assumed to be lossless.

It is clear that there are many parameters which could be varied in a study designed to give insight into field coupling of a multiconductor line. These include polarization, angle of incidence, planarity and spectral content of the incident field, physical properties of the transmission line, and the configuration of the load impedances. In the present study, however, we have elected to keep both the incident field parameters and

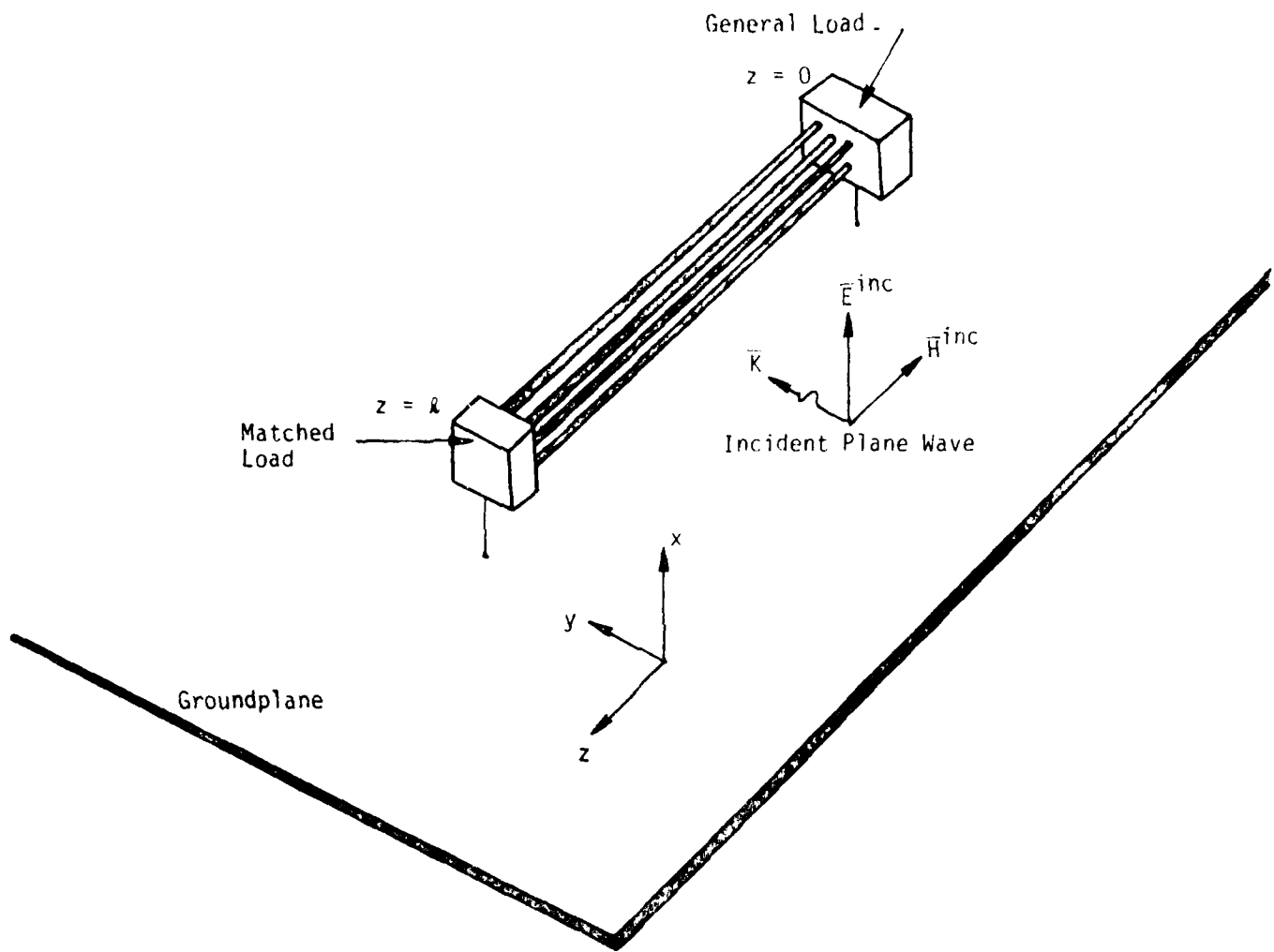


Figure 81. Geometry of four-wire multiconductor line excited by an incident, step planewave.

the transmission line parameters invariant. Furthermore, to avoid undue complications in the transmission line response, one of the load impedance matrices (at $z = l$ meter) is matched. The other impedance matrix at ($z = 0$) is allowed to have a number of different configurations, and the corresponding currents and/or voltages in the lines are computed.

2. REVIEW OF THE TRANSMISSION LINE SOLUTIONS

The solution of the currents flowing on a general multiconductor transmission line has been discussed by a number of authors (Refs. 8, 17, 21, 22). Reference 23 presents a summary of most of this past work. It is well known that the TEM currents and voltages on an n wire (plus a reference conductor) transmission line are described by the Telegrapher's equations.

$$\frac{\partial}{\partial z} (V_n) + s(L'_{nm})(I_m) = s(L_n^{(i)})H_\perp^{(i)} \quad (34a)$$

$$\frac{\partial}{\partial z} (I_n) + (G'_{nm}) + s(C'_{nm}) (V_m) = -s(C_n^{(i)})E_\perp^{(i)} \quad (34b)$$

Here, (V_n) and (I_n) represent, in vector form, the n voltages and currents at any point z along the line. The matrices $(L'_{n,m})$ and $(C'_{n,m})$ are the inductive and capacitive coefficients previously discussed and the term $(G'_{n,m})$ accounts for possible conductive loss within the dielectric surrounding the wires. The source terms of Equation 34 are related to the magnetic field linking the reference conductor and conductor in question, and the electric field in the plane of the two conductors. The above equations assume lossless conductors. If there is significant conductor loss, a term $(R'_{n,m})(I_n)$ may be added to equation 34a, as described in Reference 21.

The solution to the above equation is obtained by first obtaining a solution to the homogenous set of equations

$$\frac{\partial}{\partial z} (V_n) + (Z'_{nm})(I_m) = 0 \quad (35a)$$

$$\frac{\partial}{\partial z} (I_n) + (Y'_{nm})(V_m) = 0 \quad (35b)$$

where

$$(Z'_{nm}) = s(L'_{nm}) \quad (36a)$$

$$(Y'_{nm}) = (G'_{nm}) + s(C'_{nm}) \quad (36b)$$

Equations 35a and 35b can be manipulated in the usual manner to yield two second order, uncoupled wave equations for (v_n) and (i_n) :

$$\frac{\partial^2}{\partial z^2} (i_n) = (Y'_{nm})(Z'_{nm})(i_n) \quad (37a)$$

$$\frac{\partial^2}{\partial z^2} (v_n) = (Z'_{nm})(Y'_{nm})(v_n) \quad (37b)$$

These equations seem difficult to solve at first, since the propagation matrices $(Y'_{nm})(Z'_{nm})$ and $(Z'_{nm})(Y'_{nm})$ are full matrices. It is possible, however to diagonalize the propagation matrices by a transformation matrix (T_{nm}) consisting of the eigenvectors of the matrix $(Y'_{nm})(Z'_{nm})$, i.e.,

$$(T_{nm})^{-1}(Y'_{nm})(Z'_{nm})(T_{nm}) = (\gamma_{nn})^2 \quad (38)$$

where $(\gamma_{nn})^2$ is a diagonal matrix with elements equal to the corresponding eigenvalues.

Because (Z'_{nm}) and (Y'_{nm}) are symmetric, the matrix $(Z'_{nm})(Y'_{nm})$ can also be diagonalized with (T_{nm}) as

$$(T_{nm})^\dagger(Z'_{nm})(Y'_{nm})(T_{nm})^{\dagger-1} = (\gamma_{nn})^2 \quad (39)$$

where the superscript \dagger denotes the transpose.

Using the transformation matrices (T_{nm}) , the general coupled wave equations in Equations 37 can be transformed into a different set of wave equations

$$\frac{\partial^2}{\partial z^2} (i_n) = (\gamma_{nn})^2 (i_n) \quad (40a)$$

$$\frac{\partial^2}{\partial z^2} (v_n) = (\gamma_{nn})^2 (v_n) \quad (40b)$$

which are uncoupled for each set of modal amplitudes i_n or v_n , since

$(\gamma_{nm})^2$ is a diagonal matrix. These modal amplitudes are related to the physical currents and voltages on the line as:

$$(i_n) = (T_{nm})^{-1} (I_n) \quad (41a)$$

$$(v_n) = (T_{nm})^T (V_n) \quad (41b)$$

and have simple traveling wave solutions of the form

$$(i_n) = e^{-(\gamma_{nn})z} (A_n) + e^{(\gamma_{nn})z} (B_n) \quad (42a)$$

$$(v_n) = e^{-(\gamma_{nn})z} (C_n) + e^{(\gamma_{nn})z} (D_n) \quad (42b)$$

where (A_n) , (B_n) , (C_n) and (D_n) are n-vectors which are constants of integration that must be determined.

For a finite length of line, these constants depend on the load conditions, as well as how the line is excited. Once these coefficients are determined, the total line current and voltage at any point z can be expressed as:

$$(I_n) = (T_{nm}) e^{-(\gamma_{nn})z} (A_n) + (T_{nm}) e^{(\gamma_{nn})z} (B_n) \quad (43a)$$

$$(V_n) = (T_{nm})^T e^{-1} e^{-(\gamma_{nn})z} (C_n) + (T_{nm})^T e^{-1} e^{(\gamma_{nn})z} (D_n) \quad (43b)$$

In many applications, it is not required to find the transmission line current or voltage everywhere along the line, but rather, only at the loads at the ends. In this case, the solutions in Equations 42 can be put in the form

$$\begin{bmatrix} (I_n(0)) \\ (I_n(\ell)) \end{bmatrix} = \begin{bmatrix} ((\delta_{nm}) + (\Gamma_{1nm})) & (0_{nm}) \\ (0_{nm}) & ((\delta_{nm}) + (\Gamma_{2nm})) \end{bmatrix} \begin{bmatrix} (-\Gamma_{1nm}) & (T_{nm})e^{(\gamma_{nn})\ell} (T_{nm})^{-1} \\ (T_{nm})e^{(\gamma_{nn})\ell} (T_{nm})^{-1} & (-\Gamma_{2nm}) \end{bmatrix}^{-1} \begin{bmatrix} (S_n)_1 \\ (S_n)_2 \end{bmatrix} \quad (44)$$

where (δ_{nm}) is an identity matrix, (Γ_{1nm}) and (Γ_{2nm}) are the generalized current reflection coefficient matrices defined as

$$(\Gamma_{1nm}) = -[(Z_{Lnm}^{(1)}) + (Z_{Cnm}^{(1)})]^{-1} [(Z_{Lnm}^{(1)}) - (Z_{Cnm}^{(1)})] \quad (45)$$

for the impedance load at $z = 0$, and similarly for (Γ_{2nm}) at $z = \ell$ with $(Z_{Lnm}^{(2)})$ as the load impedance. In this equation, the term $(Z_{Cnm}^{(1)})$ represent the characteristic impedance matrix of the multiconductor line and is given by the relation

$$(Z_{Cnm}^{(1)}) = (Y'_{nm})^{-1} (T_{nm}) (\gamma_{nn}) (T_{nm})^{-1} \quad (46)$$

The terms $(S_n)_q$, $q = 1, 2$ represent the source terms on the multiconductor line and are referred to as the combined current sources. For a field excited line, these source terms are given by

$$(S_n)_1 = \frac{1}{2} \int_0^\ell (T_{nm}) e^{(\gamma_{nn})\xi} (T_{nm})^{-1} \left((Z_{Cnm}^{(1)})^{-1} (V_n^{(s)}(\xi)) + (I_n^{(s)}(\xi)) \right) d\xi \quad (47a)$$

$$(S_n)_2 = \frac{1}{2} \int_0^\ell (T_{nm}) e^{(\gamma_{nn})(\ell-\xi)} (T_{nm})^{-1} \left((Z_{Cnm}^{(1)})^{-1} (V_n^{(s)}(\xi)) - (I_n^{(s)}(\xi)) \right) d\xi \quad (47b)$$

where (V'_n) and (I'_n) are per-unit-length sources along the line which are directly related to the incident electromagnetic field. For the case of a point source excitation of the line, the above set of equations may be used, with (V'_n) and (I'_n) being considered as distributions.

The solution for the load currents $(I_n(0))$ and $(I_n(\ell))$ in Equation 44 is straightforward, but tedious, due to the potentially large number of elements in the matrix. Usually, computer solutions are used. Once the currents are found, the load voltages are found trivially as

$$(V_n(0)) = - (Z_{L_{nm}}^{(1)}) (I_n(0)) \quad (48a)$$

$$(V_n(\ell)) = (Z_{L_{nm}}^{(2)}) (I_n(\ell)) \quad (48b)$$

Although the above review of the transmission line solutions is presented only for a single section of transmission line, it is possible to extend the analysis to a more general network of interconnected transmission lines. This is discussed in Reference 20 and will not be considered further here.

The distributed current and voltages $(I_n^{(s)})$ and $(V_n^{(s)})$ for a multi-conductor transmission line have been discussed in Reference 3, and have the form

$$(I_n^{(s)}) = - s (C_{nm}^{'}) \cdot \left(\int_a^{b_n} f_n (E^{inc} + E^{st}) \cdot d\bar{\ell}_n \right) \quad (49a)$$

and

$$(V_n^{(s)}) = s \mu_0 \left(\int_a^{b_n} f_n (H^{inc} + H^{st}) \cdot \hat{n}_n d\bar{\ell}_n \right) \quad (49b)$$

where the countour C_n is from a point a on the reference conductor to a point b_n on the n^{th} conductor and E^{st} and H^{st} are the static scattered electric and magnetic fields. These expressions may be simplified considerably by introducing a set of field coupling vectors similar to that of Reference 24 for a two wire line. With this, the distributed sources become

$$(I'_n(s)) = - s (C'_{nm}) \cdot \left((\bar{E}^{\text{inc}} \cdot \bar{h}'_n)_m \right) \quad (50a)$$

and

$$(V'_n(s)) = s \mu_0 \left((\bar{h}'_n \times \hat{z}) \cdot \bar{H}^{\text{inc}} \right) \quad (50b)$$

where (\bar{h}'_n) is a vector array of n vectors in 3 space and represents the field coupling vectors for the multiconductor line.

3. CALCULATED MULTICONDUCTOR RESPONSE

Using the analysis procedure outlined above, the multiconductor cable shown in Figure 81 has been analyzed. Given the (L'_{nm}) and (C'_{nm}) matrices of Section III, the current eigenvalues and eigenvectors of the propagation matrix $s^2(C'_{nm})(L'_{nm})$ have been calculated. The eigenvalues correspond to the square of the propagation constants for each of the current eigenmodes, and it is therefore possible to obtain each of the modal velocities. Since this is a four wire line plus a reference conductor, there will be four eigenmodes and eigenvalues. Figure 82 shows a histogram of the modal velocities. As may be noted, the modal velocities are all different, an effect that is due to the inhomogenous dielectric region surrounding the conductors. The first eigenmode is seen to propagate with the largest speed and is the "bulk" mode. Figure 83a shows the current distribution for this mode and it is seen that the sum of all wire currents is non-zero. Figures 83b, 83c and 83d show the corresponding differential current modes which exist on this line. Note that for these modes, the currents sum nearly to zero in any cross-section, implying that while they may contribute strongly to the current response of an individual wire at a termination, they do not contribute significantly to the total current response.

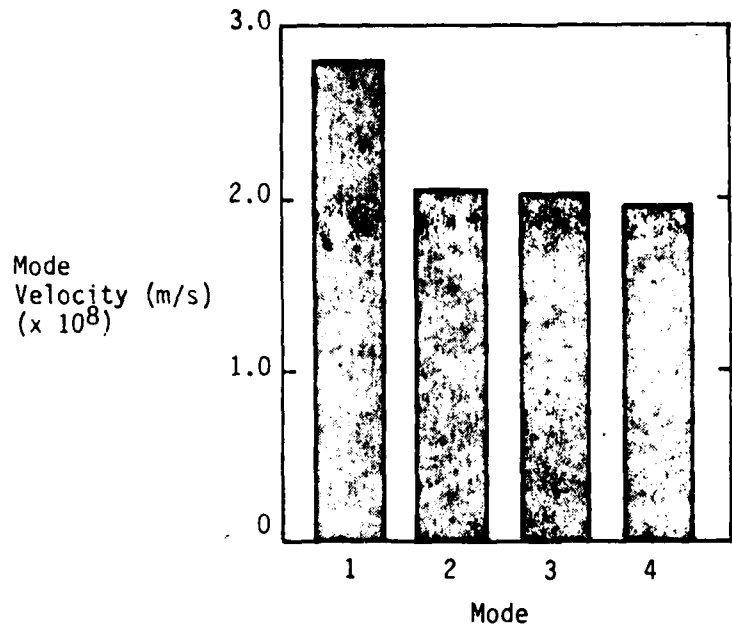


Figure 82. Histogram of current eigenmode velocities for the four-wire transmission line of Figure 19.

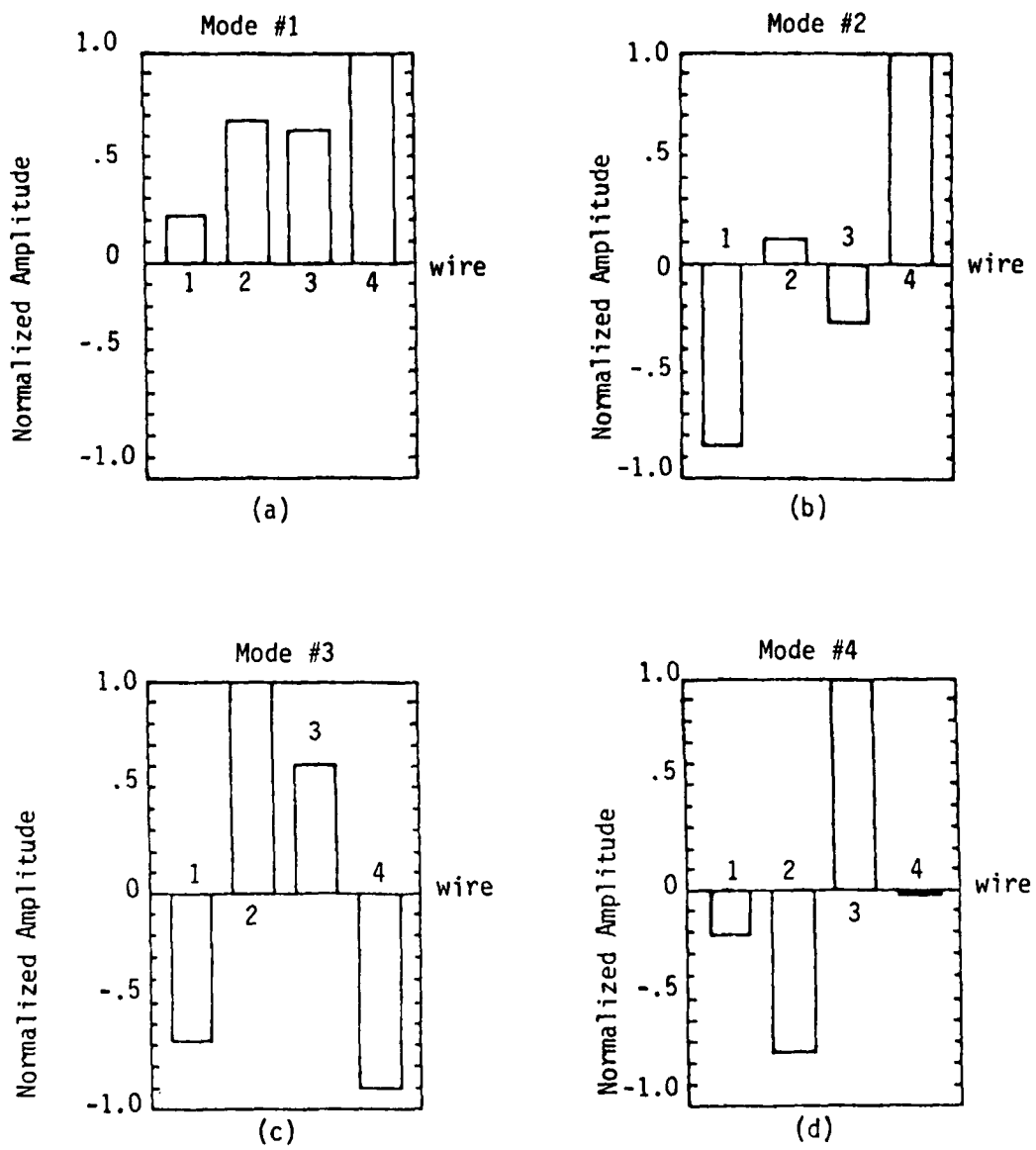


Figure 83. Histograms showing the four normalized current eigenmodes for the four-wire line of Figure 19.

As previously mentioned, the bulk mode has the largest propagation velocity on the line. This is generally true for dielectric covered cables and is due to the fact that for the bulk mode, a substantial amount of the electric field resides outside the dielectric sheaths of the conductors, thereby lowering the effective dielectric constant seen by this mode. The differential modes, on the other hand, have large electric fields between the individual wires and thus see a larger effective dielectric constant.

The difference in the propagation times for the fastest (bulk) and the slowest (differential) modes in this line amounts to approximately 1.5 ns per meter of line. In some instances, such effects might be unimportant, especially if the excitation waveform varies much more slowly than the natural oscillation time of the transmission line. In our study of this line, we shall investigate more thoroughly the effects of this multimode propagation.

In Reference 3, the field coupling vectors, (\bar{h}_n) occurring in Equations 50, were discussed. As shown in Figure 84, the i^{th} component of this n vector represents the vector distance from the ground plane to the center of charge on the i^{th} conductor, with all other conductors having zero charge. These quantities may be calculated accurately by solving a two dimensional potential problem in the transverse plane of the transmission line, or they may be approximated simply by the heights of each wire over the ground. This latter approximation is accurate for wires whose diameters are small compared with the height above the ground plane, and a rough estimate of errors involved in doing this may be obtained from the two-wire example treated by Lee (Ref. 24). For the present calculations, we take the field coupling parameters to be the wire heights.

Figures 85a through 85d show the transient currents induced in each of the wires at the $z = 0$ load end of the multiconductor cable which is excited by an incident planewave step field of 1 volt/meter. For this particular example, the loading at $z = 0$ was such that each wire had a single resistance to ground, and each resistor was identical. Thus, the $(Z_{L_{nm}}^{(1)})$ matrix is of the form

$$(Z_{L_{nm}}^{(1)}) = R_o (\delta_{nm}) \quad (51)$$

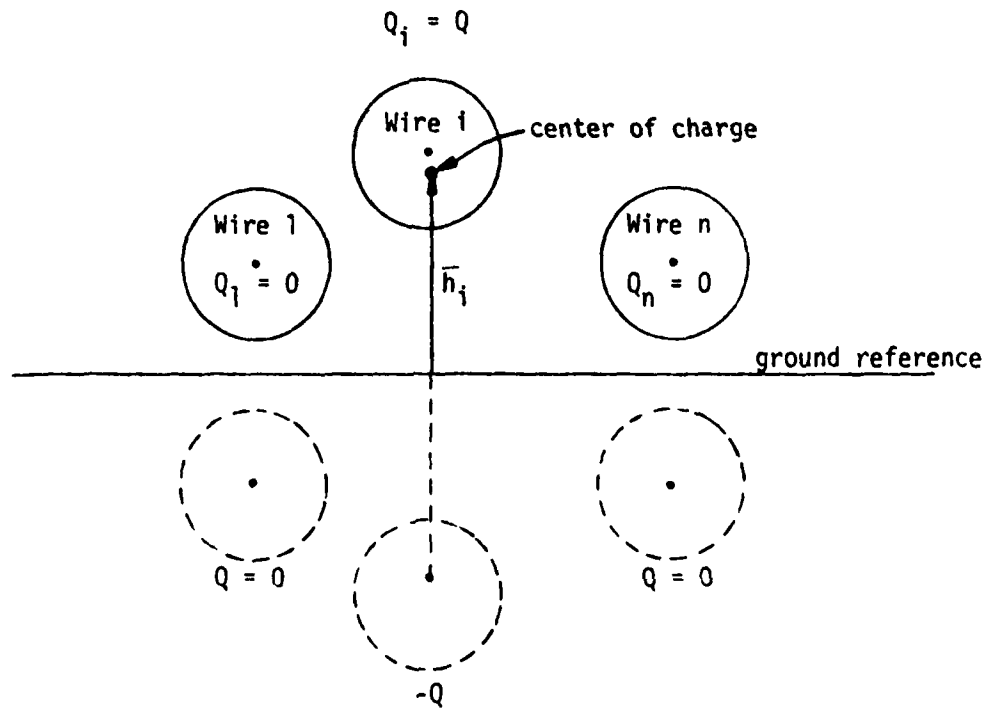


Figure 84. Field coupling vector for wire *i* of multiconductor line over a ground plane.

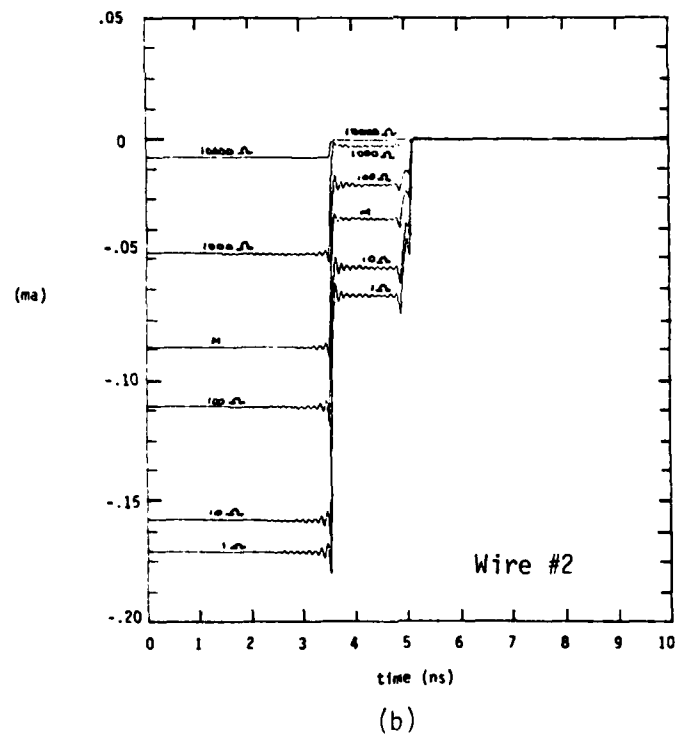
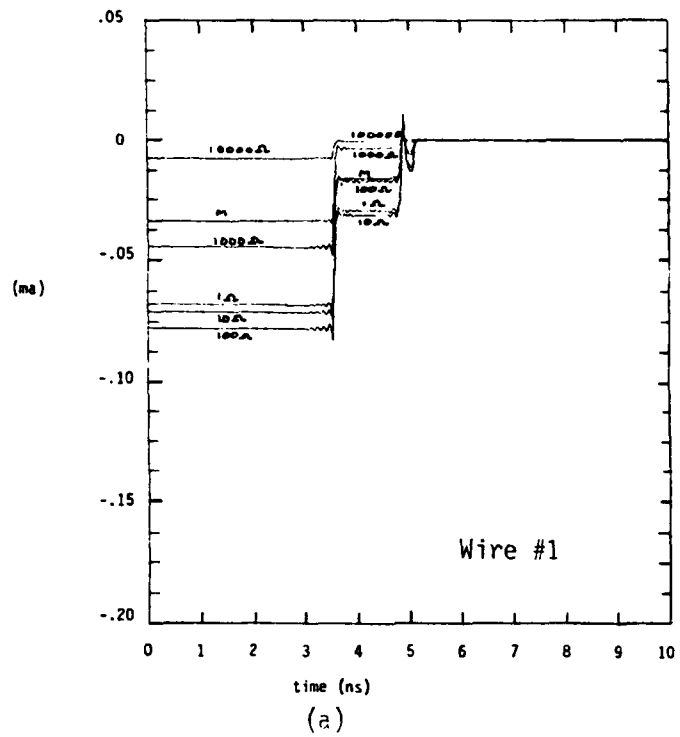


Figure 85. Transient wire currents at load end ($z=0$) for each wire of multiconductor line for various load conditions.

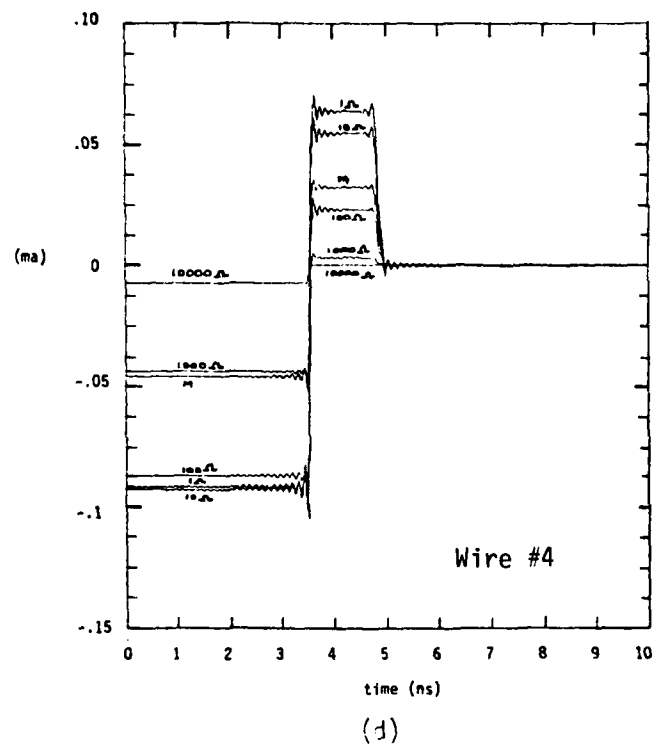
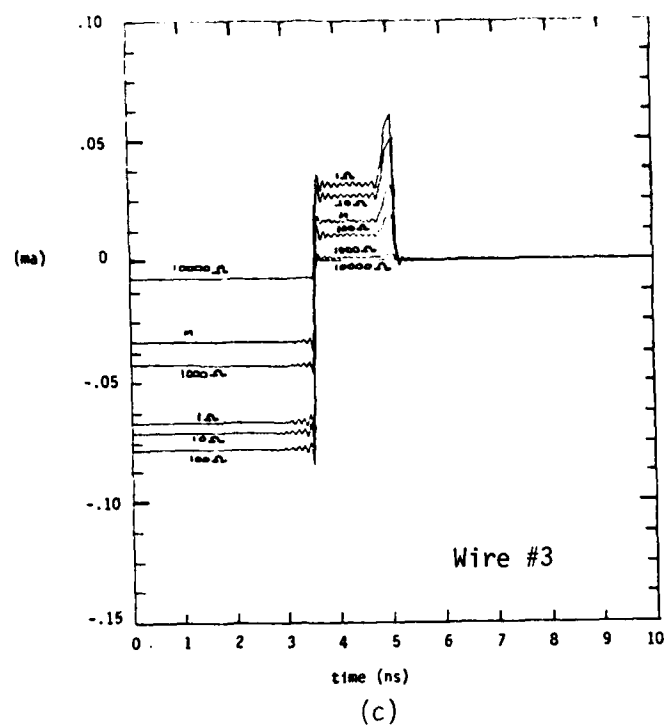


Figure 85 (concluded).

where R_0 is a scalar which has the value 1, 10, 100, 1000 and 10,000 Ω . The individual wire responses for each of these loads are presented in Figures 85, along with the special case of this impedance being matched to the line impedance. As mentioned previously, the load impedance at $z = \ell = 1$ meter is always matched.

In Figures 85, the multimode propagation effects are clearly evident. At $t = 0$ the initial effects of the incident field are first felt at the load and a current begins to flow. This current is comprised of all modes. At $t = 3.57$ ns, the fastest (bulk) mode has propagated the complete length of the line, and information from the matched load at $z = \ell$ reaches the load at $z = 0$, causing a rapid drop in current. Later, at $t = 4.86$ ns, the next fastest mode has propagated the length of the line and another discontinuity in the observed current is evident. This process continues until the last mode reaches $z = 0$, at $t = 5.11$ ns, at which point no further current flows on the line. Note that had the load impedance at $z = \ell$ not been matched, this solution would not have been so simple, since the modes reflected at $z = \ell$ would continue to propagate on the line, and thus provide "ringing" of the current response.

The voltage across each of the wires at the load at $z = 0$ may be calculated using Equation 48. Figures 86a through 86d show the transient voltages for the transmission line under consideration. Their behavior is identical to that of the current, which is expected, since except for the matched load case, the wire voltage is simply the resistance of the load element times the current through the wire at $z = 0$.

Although the individual wire currents are often of interest in trying to understand how a complicated system will respond to an EMP, it is usually impossible to carry out a detailed multiwire analysis on a large cable network. In such cases, interest is focused on the "total" current or common mode response of the cable. This is obtained by simply summing the individual wire currents at the load. As noted previously, the current on the line is comprised of four modes, one of which is a "bulk" mode and the others which are differential. Since the sum of each differential mode is almost zero, the total current on the line is described primarily by the first current eigenmode. Figure 87 shows this effect. Presented

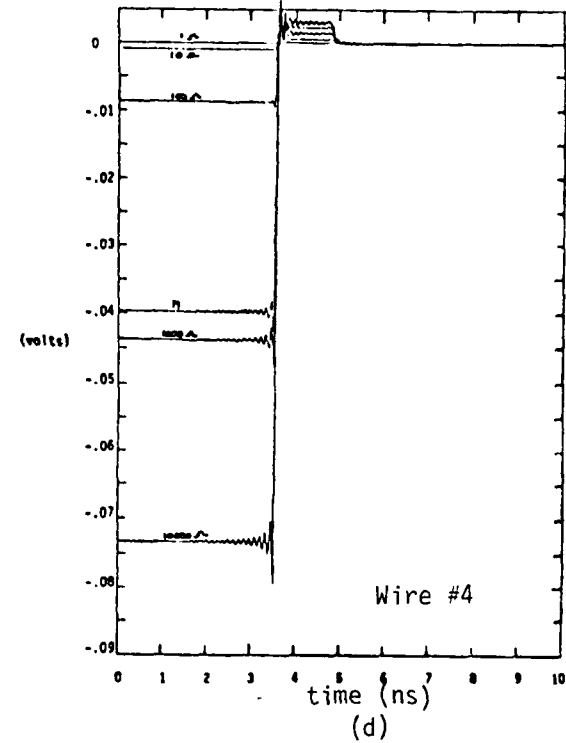
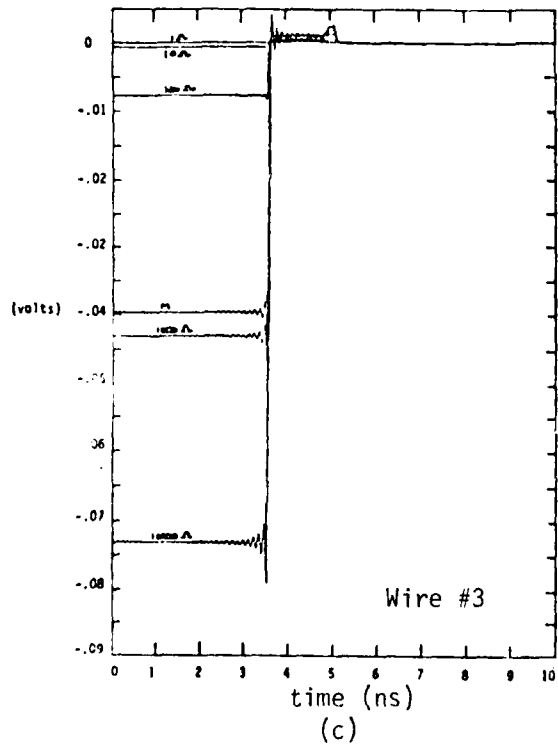
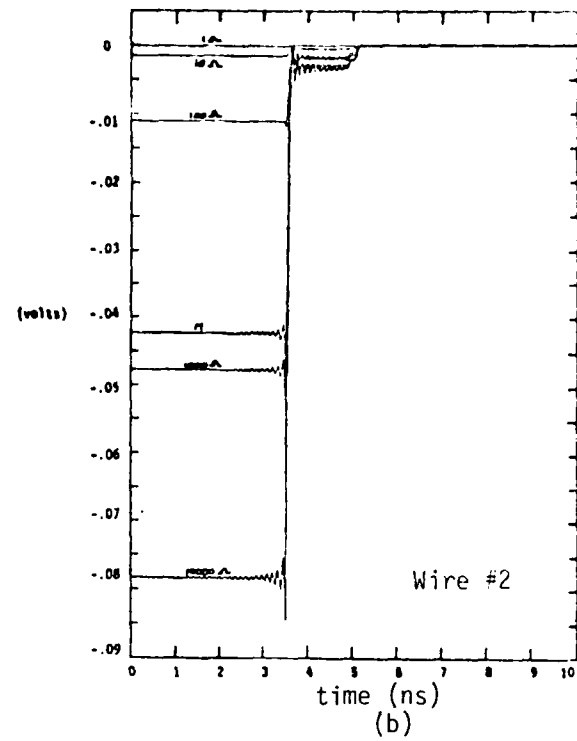
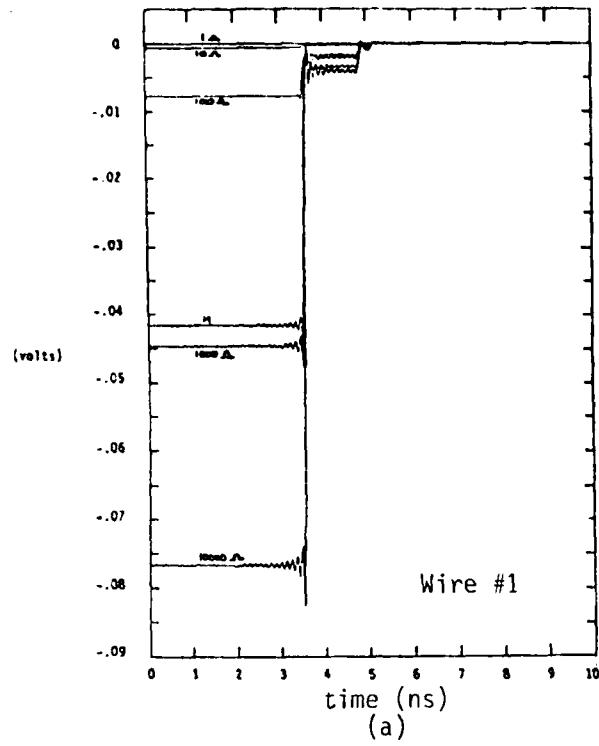


Figure 86. Transient wire voltages at load end ($z=0$) for each wire for the multiconductor line for various load impedances.

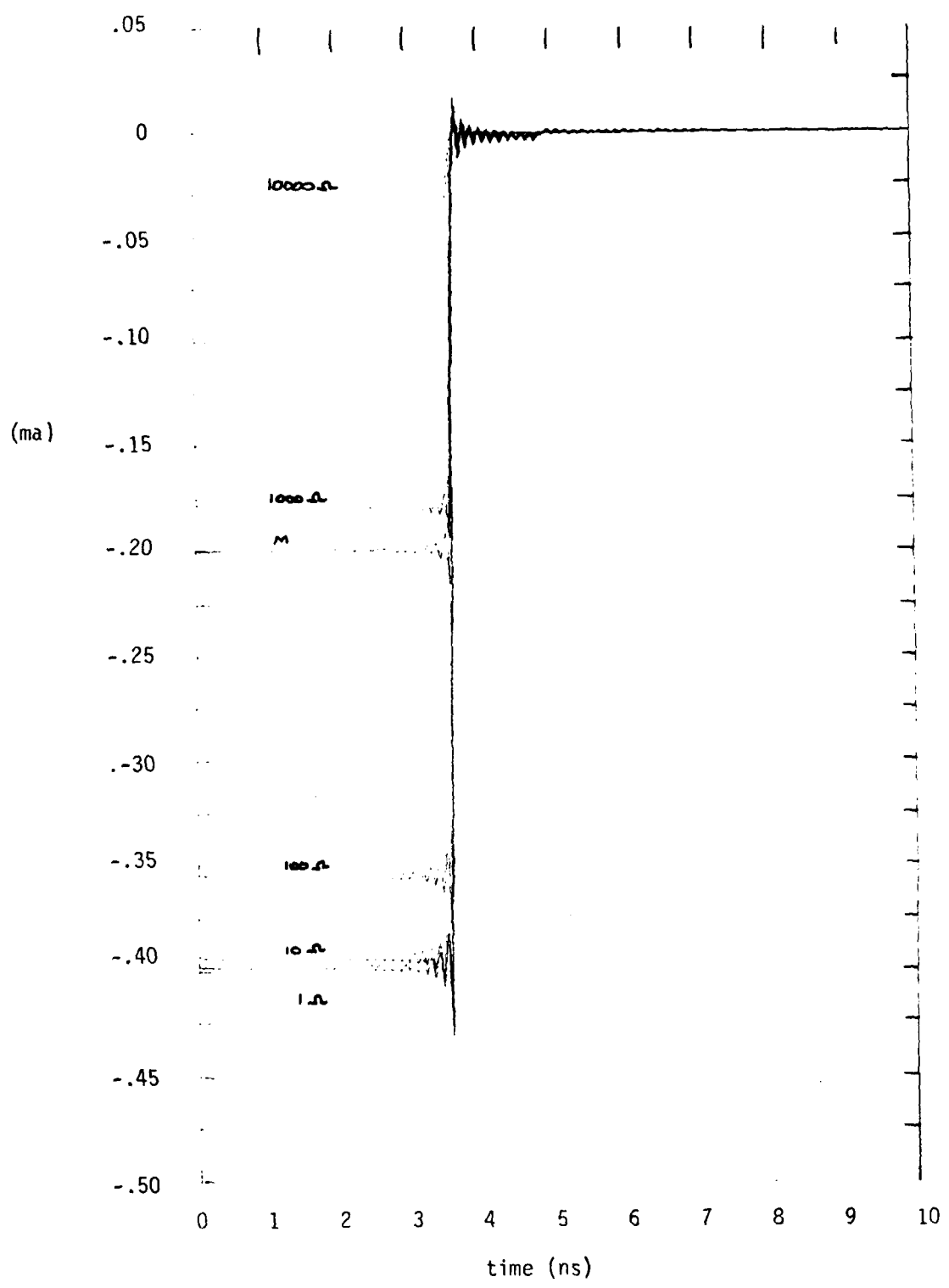


Figure 87. Total transient current at $z=0$.

in this figure is the total line current at $z = 0$, obtained by summing all wire currents. Note that the effects of the slower differential modes have virtually disappeared, and that for the first 3.6 ns the individual wire currents are always less than the total or bulk current.

A similar quantity of interest is the average voltage at the load at $z = 0$. This is presented in Figure 88 as a function of time. From this curve, and the bulk current, it is possible to infer an effective bulk mode load impedance as $Z_{LB} = I_{BULK}/V_{avg}$. As will be discussed in Section VI.4, this quantity has use in accurately modeling a multiconductor line by a single wire line. Table 1 summarizes the bulk quantities for this line as calculated from this multiconductor model.

Table 1
Bulk Quantities for Four Wire Line at $z = 0$ Load (Diagonal)

Multiconductor Load Impedance (Diagonal) (Ohms)	Bulk Current (ma)	Average Voltage (V)	Effective Bulk Load Impedance (Ohms)
1	-.398	-.0009	.25
10	-.394	-.001	2.54
100	-.355	-.0088	24.7
Matched (not diagonal)	-.201	-.041	205
1000	-.1792	-.045	256
10,000	-.0315	-.0755	2915

In many cases, a multiconductor cable in an aircraft will not have a uniform geometry as shown in Figure 81, but will be twisted randomly. There are several ways to model a random lay cable. The first is to calculate an effective inductance and capacitance capacitive coefficient matrix by averaging all diagonal and off diagonal terms in the (L'_{nm}) and (C'_{nm})

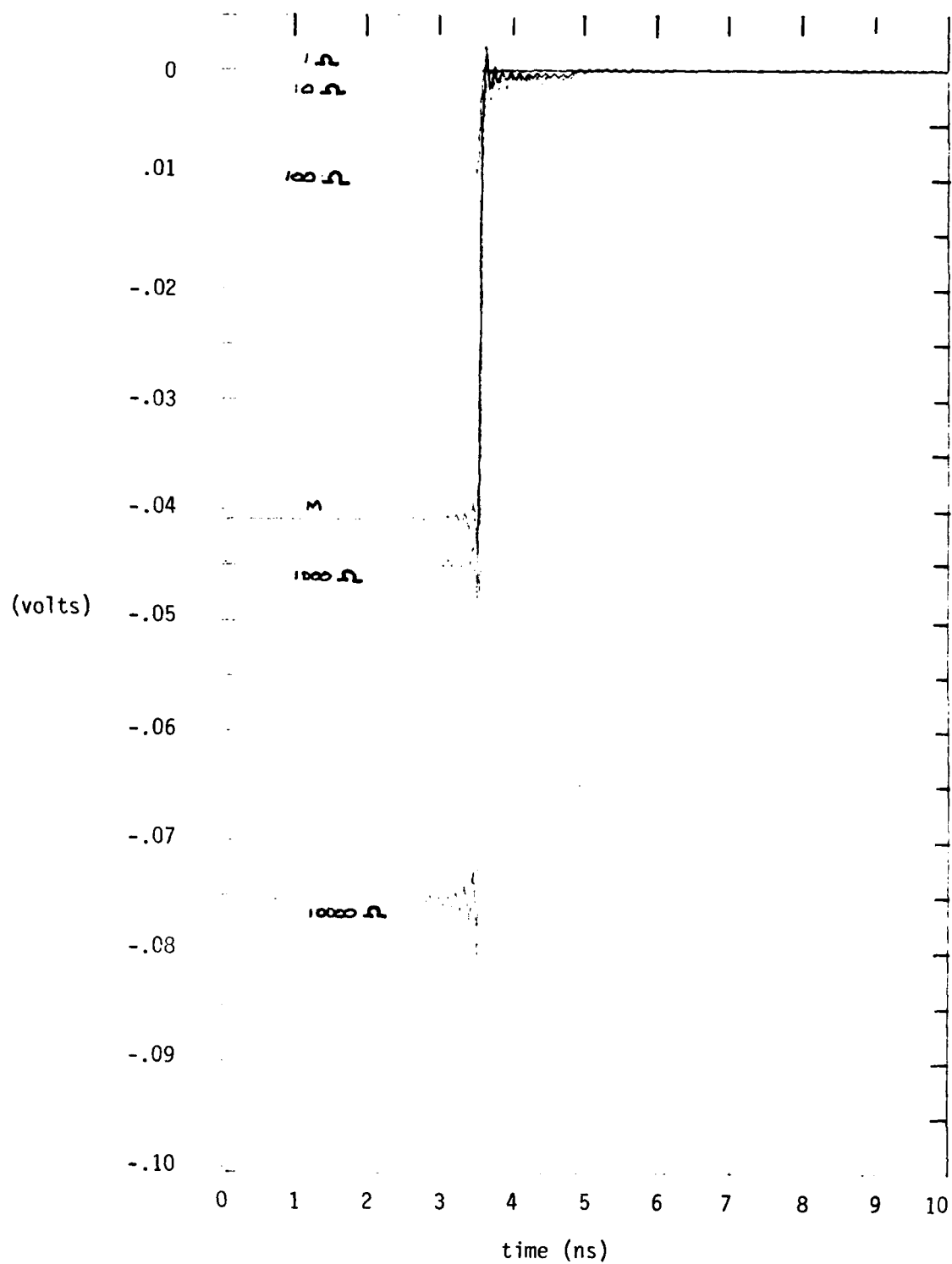


Figure 88. Average transient voltage at $z=0$.

matrices for the uniform line. Doing this for the four wire line treated previously gives the following values:

$$(L'_{nm}) = \begin{bmatrix} 9.43 & 6.69 & 6.69 & 6.69 \\ 6.69 & 9.43 & 6.69 & 6.69 \\ 6.69 & 6.69 & 9.43 & 6.69 \\ 6.69 & 6.69 & 6.69 & 9.43 \end{bmatrix} \times 10^{-7} \text{ h.}$$

$$(C'_{nm}) = \begin{bmatrix} 7.63 & -2.40 & -2.40 & -2.40 \\ -2.40 & 7.63 & -2.40 & -2.40 \\ -2.40 & -2.40 & 7.63 & -2.40 \\ -2.40 & -2.40 & -2.40 & 7.63 \end{bmatrix} \times 10^{-11} \text{ f.}$$

Similarly, the field coupling vectors must be averaged to yield

$$|h_n| = 8.156 \times 10^{-2} \text{ m}$$

for each of the four wires.

For the averaged L and C matrices, it results that the current eigenmodes consist of two types: one bulk mode with a propagation speed of 2.8×10^8 m/sec and three differential modes each having a speed of 1.90×10^8 m/sec.

The resulting transient wire current of the load at $z = 0$ is shown in Figure 89 for the six different load configurations used previously. Due to both the symmetry of the line properties and of the load impedances, all individual wire currents are identical, so only one curve suffices for their presentation. Comparing these currents with the individual wire currents presented in Figure 85 shows reasonable agreement.

Figure 90 presents the transient behavior of the total current for this case. Due to the symmetry in this special case, the total current is simply four times larger than the single wire current of Figure 89. Comparing this total current with Figure 87 shows that there is a very good agreement between the total current quantities. Notice that although the differential modes exist for this case, they are not strongly excited and do not contribute significantly to the individual wire currents.

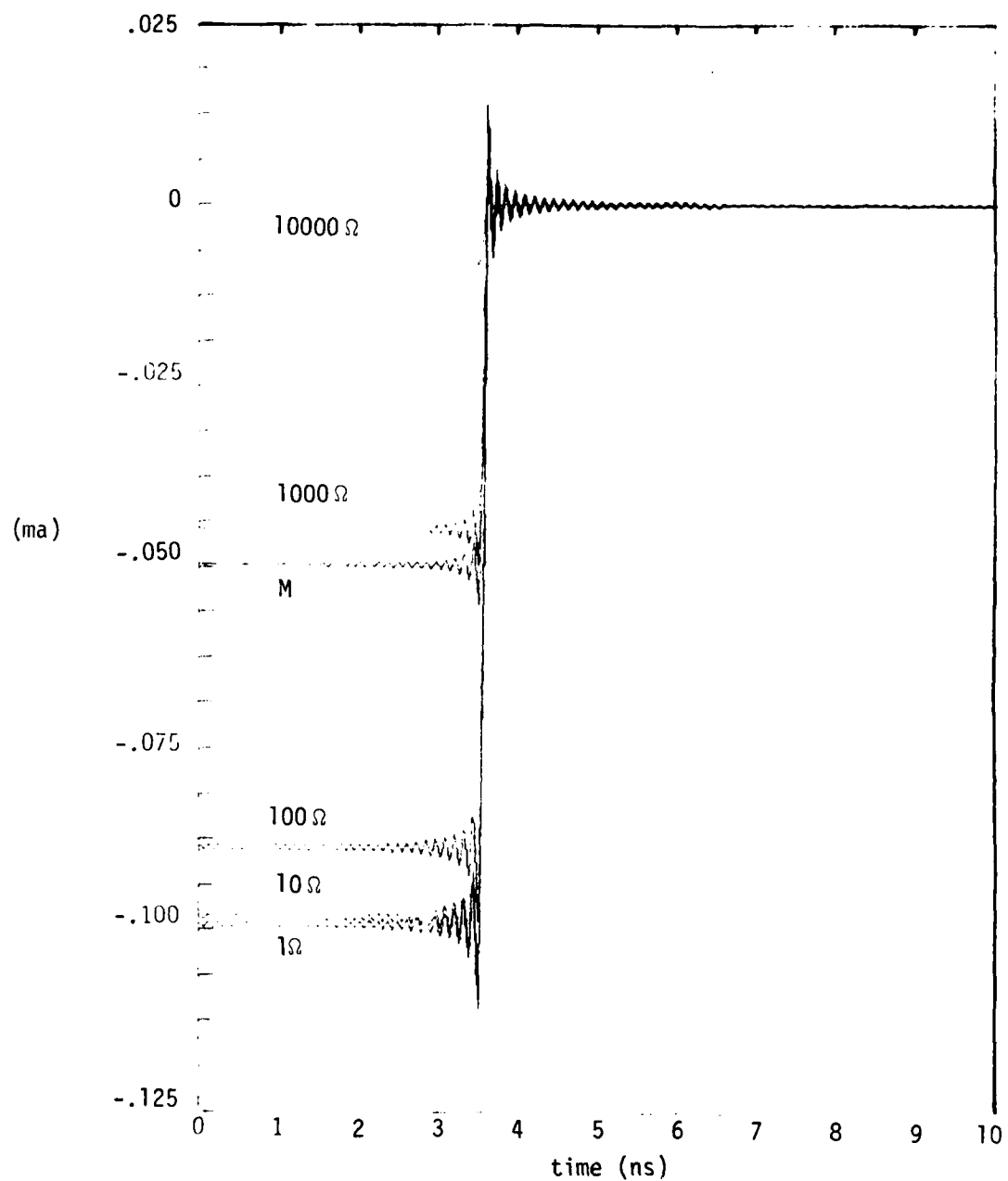


Figure 89. Plot of the transient wire current (any wire) at $z=0$ for averaged (L'_{nm}) and (C'_{nm}) matrices.

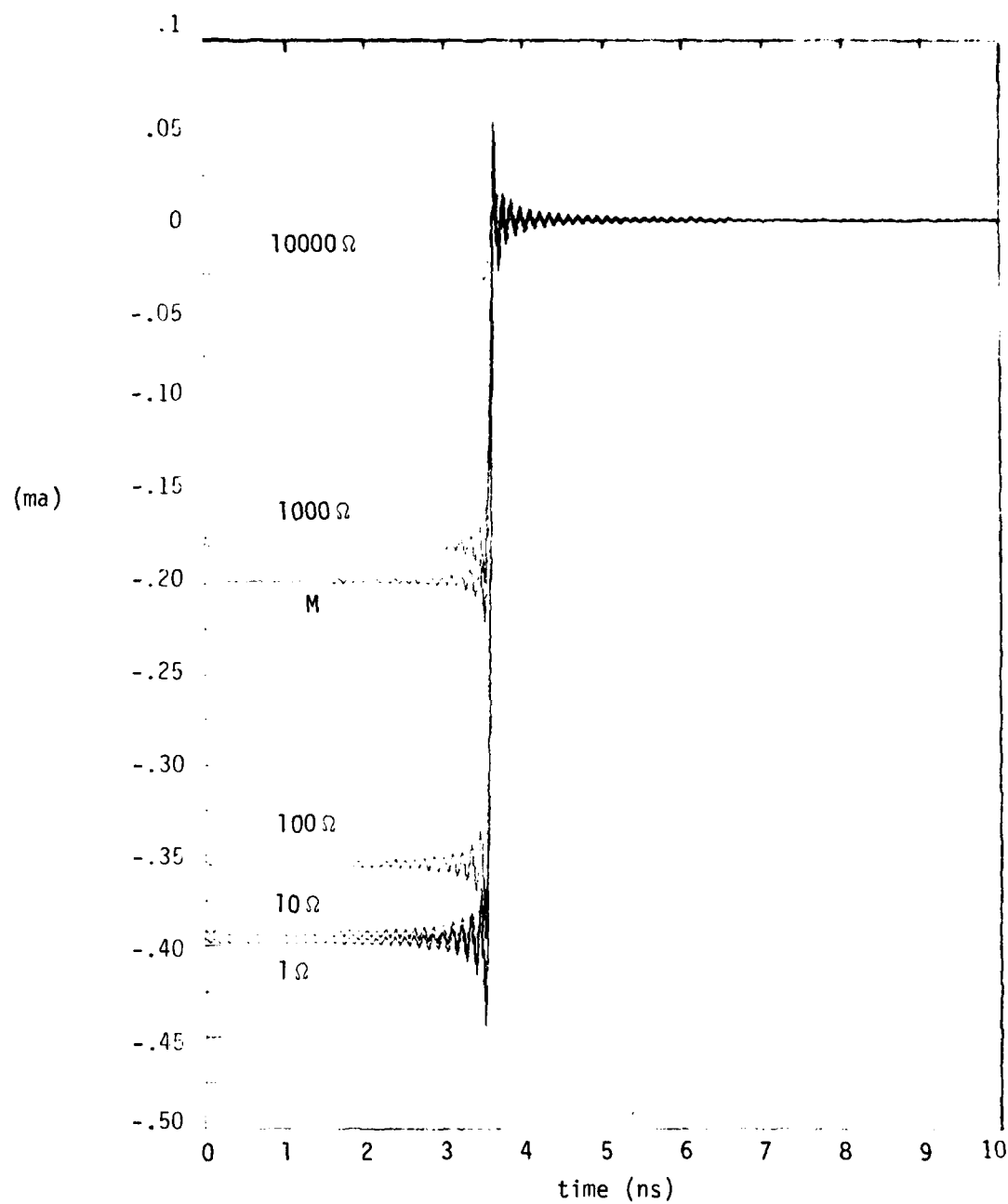


Figure 90. Plot of total transient current at $z=0$ for averaged (L'_{nm}) and (C'_{nm}) matrices.

It is useful to consider the effects that multivelocity waves have on the load current response. For the calculations shown in Figure 91, the transmission line modes were all assumed to have a velocity of 2.8×10^8 m/s, which is equivalent to the bulk mode in the first example. In addition, the characteristic-impedance matrix of the line was assumed to be unchanged. As in the previous cases, the load impedances were chosen to be diagonal with equal elements, except for the matched load case. From a careful inspection of the wire currents in Figures 91a through 91d, it is seen that the multivelocity effects showing in Figures 85a through 85d are no longer present. Figure 92 shows the resulting transient total current at the load, and it compares very closely to the total current in the multimode case.

It is often tempting to neglect completely the presence of the differential modes in a multiconductor line, either by assuming that all modes propagate with the same velocity as discussed above, or by using a single line assumption to be discussed in the next section. From the results just presented, it appears that neglecting the differential modes does not affect the individual currents drastically. It must be kept in mind, however, that the load configurations used in these cases are not general and, therefore, it is dangerous to draw general conclusions about the importance of these modes.

The fact of the matter is that under certain loading conditions, the differential modes can provide individual wire currents that are significantly larger than the total current. As an example, consider the transmission line of Figure 81 terminated with a load impedance given by

$$(Z_L^{(1)}) = \begin{bmatrix} 100 & .01 & 10^6 & 10^6 \\ .01 & 100 & 10^6 & 10^6 \\ 10^6 & 10^6 & 100 & 10^6 \\ 10^6 & 10^6 & 10^6 & 100 \end{bmatrix} \text{ Ohms}$$

Figures 93a through 93d show the transient load currents in each wire. Note that the currents in wires 1 and 2 are about three orders of magnitude larger than those of wires 3 and 4. Furthermore, the current

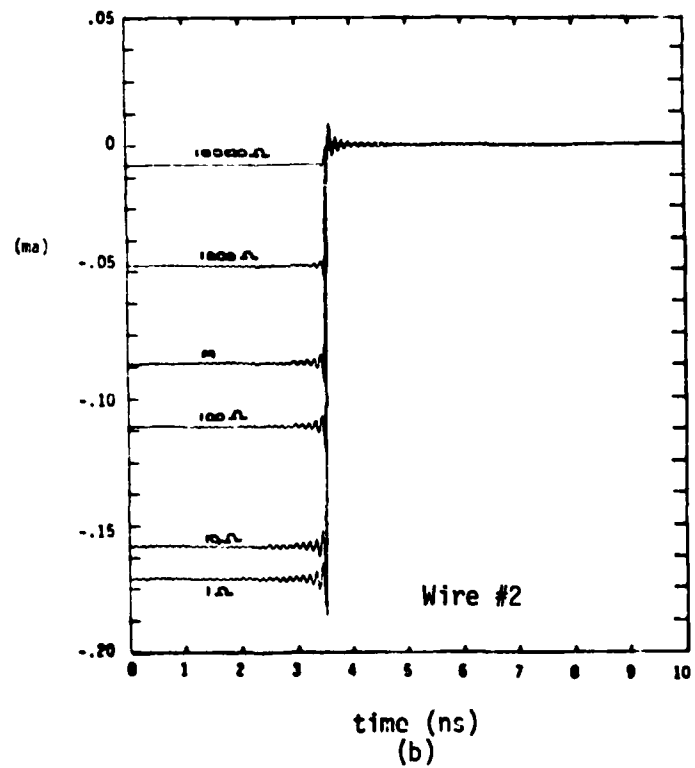
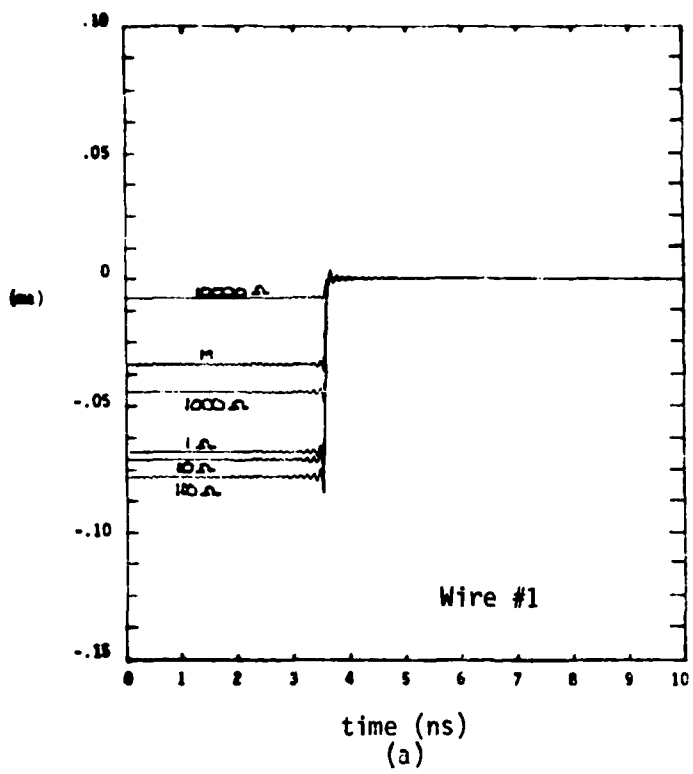


Figure 91. Plot of transient wire currents at $z=0$ for all modes having the same velocity.

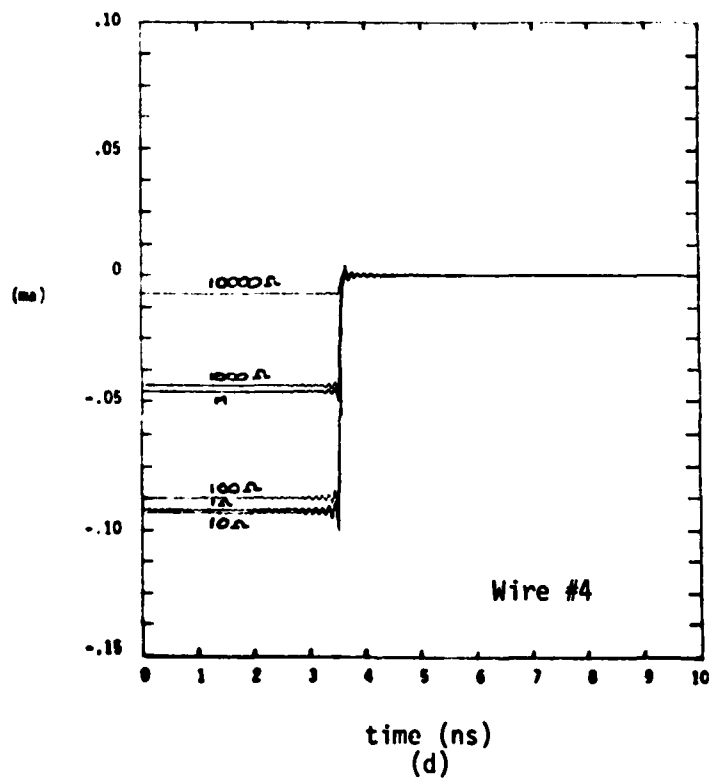
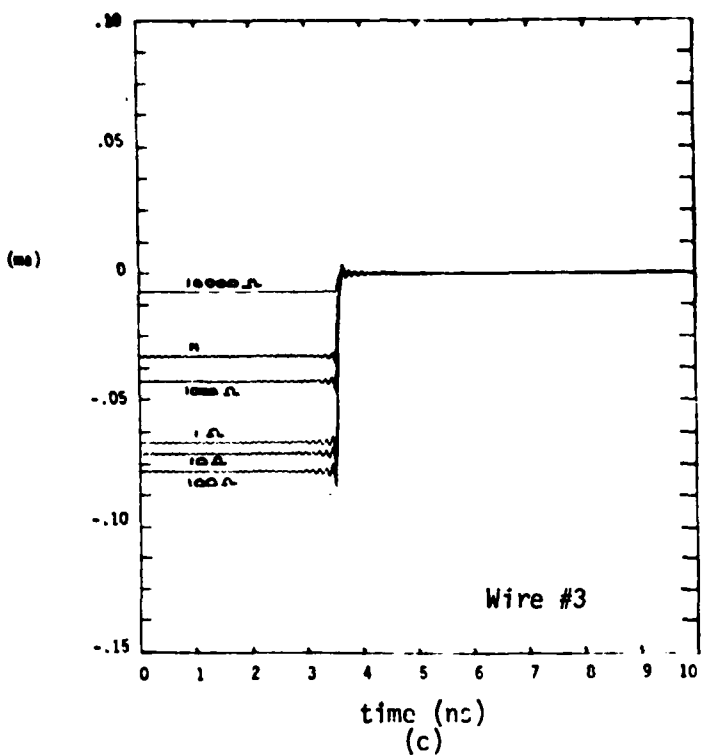


Figure 91 (concluded).

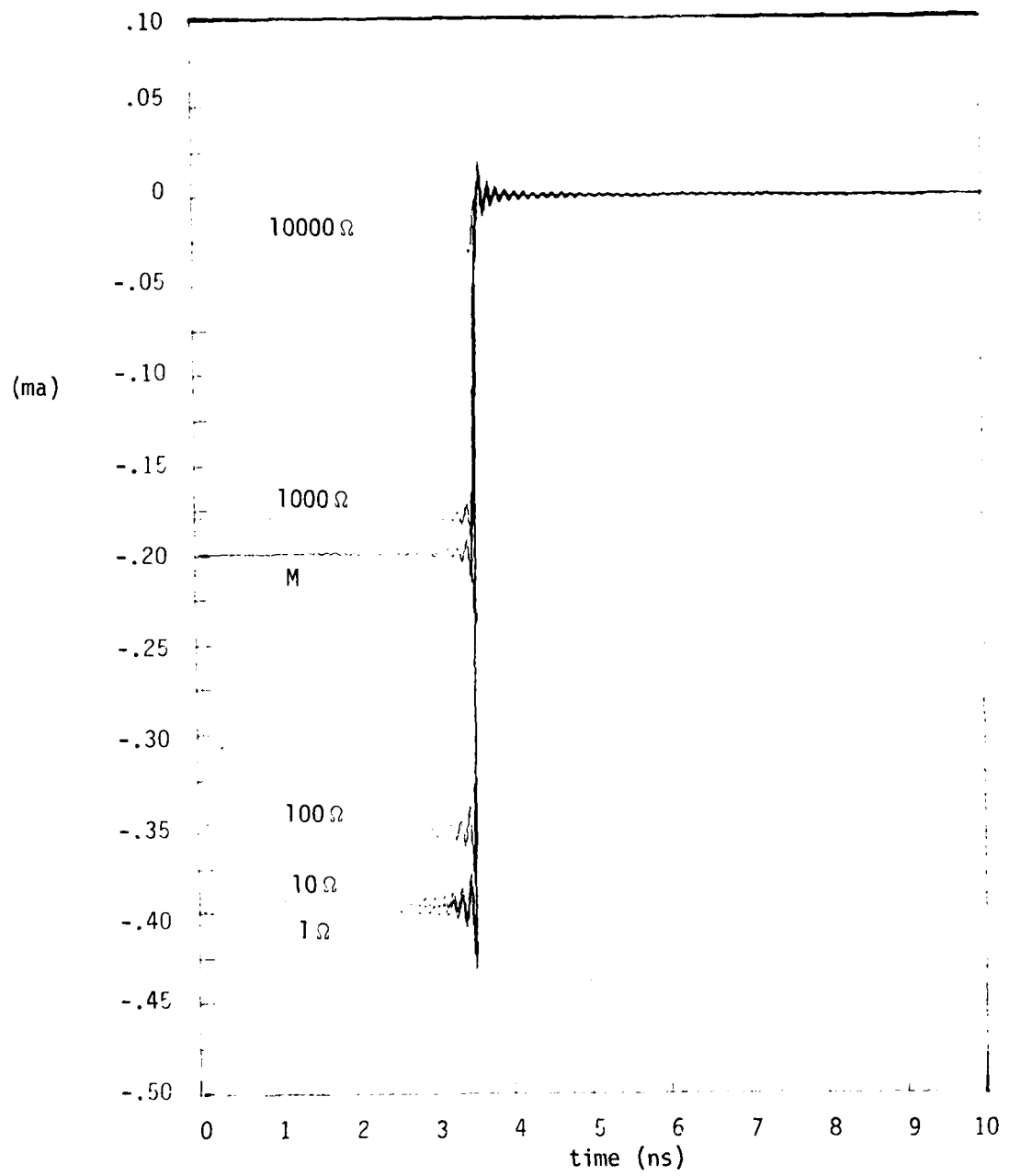


Figure 92. Plot of total transient load current at $z=0$ for all modes having the same velocity.

in wires 1 and 2 seem to be the negative of each other. Summing the total currents as in Figure 94 shows that the total current is about two orders of magnitude lower than the individual wire currents. This effect must be considered in using single wire cable models for EMP analysis.

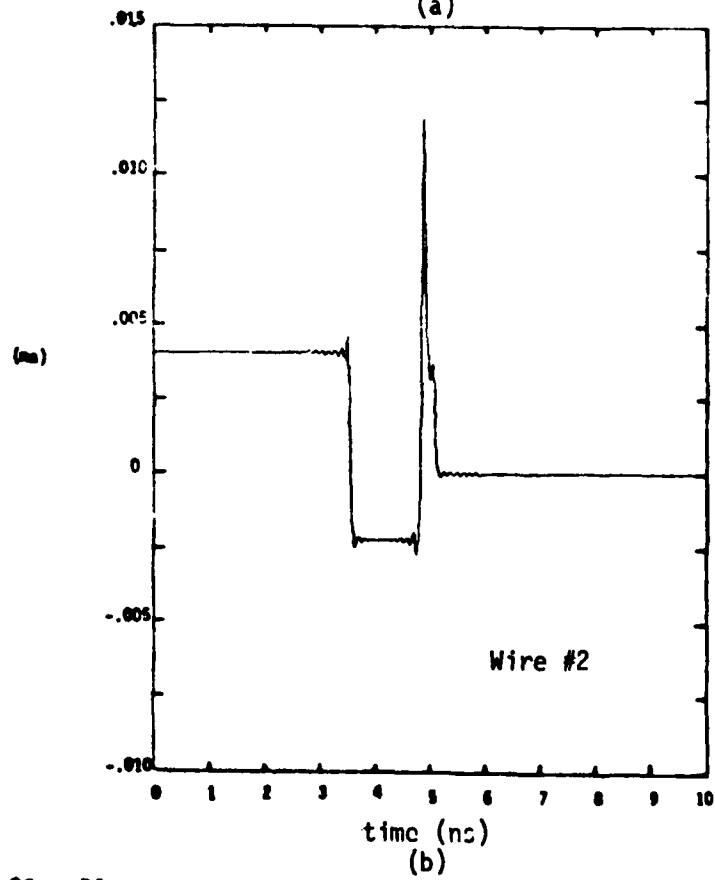
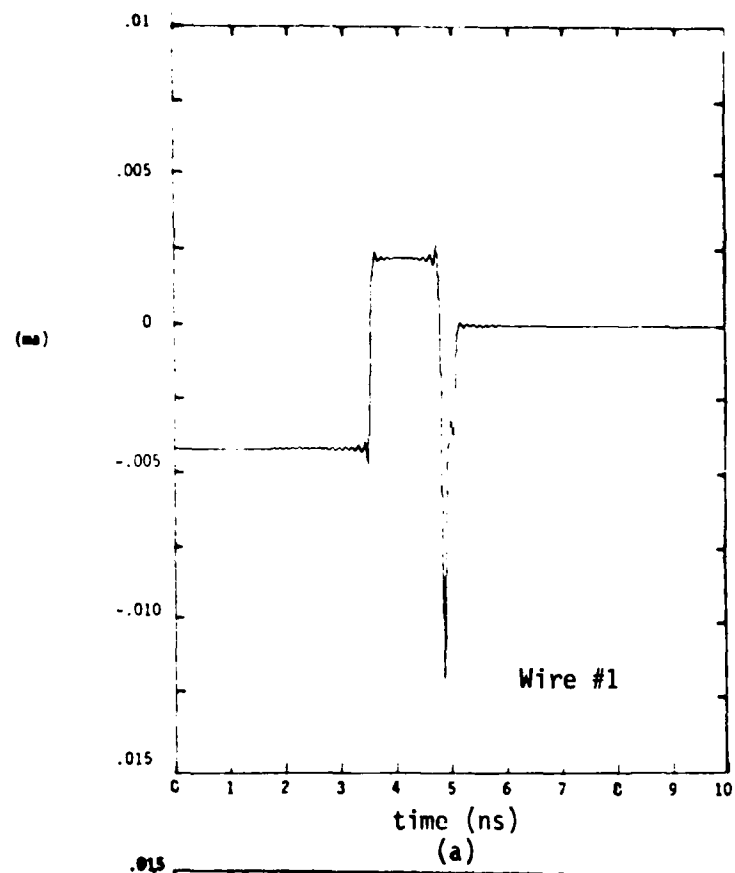


Figure 93. Plot of transient wire currents for unbalanced load.

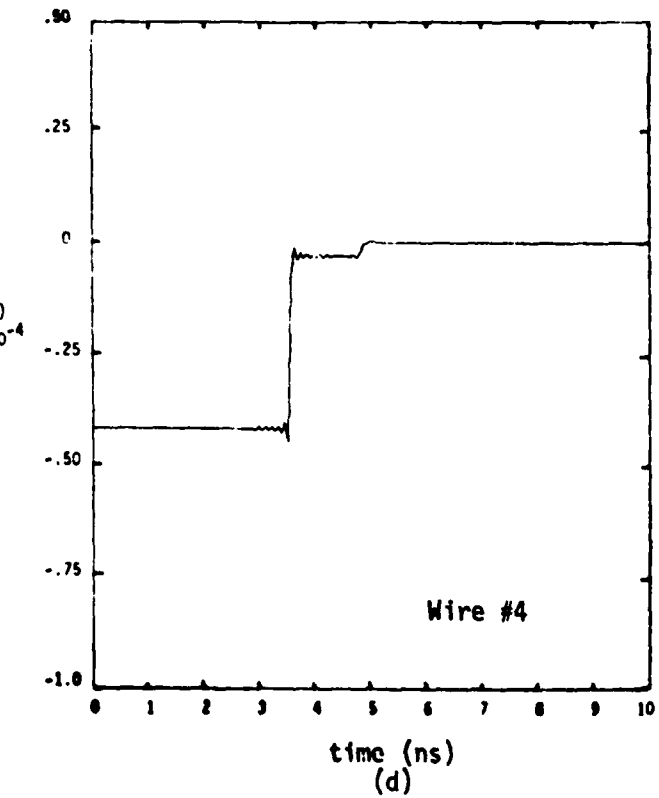
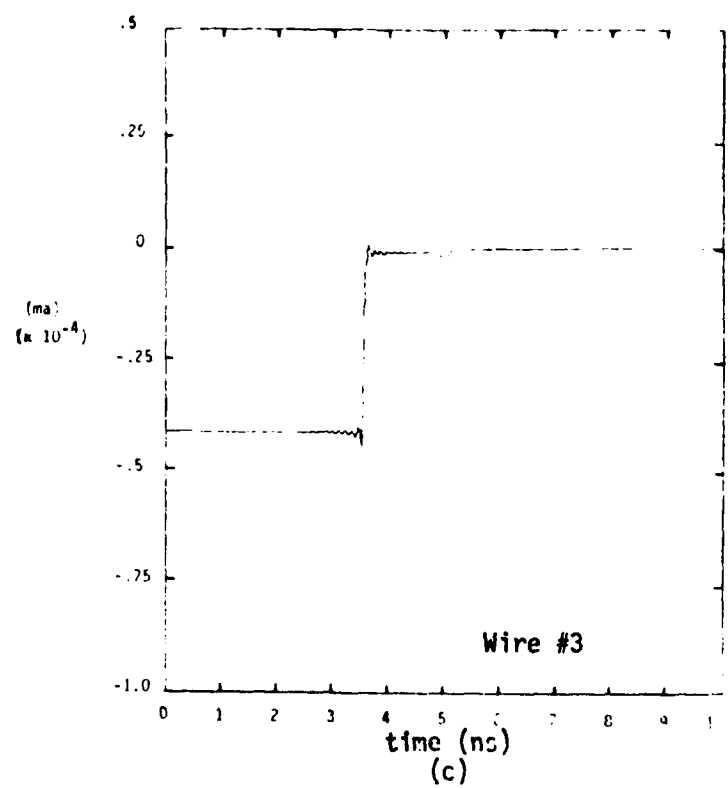


Figure 93 (concluded).

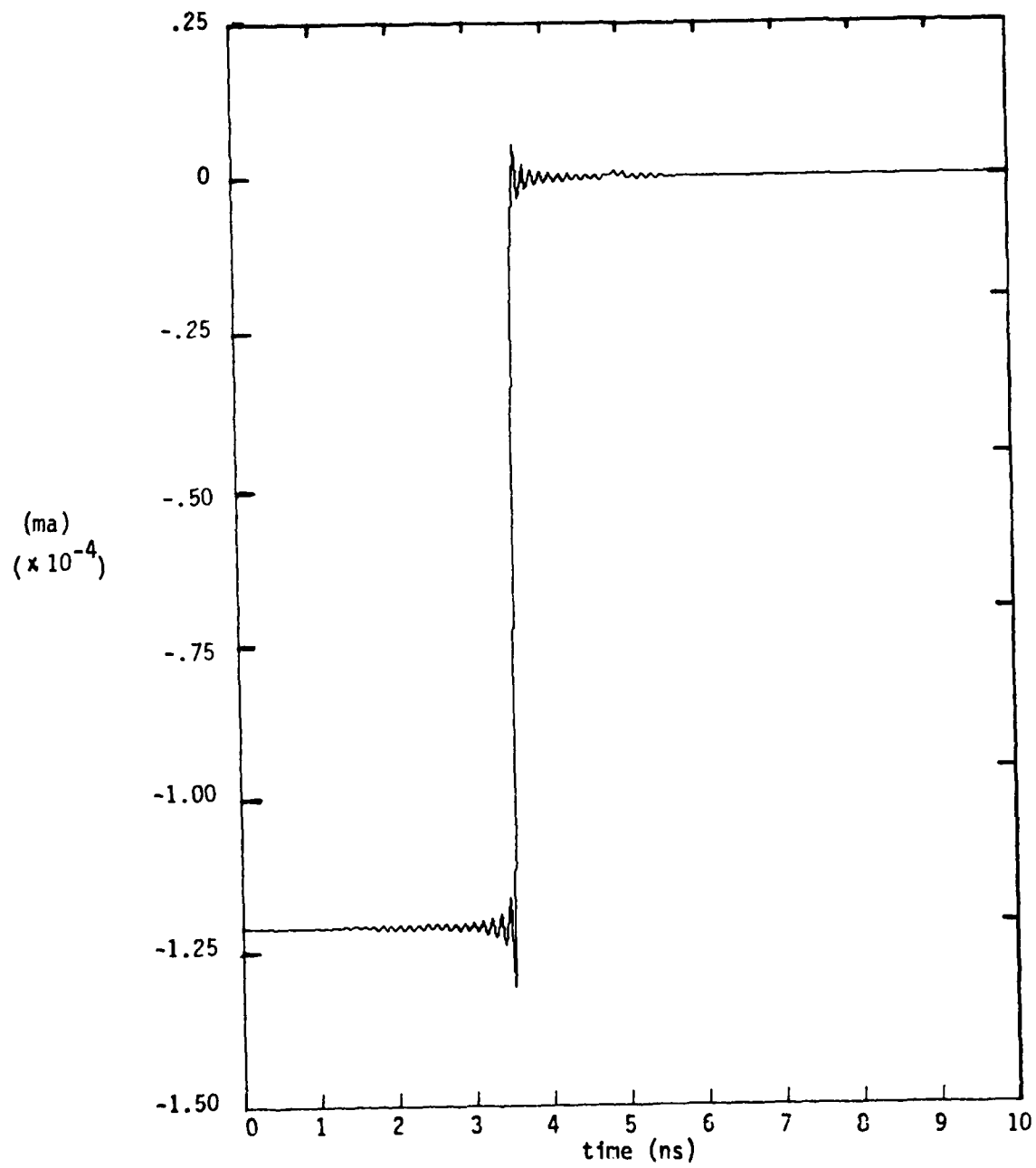


Figure 94. Plot of total transient load current at $z=0$ for case of unbalanced load impedance.

4. THE SINGLE LINE APPROXIMATION TO A MULTICONDUCTOR CABLE RESPONSE

A number of authors have discussed the possibility of describing the bulk current response on a multiconductor line in terms of a relatively simple calculation on a single wire (plus a reference) transmission line (Refs. 10, 19), and a procedure for calculating the common-mode (bulk) characteristics of a multiconductor line was discussed in Section III. Each author has developed a different approach in this modeling and, in this section, we examine the various assumptions in the modeling and the accuracies of the resulting solutions.

The method employed by Boeing (Ref. 19), and that which is used in the SNGLIN Code (Ref. 25), involves determining equivalent scalar capacitance and inductance parameters of the single wire line based on a knowledge of (L'_{nm}) and (C'_{nm}) matrices of the line. These are expressed as

$$L = \frac{L_{ii} + (n-1)L_{ij}}{n} = 7.37 \times 10^{-7} \text{ h} \quad (52)$$

$$C = \sum_{i=1}^n C_{ii} = 30.52 \times 10^{-11} \text{ f} \quad (53)$$

where L_{ii} is one of the diagonal terms of the (L'_{nm}) matrix, L_{ij} is the off diagonal term and C_{ii} is the diagonal term of (C'_{nm}) . Note that this analysis assumes a random cable lay so that the L' and C' matrices are relatively simple. Once these parameters are defined, the propagation velocity and the characteristic impedance on the line are determined as

$$v = (LC)^{-\frac{1}{2}} = 6.66 \times 10^7 \text{ m/s} \quad (54)$$

$$Z_c = (L/C)^{\frac{1}{2}} = 49.16 \Omega \quad (55)$$

In order to determine the field coupling to such a line, it is possible to use the average value of all of the field coupling parameters as the single line field coupling parameter. For this four wire-line, the resulting value is

$$|h| = 8.16 \times 10^{-2} \text{ meters} \quad (56)$$

These values must be used in conjunction with a knowledge of the load impedances on the multiconductor line. The SNGLIN approach suggests that the bulk mode load impedance, Z_L , be defined as

$$Z_L = \left(\sum_{i=1}^h \sum_{j=1}^h Y_{Lij} \right)^{-1} \quad (57)$$

where Y_{Lij} is the ij^{th} element of the load admittance matrix, defined as the inverse of the load impedance matrix. For the case of the matched load at $z = l$, the single line impedance is assumed to be equal to the line impedance.

Figure 95 shows the resulting transient current on the two-wire line using the above modeling assumptions. The form of the induced current is similar to that of the bulk current in Figure 87. Note, however, that the wave velocity is considerably slower than the actually observed bulk mode velocity shown in Figure 82. This gives rise to a considerably larger pulse width as observed at the load end.

In addition, the currents at the load are considerably higher than the actual bulk currents from the multiconductor analysis. Table 2 summarizes these results. For each of the diagonal multiconductor loads, the equivalent single line load impedance is calculated via Equation 57. The peak single line current is presented, along with a description of the percent error (defined as $(I_{\text{single line}} - I_{\text{BULK}})/I_{\text{BULK}} \times 100$) involved in using this model. Aside from the substantial error in propagation velocity, it is noted that considerable errors in the current can arise.

Another single wire model that has been suggested (Ref. 10) involves constructing a single-line characteristic impedance as

$$Z_c = \frac{\sum_{i=1}^n (z_{cij}) \cdot (\phi_{\text{BULK}})_j}{\sum_{j=1}^n (\phi_{\text{BULK}})_j} \quad (58)$$

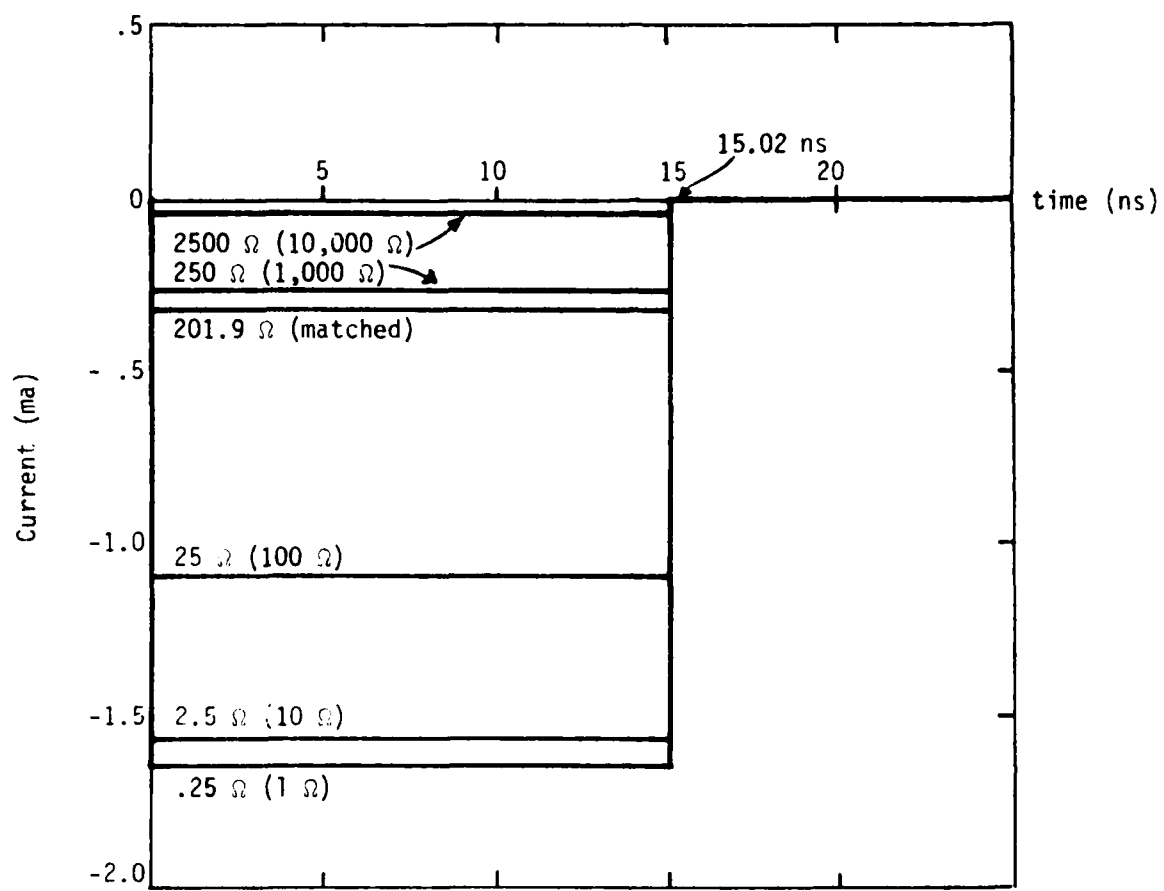


Figure 95. Plot of the time dependent single wire current at $z=0$, using SNGLIN (Ref. 25) modeling assumptions. The actual single line load impedances are indicated, and the multiconductor diagonal load impedances are shown in parenthesis.

Table 2
Summary of Single Wire Current Response Using S_NGLIN (Ref. 25)
Modeling Assumptions

Multiconductor Load Impedance (Diagonal) (Ohms)	Equivalent Single Line Load Impedance (0hms)	Single Line Current Reflection Coefficient	Single Line Current (ma)	Percent Error in Single Line Current
1	.25	.99	-1.65	315
10	2.5	.90	-1.58	301
100	25.0	.33	-1.10	209
Matched (not diagonal)	49.2	-.61	-.32	60
1000	2500.0	-.67	-.27	54
10,000	25000.0	-.96	-.03	20

where (ϕ_{BULK_j}) is the first (bulk) current mode and (Z_{cij}) is the characteristic impedance matrix of the line. Using the impedance matrix given in Section III and the modal distribution of Figure 82, we obtain a single line characteristic impedance of

$$Z_c = 202.62 \Omega \quad (59)$$

Also included in this analysis is the assumption that the propagation velocity of the single-wire line is identical to that of the bulk mode on the multi-conductor line. This is given by

$$v = 2.8 \times 10^8 \text{ m/s.} \quad (60)$$

From the usual relations for the line inductance and capacitance, the following single line quantities can be defined:

$$L = Z_c / v = 7.24 \times 10^{-7} \text{ H} \quad (61)$$

$$C = \frac{1}{Z_c v} = 1.76 \times 10^{-11} \text{ F} \quad (62)$$

The method for determining the equivalent load impedance as suggested in Reference 10 involves investigating the reflection coefficient matrix and inferring the equivalent reflection coefficient for the single wire line. This, along with knowledge of the characteristic line impedance, determines the load impedance. For a line whose propagation constants are distinct and with distinct eigenmodes, the reflection coefficient matrix for the current eigenmodes is given by

$$(o_{m_{ij}}) = (T_{ij})^{-1} (\rho_{ij}) (T_{ij}) \quad (63)$$

where (ρ_{ij}) is the reflection coefficient matrix for the physical currents on the line and is given by

$$(\rho_{ij}) = ((Z_{cij}) + (Z_{L_{ij}}))^{-1} \cdot ((Z_{cij}) - (Z_{L_{ij}})) \quad (64)$$

The first element of the modal reflection coefficient matrix, ρ_{m11} , determines how the bulk mode is reflected back at the load. Once this reflection coefficient is determined, the effective load impedance may be determined as

$$z_L = z_c \cdot \left(\frac{1 - \rho_{m11}}{1 + \rho_{m11}} \right) \quad (65)$$

As an example, for a 100 Ω diagonal load, the current reflection coefficient on this line is calculated from Equation 64 to be

$$(\rho_{ij}) = \begin{bmatrix} .11 & .27 & .28 & .16 \\ .27 & -.10 & .28 & .32 \\ .28 & .28 & -.11 & .31 \\ .16 & .32 & .31 & .04 \end{bmatrix} \quad (66)$$

and the matrix of eigenvectors, (T_{ij}) is

$$(T_{ij}) = \begin{bmatrix} .23 & -.85 & -.69 & .40 \\ .68 & .11 & 1.00 & -.76 \\ .62 & -.29 & .61 & 1.00 \\ 1.00 & 1.00 & -.91 & -.01 \end{bmatrix} \quad (67)$$

and its inverse is

$$(T_{ij})^{-1} = \begin{bmatrix} .38 & .39 & .39 & .40 \\ -.70 & -.07 & -.20 & .34 \\ -.36 & -.49 & .57 & .02 \end{bmatrix} \quad (68)$$

These when combined in Equation 63, gives the following modal reflection coefficient matrix:

$$(\rho_{mij}) = \begin{bmatrix} .76 & -.04 & -.02 & -.004 \\ -.39 & -.11 & .07 & .04 \\ -.04 & .09 & -.41 & .0004 \\ -.11 & .07 & -.008 & -.39 \end{bmatrix} \quad (69)$$

The ρ_{m11} element, having the value .76, is the reflection coefficient of the bulk mode, and when used in Equation 65 with the characteristic impedance of the single wire line, an effective load impedance of $Z_L = 27.6$ ohms is calculated.

Figure 96 shows the transient single line current for the same load configurations as in the previous cases, using the modeling concepts just described. Note that for this case the single line velocity is constrained to be identical to that of the bulk mode on the multiconductor line, thereby insuring that the time scales in Figure 96 agree with those of Figure 87. Furthermore, the peak values of the line currents agree extremely well with those of the bulk mode. Table 3 summarizes these results by showing the reflection coefficient, single line load impedance, resulting single line current and percent error of this current relative to the multiconductor bulk current. As may be noted, the error in the current is considerably lower than in the case using the SNGLIN modeling assumptions.

A third method for determining the equivalent single line properties was discussed in Section III. It was suggested that a single line impedance be determined by

$$Z_C = \left(\sum_{i,j=1}^n (Z_{cij})^{-1} \right)^{-1} \quad (70)$$

and the single line velocity be that of the multiconductor bulk mode.

Inverting the (Z_{cij}) matrix given in Section III gives the following

$$(Z_{cij})^{-1} = \begin{bmatrix} 10.3 & -4.50 & -4.93 & -.23 \\ -4.50 & 17.7 & -5.19 & -6.80 \\ -4.93 & -5.19 & 18.2 & -6.65 \\ -.23 & -6.80 & -6.65 & 15.3 \end{bmatrix} \times 10^{-3} \text{ mhos} \quad (71)$$

Equation 70 then yields the single line impedance

$$Z_C = 204.08 \Omega \quad (72)$$

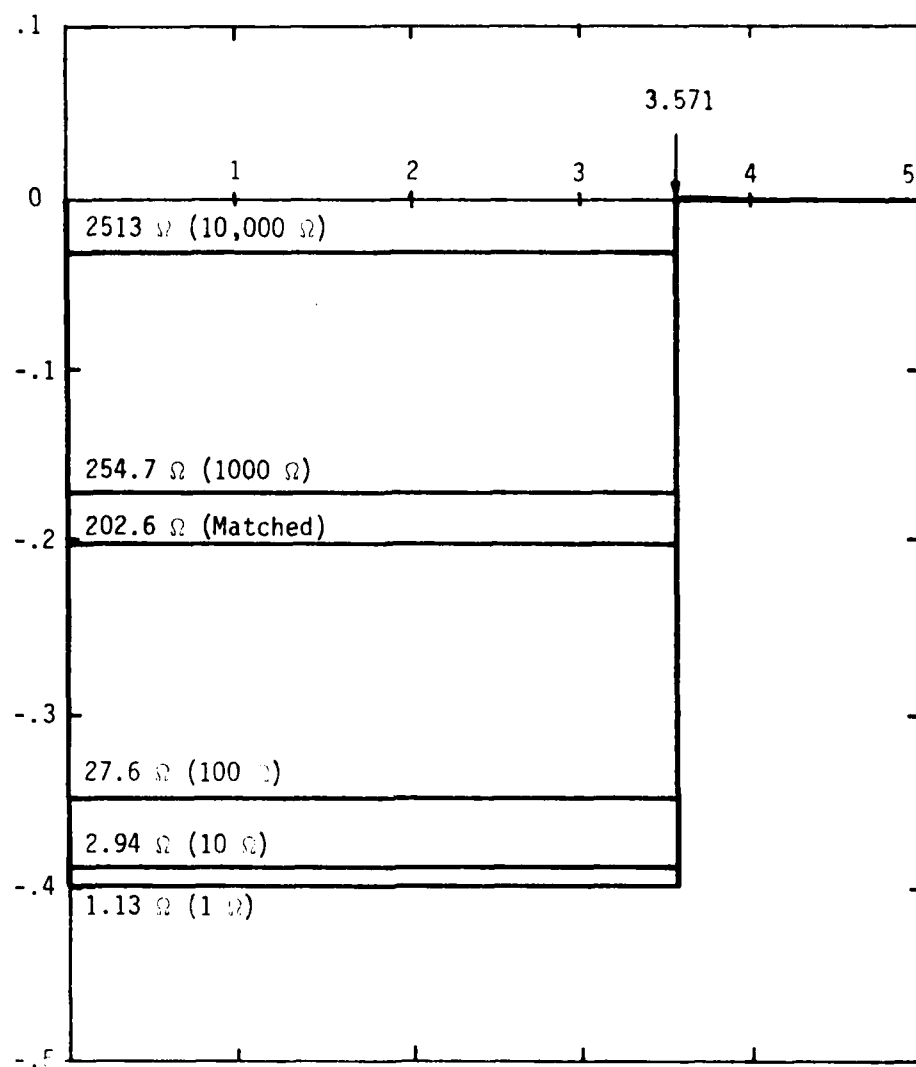


Figure 96. Plot of the time dependent, single wire current at $z=0$, using reflection coefficient modeling assumptions (Ref. 10). The actual single line impedance is indicated, and the diagonal multiconductor load impedance is shown in parenthesis.

Table 3
Summary of Single Wire Current Response Using
Reflection Coefficient Modeling Assumptions (Ref. 10)

Multiconductor Load Impedance (Diagonal) (Ohms)	Bulk Mode Current Reflection Coefficient (same as single line)	Equivalent Line Load Impedance (Ohms)	Single Line Current (ma)	Percent Error in Single Line Current
1	.99	1.13	-.400	.5
10	.97	2.94	-.395	.25
100	.76	27.6	-.354	.28
Matched (not diagonal)	0	202.6	-.201	0
1000	-.11	254.7	-.178	.66
10,000	-.85	2513.0	-.030	4.7

which is considerably different from line characteristic impedance calculated by the SNGLIN method, and agrees well with the impedance calculated using the modal concepts.

The computed values for single line impedance and capacitance are then given by

$$L = Z_C/v = 7.29 \times 10^{-7} \text{ h} \quad (73)$$

$$C = \frac{1}{Z_C v} = 1.75 \times 10^{-11} \text{ f} \quad (74)$$

which are again very close to those calculated from the modal method.

The equivalent load impedance may be defined as in Equation 57 and with these values, it is possible to compute the transient load current. The calculation produces results almost identical to those illustrated in Figure 96. Table 4 summarizes these results.

5. CONCLUDING REMARKS

This section has presented the results of a numerical study of a four-wire multiconductor transmission line under various loading configurations, and with various assumptions made regarding the multimode propagation on the line. From this study, a number of important conclusions can be drawn:

1. The effects of the differential modes (for the special case of diagonal loads) on the total current response of a multiconductor line are small.
2. The differential modes have the potential of being much larger than the bulk mode, thereby causing individual wire currents which are much larger than the total current.
3. If one is interested in only the bulk current response of a multiconductor bundle, a single line model yields accurate results, if the load impedance is calculated using the reflection coefficient method suggested in Reference 10.
4. The SNGLIN modeling assumptions for single wire lines provides results which have large errors, both in magnitude and in propagation times.

Table 4
Summary of Single Wire Response Using Common Mode
Impedance Assumptions of Section III

Multiconductor Load Impedance (Diagonal (0hms)	Equivalent Line Load Impedance (0hms)	Single Line Current Reflection Coefficient	Single Line Current (ma)	Percent Error in Single Line Current
1	.25	.99	-.401	.75
10	2.5	.98	-.392	.50
100	25.0	.78	-.356	.28
Matched (not diagonal)	32.05	.0	-.199	.99
1000	250	-.10	-.179	.11
10,000	2500	-.85	-.031	1.5

Not included in this study is an examination of an unbalanced load, with the assumption of equally propagating modes. It is suggested that this case be studied to see if large individual wire currents and a small bulk current will also exist on this type of line.

SECTION VII

CONCLUSIONS AND OBSERVATIONS

The experimental and analytical transient and CW responses of a B-52 multiconductor cable were studied in this report. A replica of the B-52 multiconductor cable was tested in a laboratory environment. A comparison between the measurement results obtained on the aircraft and laboratory cable was presented. The comparisons between the analytical and the measured results were also presented in Section V.

Only common-mode propagation on the multiconductor line was studied in this report. In Section VI, validity of common-mode representation of the multiconductor line was discussed. Several methods used to determine the single-line characteristics of the line and the equivalent single-line loads were studied in Section VI.

The cable was excited in the common-mode by exciting all the wires with identical voltages. Three different models were considered in the laboratory. The first model was an attempt to model the aircraft cable in the laboratory as close as possible by modeling the discontinuities such as metallic ribs, cable clamps, bulkheads, etc. This model was driven in the same manner as the aircraft cable. The second cable model was the same as the first model, except that the two grounding wires were removed. This simplification allowed the line to be treated as a four-wire line over a ground plane, rather than a six-wire line over a ground plane, where one of the wires was used as a reference conductor. The third model was a simplified version of the second model consisting of eight uniform sections, each containing only periodic discontinuities.

Along some sections of the cable, the discontinuities are periodic. A transmission line loaded at periodic intervals is referred to as a periodic structure. Periodic structures have two basic properties, namely, 1) passband stopband characteristics, and 2) the support of waves with phase velocities less than the velocity of light. Metallic ribs and

clamps essentially add a shunt capacitance at periodic intervals to the smooth line, without affecting the per-unit-length inductance of the line. Thus the sections of a line, where discontinuities occur at periodic intervals, can be treated as periodic structures, thereby reducing the computational effort. The method for the determination of the characteristics of the periodically loaded line is described in Section III.

In Section III, experimental and numerical methods were presented for the calculation of the common-mode characteristic impedance of the multi-conductor transmission line. The difference between the calculated and measured common-mode characteristic impedance of the four-wire line over a ground plane was only 3.8 percent. In the calculation of the common-mode characteristic impedance of the multiconductor line, the medium surrounding the conductors was assumed to be homogeneous. It was observed in Section III that if the height of the cable above the ground plane is large compared to the equivalent radius of the cable, the common-mode characteristic impedance of the cable, calculated with the assumption of the homogeneous medium, is very close the actual value for the cable. To calculate the common-mode characteristic impedance (or the characteristic-impedance matrix of the multiconductor line) more accurately, existing codes will have to be modified, or new codes developed. If the height of the cable above ground is not large compared to the radius of the cable, large errors may be expected.

A comparison of measured results on the aircraft and in the laboratory was presented in Section IV. It was observed in that section that the pulse becomes more dispersive as it travels down the line, indicating the presence of losses on the line. The decrease in amplitude of the pulse occurs as a result of reflections along the line due to discontinuities, and the losses on the line. It was concluded that the location of the discontinuities cannot be readily determined from the transient current response of the line. This is due to the fact that there are a large number of closely spaced discontinuities and the reflections from both sides of the measurement point compound the problem even further.

A comparison of the transient response between aircraft cable and the laboratory models, shows that when the peak currents are of major interest (i.e., for the determination of the damage to the circuit elements due to the EMP) the aircraft cable may be modeled by the four-wire cable model, or slightly more accurately by the simulated cable. It was observed in Section IV, that the discrepancies between the aircraft cable data and the laboratory cable model data are primarily due to the discontinuities and structures which were not modeled in the laboratory. The effect of other cables running parallel to the test cable and bundled together when passing through bulkhead penetrations was studied in Section IV. It was observed that the amplitude of the pulse was reduced when the other cables are in close proximity, indicating the coupling of the energy to those cables. Comparisons show improved agreement between the laboratory data and the aircraft data as the other cables are brought into proximity in the laboratory, simulating the aircraft environment more closely. It was further observed that if the other cables are further than six inches from the test cable, the transient response of the cable is not appreciably affected by their presence. Thus we need only consider those cables which are within six inches of the cable of interest.

A look at the frequency-domain data reveals that the attenuation increases as we move towards the load end and is higher at higher frequencies. Comparison between the simulated cable and four-wire model data are only slightly different from each other, indicating that the aircraft cable may be reasonably modeled by the four-wire cable. The discrepancies between the aircraft and simulated cable data are higher above 40 MHz. Comparisons between the simplified cable and the simulated cable response is not as good. Thus to model the aircraft cable more accurately, the four-wire cable model or the simulated cable model should be employed.

Analytical modeling of the multiconductor line was presented in Section V. An attempt was made to reasonably model the complex aircraft cable. In this modeling, the cable bundle is represented by a single-wire transmission line above a ground plane. An equivalent radius was

established that gives the same characteristic impedance of the line as the common-mode (bulk current) impedance of the multiconductor cable. The single-wire line was modeled by a varying degree of complexity to observe the trade-off between modeling details and accuracies. The following six cases were studied:

1. A uniform line terminated by 50Ω resistances
2. A line with one characteristic impedance and 98 capacitances, each capacitance has the same value ($C = 6.3 \text{ pF}$). The number 98 corresponds to the number of cable clamps and/or ribs.
3. A line with one characteristic impedance and 6 divisions. Within each division, the capacitance values are the same. There are altogether 98 capacitances.
4. A line with 6 divisions, within each division, the capacitance values are the same. Capacitance values and characteristic impedances of different divisions may be different.
5. Same as 4, except there are 7 capacitances being added to model the bulkheads, where the capacitance value is 10 pF .
6. Same as 5, except the extra capacitance values are 15 pF .

From the study of the above six cases it was concluded that

- a. It is necessary to include losses in the model,
- b. To obtain very accurate results, it is necessary to model in great geometrical detail, and have very accurate capacitance values,
- c. For moderate accuracy (within a few dB), the results of case 2 is quite adequate.

Various assumptions made in modeling multiconductor transmission lines by a single-wire transmission line and the accuracies of the resulting solutions were discussed in Section VI. The method employed by Boeing (Ref. 19), and that which is used in the SNGLIN code (Ref. 25), gives the

wave velocity which is considerably slower than the actually observed bulk (common) mode velocity and gives rise to a considerably larger pulse width as observed at the load end. In addition, the currents at the load are considerably higher than the actual bulk currents from rigorous multi-conductor analyses. Table 2 shows that depending on the size of the load, the errors could be very large. On the other hand, the methods employed in Reference 10 and in Section III give rise to the propagation velocity of the bulk mode and the load currents very close to those rigorously calculated. If one is interested in only the bulk current response of a multiconductor line, a single-line model yields accurate results, provided that the characteristic impedance is calculated using the modal method suggested in Reference 10, or the method described in Section III.

The results of a numerical study of a field-excited four-wire multi-conductor transmission line under various loading configurations were also presented in Section VI. Although the individual wire currents are often of interest in trying to understand how a complicated system will respond to an EMP, it is practically impossible to carry out a detailed multiwire analysis on a large cable network. In such cases, interest is focused on the "total" current or common-mode response of the cable. It was observed in Section VI that the effects of the differential modes (for the special case of diagonal loads) on the total current response of a multiconductor line are small, since the sum of each differential mode is almost zero, and the total current on the line is described primarily by the common mode. It was noted, however, that under certain loading conditions, the differential modes can provide individual wire currents that are significantly larger than the total current.

REFERENCES

1. Tesche, F. M. and T. K. Liu, "User Manual and Code Description for QV7TA: A General Multiconductor Transmission-Line Analysis Code", AFWL Interaction Application Memos, Memo 26, Kirtland Air Force Base, New Mexico, August 1978.
2. Agrawal, A. K., H. J. Price, and S. H. Gurbaxani, "Transient Response of Multiconductor Transmission Lines Excited by Nonuniform Electromagnetic Field", AFWL Interaction Notes, Note 367, Kirtland Air Force Base, New Mexico, July 1969.
3. Tesche, F. M., T. K. Liu, S. K. Chang, and D. V. Giri, "Field Excitation of Multiconductor Transmission Lines", AFWL-TR-78-185, Kirtland Air Force Base, New Mexico, February 1979.
4. Fowles, H. M., L. D. Scott, A. K. Agrawal, and K. M. Lee, Aircraft Cable Parameter Study, AFWL-TR-77-177, Air Force Weapons Laboratory, Kirtland Air Force Base, New Mexico, July 1977.
5. Fowles, H. M., A. K. Agrawal, L. D. Scott, and L. T. Simpson, Experimental Methods for the Characterization of Multiconductor Cable Systems, AFWL-TR-78-82, Air Force Weapons Laboratory, Kirtland Air Force Base, New Mexico, March 1979.
6. Agrawal, A. K., K. M. Lee, L. D. Scott, and H. M. Fowles, "Experimental Characterization of Multiconductor Transmission Lines in the Frequency Domain", AFWL Interaction Notes, Note 311, June 1977; also published as IEEE Trans. EMC, Vol. EMC-21, No. 1, pp. 22-27, February 1979.
7. Agrawal, A. K., H. M. Fowles, and L. D. Scott, "Experimental Characterization of Multiconductor Transmission Lines in Inhomogeneous Media Using Time Domain Techniques", AFWL Interaction Notes, Note 332,; also published as IEEE Trans. EMC, Vol. EMC-21, No. 1, pp. 28-32, February 1979.
8. Agrawal, A. K., H. M. Fowles, L. D. Scott, and S. H. Gurbaxani, "Application of Modal Analysis to the Transient Response of Multiconductor Transmission Lines with Branches", IEEE Trans. EMC, Vol. EMC-21, No. 3, pp. 256-262, August 1979.
9. Chang, S. K., F. M. Tesche, T. K. Liu, and D. V. Giri, Transient Analysis of Multiconductor Transmission Line Networks: A Comparison of Experimental and Numerical Results, AFWL-TR-78-152, Air Force Weapons Laboratory, Kirtland Air Force Base, New Mexico, February 1979.

10. Tesche, F. M. and T. K. Liu, "Selected Topics in Transmission-Line Theory for EMP Internal Interaction Problems", AFWL-TR-77-73, Air Force Weapons Laboratory, Kirtland Air Force Base, New Mexico, August 1977.
11. Coen, S., T. K. Liu, and F. M. Tesche, Calculation of the Equivalent Capacitance of a Rib Near a Single-Wire Transmission Line, AFWL-TR-77-60, Air Force Weapons Laboratory, Kirtland Air Force Base, New Mexico, February 1977.
12. Tesche, F. M. and T. K. Liu, "An Electrical Model for a Cable Clamp on a Single-Wire Transmission Line", AFWL-TR-76-325, Air Force Weapons Laboratory, Kirtland Air Force Base, New Mexico, December 1976.
13. Collin, R. E., Foundations for Microwave Engineering, McGraw-Hill, 1966.
14. Feather, A. E. and C. R. Paul, Computation of the Capacitance Matrices for Ribbon Cables, RADC-TR-76-101, Volume II, Rome Air Development Center, New York, April 1976.
15. Chang, S. K., T. K. Liu, and F. M. Tesche, "Calculation of the Per-Unit-Length Capacitance Matrix for Shielded Insulated Wires", AFWL Interaction Notes, Note 319, Air Force Weapons Laboratory, Kirtland Air Force Base, New Mexico, April 1977.
16. Agrawal, A. K., CAPCODE User's Manual, Mission Research Corporation, AMRC-R-131, Albuquerque, New Mexico, May 1978.
17. Baum, C. E., T. K. Liu, F. M. Tesche, and S. K. Chang, "Numerical Results for Multiconductor Transmission Line Networks", AFWL-TR-77-123, Air Force Weapons Laboratory, Kirtland Air Force Base, New Mexico, June 1977.
18. Bevensee, R. M., et al, "Computer Codes for EMP Interaction and Coupling", IEEE Trans. EMC, Vol. EMC-20, No. 1, pp. 156-165, February 1978.
19. "Common Mode Model Development for Complex Cable Systems", Boeing Report D224-10015-4, under Contract F29601-72-C-0028, June 1973.
20. Baum, C. E., T. K. Liu, and F. M. Tesche, "On the General Analysis of Multiconductor Transmission Line Networks", AFWL Interaction Notes, Note 350, November 1978.
21. Frankel, S., Multiconductor Transmission Line Analysis, Artech House, Dedham, Massachusetts, 1978.

REFERENCES (Concluded)

22. Paul, C. R., "On Uniform Multimode Transmission Lines", IEEE Trans. MTT, Vol. MTT-21, pp. 556-558, August 1973.
23. Lee, K. S. H., Editor, EMP Interaction: Principles, Techniques and Reference Data, Air Force Weapons Laboratory, AFWL-TR-79-403, December 1979.
24. Lee, K. S. H., "Two Parallel Terminated Conductors in External Fields", IEEE Trans. EMC, Vol. EMC-20, No. 2, pp. 288-296, May 1978.
25. "SNGLIN Program Manual", Boeing Report D224-13072-1, May 1975.

APPENDIX A

DETAILED DESCRIPTION OF THE CLAMPING LOCATIONS ON THE
AIRCRAFT CABLE AND THE LABORATORY CABLE MODEL

1. DETAILED DESCRIPTIONS OF THE AIRCRAFT CABLE CLAMPING LOCATIONS

STATION NUMBERS

648.9 The cable begins at this point and is connected to the EMP hydraulic pump #1 relay on the back of engine #1 generator power box (A181). There is a major structural girder 7" below the power box, extending 8" out from the skin. The cable leaves the relay in a large bundle and runs 12" straight back to a rib 3" high and 2" wide. At this point the cable is clamped to the rib and branches out from the bundle.

658 The cable is clamped on a 3" high by 2" wide rib, and is 3" and 7" away from the skin and the girder, respectively. There are other bundles of cables running parallel on either side of the cable 1" to 3" away.

658-667 Between these stations the cable runs about 1" below a flat metal plate which has several large cutouts. At station 666 the cable branches into a large bundle and is clamped. At this point the cable is 3.75" away from the skin.

667 The cable runs over the top of a 3" by 2" rib. There is a 1" spacing between the cable and rib. The cable then runs up along the aft side of the rib for 27". The cable is clamped at two places along the 27" run on stand-offs, 1.5" away from the skin and 2" above the rib. The two points are 2" from the top and bottom of the 27" run. Along the run there are other cables running parallel to the cable within 0.5".

676 The cable is clamped on a 3" by 2" rib. There are other cables running parallel to the cable within 2".

685 At this point there is a support that comes out from a 3" high and 2" wide rib. The cable branches into a large bundle and is clamped on the support 5" away from the skin.

STATION
NUMBERS

694 The cable runs from 685 to the complete bulkhead at 694, and passes through a 3" long by 1.5" high oval hole. The center of the hole is 9" away from the bottom of the fuel tank and 9" away from the skin. The cable is bundled together with a large bundle on the aft side of the bulkhead. The bundle extends for 10" on the wheel well side of the bulkhead.

698.5 A small support comes out from the bulkhead to which the cable is clamped. At this point the cable is in a large bundle and is 7", 5" and 11" away from the skin, bulkhead, and the bottom of the fuel tank, respectively.

705 The cable is in a large bundle. The clamp is on a stand-off which is in turn attached to a 2.75" by 1" rib. The clamp is 5.5", and 11" away from the skin and the bottom of the fuel tank, respectively. (After this point all ribs are 2.75" high and 1" wide unless otherwise noted. All standoffs have shafts of $\frac{1}{4}$ " O.D. Al. rod.)

715 The cable is in a large bundle and clamped to a rib. The clamp is 3" and 9.5" away from the skin and the bottom of the fuel tank, respectively. At this point a large structural girder extends 11.5" below the bottom of the fuel tank and 21" away from the skin.

725 The cable is in a large bundle clamped on a 2.75" by 1" rib. The clamp is 3", 7.75", and 18" away from the skin, the bottom of the fuel tank, and the girder, respectively.

733 The cable branches out of the bundle, and is clamped on a standoff on the bottom of the fuel tank. The clamp is 2.5" and 9", repectively, away from the bottom of the fuel tank and the skin. There are other cables running parallel to the cable within 3".

STATION
NUMBERS

754 Same as 733 except clamp is 2.5" and 8" away from the bottom of the fuel tank and the skin, respectively.

763 Same as 754.

773 Standoff on top of small metal support. The clamp is 4" and 7" away from the bottom of the fuel tank and the skin, respectively.

793 There is a metal structure that comes out from the skin between stations 795 and 800. The cable is 2" away from the bottom of it. At Station 793 the cable is clamped on a standoff 2.5" away from the bottom of the fuel tank and 7" away from the skin. At Station 795 the cable branches into a large bundle.

805 Station 805 is a partial bulkhead. The cable passes through the bulkhead in a large bundle. The clamp is on the aft side of the bulkhead, positioned in the center of the hole. The hole is 2" in diameter, and 1" away from the bottom of the fuel tank and 12" away from the skin. On the aft side of the bulkhead the girder extending down from the fuel tank now extends 14" down and is still 21" away from the skin.

810 There is a large girder support 1" wide. The cable at 810 is 0.25" from the support, 10" and 4" away from the skin, and the bottom of the fuel tank, respectively.

813.3 The cable is clamped on a standoff to the bottom of the fuel tank. The clamp is 4.25" and 6.75", respectively, away from the bottom of the fuel tank, and the skin. There are also other cables running parallel within 3" of the cable.

830.9 Same as 813.3 except the clamp is 3.75" and 6.5", respectively, away from the bottom of the fuel tank and to the skin.

STATION
NUMBERS

849.5 Same as 830.9 except clamp is 2.75" and 5.75" away from the bottom of the fuel tank and to the skin, respectively.

860.8 There is a large girder support which is 3" wide. At 860.8 the cable is 0.75", 2.75" and 5.75" away from the support, the bottom of the fuel tank, and the skin, respectively. There is no clamp.

868.1 Same as 849.5.

886.7 Same as 830.9 except the clamp is 3" and 7" away from the bottom of the fuel tank and the skin, respectively.

907.3 Same as 886.7.

917 There is a partial bulkhead. The cable branches into a large bundle at station 911, and branches out of the bundle at station 921. The cable passes through a 2" diameter hole in the bulkhead which is 2.5" and 12" away from the bottom of the fuel tank and the skin, respectively. The bundle is clamped on the aft side of the bulkhead.

925.8 The cable is clamped on a standoff. The clamp is 3" and 7" away from the bottom of the fuel tank and the skin, respectively. There are again other cables running parallel within 3" of the cable.

944.2-1017.8 Stations 944.2, 962.6, 981, 999.4, and 1017.8 on the same as 925.8.

1028 On the forward side of the bulkhead the cable is clamped at two places on the bulkhead with standoffs. At the first clamp the cable branches into a large bundle. The clamp is 2", 4" and 8.5" away from the bulkhead, the bottom of the fuel tank and the skin, respectively. The second clamp is 16", 14" and 1.5" away from the bottom of the fuel

STATION
NUMBERS

tank, the skin, and the bulkhead, respectively. The cable bundle then passes through the bulkhead, and is clamped on the aft side. The hole is 2" in diameter and is centered 13.5" and 21.5" away from the skin and the bottom of the fuel tank, respectively.

On the aft side of the bulkhead the cable runs over the top of a small girder on the bulkhead which is 2" wide, 4" high, and 8" to the edge of the hole. The cable is clamped on the girder and is in a large bundle. The large structural girder on the bottom of the fuel tank now extends 9" below and is 28" from the skin. The cable is now in the rear wheel well and is clamped on standoffs to the side of the girder instead of the bottom of the fuel tank.

1037.2 The cable branches out of the bundle and is clamped on a standoff to the side of the girder, 2" and 3.5" away from the bottom of the fuel tank and the girder, respectively. There are other cables running parallel within 1" of the cable.

1046.4-1123 Stations 1046.4, 1055.6, 1064.8, 1074, 1082.7, 1092.7, 1102.8, 1107.8, 1112.9 and 1123 are the same as 1037.2.

1135 Same as 1037.2 except the clamp is 3.5" and 4" away from the girder and the bottom of the fuel tank, respectively.

1150 The clamp is 10.25" and 23" away from the bottom of the fuel tank and the girder, respectively. Here the cable is actually below the bottom of the girder. The clamp is still on a standoff anchored to the side of the girder.

1158 Same as 1150 except the clamp is 10.5" and 23" away from the bottom of the fuel tank and the skin, respectively.

STATION
NUMBERS

1167 Same as 1150 except the clamp is 11" and 23" away from the bottom of the fuel tank and the skin, respectively.

1178 Same as 1037.2 except the clamp is 5" and 3.25" away from the bottom of the fuel tank and the girder, respectively.

1188 Same as 1037.2 except the clamp is 4.5" to the bottom of the fuel tank and 3" to the girder.

1198-1228 Stations 1198, 1208, 1218, and 1228 are the same as 1188.

1237 The cable is clamped to the front of the bulkhead in one place on a standoff, which is 3.5", 12", and 10", respectively, away from the bulkhead, the bottom of the fuel tank and the skin. There is a 1" hole in the bulkhead which is grommetted. The hole is 18" and 16.5" away from the bottom of the fuel tank and the skin, respectively. On the aft side of the bulkhead there is 22" of cable between the hole and the first clamp.

1247 Here the cable is clamped to a girder support 5.5", 11", and 7.5", respectively, away from the bottom of the fuel tank, the skin, and the girder. There are no other cables close to the cable from Station 1247 to 1317.

1257-1317 Stations 1257, 1267, 1277, 1287, 1297, 1307, and 1317 are the same as 1247.

1327 The cable comes out from under the fuel tank and passes through a partial bulkhead. The hole is 6.5" and 10" away from the bottom of the fuel tank and the skin, respectively, and 2" in diameter. The cable is clamped on the aft side of the hole.

On the aft side of the bulkhead there is a small support to which the cable is clamped. The clamp is 3" and 5" away from the bulkhead and the skin, respectively.

STATION
NUMBERS

1337 The cable is clamped on a rib 2.75" high and 1" wide. There are other cables running parallel within 3" of the cable.

1347-1475 Stations 1347, 1357, 1367, 1377, 1387, 1397, 1407, 1417, 1427, 1437, 1447, 1457, 1466 and 1475 are the same as 1337.

1484 At this station there is a large structural girder which encircles the aft section of the plane. The cable follows this girder from the port to the starboard side of the aircraft. Around the girder the cable is clamped on stand-offs. There are no other cables running beside the cable around the girder. The following is a description of the clamps around the girder at station 1484.

CLAMP
NUMBER

1 The cable is clamped to the bottom of a 4" diameter hole in a girder support. The clamp is 3" and 2.75" away from the skin and the girder, respectively.

2 There is 9" of cable between clamp 1 and clamp 2. The clamp is 6" and 2.25" away from the skin and the girder, respectively.

3 10" of cable between clamps 2 and 3. Clamp position is the same as #2.

4 9" of cable between clamps 3 and 4. Clamp position same as #2.

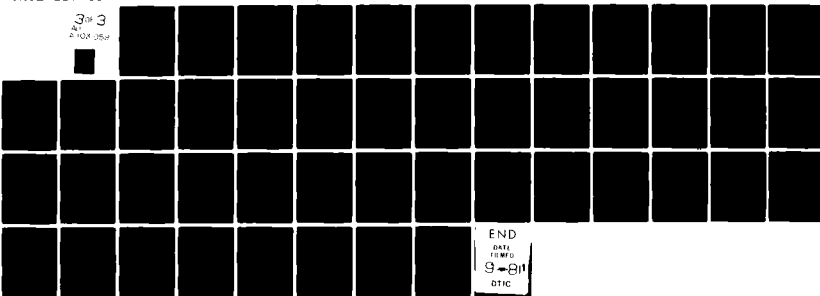
5 16" of cable between clamps 4 and 5. The clamp is 3" and 2.25" away from the skin and the girder, respectively.

AD-A103 059

MISSION RESEARCH CORP ALBUQUERQUE NM
EXPERIMENTAL AND ANALYTICAL METHODS FOR THE CHARACTERIZATION OF--ETC(U)
SEP 80 A K AGRAWAL, J R BARNUM, L D SCOTT F29601-78-C-0082
AFWL-TR-80-35 NL

UNCLASSIFIED

3 of 3
4-103-354



END

11

FORM 161

9-811

DTIC

CLAMP NUMBER	
6	16" of cable between clamps 5 and 6. The clamp is 3" and 2" away from the girder and the skin, respectively. A small section (3") of the cable is 0.25" from the skin. For 20" the cable runs under a catwalk. The cable is 3", 2", and 1", respectively from the girder, the skin, and 1" the catwalk. The cable is clamped on either side of the walk. The clamping points are on the bottom of 4" diameter holes in girder supports.
7	10" of cable between clamps 6 and 7. Clamp position 3" to the skin and 2.5" to the girder.
8	8" of cable between clamps 7 and 8. Clamp position same as #7.
9	15" of cable between clamps 8 and 9. Clamp position 2.5" to the girder and 7" to the skin.
10	8" of cable between clamps 9 and 10. Clamp position is 2.5" to the girder and 5.75" to the skin.
11	9" of cable between clamps 10 and 11. The cable runs over the top of the girder and is clamped at two places on top of the girder. The girder is 9" high and 3" wide.
STATION NUMBERS	
1493.5	The cable is clamped on a rib 1" wide and 2.75" high. At this point a 10 gauge ground wire is added to the cable.
1503	The cable is clamped on top of a metal plate. The plate is supported on two ribs. The position of the clamp is at 1503 directly over the top of the rib. A second 10 gauge ground wire is added to the cable at this point.
1513	The metal plate ends on the rib at 1513. At 1513 the cable is clamped on top of the plate.

STATION
NUMBERS

1523 The cable is clamped on top of a rib 1" wide by 2.75" high.

1528.5 The cable terminates at this point into the EMP hydraulic pump #1. There is a right-angle 7 pin connector which connects the cable to the EMP hydraulic pump.

2. DETAILED DESCRIPTION OF THE CLAMPING LOCATIONS ON THE LABORATORY
CABLE MODEL

STATION
NUMBERS

648 The cable is supported 7" above the ground plane to match the height of the cable above the girder at the EMP pump #1 relay.

658 The cable was clamped on a 3" x 2" rib as in the aircraft 3" above the ground plane.

658-667 The metal plate in the aircraft was not modeled. The cable was supported 3.75" above the ground plane, on a 3" high and 2" wide rib and a 0.75" foam block. The clamp was grounded to the rib.

667 The cable is supported on foam blocks 1.5" above the ground plane and clamped at the same points as the aircraft. The clamps are grounded with copper tape.

676 The cable is clamped on a 3" x 2" rib, as in the aircraft.

685 The support coming out from the rib is modeled by a rib on top of the rib. See mockup #1. The base rib is 3" high and 2" wide. The support rib is 2" high and 1" wide.

694 The bulkhead was modeled by a 1/16" aluminum sheet, 16" high, 14" wide, and 3" wide with a 1.5" diameter hole centered 9" above the ground plane. The cable is clamped at the center of the hole.

STATION
NUMBERS

698.5 The clamp on the support in the aircraft is modeled by supporting the cable on a foam block 5" high. The clamp is then grounded to the ground plane with copper tape.

705 The standoff on the rib was modeled by a foam block on top of a 2.75" by 1" rib. The clamp was grounded to the rib.

715 The cable is clamped on a rib 2.75" high and 1" wide.

725 Same as 715.

733 The clamp on a standoff is modeled by supporting the clamp on a foam block and grounding the clamp with a strip of copper tape. The clamp is 2.5" above the ground plane.

754 Same as 733.

763 Same as 733.

777 The standoff on top of the small metal support is modeled as a standoff 4" high.

793 The metal structure was deleted between stations 795 and 800. At station 793 the clamp on a standoff was modeled as at station 733.

805 The bulkhead is a sheet of aluminum 14" high and 14" wide. A 2" hole was cut 1" above the ground plane, and the cable was clamped towards the top of the hole. The reason for this is that the cable in the aircraft was in a large bundle, but towards the top of the hole.

810 The girder support is modeled by a 1" wide and 4" high rib. On top of the rib there is a 0.25" foam spacer. There is no clamp at this station.

STATION
NUMBERS

813.3 The clamp on a standoff is modeled the same way as the other standoffs except the height is 4.25".

830.9 Same as 813.3, except the height is 3.75".

849.5 Same as 813.3, except the height is 2.75".

860.8 The girder support is modeled by a rib 3" wide and 2" high. On top of the support there is a 0.75" foam spacer.

868.1 Same as 849.5.

886.7 Same as 849.5, except the height is 3".

907.3 Same as 886.7.

917 The bulkhead was modeled the same as the bulkhead at Station 805. The center of the 2" diameter hole was 3.5" above the ground plane. The cable was clamped at the center of the hole.

925.8 The standoff is modeled as at previous stations. The height is 3".

944.2-1017.8 Stations 944.2, 962.6, 981, 999.4, and 1017.8 are the same as 925.8.

1028 The two clamping points on the front side of the bulkhead are modeled by a cable above a ground plane. The first clamp is 2" above the ground plane, the second clamp is 1.5" above the ground plane. The bulkhead is modeled as before. The hole is 2" in diameter and its center is 2.5" above the ground plane. The cable is clamped on the bottom of the hole.

On the aft side of the bulkhead the girder was modeled by a 2" wide and 4" high rib, and the cable was clamped to it.

STATION
NUMBERS

1037.2 The clamp on a standoff is modeled the same as other standoffs. The height is 2" above the ground plane.

1046.4-1123 Stations 1046.4, 1055.6, 1064.8, 1074, 1082.7, 1092.7, 1102.8, 1107.8, 112.9, and 1123 are the same as 1037.2.

1135 Here the cable is modeled by a clamp on a standoff. The height of the cable is determined by finding the impedance of a cable in a corner. The distance used was 3.75" and the height was found to be 1.88" above the ground plane.

1150 The cable is modeled as a cable clamped on a standoff. The height above the ground plane is determined by taking the distance from the clamp to the edge of the girder which is 5.64".

1158 Same as 1150 except the height is found to be 5.7".

1167 Same as 1150 except the height is 5.82".

1178 Same as 1037.2 except the height is 3.25".

1188 Same as 1037.2 except the height is 3".

1198-1228 Stations 1198, 1208, 1218, and 1228 are the same as 1188.

1237 Since the cable runs for 22" on the bulkhead, this portion of the bulkhead was converted to a horizontal ground plane. The clamp on a standoff was modeled as before, 3.75" above the ground plane. A 1" hole was placed in a bulkhead model as before such that as the cable got closer to the bulkhead hole, the distance to the bulkhead became the primary factor over the distance to the ground plane. This was done to match the aircraft cable as close as possible.

STATION
NUMBERS

1247 The girder support was modeled by a rib 1" wide and 5.5" high.

1257-1317 Stations 1257, 1267, 1277, 1287, 1297, 1307, and 1317 are the same as 1247.

1327 This bulkhead is modeled the same as before. A 2" diameter hole was centered 7" above the ground plane. The clamp on the small support on the back of the bulk-head is modeled by a rib 3" high.

1337 The rib is modeled by a piece of wood 1" wide and 2.75" high.

1347-1475 Stations 1347, 1357, 1367, 1377, 1387, 1397, 1407, 1417, 1427, 1437, 1447, 1457, 1466, and 1475 are the same as 1337.

1484 The following 12 points describe points along the cable around the girder.

1 The girder support is modeled as a bulkhead with a 4" diameter hole. The bottom of the hole is 2.5" from the ground plane, and the cable is clamped to the hole 2.75" above the ground plane.

2 Clamp on model standoff, 2.25" above the ground plane.

3 Same as #2.

4 Same as #2.

5 Here the cable is modeled as if it were in a corner. The equivalent height of 1.25" is used with the standoff.

6 A portion of the cable drops to within 0.25" of the skin. There is no clamp at this point. See mockup #8.

7 To model the cable through the two girder supports and under the catwalk, the following was done. The two girder supports were modeled as bulkhead with 4" diameter holes. The bottom of the hole was 2.5" above the ground plane. The cable was clamped on the bottom of the holes. The cable under the catwalk was modeled as a cable in a trough. The equivalent height was found to be 1".

8 Here the cable was modeled as if it were in a corner. The equivalent height was found to be 1.25".

9 Same as #8.

10 The clamp on a standoff model was used. The height was 2.5".

11 Same as #10.

12 The point where the cable runs over the top of the girder, it is modeled by a 9" high and 3" wide rib. The cable is clamped at two points on top of the rib.

STATION
NUMBERS

1493.5 The cable is clamped on a 1" wide by 2.75" high rib. An 8-gauge wire is added to the cable to model the 10 gauge ground wire.

1503 Between Stations 1503 and 1513 a 1/16" thick aluminum plate is placed on top of the 2.75" high by 1" wide ribs. At this point another 8 gauge ground wire is added to the cable. The cable now consists of 6 wires and is clamped at 1503.

1513 The aluminum plate stops on top of a 2.75" high rib. The cable is clamped on top of the plate at 1513.

1523 The cable is clamped on a 1" wide by 2.75" high rib.

STATION
NUMBERS

1528.5 The end of the cable was terminated in several different ways which was discussed in the general discussion of the simulated cable. The end of the cable was terminated with 20 gauge contacts to allow the cable to be terminated in different ways.

APPENDIX B

MEASURED INPUT IMPEDANCE AND ADMITTANCE DATA
(FOUR-WIRE LINE OVER STYROFOAM BLOCKS)

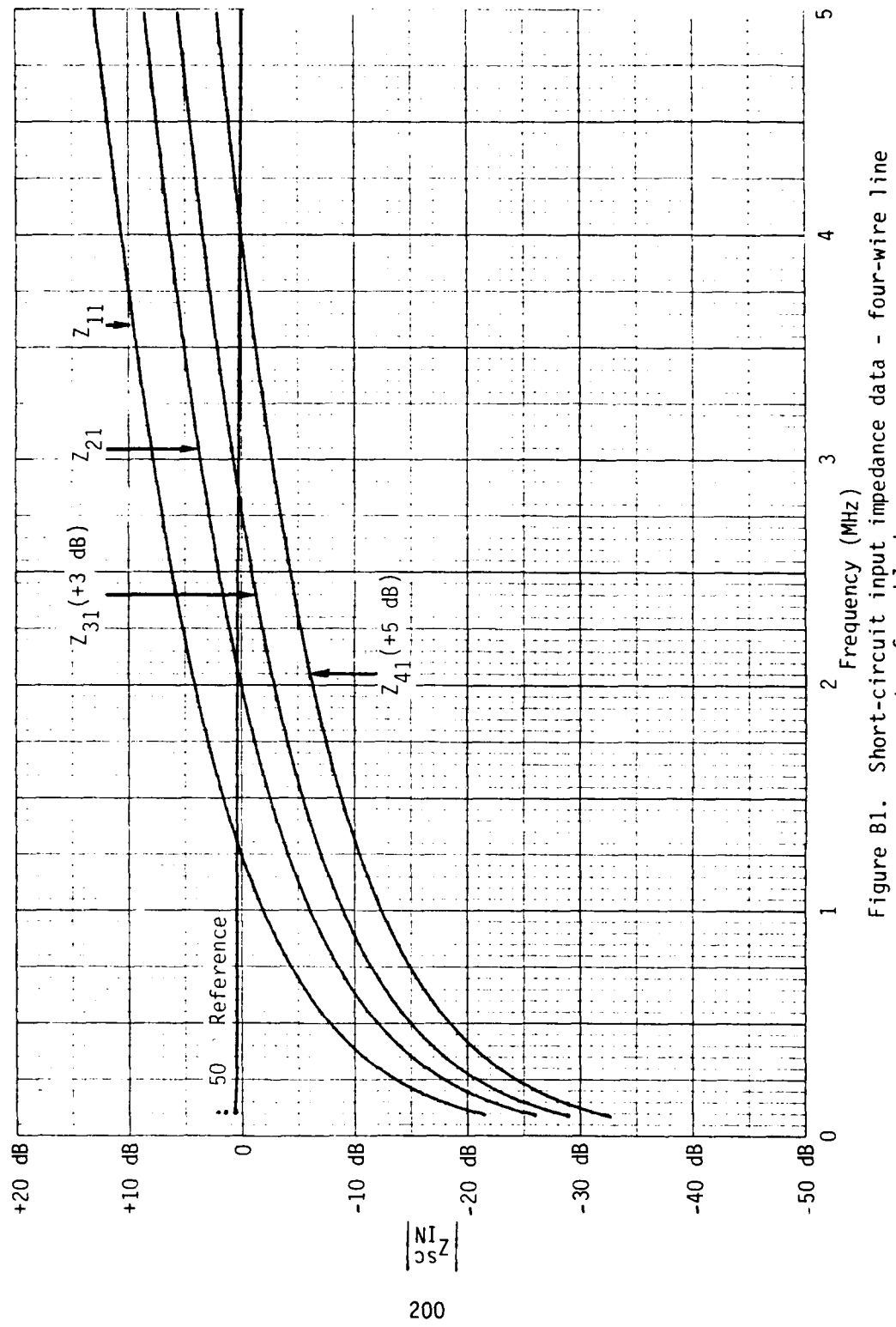


Figure B1. Short-circuit input impedance data - four-wire line over styrofoam blocks.

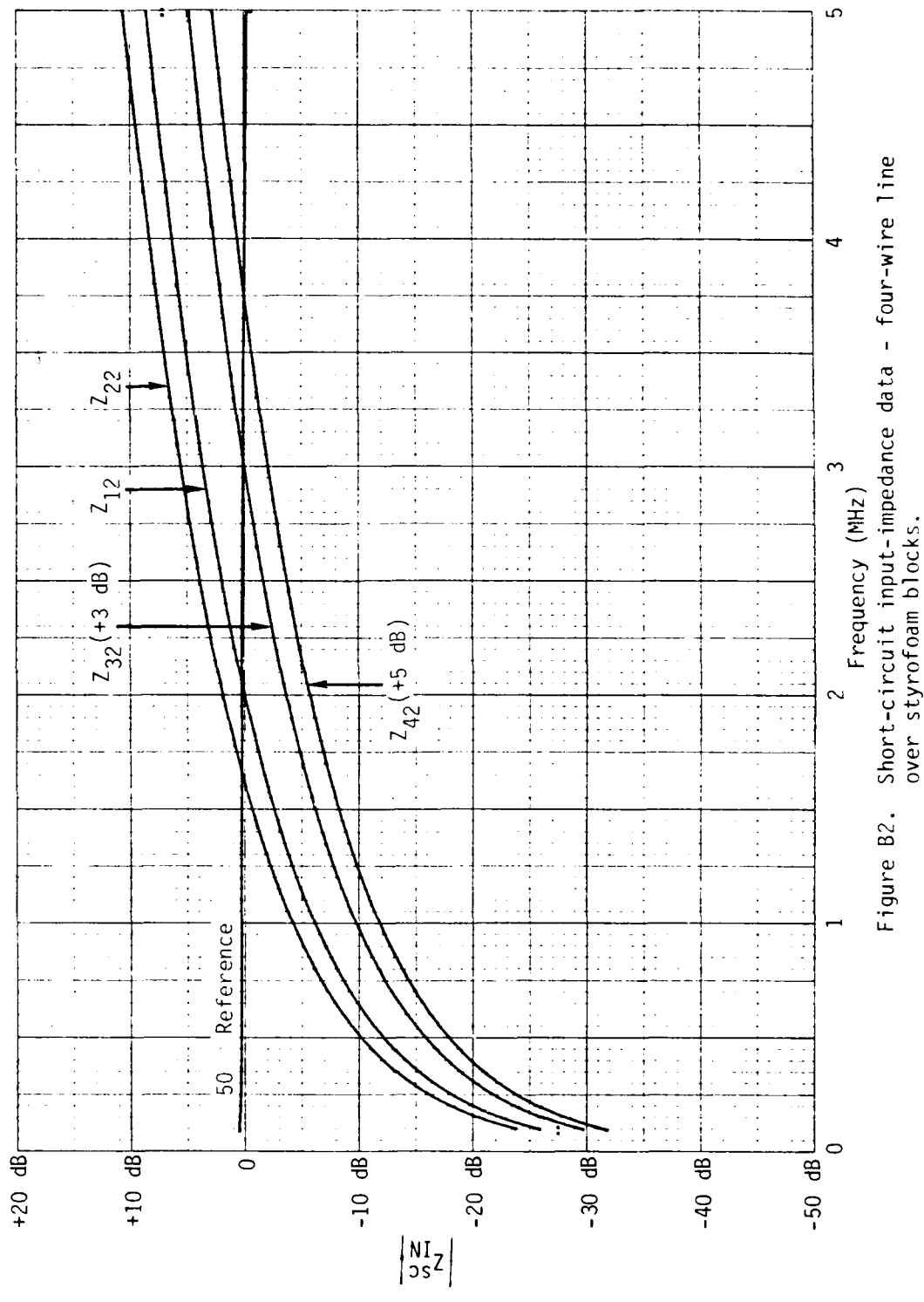


Figure B2. Short-circuit input-impedance data - four-wire line over styrofoam blocks.

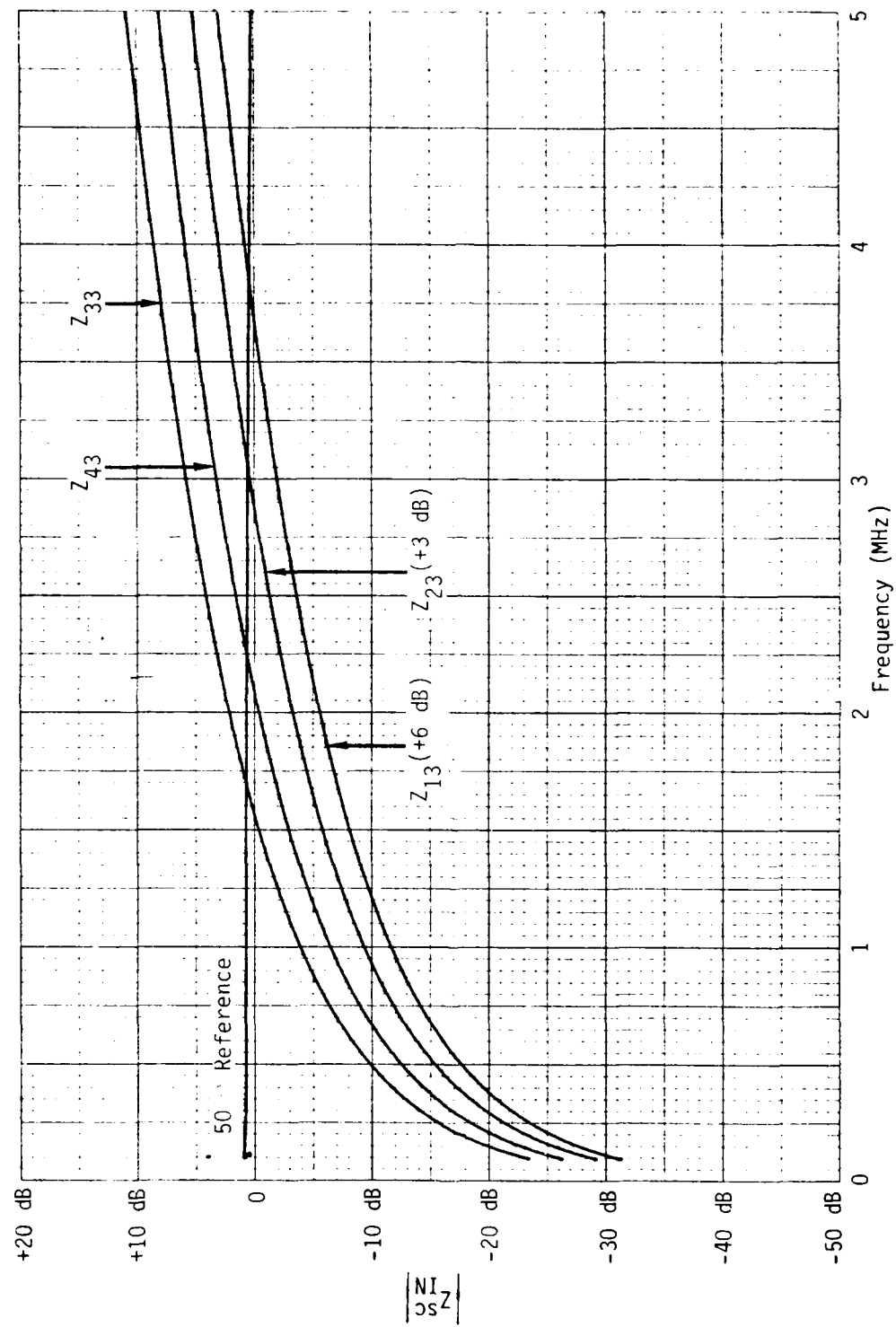


Figure B3. Short-circuit input-impedance data - four-wire line over styrofoam blocks.

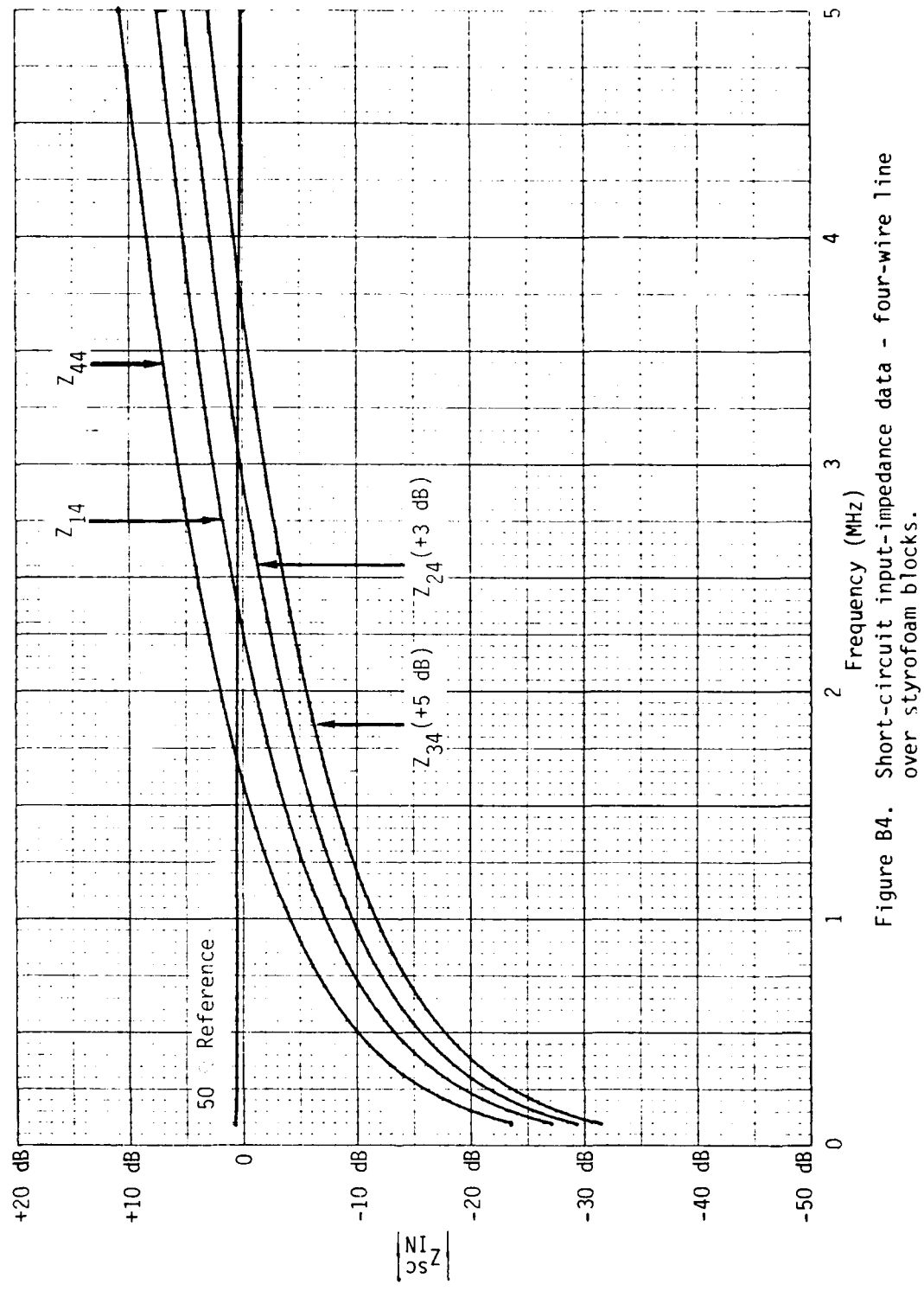


Figure B4. Short-circuit input-impedance data - four-wire line over styrofoam blocks.

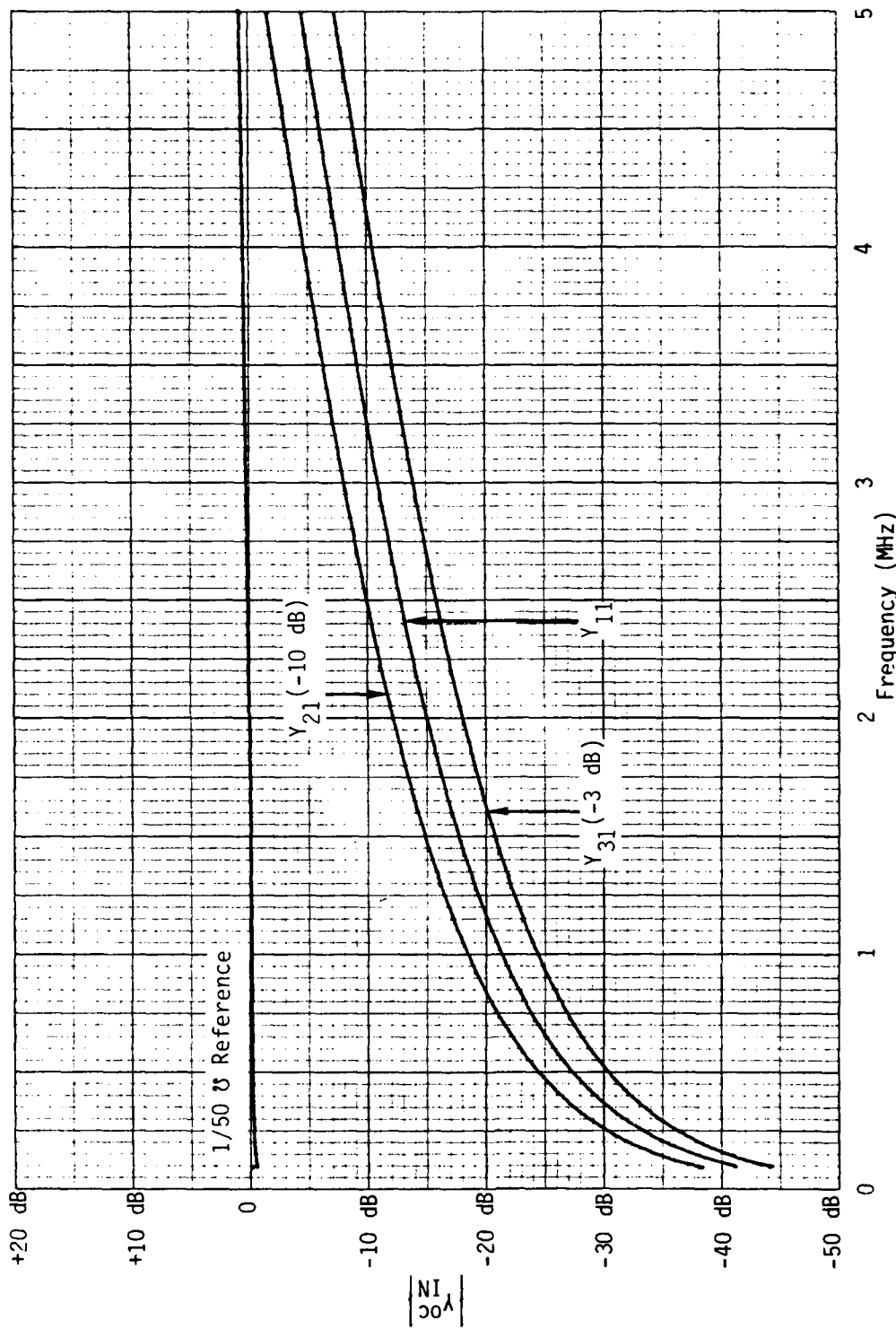


Figure B5. Open-circuit input-admittance data - four-wire line over styrofoam blocks.

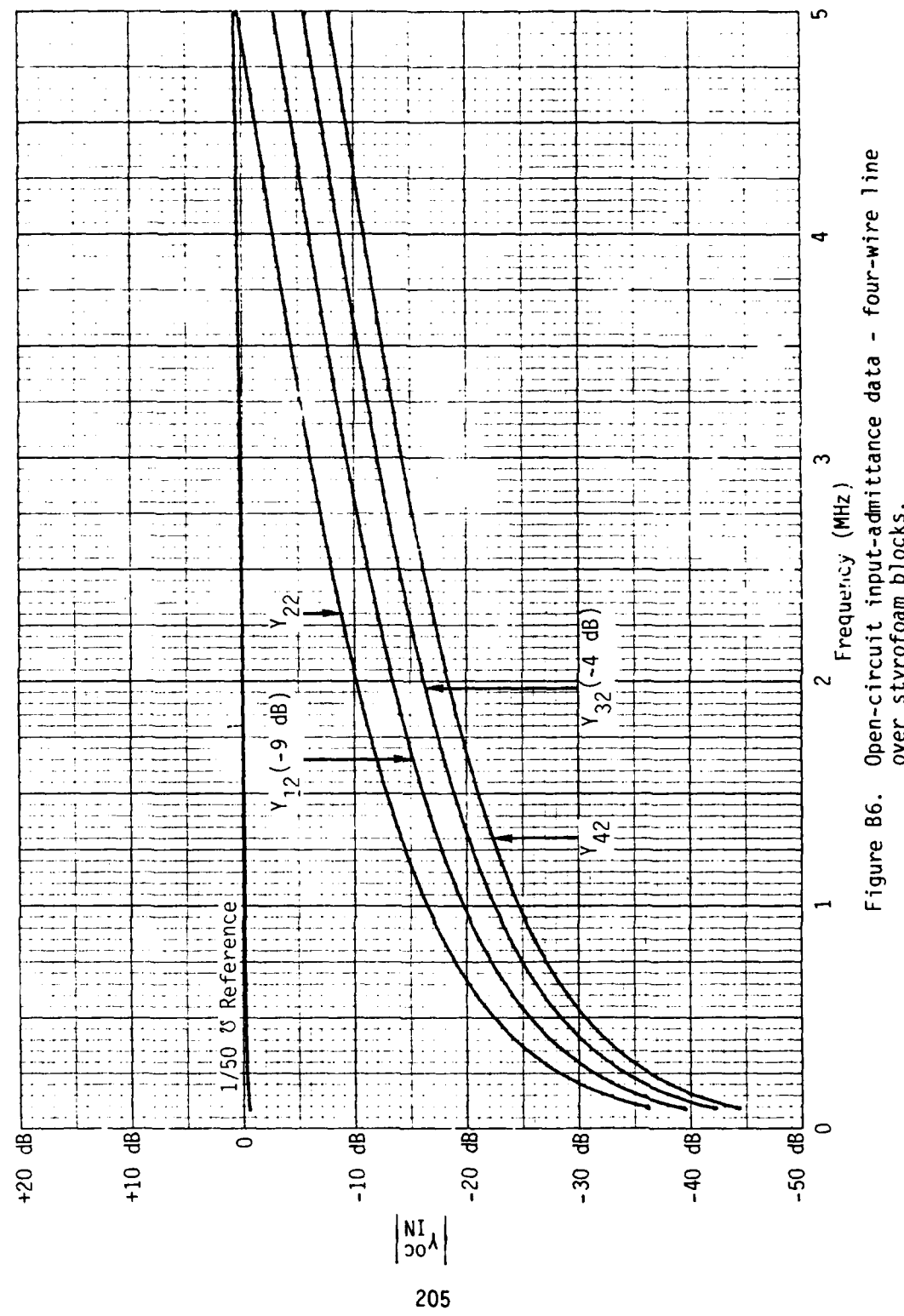


Figure B6. Open-circuit input-admittance data - four-wire line over styrofoam blocks.

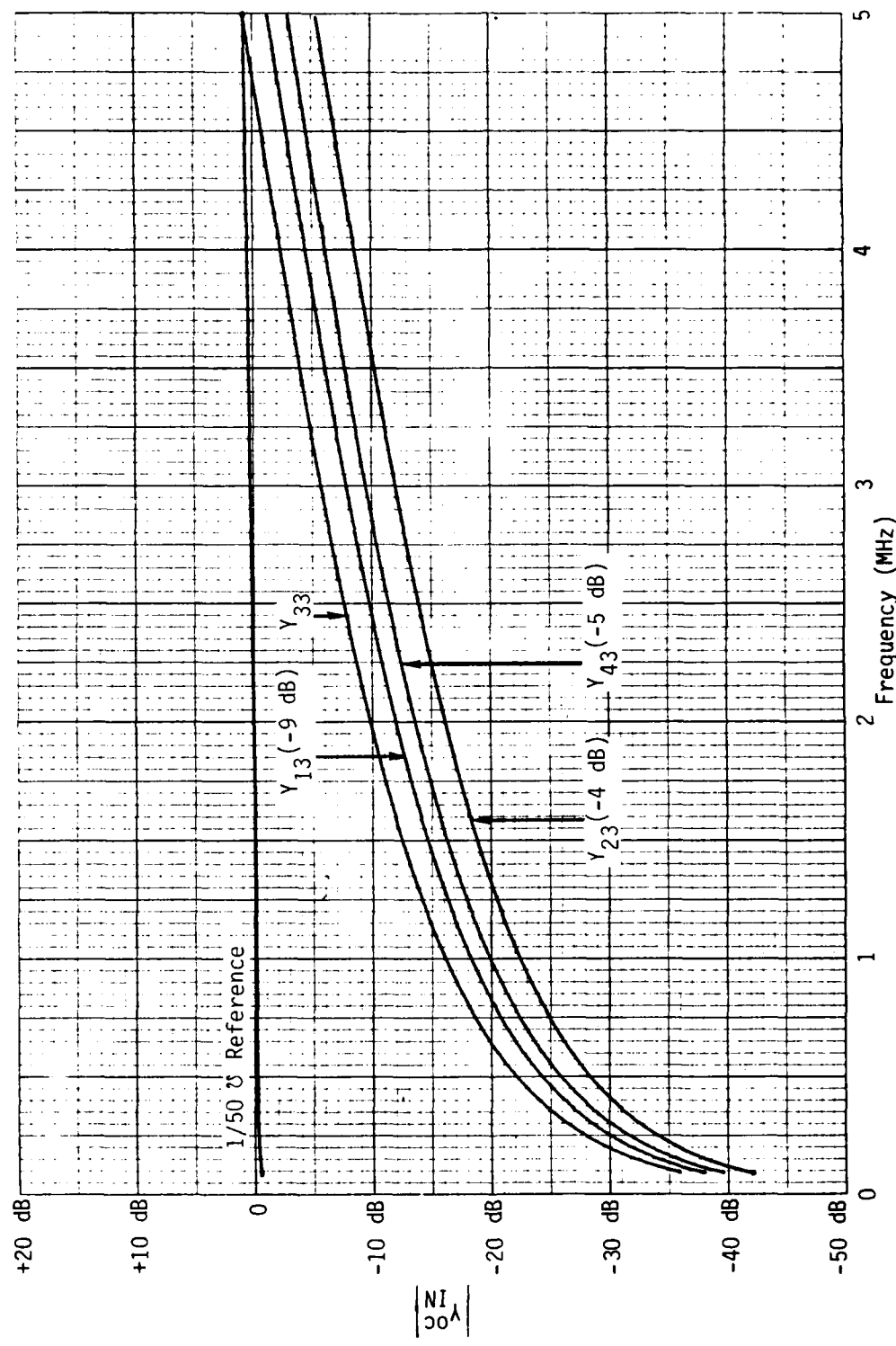


Figure B7. Open-circuit input-admittance data - four-wire line over styrofoam blocks.

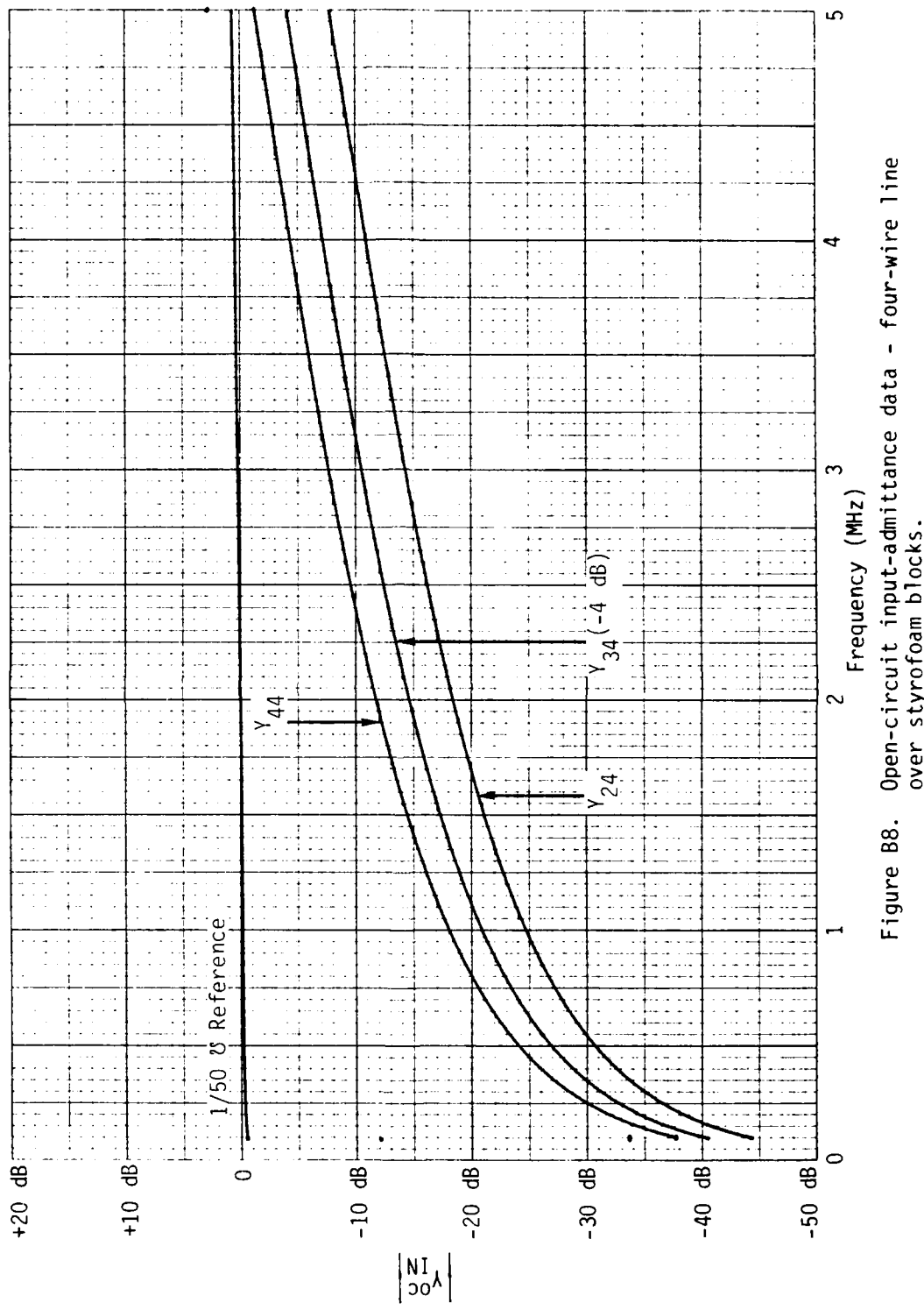


Figure B8. Open-circuit input-admittance data - four-wire line over styrofoam blocks.

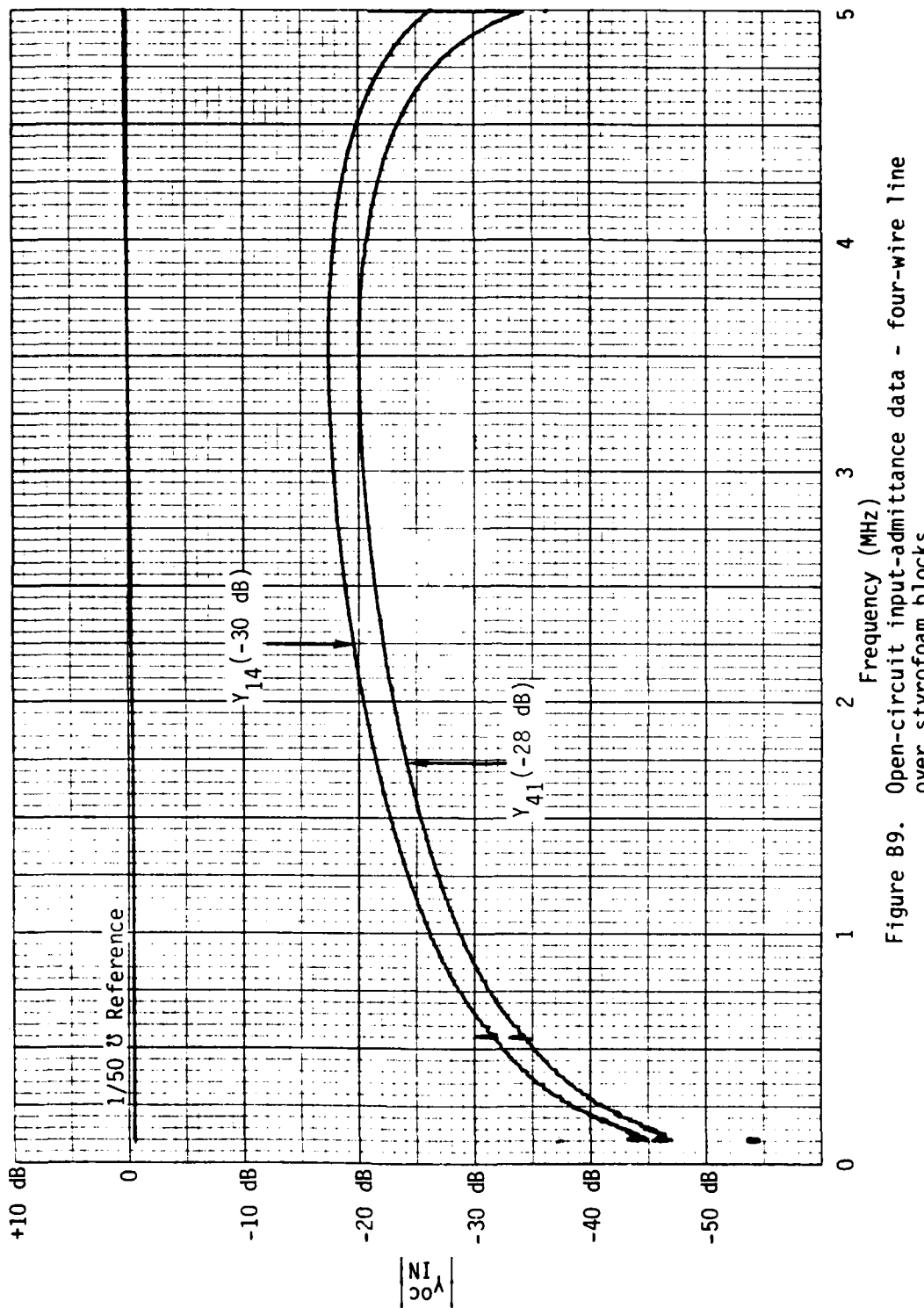


Figure B9. Open-circuit input-admittance data - four-wire line over styrofoam blocks.

APPENDIX C
MEASURED INPUT IMPEDANCE AND ADMITTANCE DATA
(FOUR-WIRE LINE OVER RIBS)

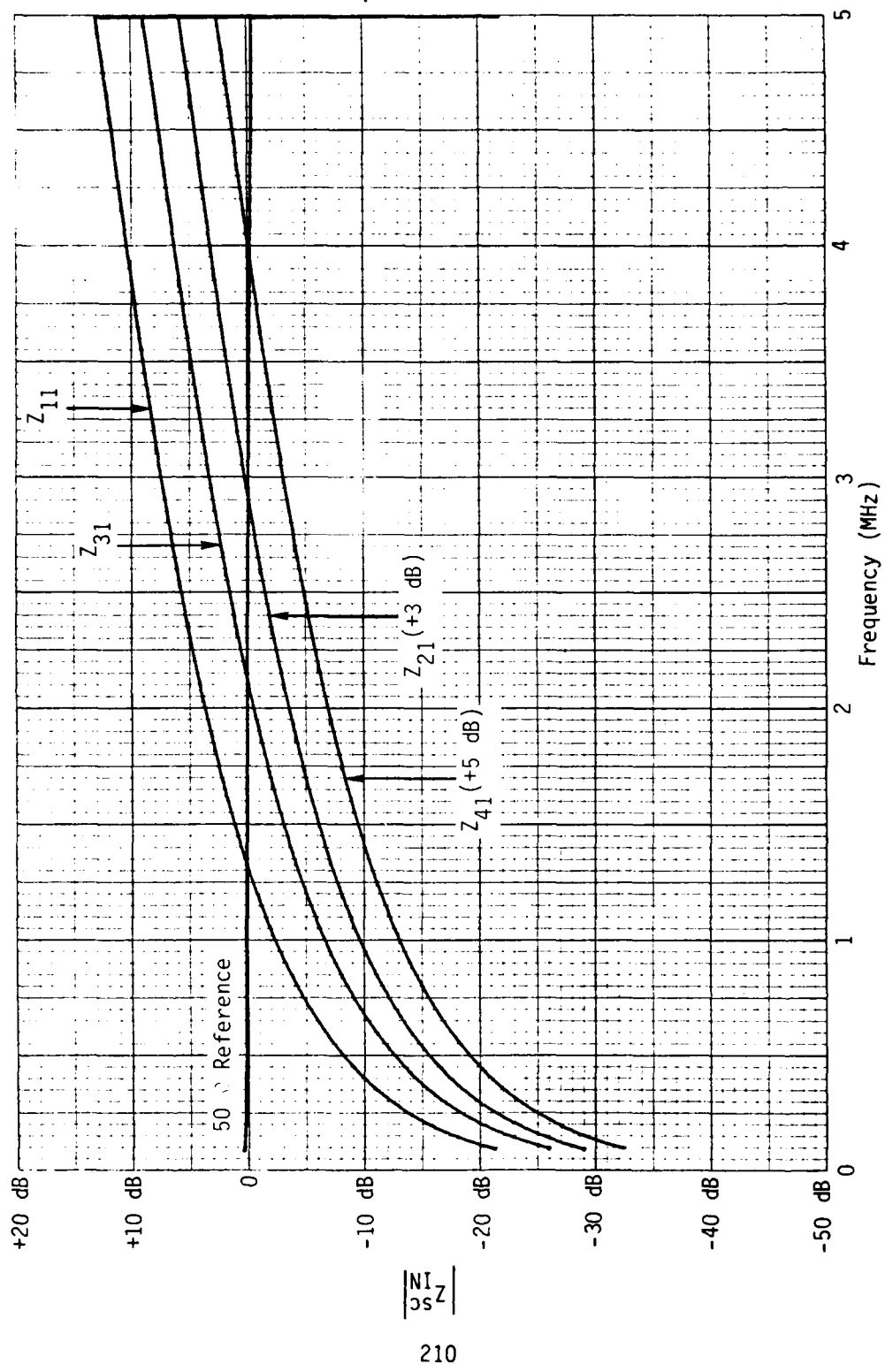


Figure C1. Short-circuit input-impedance data - four wire line over ribs.

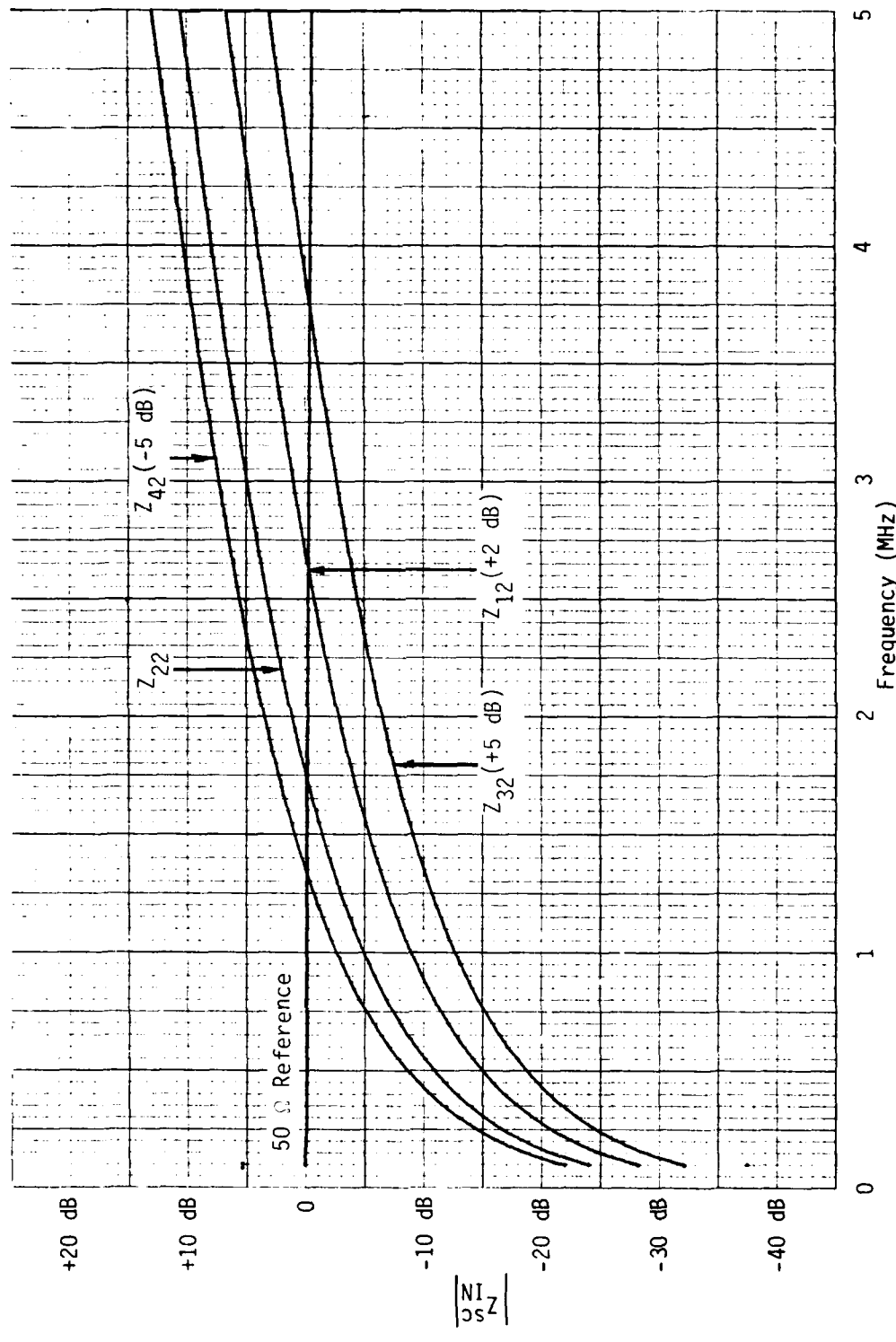


Figure C2. Short-circuit input-impedance data - four-wire line over ribs.

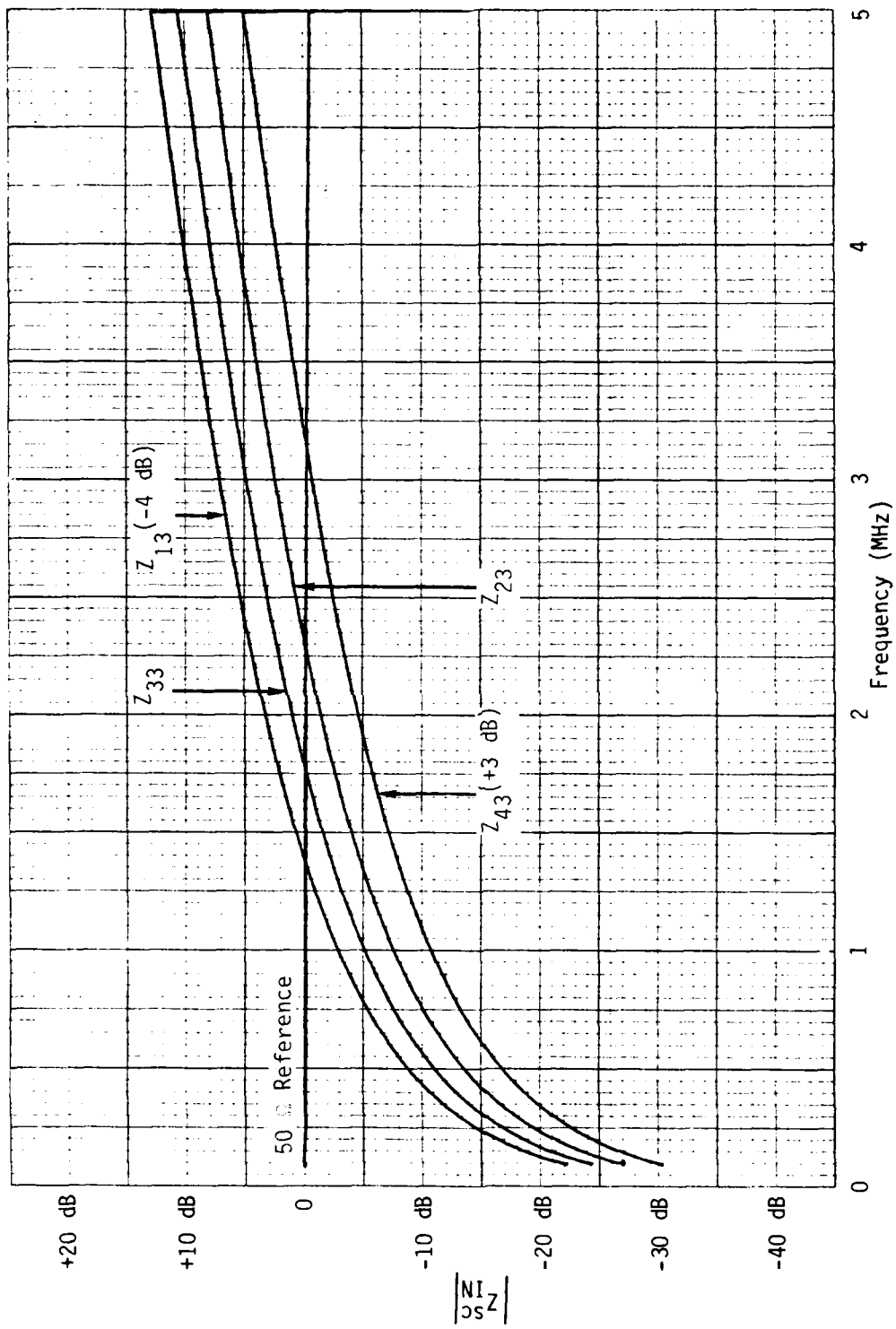


Figure C3. Short-circuit input-impedance data - four-wire line over ribs.

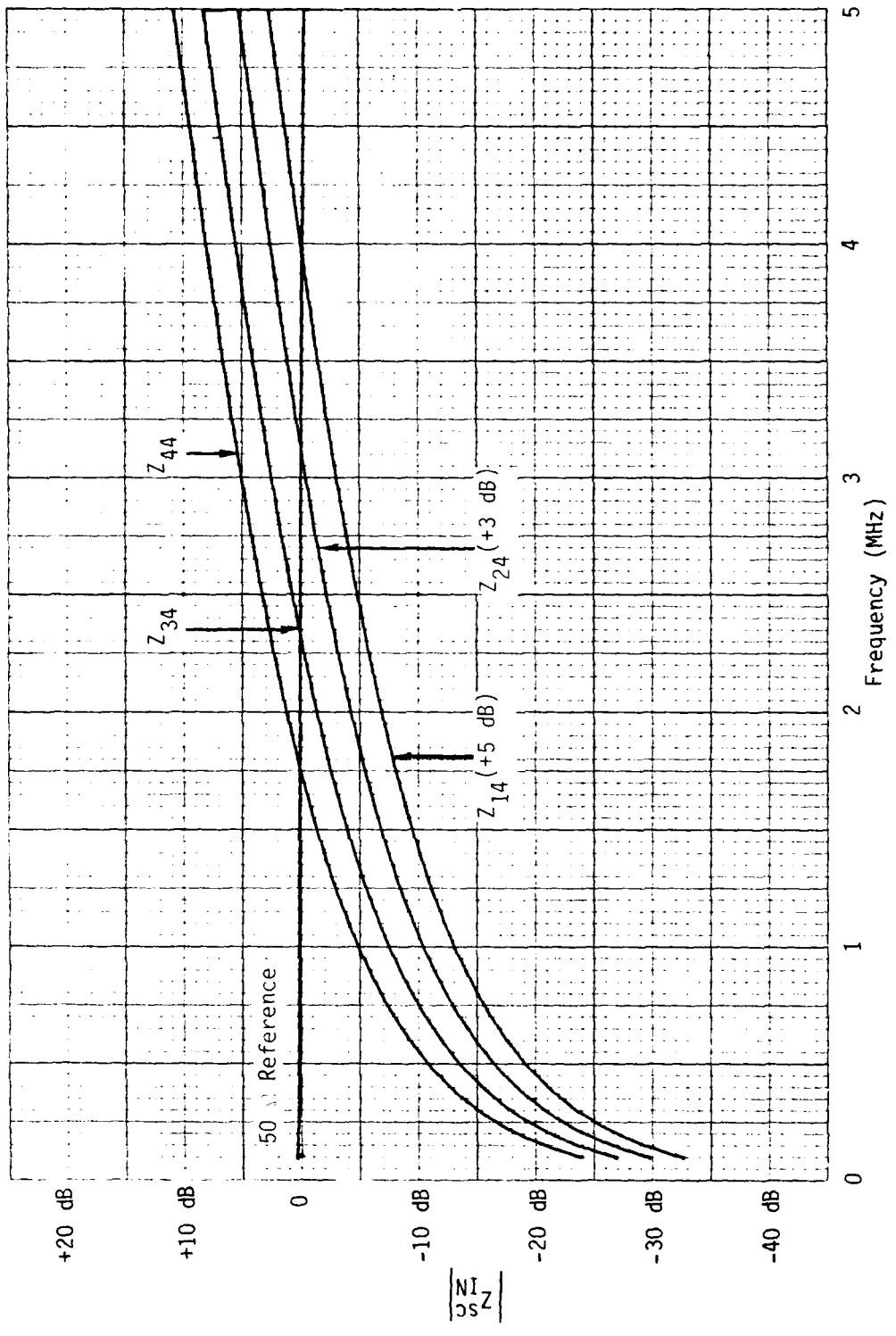
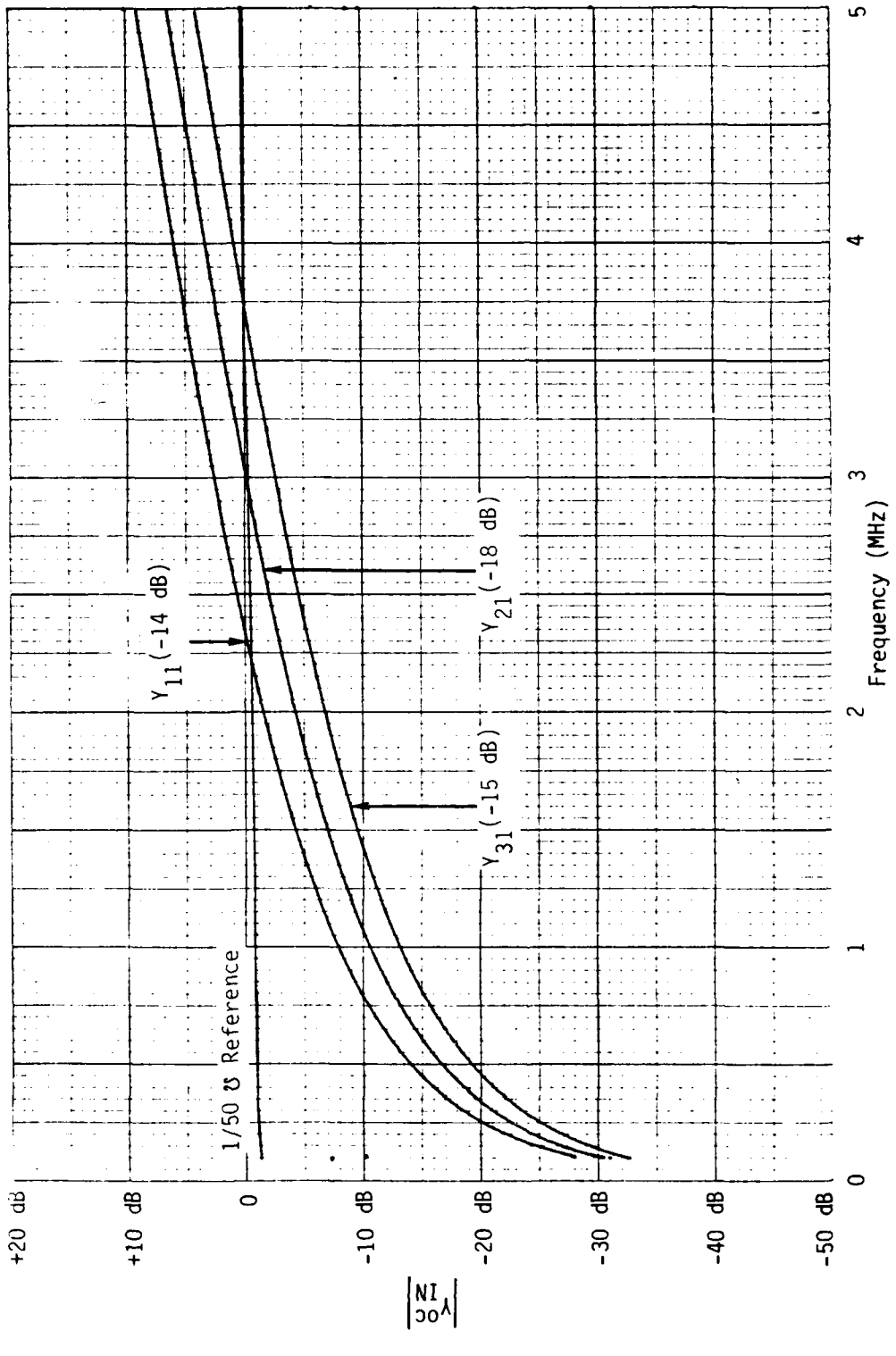


Figure C4. Short-circuit input-impedance data - four-wire line over ribs.



214

Figure C5. Open-circuit input-admittance data - four-wire line over ribs.

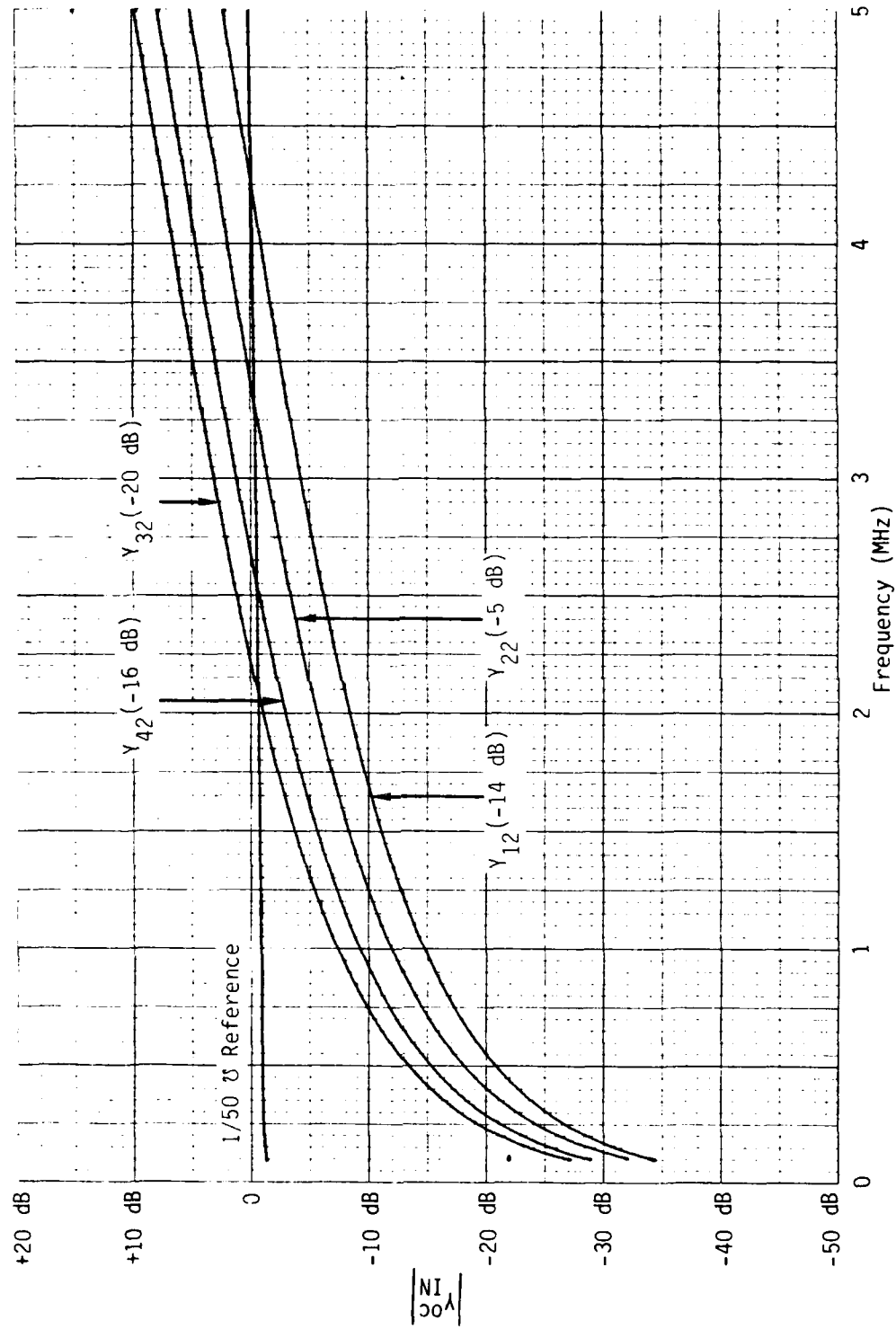


Figure C6. Open-circuit input-admittance data - four-wire line over ribs.

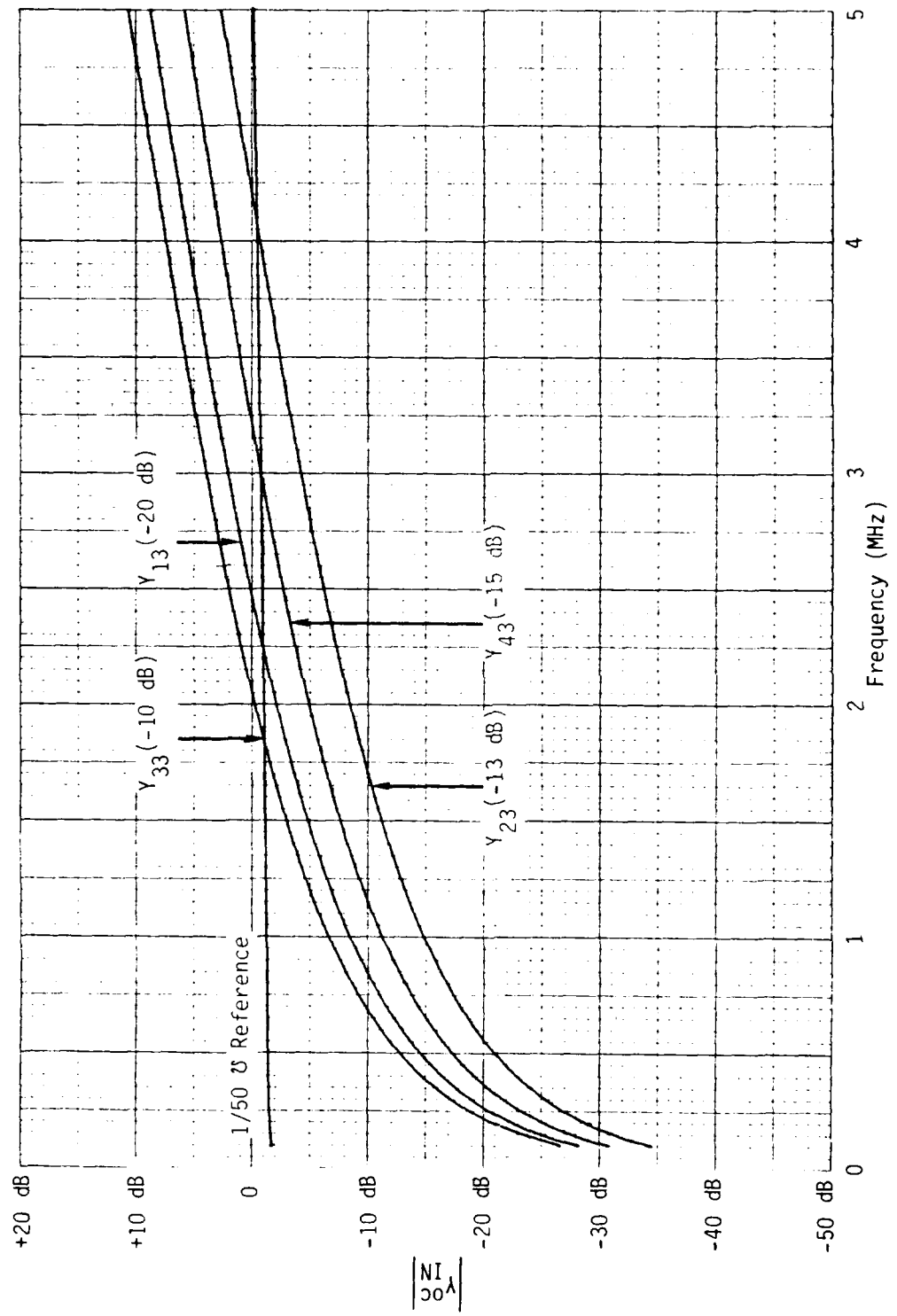


Figure C7. Open-circuit input-admittance data - four-wire line over ribs.

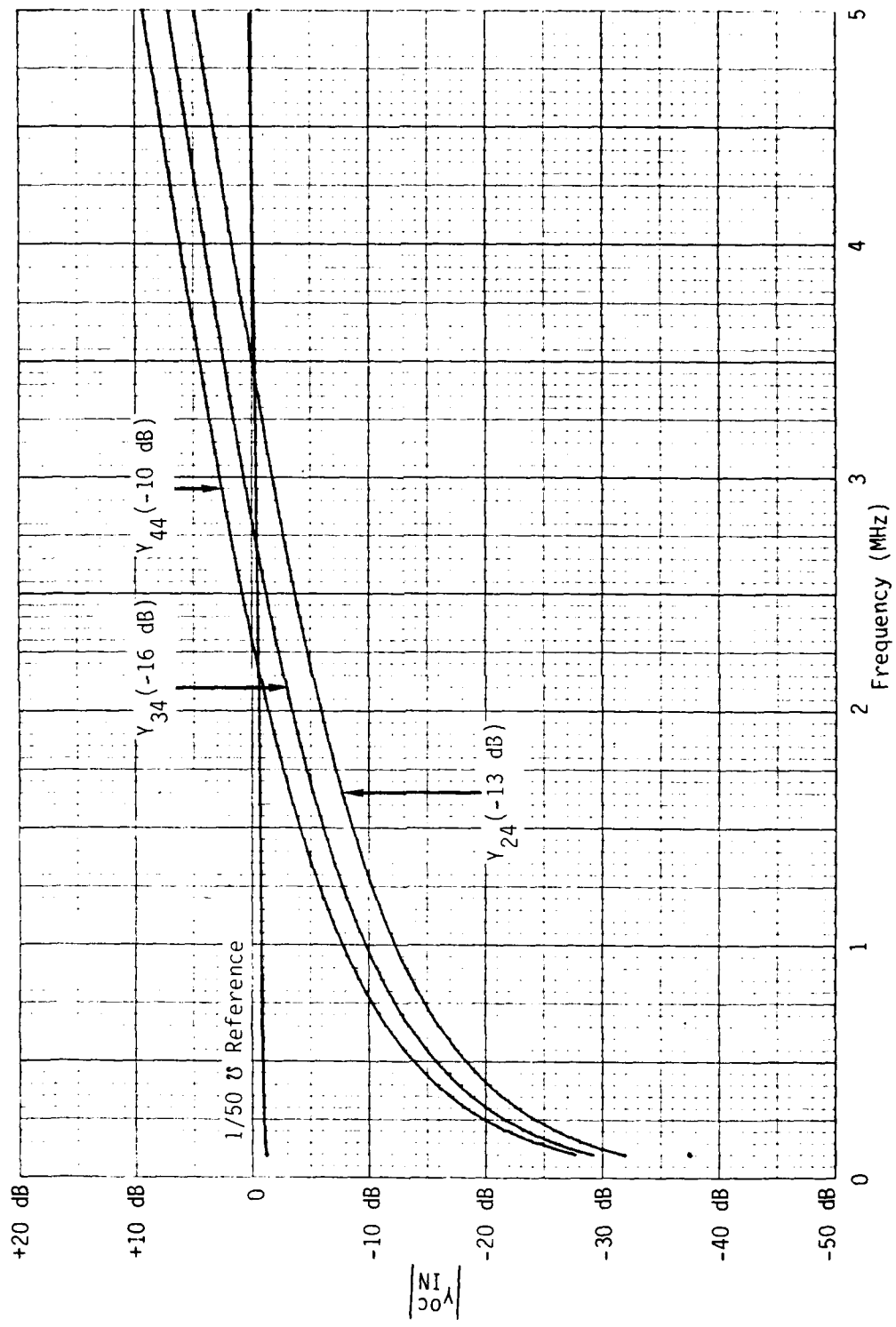


Figure C8. Open-circuit input-admittance data - four-wire line over ribs.

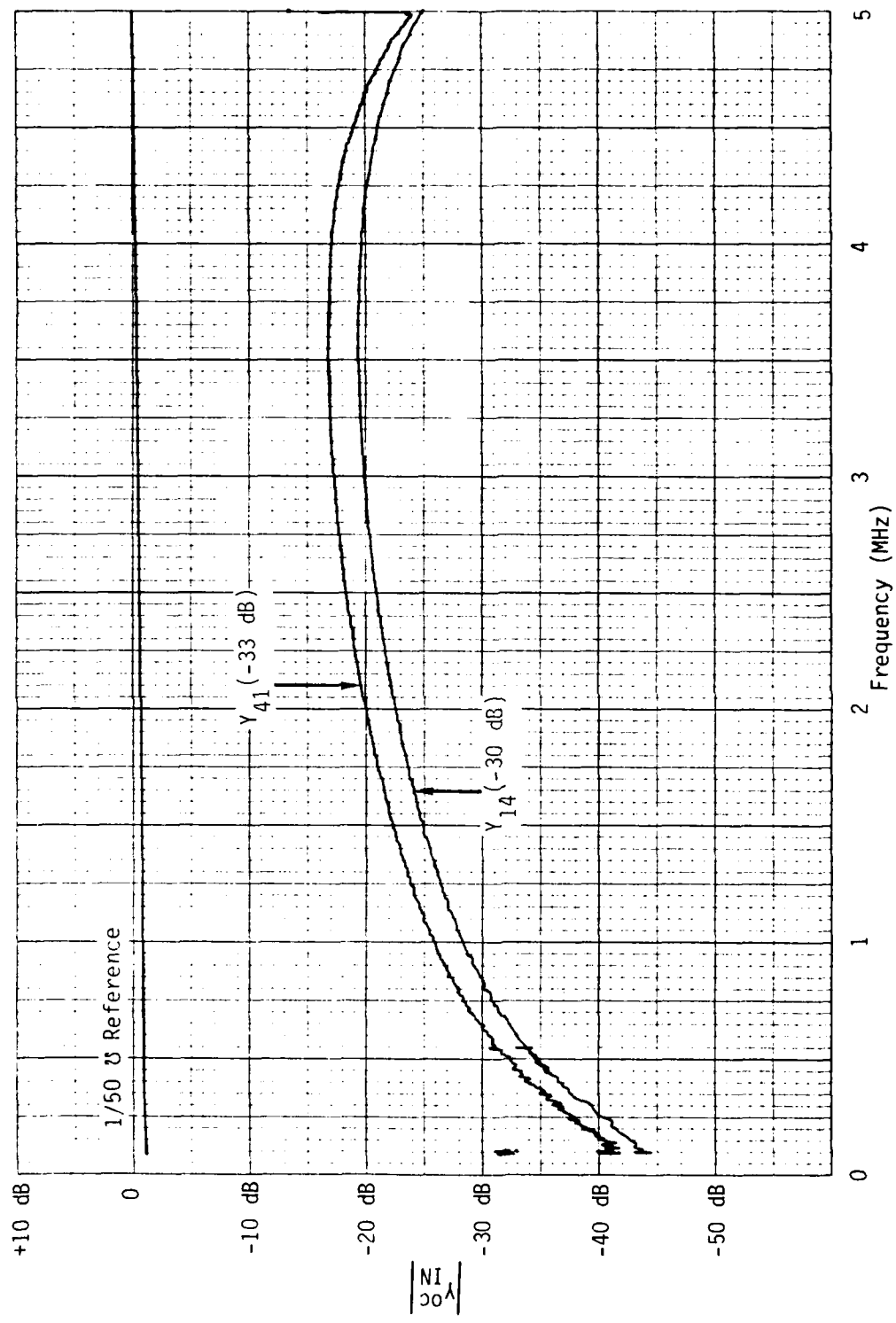


Figure C9. Open-circuit input-admittance data - four-wire line over ribs.

APPENDIX D

MEASURED INPUT IMPEDANCE AND ADMITTANCE DATA
(FOUR-WIRE LINE OVER RIBS WITH CLAMPS)

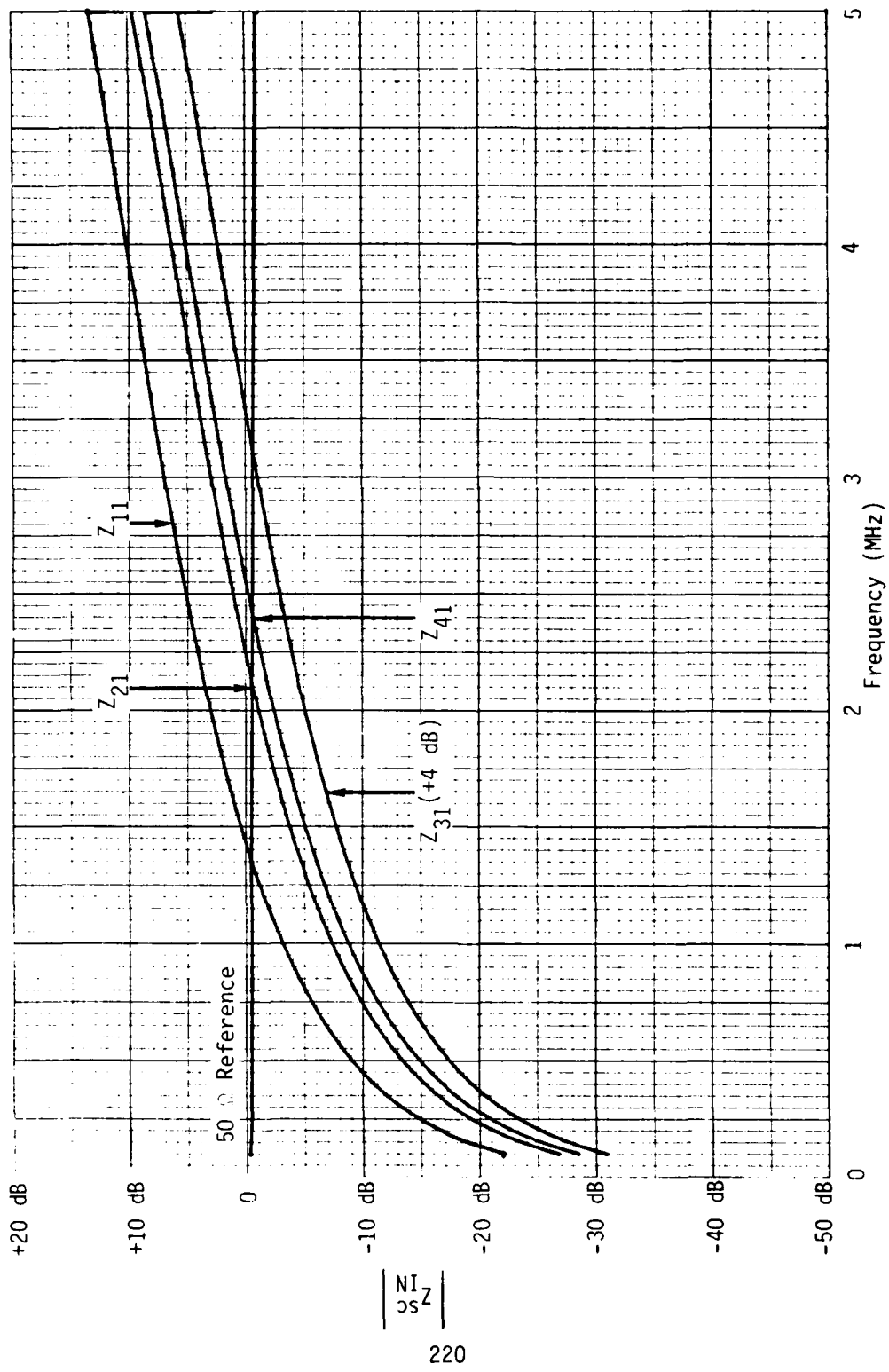


Figure D1. Short-circuit input-impedance data - four-wire line over ribs with clamps.

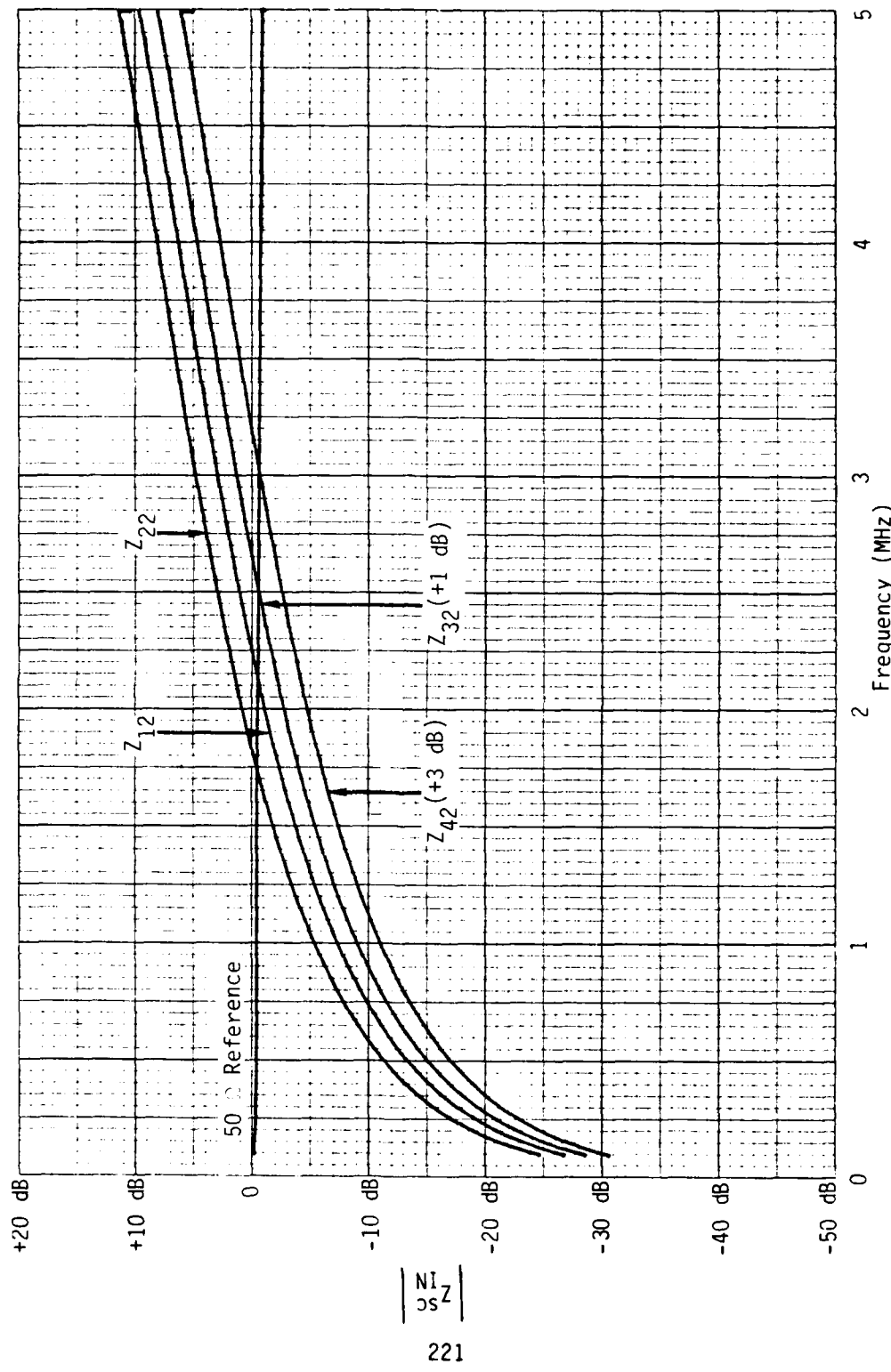


Figure D2. Short-circuit input-impedance data - four-wire line over ribs with clamps.

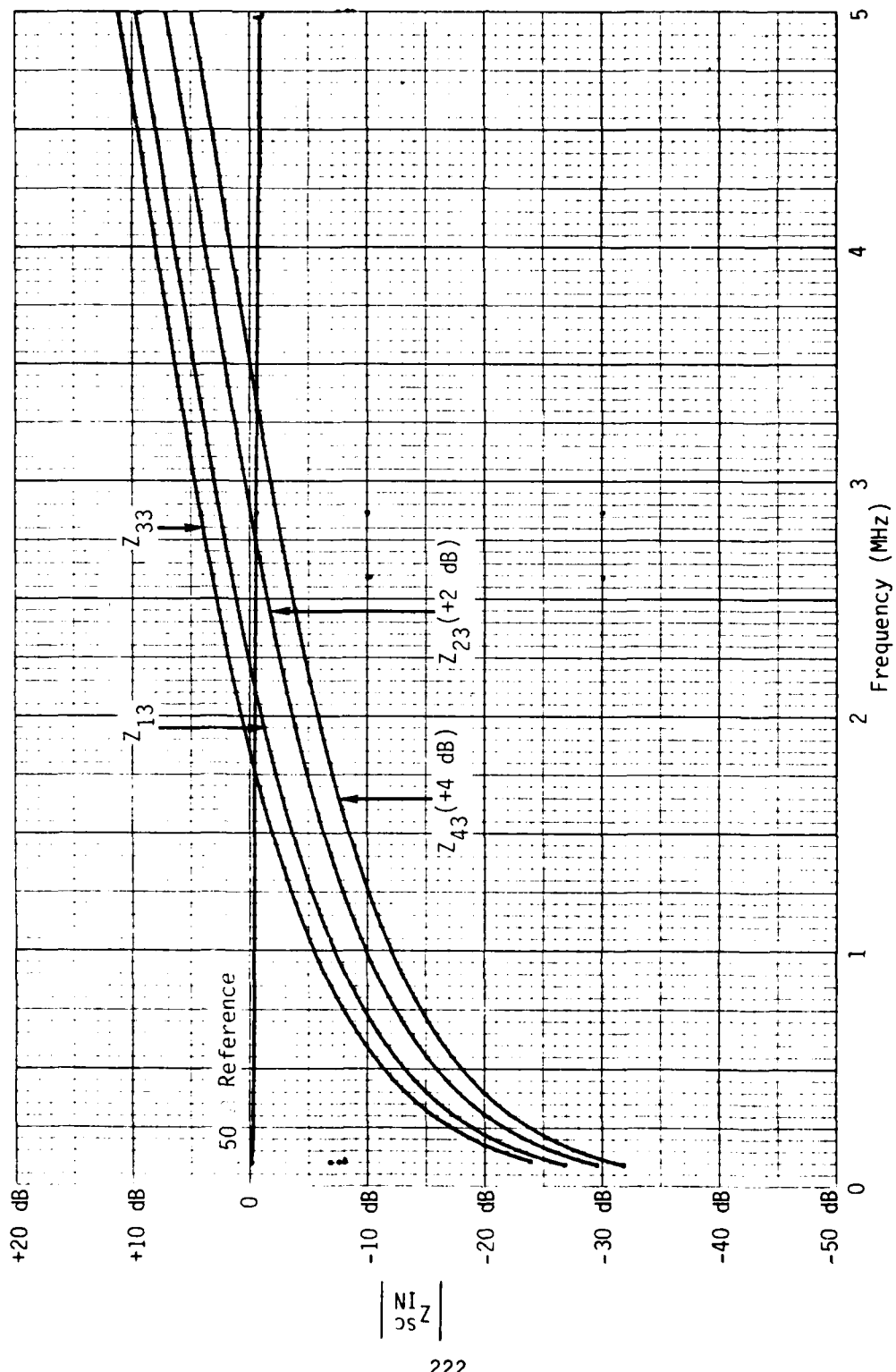
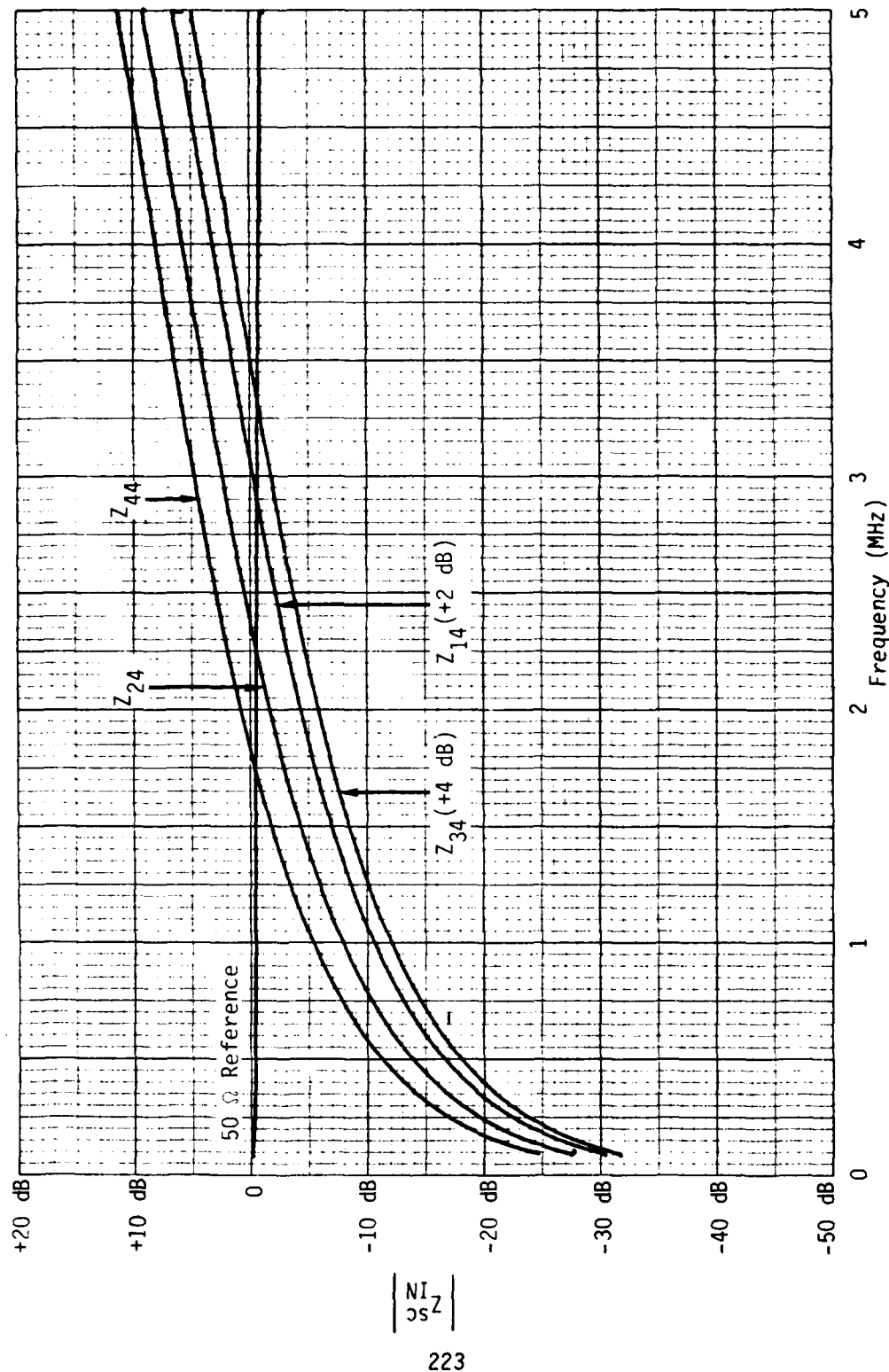


Figure D3. Short-circuit input-impedance data - four-wire line over ribs with clamps.



223

Figure D4. Short-circuit input-impedance data - four-wire line over ribs with clamps.

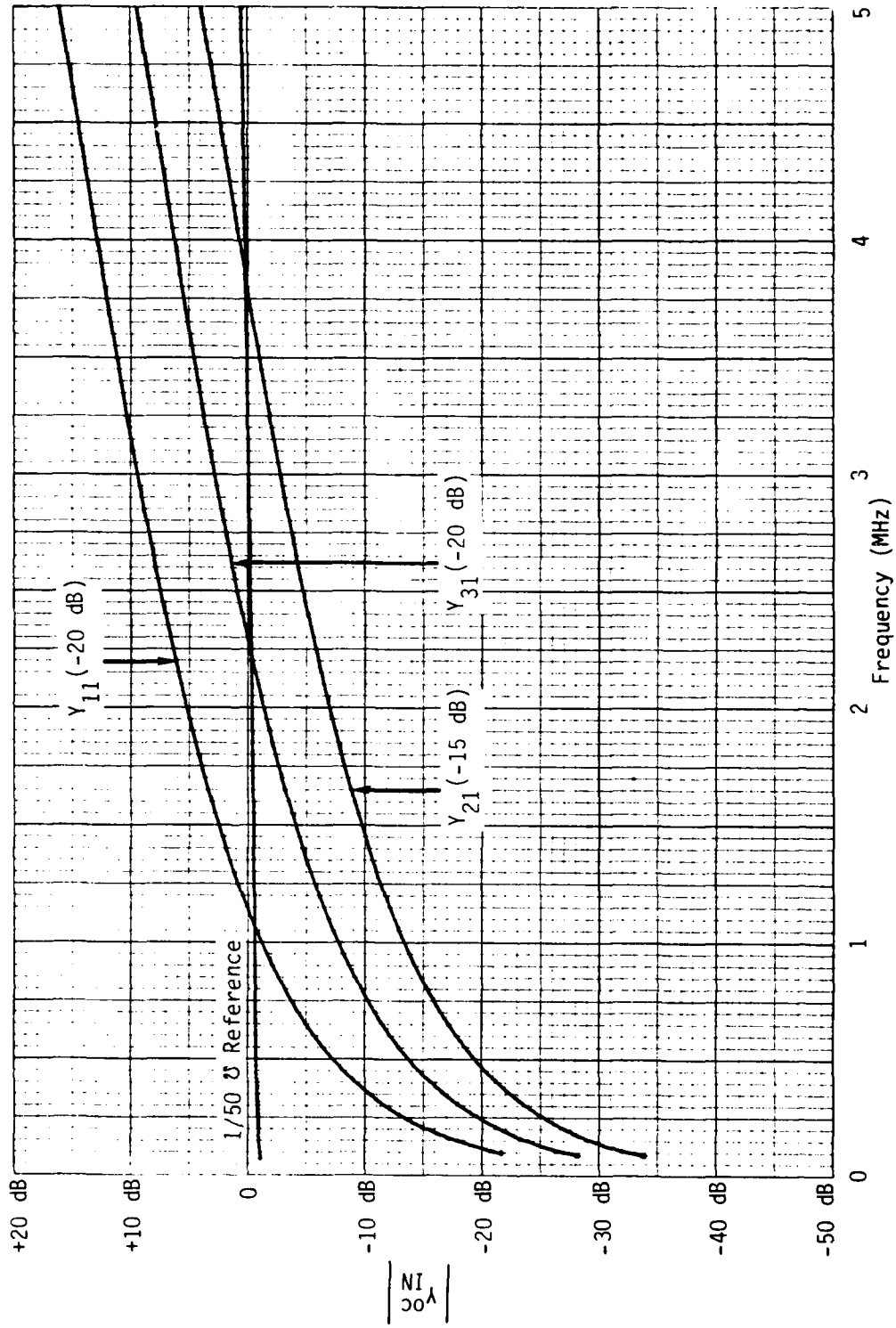


Figure D5. Open-circuit input-admittance data - four-wire line over ribs with clamps.

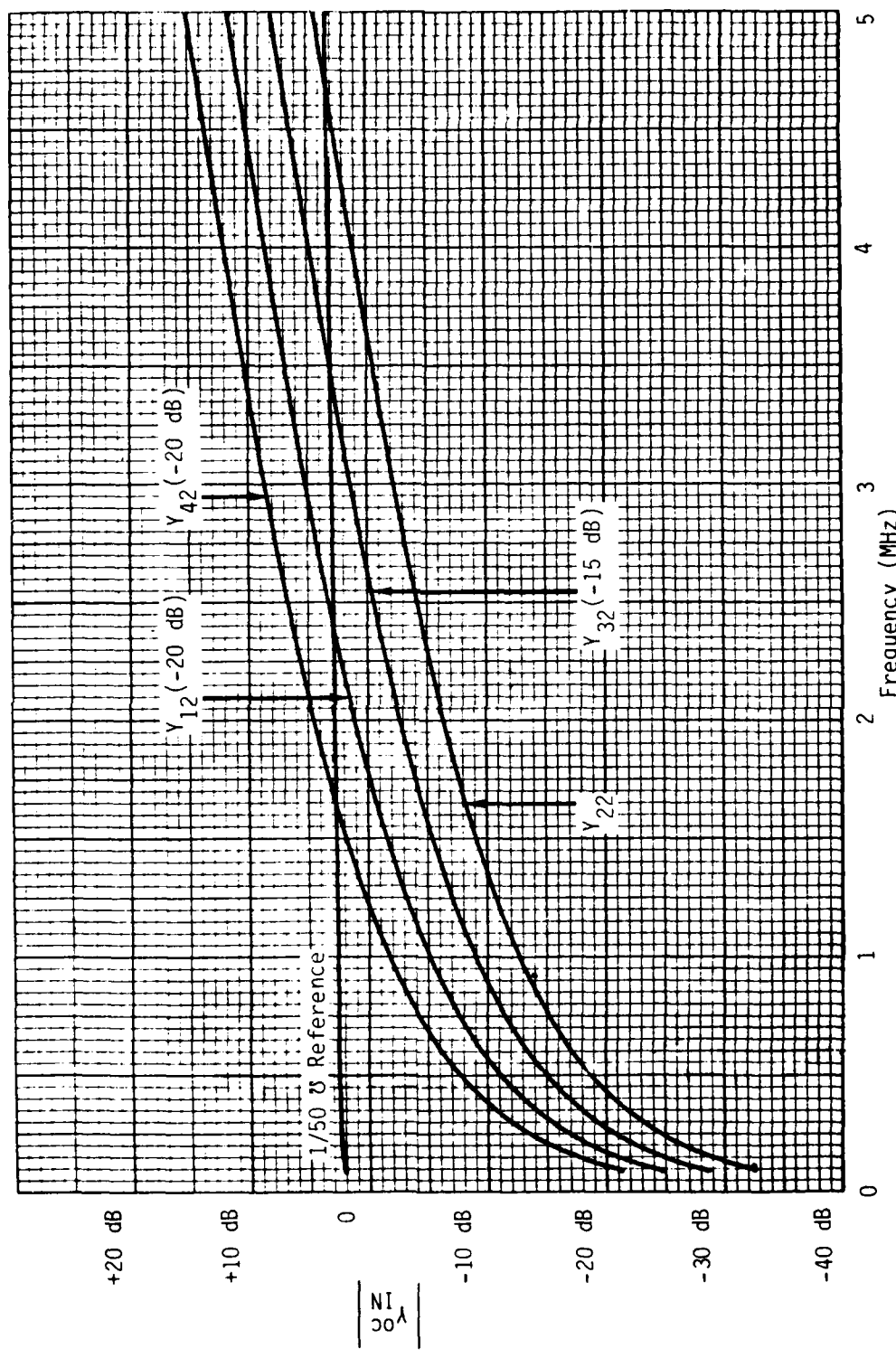


Figure 66. Open-circuit input-admittance data - four-wire line over ribs with clamps.

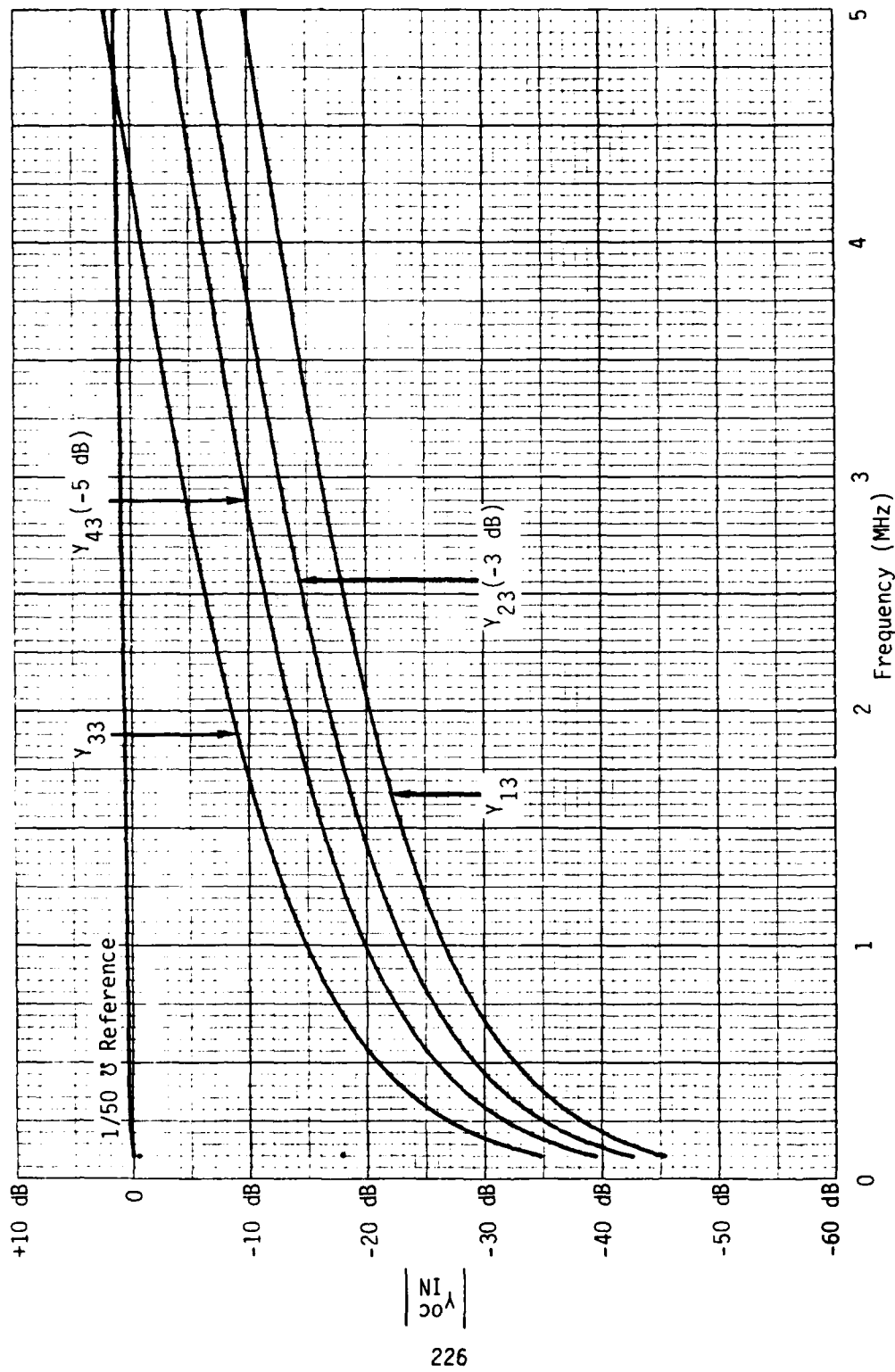


Figure D7. Open-circuit input-admittance data - four-wire line over ribs with clamps.

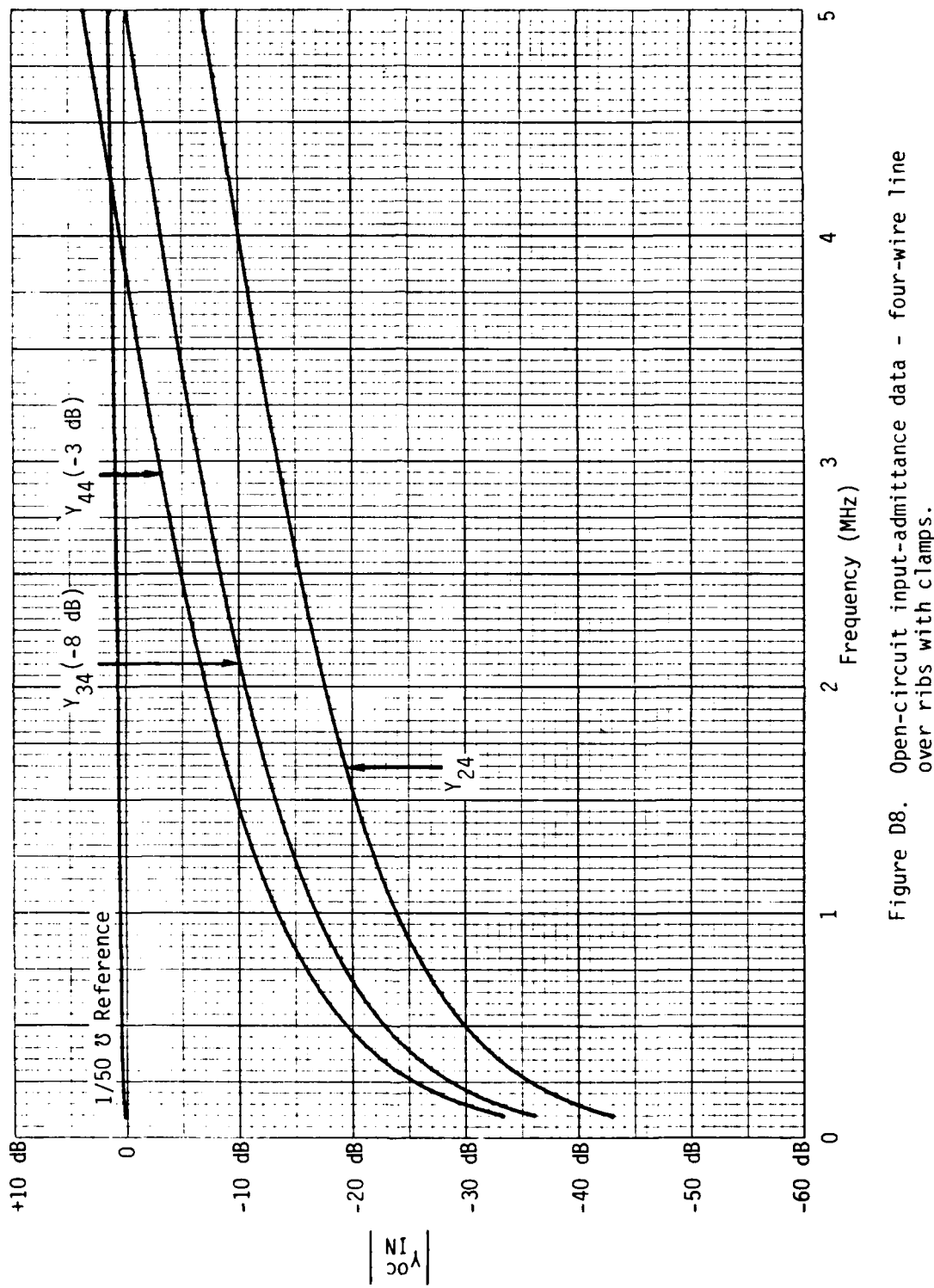


Figure D8. Open-circuit input-admittance data - four-wire line over ribs with clamps.

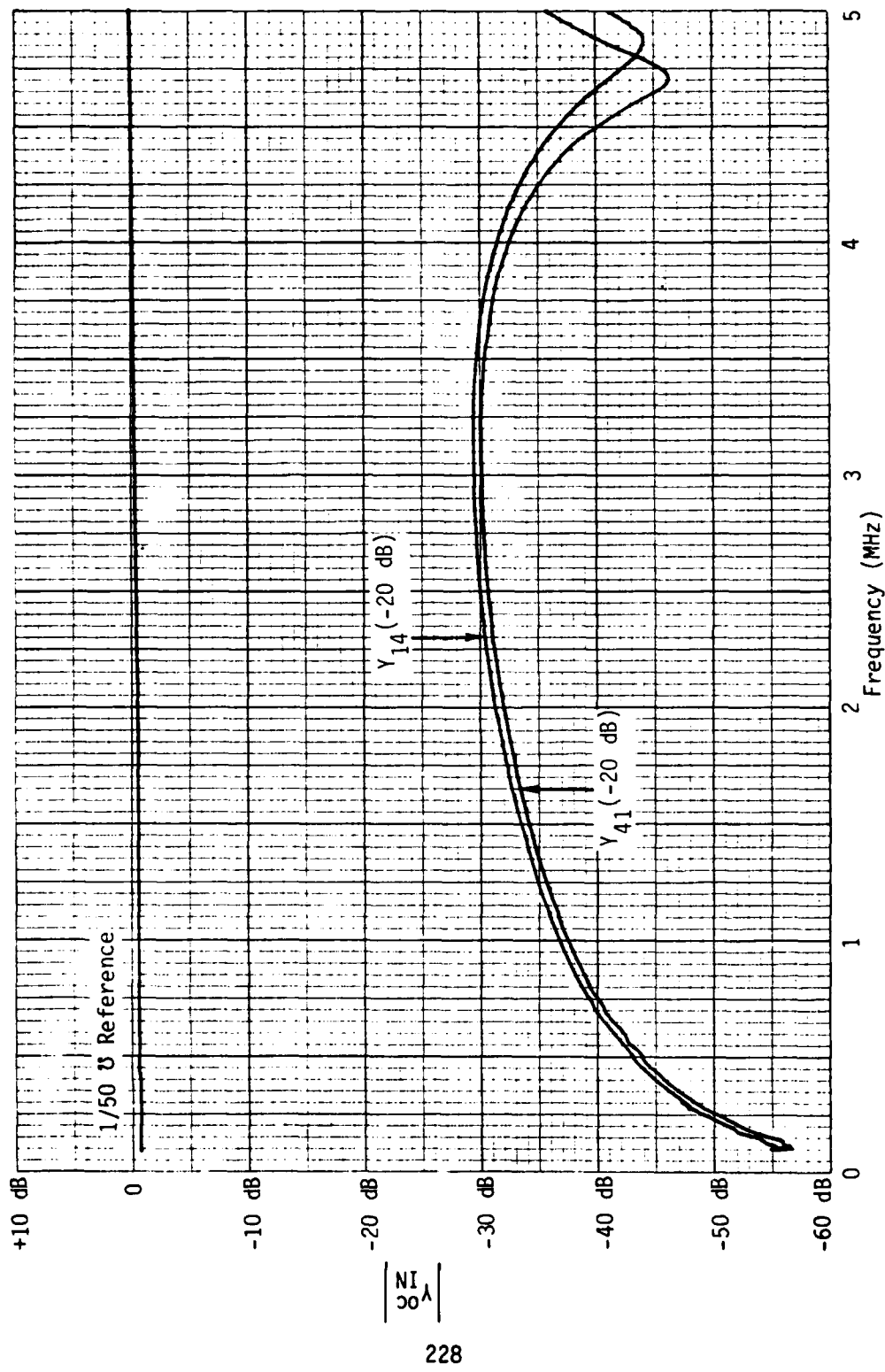


Figure D9. Open-circuit input-admittance data - four-wire line over ribs with clamps.

APPENDIX E
MEASURED INPUT IMPEDANCE AND ADMITTANCE DATA
(FOUR-WIRE LINE THROUGH 2" BULKHEADS)

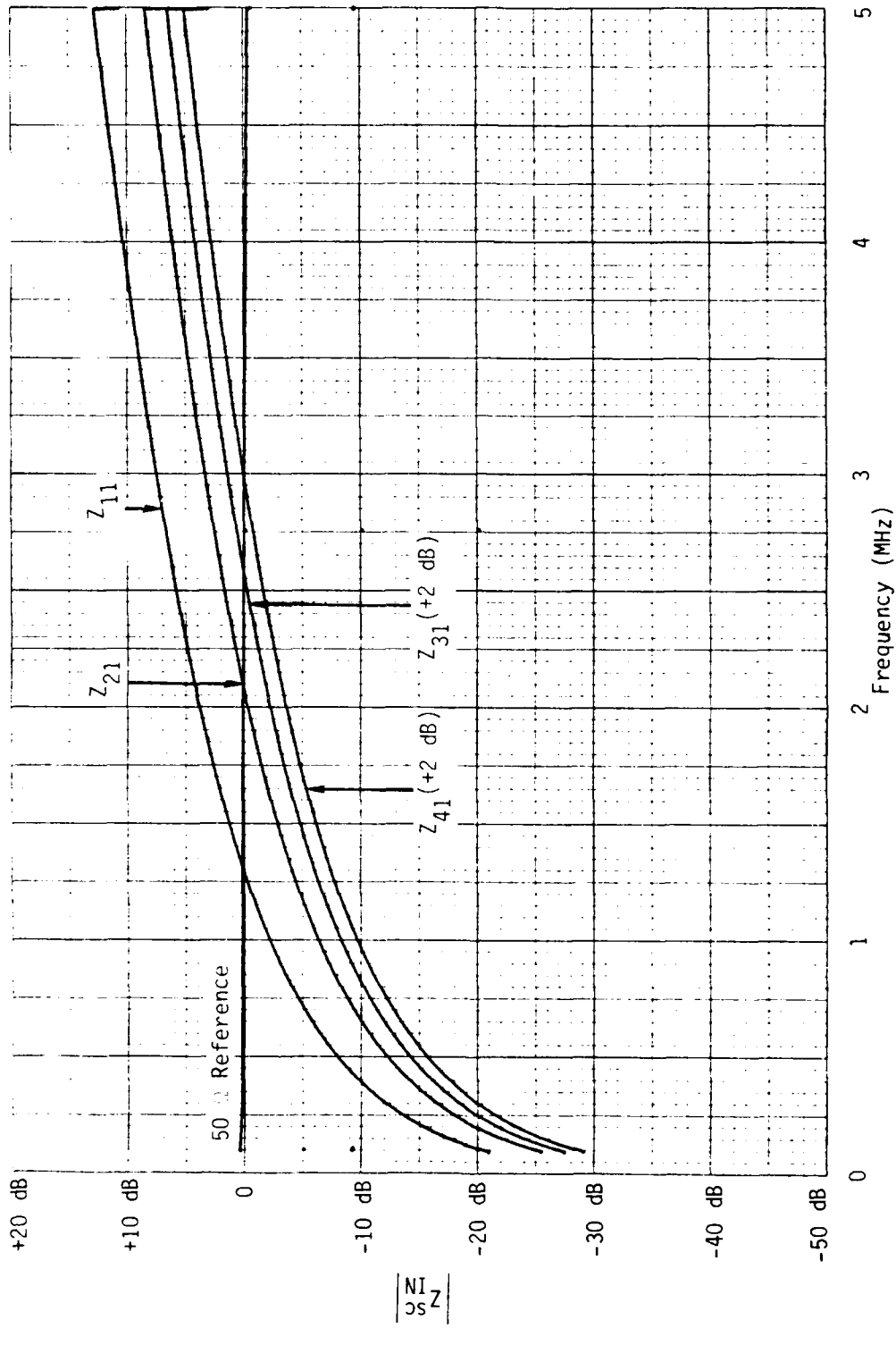


Figure E1. Short-circuit input-impedance data - four-wire line through 2" bulkheads.

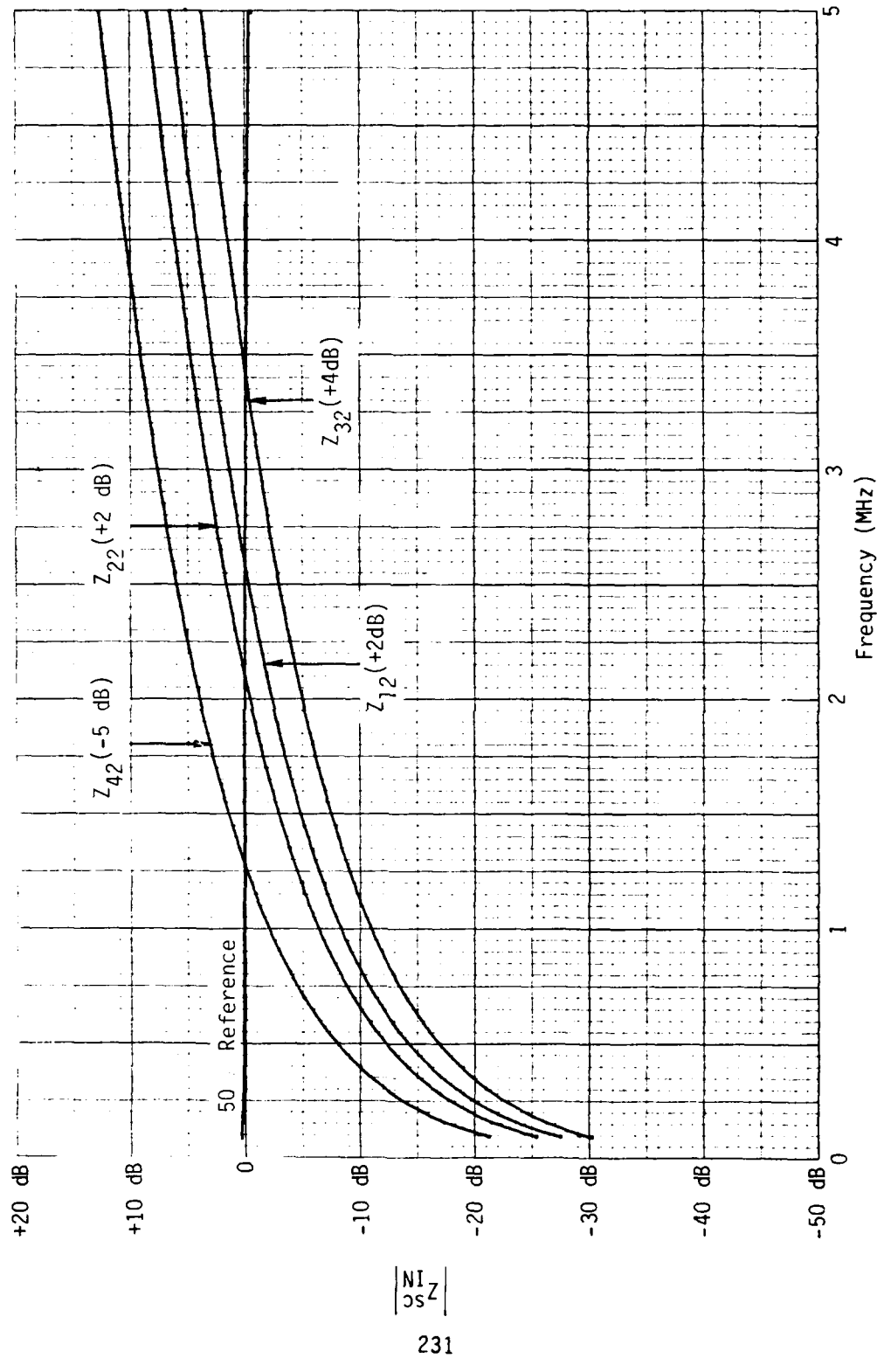


Figure E2. Short-circuit input-impedance data - four-wire line through 2" bulkheads.

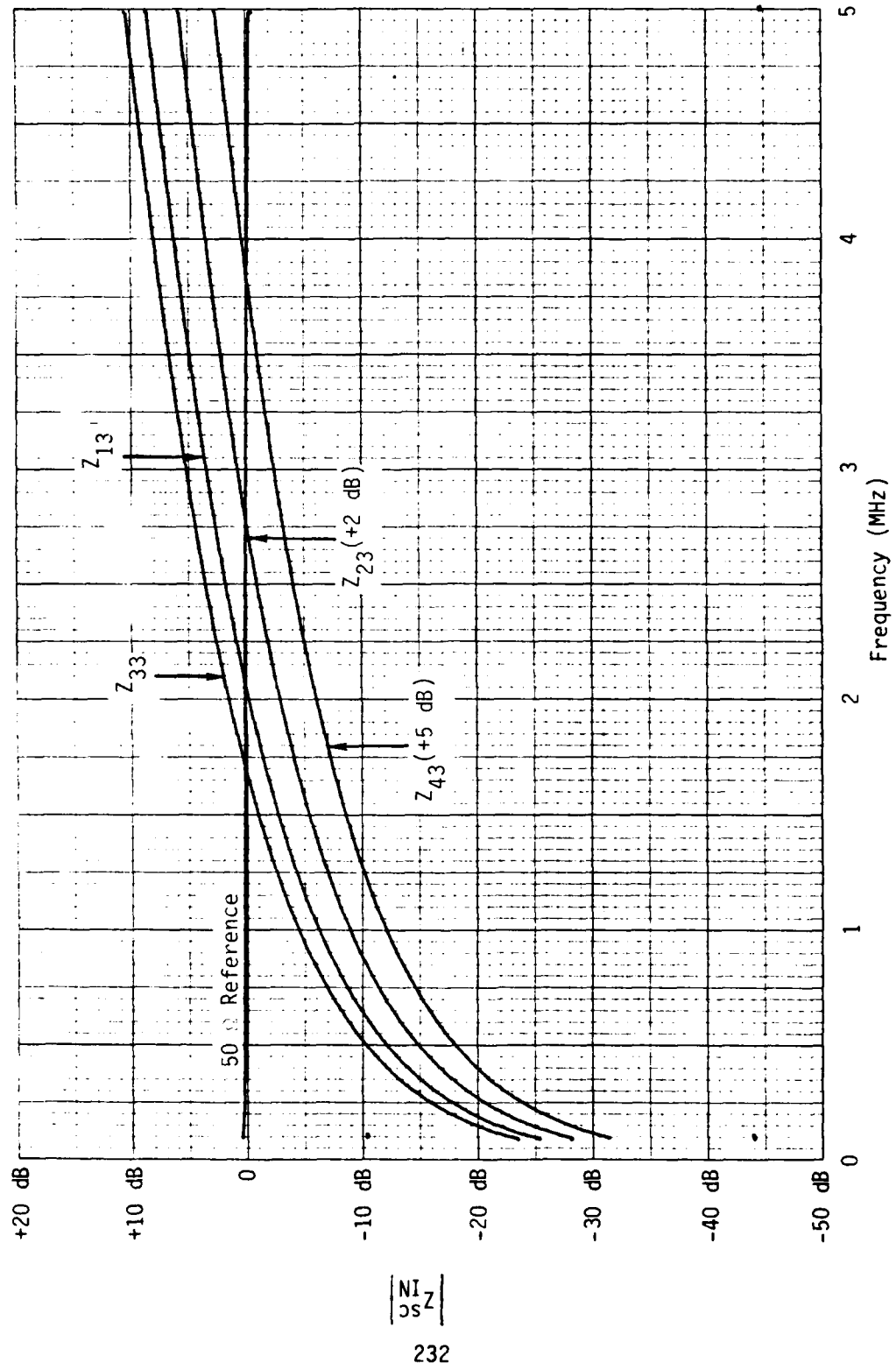


Figure E3. Short-circuit input-impedance data - four-wire line through 2" bulkheads.

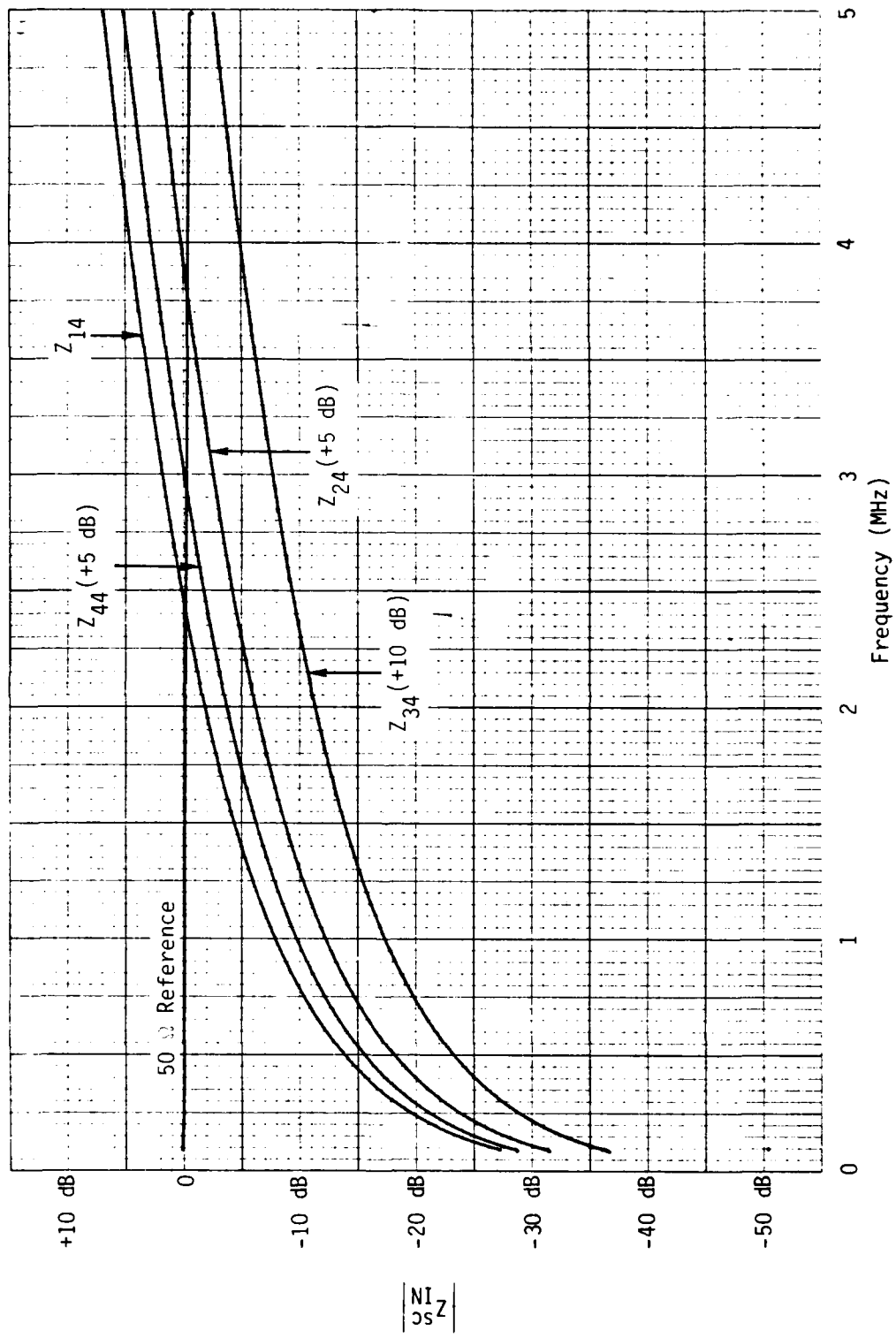
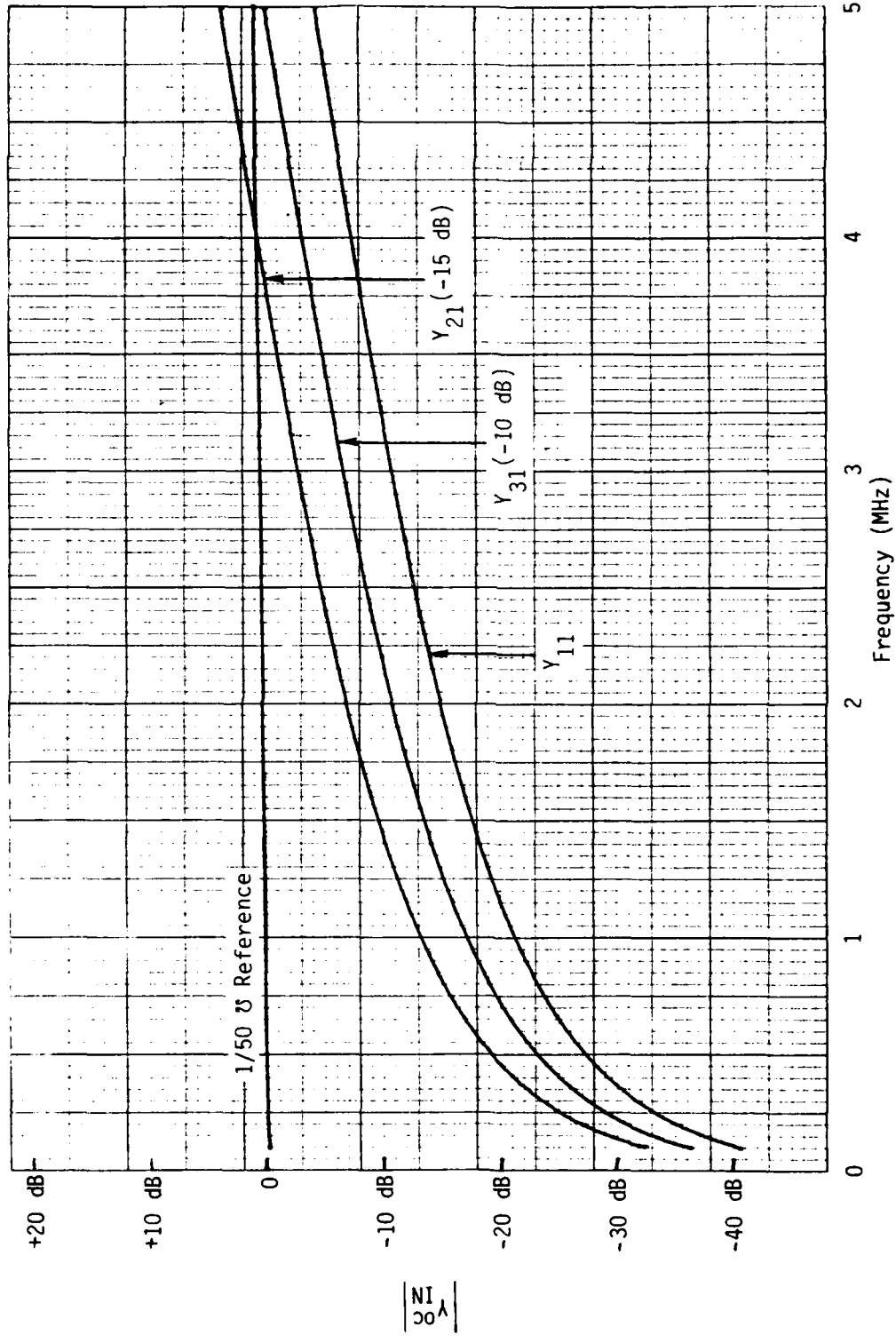


Figure E4. Short-circuit input-impedance data - four-wire line through 2" bulkheads.



234

Figure E5. Open-circuit input-admittance data - four-wire line through 2" bulkheads.

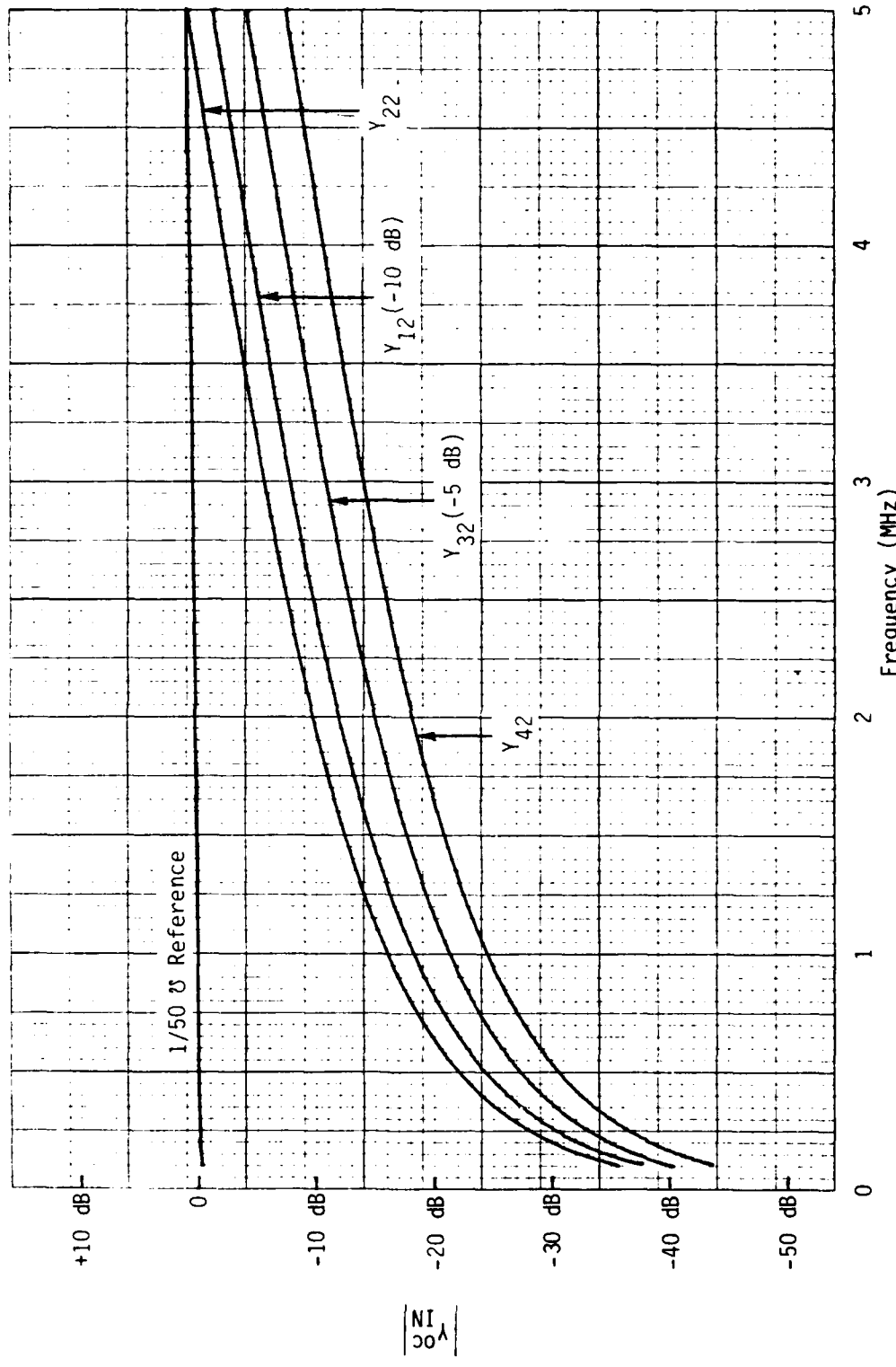


Figure E6. Open-circuit input-admittance data - four-wire line through 2" bulkheads.

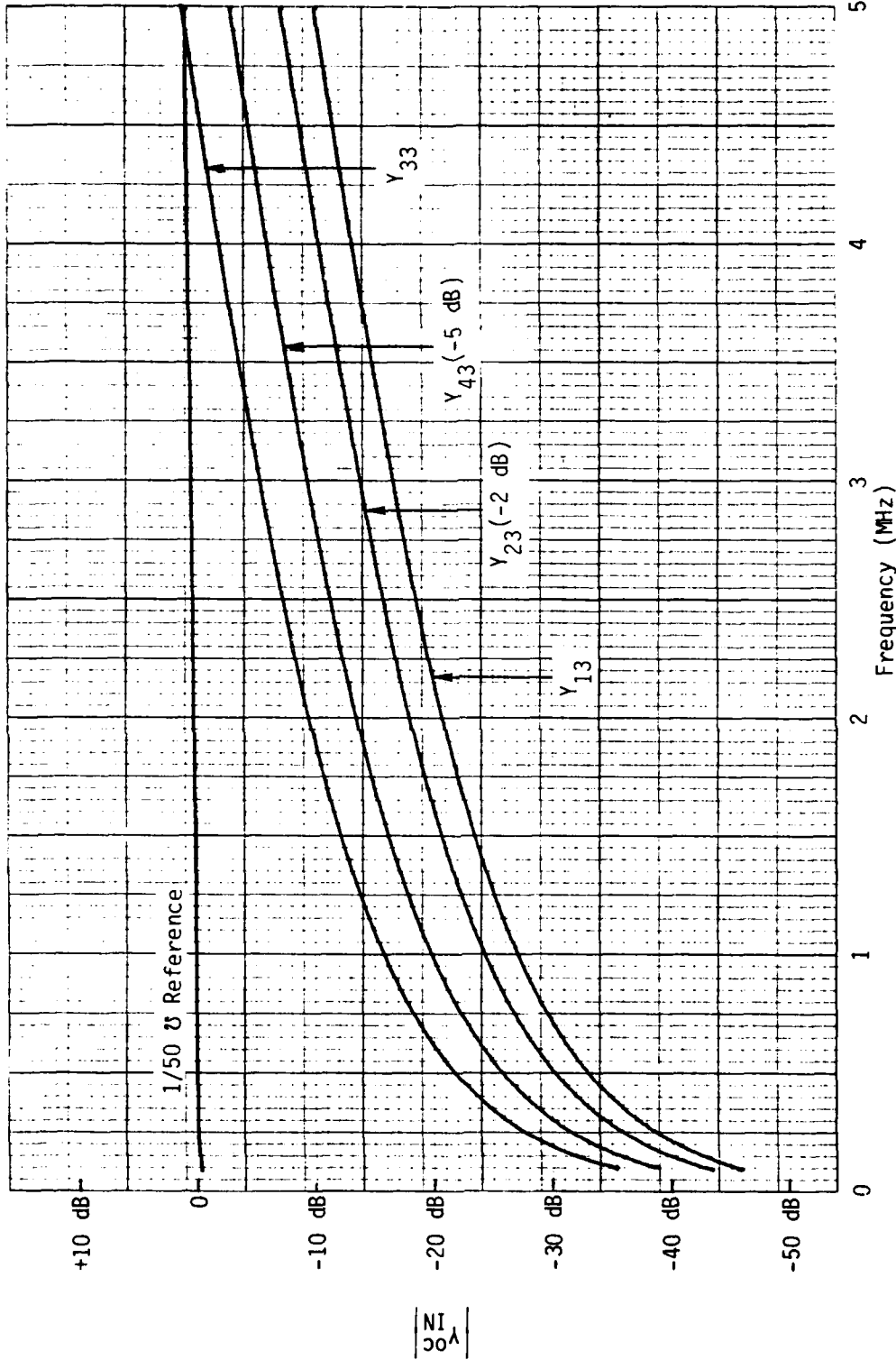


Figure E7. Open-circuit input-admittance data - four-wire line through 2" bulkheads.

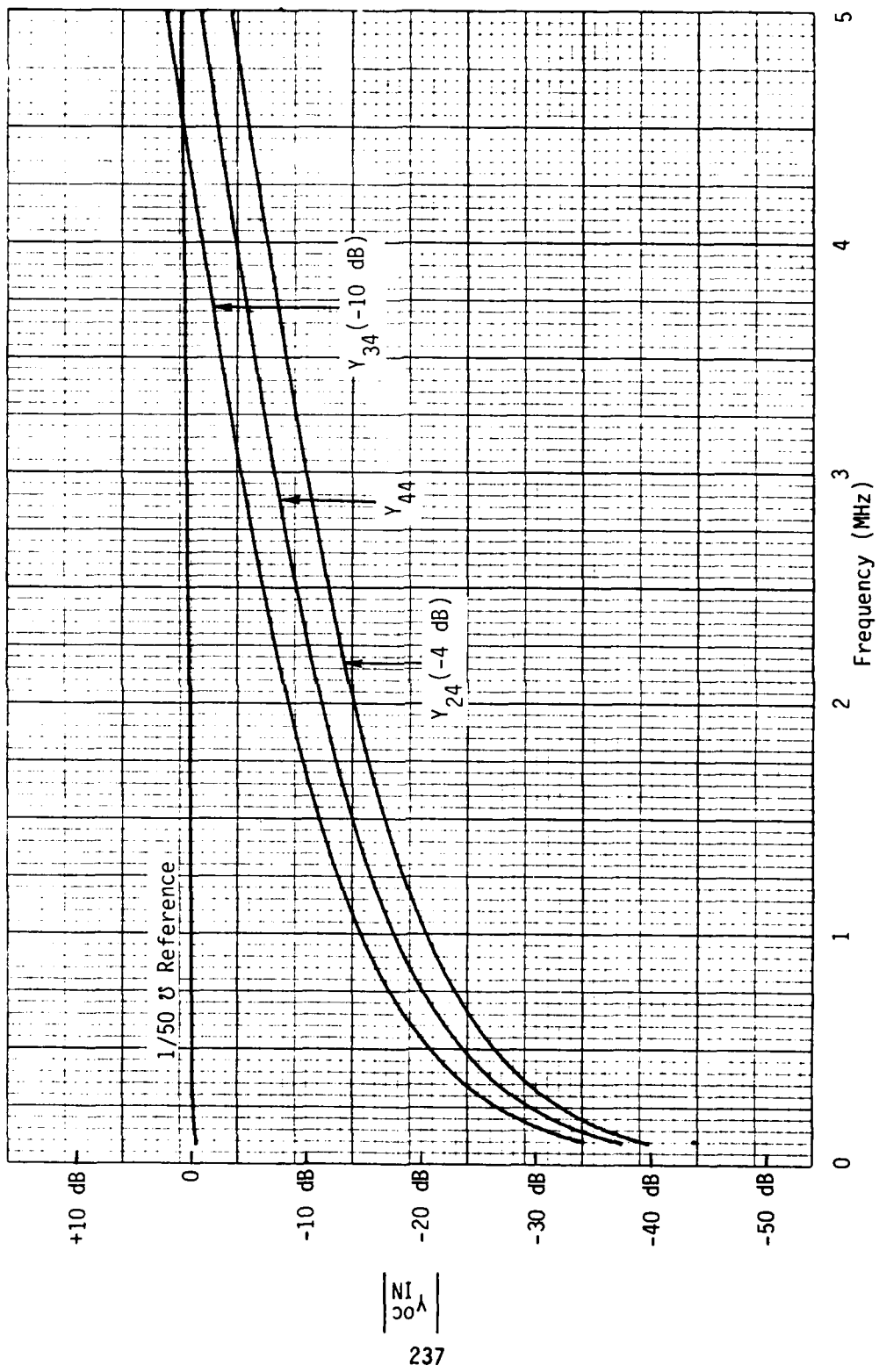


Figure E8. Open-circuit input-admittance data - four-wire line through 2" bulkheads.

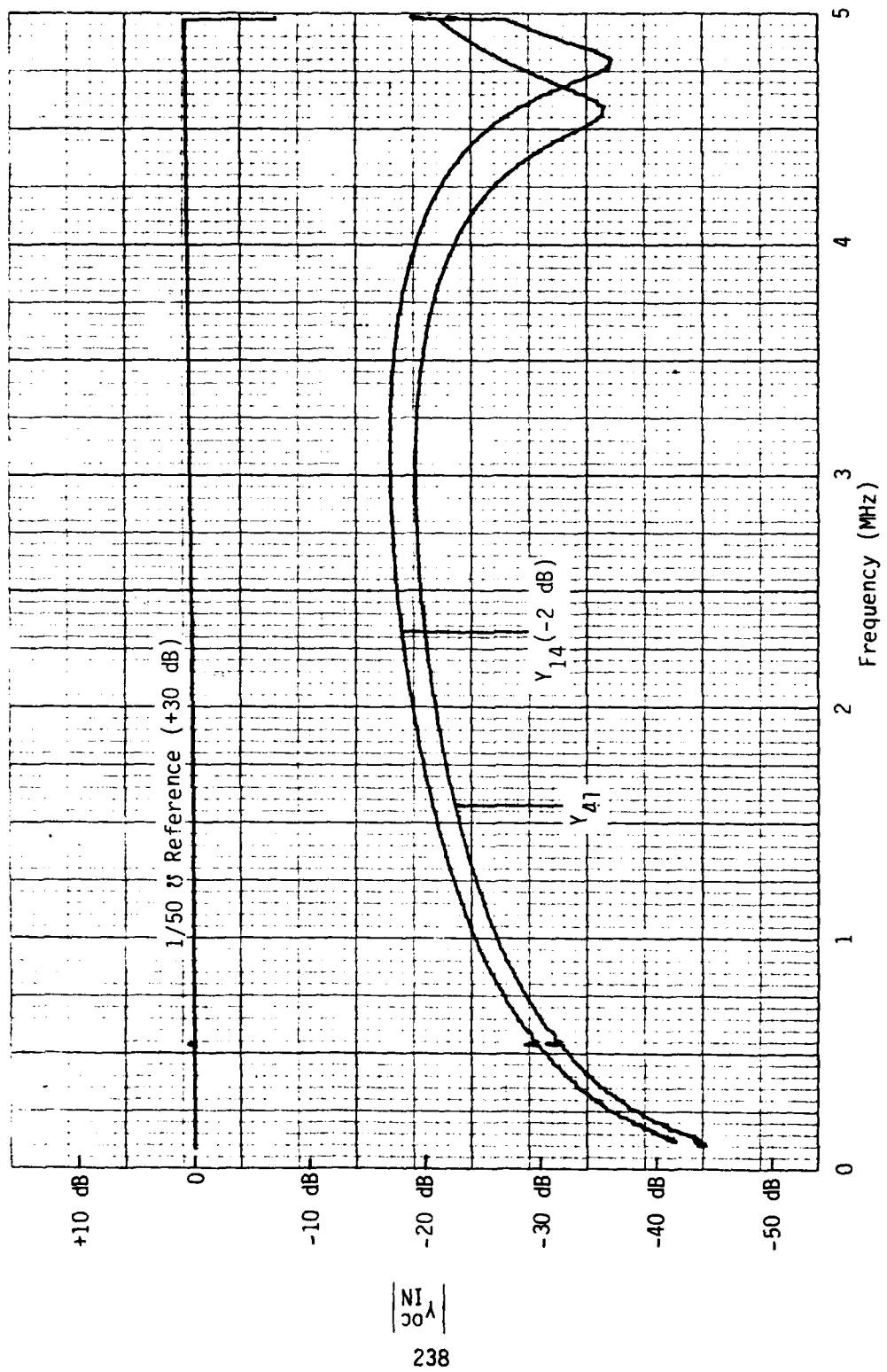


Figure E9. Open-circuit input-admittance data - four-wire line through 2" bulkheads.

